Technical Report Documentation Page

1. Report No.	2. Government Accession No.	3. Recipient's Catalog No.
CA15-2560		

4. Title and Subtitle	5. Report Date
Development Length for Headed Bars in Slab-Column Joints of RC Slab Bridges	12/4/2015
	6. Performing Organization Code
7. Author(s)	8. Performing Organization Report No.
Vasileios Papadopoulos, Juan Murcia-Delso and P. Benson Shing	UCSD/SSRP-15/10
9. Performing Organization Name and Address	10. Work Unit No. (TRAIS)
Department of Structural Engineering University of California, San Diego 9500 Gilman Drive, Mail Code 0085 La Jolla, California 92093-0085	11. Contract or Grant No. 65A0498
12. Sponsoring Agency Name and Address	13. Type of Report and Period Covered
California Department of Transportation Division of Engineering Services 1801 30th St., MS #9-2/5I Sacramento, California 95816	Final Report 14. Sponsoring Agency Code

15. Supplementary Notes

Prepared in cooperation with the State of California Department of Transportation.

16. Abstract

In accordance with the Caltrans Seismic Design Criteria, the superstructure in a slab bridge should remain essentially elastic and only the pile extensions/columns are permitted to develop inelastic deformations during a seismic event. Hence, the longitudinal reinforcement extending from a pile extension must have sufficient embedment length in the slab to develop the full tensile strength of the bars. The use of headed deformed bars can significantly reduce the required embedment length and also avoid congestion that could be introduced by hooked bars. According to ACI 318, for 5,000-psi concrete and Grade-60 bars, a minimum development length of 14 times the bar diameter (d_b) is required for headed bars. This may increase the cost of slab bridges because it may call for a thicker slab to accommodate the development length. However, the ACI specification does not take into account of the benefits of vertical stirrups present in the slab-column joint region of a slab bridge. The main objective of the research presented in this report is to determine the minimum development length required for headed bars in the slab-column joint region of a slab bridge designed according to MDT 20-7 (October 2014) of Caltrans, and to investigate if the development length can be reduced to $10d_b$. To this end, three full-scale slab-column assemblies were tested. The specimens had a 2-ft. diameter, 12-ft. tall cast-in-place RC column and a 16-in. thick slab. The columns were connected to the slabs with headed bars. Specimen #1 had an embedment length of $9.8d_b$ for the headed bars, while Specimens #2 and #3 had embedment lengths of $8.7d_b$ and $11d_b$, respectively. Specimen #3 had a drop cap in the slab to accommodate the longer development length. Grade-60 steel was used and the concrete had a target compressive strength of 5,000 psi. The study also includes nonlinear finite element analyses of slab-column assemblies and a numerical parametric study to evaluate design variables not covered in the experimental program. This study has shown that for slab concrete with an expected compressive strength of 4.5 ksi and Grade-60 steel, an embedment length of $11d_b$ is adequate for headed bars in slab-column joints designed according to MTD 20-7 (Caltrans, October 2014). Based on the test data, it is recommended that MTD 20-7 be modified to include four additional stirrups adjacent to the column cage, as it was done for Specimens #2 and #3. Furthermore, the amount of vertical stirrups in the 2nd row and farther away from the column cage can be reduced. The bar heads should be below the top mat of reinforcement in the deck slab. Embedment lengths of $8.7d_b$ and $9.8d_b$ were able to develop the moment capacity of the columns but resulted in moderate to severe punching cracks in the cover concrete of the slabs and more pinched lateral column force-vs.-column displacement hysteresis curves. However, a finite element analysis has shown that if there is not enough room to provide an embedment length of $11d_b$ in a 16-in. slab, it may be possible to reduce the embedment length and increase the distance of the bar head from the slab surface to reduce or avoid punching damage. This has to be confirmed by an experimental study.

17. Key Words	18. Distribution Statement
Headed bars, development length, anchorage, slab bridge, slab-column joint, punching, breakout, experimental, numerical, finite element analysis.	No restrictions. This document is available to the public through the National Technical Information Service, Springfield, Virginia 22161.

19. Security Classification (of this report)	20. Security Classification (of this page)	21. No. of Pages	22. Price
Unclassified	Unclassified	197	

Form DOT F 1700.7 (8-72) Reproduction of completed page authorized

STRUCTURAL SYSTEMS

RESEARCH PROJECT

Report No.
SSRP-15/10

Development Length for Headed Bars in Slab-Column Joints of RC Slab Bridges

by

Vasileios Papadopoulos
Juan Murcia-Delso
P. Benson Shing

Report Submitted to the California Department of Transportation under Contract No. 65A0498

December 2015

Department of Structural Engineering
University of California, San Diego
La Jolla, California 92093-0085

University of California, San Diego
Department of Structural Engineering
Structural Systems Research Project
Report No. SSRP-15/10

Development Length for Headed Bars in Slab-Column Joints of RC Slab Bridges

by

Vasileios Papadopoulos
Graduate Student Researcher

Juan Murcia-Delso
Postdoctoral Researcher

P. Benson Shing
Professor of Structural Engineering

Final Report Submitted to the California Department of Transportation under
Contract No. 65A0498

Department of Structural Engineering
University of California, San Diego
La Jolla, California 92093-0085
December 2015

DISCLAIMER

This document is disseminated in the interest of information exchange. The contents of this report reflect the views of the authors who are responsible for the facts and accuracy of the data presented herein. The contents do not necessarily reflect the official views or policies of the State of California or the Federal Highway Administration. This publication does not constitute a standard, specification or regulation. This report does not constitute an endorsement by the California Department of Transportation of any product described herein.

For individuals with sensory disabilities, this document is available in Braille, large print, audiocassette, or compact disk. To obtain a copy of this document in one of these alternate formats, please contact: the Division of Research and Innovation, MS-83, California Department of Transportation, P.O. Box 942873, Sacramento, CA 94273-0001.

TABLE OF CONTENTS

DISCLAIMER i

TABLE OF CONTENTS ii

LIST OF FIGURES v

LIST OF TABLES xii

ACKNOWLEDGMENTS xiii

ABSTRACT xiv

CHAPTER 1

INTRODUCTION 1

1.1 Background and Motivation of the Study 1

1.2 Scope of this Study and Organization of the Report 2

CHAPTER 2

DEVELOPMENT OF HEADED BARS: A LITERATURE REVIEW 5

2.1 Anchorage Behavior of Headed Bars 5

2.2 Experimental Studies on the Development of Headed Bars 6

2.3 Predictive Equations for the Anchorage Capacity of Headed Bars 10

2.4 Design Equations for the Development Length of Headed Bars 11

2.5 Final Remarks 11

CHAPTER 3

SLAB-COLUMN ASSEMBLY TEST PROGRAM 16

3.1 Test Specimens and Test Setup 16

3.2 Design Details and Materials 18

3.2.1 Specimen #1 18

3.2.2 Specimen #2 21

3.2.3 Specimen #3 22

3.3 Instrumentation 22

3.4 Loading protocol 23

CHAPTER 4

SLAB-COLUMN ASSEMBLY TEST RESULTS 42

4.1 General Observations and Lateral Load-vs.-Displacement Response 42

4.2 Detailed Test Observations 44

4.2.1 Specimen #1 44

4.2.2 Specimen #2 45

4.2.3 Specimen #3 47

4.3 Global Lateral Deformations 48

4.4 Strains in Column Longitudinal Bars 49

4.5 Strains in J-bars 50

4.6 Strains in Vertical Stirrups 51

4.7 Strains in Longitudinal Bars in Slabs 52

4.8 Conclusions 53

CHAPTER 5

FINITE ELEMENT ANALYSIS OF SLAB-COLUMN ASSEMBLIES 95

5.1 Finite Element Analysis of Pullout Tests on Headed Bars 95

5.2 Finite Element Analysis of Column-Slab Assemblies 97

5.2.1 Finite Element Model 98

5.2.2 Lateral Load-vs.-Displacement Response 99

5.2.3 Vertical Displacement underneath the Test Slabs 100

5.2.4 Strains in Column Longitudinal Bars 101

5.2.5 Strains in J-Bars 103

5.2.6 Strains in Vertical Stirrups 104

5.2.7 Strains in Longitudinal Bars in Slabs 105

5.2.8 Effectiveness of Slab Vertical Reinforcement to the Development of Headed Bars 106

5.2.9 Influence of Concrete Cover Thickness 107

5.3 Conclusions 108

CHAPTER 6

SUMMARY AND CONCLUSIONS 137

6.1 Summary 137

6.2 Observations 138

6.3 Conclusions and Recommendations 139

APPENDIX A: DESIGN DRAWINGS OF SLAB COLUMN ASSEMBLIES 141

REFERENCES 168

LIST OF FIGURES

Figure 1.1 – Available development length for a 16-in.-thick slab 4

Figure 2.1 – Anchorage of a headed bar (Thompson et al. 2002)..... 13

Figure 2.2 – Side-blowout failure (De Vries et al. 1996)..... 13

Figure 2.3 – Concrete breakout failure (De Vries et al. 1996)..... 14

Figure 2.4 – Bearing failure (Thompson et al. 2002)..... 14

Figure 2.5 – Concrete Breakout failure in a shallow embedment test (De Vries et al. 1999)..... 15

Figure 2.6 – Side-blowout failure in a beam-column joint test (Bashandy 1996) 15

Figure 3.1 – Slab-column assembly of a slab bridge 29

Figure 3.2 – Test setup for a slab-column assembly..... 30

Figure 3.3 – Picture of test setup (Specimen #1) 31

Figure 3.4 – Slab with drop cap in Specimen #3 31

Figure 3.5 – Column reinforcement for Specimen #1..... 32

Figure 3.6 – Plan view of slab reinforcement for Specimen #1 33

Figure 3.7 –Regions in a slab-column joint defined in MTD 20-7(October 2014) 34

Figure 3.8 – Picture of the slab and column reinforcement of Specimen #1 during construction 34

Figure 3.9 – Picture of the slab and column reinforcement of Specimen #1 prior to cast 35

Figure 3.10 – Stress-strain curve for material sample of column hoops in Specimen #1 35

Figure 3.11 – Column reinforcement for Specimen #2..... 36

Figure 3.12 – Plan view of slab reinforcement for Specimen #2..... 37

Figure 3.13 – Plan and elevation views for Specimen #3 38

Figure 3.14 – Plan view of slab reinforcement for Specimen #3..... 39

Figure 3.15 – Picture of slab and column reinforcement of Specimen #3 prior to casting..... 40

Figure 3.16 – Loading protocol..... 41

Figure 4.1 – Lateral force-vs.-drift ratio for Specimens #1 and #2 58

Figure 4.2 – Deflected shape of Specimen #1 at ductility 6 58

Figure 4.3 – Lateral force-vs.-drift ratio for Specimens #2 and #3 59

Figure 4.4 – Flexural cracks at the south face of the columns of Specimens #1 and #2 at Cycle 4 (1st yield) 59

Figure 4.5 – Evolution of damage at the bottom of the column of Specimen #1 60

Figure 4.6 – Strains in confining steel straps around the column of Specimen #1 60

Figure 4.7 – Evolution of damage in the slab of Specimen #1 61

Figure 4.8 – Damage at the bottom face of the slab (top face in the specimen) of Specimen #1 at the end of testing 61

Figure 4.9 – Crack pattern at the top face of the slab (bottom face in the specimen) after the testing of Specimen #1 62

Figure 4.10 – Exposure of fracture surface at the top face of the slab (bottom face in the specimen) of Specimen #1 63

Figure 4.11 – Evolution of damage at the bottom of the column of Specimen #2 63

Figure 4.12 – Evolution of damage at the bottom face of the slab (top face in the specimen) of Specimen #2 64

Figure 4.13 – Evolution of damage at the top face of the slab (bottom face in the specimen) of Specimen #2 65

Figure 4.14 – Damage at the top face of the slab (bottom face in the specimen) of Specimen #2 at the end of testing 66

Figure 4.15 – Exposure of fracture surface at the top face of the slab (bottom face in the specimen) of Specimen #2 67

Figure 4.16 – Evolution of damage at the base of the column of Specimen #3 68

Figure 4.17 – Evolution of damage at the bottom face of the slab (top face in the specimen) of Specimen #3 69

Figure 4.18 – Damage at the slab-column interface after the testing of Specimen #3 69

Figure 4.19 – Evolution of damage at the top face of the slab (bottom face in the specimen) of Specimen #3 70

Figure 4.20 – Vertical displacement of the top face of the slab (bottom face in the specimen) of Specimen #2 71

Figure 4.21 – Vertical displacement of the top face of the slab (bottom face in the specimen) of Specimen #3 71

Figure 4.22 – Lateral displacement of the column of Specimen #1 72

Figure 4.23 – Lateral displacement of the column of Specimen #2 72

Figure 4.24 – Lateral displacement of the column of Specimen #3 73

Figure 4.25 – Lateral load-vs.-slab rotation (at center) curves for Specimen #1 73

Figure 4.26 – Lateral load-vs.-slab rotation (at center) curves for Specimen #2 74

Figure 4.27 – Lateral load-vs.-slab rotation (at center) curves for Specimen #3 74

Figure 4.28 – Strains along Bar 1 in Specimen #1 75

Figure 4.29 – Stains along Bar 5 in Specimen #1 76

Figure 4.30 – Strain-vs.-ductility curves for Bar 1 in the slab-column joint of Specimen #1 77

Figure 4.31 – Strain-vs.-ductility curves for Bar 5 in the slab-column joint of Specimen #1 77

Figure 4.32 – Strains along Bar 1 in Specimen #2 78

Figure 4.33 – Strains along Bar 4 in Specimen #2 79

Figure 4.34 – Strain-vs.-ductility curves for Bar 1 in the slab-column joint of Specimen #2 80

Figure 4.35 – Strain-vs.-ductility curves for Bar 4 in the slab-column joint of Specimen #2 80

Figure 4.36 – Strains along Bar 1 in Specimen #3 81

Figure 4.37 – Strains along Bar 4 in Specimen #3 82

Figure 4.38 – Strain-vs.-ductility curves for Bar 1 in the slab-column joint of Specimen #3 83

Figure 4.39 – Strain-vs.-ductility curves for Bar 4 in the slab-column joint of Specimen #3 83

Figure 4.40 – Strains in J-bars of Specimen #1 84

Figure 4.41 – Strains in J-bars of Specimen #2 85

Figure 4.42 – Strains in J-bars of Specimen #3 86

Figure 4.43 – Strains in the 1st row of vertical stirrups of Specimen #1 87

Figure 4.44 – Strains in the 1st row of vertical stirrups of Specimen #2 88

Figure 4.45 – Strains in the 1st row of vertical stirrups of Specimen #3 89

Figure 4.46 – Strains in the 2nd row of vertical stirrups of Specimen #1 90

Figure 4.47 – Strains in the 2nd row of vertical stirrups of Specimen #2 91

Figure 4.48 – Strains in the 2nd row of vertical stirrups of Specimen #3 91

Figure 4.49 – Strains in longitudinal bars at the bottom face of the slab (top face in the specimen) of Specimen #1 92

Figure 4.50 – Strains in longitudinal bars at the bottom face of the slab (top face in the specimen) of Specimen #2 92

Figure 4.51 – Strains in longitudinal bars at the bottom face of the slab (top face in the specimen) of Specimen #3 93

Figure 4.52 – Strains in longitudinal bars at the top face of the slab (bottom face in the specimen) of Specimen #1 93

Figure 4.53 – Strains in longitudinal bars at the top face of the slab (bottom face in the specimen) of Specimen #2 94

Figure 4.54 – Strains in longitudinal bars at the top face of the slab (bottom face in the specimen) of Specimen #3 94

Figure 5.1 – FE model for pullout tests 112

Figure 5.2 – Stress-strain curve for steel model 112

Figure 5.3 – Tests by De Vries et al. (1996) 113

Figure 5.4 – Maximum principal strains in FE model of Specimen C16-6DB-1A by Choi et al. (2002) 113

Figure 5.5 – Maximum principal strains in FE model of Specimen C16-6DB-1D by Choi et al. (2002) 113

Figure 5.6 – FE model of slab-column Specimen #1 114

Figure 5.7 – FE assembly for reinforcement cage of Specimen #1 115

Figure 5.8 – Close-up details for the FE model of Specimen #1 115

Figure 5.9 – FE model of Specimen #3 116

Figure 5.10 – Lateral load-vs.-top drift curves from test and FEA of Specimen #1 117

Figure 5.11 – Lateral load-vs.-top drift curves from test and FEA of Specimen #2 117

Figure 5.12 – Lateral load-vs.-top drift curves from test and FEA of Specimen #3 118

Figure 5.13 – Vertical displacement of the top face of the slab (bottom face in the specimen) at the position of the headed bar on the south side of Specimen #1 $\left(l_e = 9.8d_b\right)$ 118

Figure 5.14 – Deformed FE mesh for Specimen #1 $\left(l_e = 9.8d_b\right)$ 119

Figure 5.15 – Vertical displacement of the top face of the slab (bottom face in the specimen) at the position of the headed bar on the south side of Specimen #2 $\left(l_e = 8.7d_b\right)$ 119

Figure 5.16 – Deformed FE mesh for Specimen #2 $\left(l_e = 8.7d_b\right)$ 120

Figure 5.17 – Vertical displacement of the top face of the slab (bottom face in the specimen) at the position of the headed bar on the south side of Specimen #3 $\left(l_e = 11d_b\right)$ 120

Figure 5.18 – Deformed FE mesh for Specimen #3 $\left(l_e = 11d_b\right)$ 121

Figure 5.19 – Strains in longitudinal Bar 1 from FEA (microplane) of Specimen #1 122

Figure 5.20 – Strains in longitudinal Bar 1 from FEA (microplane) of Specimen #2 123

Figure 5.21 – Strains in longitudinal Bar 1 from FEA (microplane) of Specimen #3 124

Figure 5.22 – Forces in longitudinal Bar 1 from FEA (microplane) of Specimen #2 125

Figure 5.23 – Forces in longitudinal Bar 1 from FEA (microplane) of Specimen #3 125

Figure 5.24 – Strains in J-bars of Specimen #1 126

Figure 5.25 – Strains in J-bars of Specimen #2 126

Figure 5.26 – Strains in J-bars of Specimen #3 127

Figure 5.27 – Strains in a vertical stirrup in the 1st row in the slab of Specimen #1 127

Figure 5.28 – Strains in a vertical stirrup in the 1st row in the slab of Specimen #2 128

Figure 5.29 – Strains in a vertical stirrup in the 1st row in the slab of Specimen #3 128

Figure 5.30 – Strains in a vertical stirrup in the 2nd row in the slab of Specimen #1 129

Figure 5.31 – Strains in a vertical stirrup in the 2nd row in the slab of Specimen #2 129

Figure 5.32 – Strains in a vertical stirrup in the 2nd row in the slab of Specimen #3 130

Figure 5.33 – Strains in the top longitudinal bar T3 in the slab of Specimen #1 130

Figure 5.34 – Strains in the top longitudinal bar T3 in the slab of Specimen #2 131

Figure 5.35 – Strains in the top longitudinal bar T3 in the slab of Specimen #3 131

Figure 5.36 – Strains in the bottom longitudinal bar B3 in the slab of Specimen #2 132

Figure 5.37 – Strains in the bottom longitudinal bar B3 in the slab of Specimen #3 132

Figure 5.38 – Deformed column and slab reinforcement from the FEA with the microplane model 133

Figure 5.39 – Lateral load-vs.-top drift curve from the FEA of Specimen #3B 133

Figure 5.40 – Deformed FE mesh for Specimens #3 and #3B $\left(l_e = 11d_b\right)$ 134

Figure 5.41 – Lateral load-vs.-top drift curve from the FEA of Specimen #3C 134

Figure 5.42 – Deformed FE mesh for Specimens #3 and #3C $\left(l_e = 11d_b\right)$ 135

Figure 5.43 – Lateral load-vs.-top drift curve from the FEA of Specimen #2B 135

Figure 5.44 – Deformed FE meshes for Specimens #2 and #2B 136

Figure 5.45 – Strains in vertical stirrup, V13, in the slab of Specimens #2 and #2B 136

Figure A.1 – Plan and elevation views for Specimen #1 141

Figure A.2 – Plan view of slab reinforcement for Specimen #1 142

Figure A.3 – Elevation view of slab reinforcement at Section BB for Specimen #1 142

Figure A.4 – Elevation view of slab reinforcement at Section CC for Specimen #1 143

Figure A.5 – Elevation view of slab reinforcement at Section DD for Specimen #1 143

Figure A.6 – Elevation view of slab reinforcement at Section EE for Specimen #1 143

Figure A.7 – Plan view of head reinforcement for Specimen #1 (same for Specimens #2 and #3) 144

Figure A.8 – Elevation views of head reinforcement at different sections for Specimen #1 (same for Specimens #2 and #3) 144

Figure A.9 – Plan and elevation views for Specimen #2 145

Figure A.10 – Plan view of slab reinforcement for Specimen #2 146

Figure A.11 – Elevation view of slab reinforcement at Section BB for Specimen #2 146

Figure A.12 – Elevation view of slab reinforcement at Section CC for Specimen #2 147

Figure A.13 – Elevation view of slab reinforcement at Section DD for Specimen #2 147

Figure A.14 – Elevation view of slab reinforcement at Section EE for Specimen #2 147

Figure A.15 – Plan and elevation views for Specimen #3 148

Figure A.16 – Column reinforcement for Specimen #3 149

Figure A.17 – Plan view of slab reinforcement for Specimen #3 150

Figure A.18 – Elevation view of slab reinforcement at Section BB for Specimen #3 150

Figure A.19 – Elevation view of slab reinforcement at Section CC for Specimen #3 151

Figure A.20 – Elevation view of slab reinforcement at Section DD for Specimen #3 151

Figure A.21 – Elevation view of slab reinforcement at Section EE for Specimen #3 152

Figure A.22 – Strain gages on longitudinal bars in the column of Specimen #1 153

Figure A.23 – Strain gages on J-bars and vertical stirrups in the slab of Specimen #1 154

Figure A.24 – Strain gages on the longitudinal bars in the slab of Specimen #1 155

Figure A.25 – Strain pots and inclinometers mounted on Specimens #1 156

Figure A.26 – Linear pots mounted on Specimen #1 157

Figure A.27 – Strain gages on longitudinal bars in the column of Specimen #2 158

Figure A.28 – Strain gages on J-bars and vertical stirrups in the slab of Specimen #2 159

Figure A.29 – Strain gages on the longitudinal bars in the slab of Specimen #2 160

Figure A.30 – Strain pots and inclinometers mounted on Specimens #2 161

Figure A.31 – Linear pots mounted on Specimen #2 162

Figure A.32 – Strain gages on J-bars and vertical stirrups in the slab of Specimen #3 163

Figure A.33 – Strain gages on longitudinal bars in the column of Specimen #3 164

Figure A.34 – Strain gages on the longitudinal bars in the slab of Specimen #3 165

Figure A.35 – Strain pots and inclinometers mounted on Specimen #3 166

Figure A.36 – Linear pots mounted on Specimen #3 167

LIST OF TABLES

Table 3.1 – Design details of slab-column specimens 25

Table 3.2 – Slab reinforcement in the slab-column joint region per MTD 20-7 (October 2014) 26

Table 3.3 – Concrete mix design for the slab of slab-column specimens 27

Table 3.4 – Concrete mix design for the column of slab-column specimens 27

Table 3.5 – Compressive and tensile strengths of concrete on the day of test 28

Table 3.6 – Yield and tensile strengths of steel reinforcement 28

Table 4.1 – Loading Protocol for Specimen #1 55

Table 4.2 – Loading Protocol for Specimen #2 55

Table 4.3 – Loading Protocol for Specimen #3 55

Table 4.4 – Contributions of different deformation sources to the column drift in Specimen #1 56

Table 4.5 – Contributions of different deformation sources to the column drift in Specimen #2 56

Table 4.6 – Contributions of different deformation sources to the column drift in Specimen #3 57

Table 5.1 – Key parameters of the D-P model for concrete 109

Table 5.2 – Key parameters of the microplane model for pullout tests 109

Table 5.3 – Numerical results for pullout tests 110

Table 5.4 – Steel material parameters for column longitudinal reinforcement 110

Table 5.5 – Compressive strengths of concrete (in ksi) for slab-column specimens 111

Table 5.6 – Calibration of the microplane model for the slab-column assemblies 111

ACKNOWLEDGMENTS

Funding for the investigation presented in this report was provided by the California Department of Transportation (Caltrans) under Contract No. 65A0498. The authors are most grateful to Mark Mahan, Mark Yashinsky, Ron Bromenschenkel, and Charles Sikorsky of Caltrans for their continuous technical input and advice throughout this study. Charles Sikorsky, who was the project manager, provided unfailing support and guidance to ensure the successful completion of this study.

The experiments presented in this report were conducted in the Charles Lee Powell Structural Engineering Laboratories at the University of California at San Diego. The authors would like to express their sincere gratitude to the laboratory staff, Christopher Latham, Paul Greco, Noah Aldrich and Darren McKay.

ABSTRACT

In accordance with the Caltrans Seismic Design Criteria, the superstructure in a slab bridge should remain essentially elastic and only the pile extensions/columns are permitted to develop inelastic deformations during a seismic event. Hence, the longitudinal reinforcement extending from a pile extension must have sufficient embedment length in the slab to develop the full tensile strength of the bars. The use of headed deformed bars can significantly reduce the required embedment length and also avoid congestion that could be introduced by hooked bars. According to ACI 318, for 5,000-psi concrete and Grade-60 bars, a minimum development length of 14 times the bar diameter (d_b) is required for headed bars. This may increase the cost of slab bridges because it may call for a thicker slab to accommodate the development length. However, the ACI specification does not take into account of the benefits of vertical stirrups present in the slab-column joint region of a slab bridge.

The main objective of the research presented in this report is to determine the minimum development length required for headed bars in the slab-column joint region of a slab bridge designed according to MDT 20-7 (October 2014) of Caltrans, and to investigate if the development length can be reduced to $10d_b$. To this end, three full-scale slab-column assemblies were tested. The specimens had a 2-ft. diameter, 12-ft. tall cast-in-place RC column and a 16-in. thick slab. The columns were connected to the slabs with headed bars. Specimen #1 had an embedment length of $9.8d_b$ for the headed bars, while Specimens #2 and #3 had embedment lengths of $8.7d_b$ and $11d_b$, respectively. Specimen #3 had a drop cap in the slab to accommodate the longer development length. Grade-60 steel was used and the concrete had a target compressive strength of 5,000 psi. The study also includes nonlinear finite element analyses of slab-column assemblies and a numerical parametric study to evaluate design variables not covered in the experimental program.

This study has shown that for slab concrete with an expected compressive strength of 4.5 ksi and Grade-60 steel, an embedment length of $11d_b$ is adequate for headed bars in slab-column joints designed according to MTD 20-7 (Caltrans, October 2014). Based on the test data, it is recommended that MTD 20-7 be modified to include four additional stirrups adjacent to the column cage, as it was done for Specimens #2 and #3. Furthermore, the amount of vertical stirrups in the 2nd row and farther away from the column cage can be reduced. The bar heads should be below the top mat of reinforcement in the deck slab.

Embedment lengths of $8.7d_b$ and $9.8d_b$ were able to develop the moment capacity of the columns but resulted in moderate to severe punching cracks in the cover concrete of the slabs and more pinched lateral column force-vs.-column displacement hysteresis curves. However, a finite element analysis has shown that if there is not enough room to provide an embedment length of $11d_b$ in a 16-in. slab, it may be possible to reduce the embedment length and increase the distance of the bar head from the slab surface to reduce or avoid punching damage. This has to be confirmed by an experimental study.

CHAPTER 1

INTRODUCTION

1.1 Background and Motivation of the Study

Slab bridges are economical to construct. For seismic resistance, Caltrans requires that these bridges, like other bridge types, be so designed that plastic hinges will be formed in substructure elements in the event of a major earthquake. The substructure elements can be RC pile *extensions*, columns, or pier walls. This requirement is stated in Memo to Designer (MTD) 20-7 (Caltrans, October 2014), and the Seismic Design Criteria (SDC) (Caltrans, April 2013). The pile extensions must behave in a ductile manner and meet the ductility requirements for column elements specified in Section 4.1 of SDC. In order for this to happen, a substructure element can be pin-connected to the deck slab, or the longitudinal reinforcement extending from a substructure element must have a sufficient embedment length in the slab to develop the full tension capacity of the longitudinal bars. Nevertheless, slab thickness determined in accordance with Bridge Design Aids (BDA) 4-10 – Design of Standard Slab Bridge (Caltrans 2009), which complies with the AASHTO LRFD Bridge Design Specifications (AASHTO 2014), often may not provide a sufficient embedment length to develop the longitudinal reinforcement even when standard hooks are provided. The use of headed deformed bars can significantly reduce the required embedment length and also avoid the congestion that could be introduced by hooked bars. For example, with 4,000 psi concrete, a Grade 60 No. 9 bar with a standard hook requires a development length of $19d_b$ according to Section 5.11.2.4 of the AASHTO LRFD Specifications (2014). If a headed bar is used, the development length can be reduced to $15d_b$ according to Section 12.6.2 of ACI 318-11 (ACI 2011). Considering that the expected compressive strength of concrete is at least 5,000 psi, MTD 20-7 (Caltrans 2014) and MTD 20-19 (Caltrans 2013) have an interim requirement that for a bar with a full-size head,

which has a net bearing area 9 times the bar cross-sectional area, the development length inside the slab be at least $14d_b$.

In spite of the aforementioned benefits, the use of headed bars in slab bridges had two major concerns. First, it was not clear as to whether the ACI 318-11 specification was intended for developing the full tensile strength of a bar or just the expected yield strength. Second, a development length of $14d_b$, as recommended in Caltrans MTD 20-19, might still be too long to be accommodated in a deck slab designed according to Caltrans BDA 4-10 and the AASHTO LRFD Specifications. For example, for No. 9 bars, $14d_b$ is 15.8 inches, while a multi-span slab bridge that has a maximum span length of 30 ft. can have a 16-in. thick slab, which can provide no more than 11.25 in. of embedment, as shown in Figure 1.1. Hence, there was a need to investigate if the development length for headed bars could be reduced to $10d_b$ not to have an unnecessarily thick slab.

1.2 Scope of this Study and Organization of the Report

The research reported here was conducted to determine the minimum development length required for headed longitudinal bars extending from the substructure elements into the deck slab of a slab bridge, and to investigate if the development length could be as short as $10d_b$.

Laboratory tests were conducted on three full-scale slab-column assemblies in an upside down position. Each of the slab-column assemblies had a 2-ft. diameter, 12-ft. tall, cast-in-place column, with the column height measured from the top surface of the slab to the elevation at which the lateral load was applied. The reinforcement details for the slabs and slab-column joints conform to Caltrans BDA 4-10 and MTD 20-7. With the tests, the performance of the slab-column joints for different embedment lengths was evaluated. For Specimen #1, eight No. 9 headed bars were used for the longitudinal reinforcement of the column. The thickness of the slab was 16 in. The embedment length was 11 in., which is $9.8d_b$ for No. 9 bars. For Specimen #2, the column longitudinal reinforcement consisted of six No. 10 headed bars.

It had the same thickness and same embedment length as Specimen #1. For No. 10 bars, an 11-in. embedment length corresponds to $8.7d_b$. For Specimen #3, six No. 10 headed bars were used for the column longitudinal reinforcement. A 3-in. drop cap was added to the 16-in. thick slab, providing an embedment length of $11d_b$ for No. 10 bars.

The study also includes nonlinear finite element analyses (FEA) of slab-column assemblies to evaluate the performance of the tests specimens before and after the tests, and a numerical parametric study to evaluate additional design variables.

Based on the experimental and numerical studies, the minimum desired development length has been determined and possible changes to MTD 20-7 for the design of slab-column joints have been suggested. Chapter 2 discusses the anchorage mechanism and capacity of headed reinforcing bars embedded in concrete, and presents a concise literature review of experimental studies conducted on this topic. Chapter 3 presents the test program and the design of the test specimens. Chapter 4 presents the experimental results. Chapter 5 presents the nonlinear finite element models for bar pull-out tests and slab-column tests and the numerical results, including a parametric study. Finally, the conclusions and design recommendations are presented in Chapter 6.

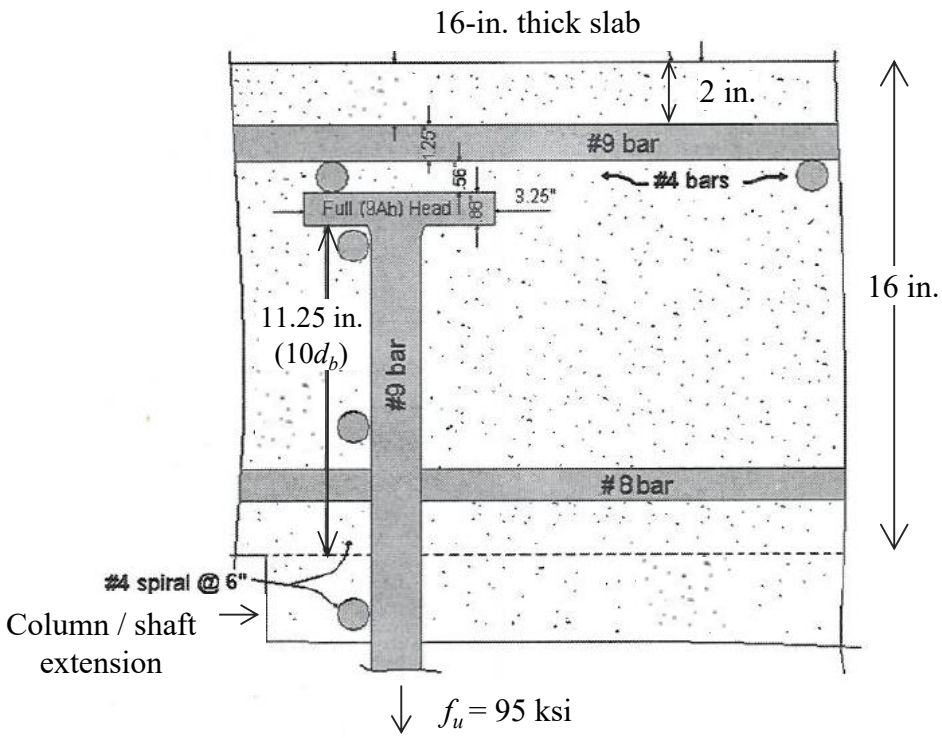

Figure 1.1 – Available development length for a 16-in.-thick slab

(MTD 20-19, Caltrans 2013)

CHAPTER 2

DEVELOPMENT OF HEADED BARS: A LITERATURE REVIEW

Reinforcing bars with headed ends (headed bars) are being increasingly used in reinforced concrete structures because they require less development length as compared to straight bars, and can reduce reinforcement congestion as compared to hooked bars. The development of tensile or compressive stress in a headed bar relies on the bearing action of the head as well as the bond stress along the embedment length of the bar. Headed bars have been extensively used in offshore platforms and nuclear power plant structures, which often have a large amount of large-diameter bars and do not have sufficient room to accommodate hooked bars. Headed bars are also desirable for joints in bridge and building structures, e.g., column-bent cap joints in bridges, and beam-column joints in buildings.

This chapter discusses the anchorage mechanism of headed reinforcing bars in concrete, and presents a concise literature review of experimental studies conducted to investigate the anchorage mechanism and capacity, and formulas and design equations available to determine the anchorage capacity and development length required of headed bars. A comprehensive literature review and summary of some of the early studies can be found in Thompson et al. (2002).

2.1 Anchorage Behavior of Headed Bars

The anchorage capacity of a headed bar is contributed by the bearing of the head against the concrete and the bond between the bar and the surrounding concrete, as shown in Figure 2.1. Past research has shown that the anchorage failure of a headed bar is governed by three main mechanisms: (1) side-face blowout failure of concrete when the bar is close to the edge of a concrete slab or block; (2)

concrete breakout failure when the embedment length is shallow; and (3) bearing failure at the anchor head. A side-blowout failure is characterized by the spalling of the concrete cover on the surface parallel and adjacent to the bar, as shown in Figure 2.2. This type of failure can occur in beams and columns, and has been observed in tests on bars with deep embedment lengths (as compared to the side cover) and in beam-column joint tests. Breakout failures are characterized by the formation of a pullout cone failure on the concrete surface perpendicular to the bar, as shown in Figure 2.3. A bar with a short embedment length, compared to the lateral concrete cover, such as a bar embedded in the central portion of a slab, may experience this type of failure. Bearing failure at the anchor head can be characterized by the lateral splitting and/or crushing of the concrete in front of the head, as shown in Figure 2.4. This type of failure has been observed in the anchorage region of longitudinal bars at the end of a beam.

2.2 Experimental Studies on the Development of Headed Bars

Stoker et al. (1974) conducted 18 pullout tests on No. 11, 14, and 18 Grade 60 headed bars, and one test on a straight No. 18 bar for comparison. The variables considered in their study included the embedment length, the concrete cover, and the concrete strength. The embedment length considered for the headed bars ranged from $11d_b$ to $37d_b$. The concrete specimens had reinforcement details representative of those in the cap beams of a box-girder bridge designed according to the specifications used in that time period. Four of the specimens had 4 No. 11 bars in a group, while the rest had single bars. In eight of these tests, loading was terminated before any failure occurred. Six of the specimens developed concrete failure in the anchorage region, and three had bar failure. The shortest embedment length that resulted in bar failure was $17d_b$, with the concrete strength equal to 4,840 psi. Their results also showed that bar groups had a weaker anchorage than single bars.

De Vries et al. (1996 and 1999) conducted over 140 pullout tests to evaluate the anchorage behavior and capacities of headed bars with variables including the embedment length (distance from the bearing surface of the bar head to the concrete surface), bonded length (less than or equal to the

embedment length), concrete strength, transverse reinforcement, head geometry, and edge distance of bars. Eighteen of these tests (De Vries et al. 1999) were conducted with shallow embedment lengths varying from $1.8d_b$ to $11.5d_b$. Some of the bars had a small edge distance of 2 in. Some of the concrete specimens had transverse reinforcement perpendicular to the bars. Of the 18 specimens, 3 had bar fracture while the rest had anchorage failure. Two of the specimens with bar fracture had an embedment length of $5.7d_b$ and a concrete compressive strength of 12,000 psi, while the third had twice as much embedment length and a concrete strength of 4,000 psi. These three specimens had the bar located at least 18 in. from the edges. Furthermore, the bars did not have bonding with the concrete. Therefore, the anchorage capacity was entirely provided by the bearing of the bar head against the concrete. For the other specimens, the failure mechanism was concrete breakout (with cone-shaped fracture) as shown in Figure 2.5. Their results showed that an embedment length as short as $11.5d_b$ could be sufficient to develop the full tensile capacity of headed bars embedded in 4,000-psi concrete without breakout failure. Furthermore, they observed that the bond force between a bar and the surrounding concrete slightly increased the anchorage capacity, and that the transverse reinforcement did not affect the anchorage capacity.

Bashandy (1996) conducted 32 pullout tests to study the anchorage behavior of headed bars in exterior beam-to-column joints. Each specimen had two headed reinforcing bars (mimicking the longitudinal bars extending from the beam) anchored in the column. The variables included the bar size (No. 8 and No. 11), the embedment length ($6d_b$ to $13d_b$), the ratio of the head area to the bar area (3 to 8.1), and the presence or absence of confining reinforcement in the joint. The compressive strength of concrete in the specimens was between 3,000 psi and 5,800 psi. The yield strength of the headed bars was approximately 80 ksi. During the tests, the bars did not yield and the load capacity was governed by anchorage failure in these tests. Eighteen specimens had side-blowout failure, as shown in Figure 2.6. The remaining fourteen had shear failure in the joint region. His study showed that the concrete cover,

embedment length, and confining reinforcement were the primary factors affecting the anchorage capacity, while the size of a head had little influence on the anchorage capacity.

Wright and McCabe (1997) conducted "beam-end" tests to examine the anchorage capacities of headed bars. The bars in their beam-end specimens had limited concrete cover. They considered only Grade 75 No. 8 bars with an embedment length of 12 in. ($12d_b$), and a concrete strength of 4,500 to 5,000 psi. The variables investigated were the concrete cover ($2d_b$ and $3d_b$), the bonded length of the bars, and the quantity and spacing of transverse reinforcement. The bars yielded in some of the tests, but none of the specimens was loaded to bar fracture. They observed that for a concrete cover of $2d_b$, the presence of transverse reinforcement enhanced the anchorage capacity of a bar. However, for a cover of $3d_b$, the effect of transverse reinforcement is not noticeable. Interestingly, they also showed that the addition of a PVC tube to avoid the bonding of the bar with the surrounding concrete reduced concrete cracking and increased the anchorage capacity. However, this seems to be related to the fact that the specimens had side-blowout failure.

The anchorage capacity of headed bars in compression-compression-tension (CCT) nodes of an idealized strut-&-tie model was studied by Thompson et al. (2005 and 2006a). In their tests, they observed that the anchorage failure in CCT nodes is characterized by the crushing of concrete in front of the bar ribs and lateral splitting. They postulated that the anchorage capacity of a headed bar in a CCT node was contributed by the bearing capacity of the concrete at the bar head and the bond force between the bar and the concrete. However, because the bond force would have passed the peak value before the peak bearing capacity would develop, a reduced bond strength should be considered in calculating the anchorage capacity. They also studied experimentally the behavior of lap splices using headed bars (Thompson et al. 2006b). Based on their experimental data, they proposed formulas to calculate the reduced bond strength and the bearing capacity of concrete against a bar head in CCT nodes and lap splices (Thompson et al. 2006c). They further concluded that the formulas were also applicable to headed

bars with deep embedment and beam-column joints. However, it seems that their model is valid only when the breakout failure of concrete is prohibited.

Choi et al. (2002) conducted pullout tests of headed bars to study the pullout capacity of a beam longitudinal bar terminated in a column-beam joint. They studied the effect of the column longitudinal and transverse reinforcement on the anchorage of single as well as multiple headed bars. No. 5, No. 6, and No. 7 bars were tested with concrete compressive strengths of 3.9 and 5.7 ksi. The bars had embedment lengths between $6d_b$ and $10d_b$. The column sections and reinforcement were different depending on the size and number of bars. The smallest section was 11.8 in. x 5.8 in., and the largest was 15.7 in. x 19.6 in. The column reinforcement consisted of No. 5 or No. 6 longitudinal bars and No. 3 or No. 4 stirrups. Only the bars which had an embedment length of $10d_b$ yielded. The tests revealed that reducing the spacing of the stirrups increased the pullout strengths of the bars. The amount of longitudinal reinforcement in the column did not affect the pullout strengths.

Kang et al. (2010) studied the behavior of bars with small heads ($2.7A_b$) in exterior beam-column joints. Pullout tests were conducted on No. 6 bars with a specified yield strength of 58 ksi. The bars were embedded $10d_b$ in 5,000-psi concrete blocks. Different types of heads and loading conditions (monotonic and cyclic) were tested. They were subjected to monotonic and cyclic loads. All the bars yielded and experienced strain hardening. The specimens failed by the splitting of the concrete and the local concrete crushing in front of the head. The anchorage strength was not significantly affected by the difference in the heads and the cyclic loading. Two beam-column assemblies were also tested under cyclic loading. One assembly had headed bars as the beam longitudinal reinforcement, and the other had hooked bars. Both had a development length of $15d_b$ in the beam-column joint. While the specimen with headed bars performed adequately, the anchorage failure of the hooked bars triggered an early failure of the joint.

2.3 Predictive Equations for the Anchorage Capacity of Headed Bars

De Vries et al. (1999) proposed the concrete capacity design (CCD) method, which was originally developed by Fuchs et al. (1995) and Eligehausen and Balogh (1995) for anchor bolts in concrete, for calculating the anchorage capacity of a headed bar in plain concrete. They validated this method with their test data from shallow-embedment pullout tests. For single headed bars with sufficient edge distance to allow a full cone-shaped failure, the following formula has been proposed:

$$P_n = 21.2 h_d^{1.5} \sqrt{f_c'} \tag{2.1}$$

in which P_n is the anchor capacity, h_d is the embedment length and f_c' is the specified concrete strength, with all units in pounds and inches. This formula was derived for a failure surface with a pyramidal shape and a $3\,h_d$ x $3\,h_d$ square base. For a group of bars, the failure surfaces of individual anchors may intersect, resulting in a total capacity less than the sum of the capacities of the individual anchors. To account for the group effects, as well as the reduction of the failure surface area due to edge placements, they have proposed a more general equation:

$$P_n = \Psi \frac{A_n}{9 h_d^{\,2}} 21.2 h_d^{1.5} \sqrt{f_c'} \tag{2.2}$$

in which P_n is the pullout capacity of the entire group of bars, A_n is the total failure surface area available, $9h_d^2$ is the failure surface for one bar, and Ψ is a factor to account for the reduction due to edge placement and is calculated as:

$$\Psi = 0.7 + 0.3 \frac{C_1}{1.5 h_d} \leq 1 \tag{2.3}$$

where C_1 is the minimum edge distance. The equations proposed by De Vries et al. (1999) do not consider the effect of the slab reinforcement on the capacity of the anchors.

2.4 Design Equations for the Development Length of Headed Bars

Based on the work of Thompson et al. (2005 and 2006a), ACI 318-11 (Section 12.6.2) has the minimum development length for headed bars in tension calculated with the following formula:

$$l_{dt} = \frac{0.016\psi_e f_y}{\sqrt{f_c'}} d_b \tag{2.4}$$

in which ψ_e shall be taken as 1.2 for epoxy-coated reinforcement and 1.0 for other cases, f_y is the specified yield strength of the reinforcing bar, d_b is the bar diameter, and f_c' is the specified compressive strength for concrete, which shall not exceed 6,000 psi. All units are in pounds and inches. The commentary in ACI 318-11 states that this formula considers the different possible failure modes of an anchorage, such as concrete breakout, side-face blowout, and pullout failures. By referring to the work of Thompson et al. (2005 and 2006b), it implies that bearing failure is also considered. Transverse reinforcement is perceived to be largely ineffective in improving the anchorage of headed bars. Therefore, it is not considered. Evidently, a formula that accounts for all these vastly different mechanisms must be empirical. However, it is not clear as to whether the formula is intended to develop the full tensile capacity of a bar or just the yield strength. For Grade 60 No. 9 bars and concrete with a specified compressive strength of 4,500 psi, Eq. (2.4) yields a minimum embedment length of 16 in., which cannot be accommodated in a typical slab bridge whose deck slab can have a thickness as small as 16 in. Furthermore, it is not clear as to whether the above formula applies to multiple headed bars in a slab-column joint, which may lead to intersecting failure surfaces and thereby reduce the anchorage capacity.

2.5 Final Remarks

In spite of the fact that a number of experimental studies have been conducted to evaluate the anchorage behavior and capacities of headed bars in concrete, there is no conclusive data or analytical models available to determine the minimum embedment length required for headed bars embedded in

concrete. Most of the tests conducted so far had either long development lengths or very short development lengths that resulted in anchorage failure. Some of the tests were terminated before reaching bar fracture or anchor failure. However, limited data have shown that an embedment length of $11d_b$ is a borderline condition to develop the full tension capacity of a single headed bar. The development length required is likely to be longer for groups of bars.

For slab bridges, if a column or pile extension is sufficiently far away from the edge of the deck slab, the anchorage failure of a headed bar will likely be caused by concrete breakout failure or the bearing failure at the anchor head. Studies have shown that the anchorage capacity of a headed bar group like that in a column or pile extension is weaker than that of a single bar. As to reinforcing details, there is limited data that indicates that stirrups placed parallel to an anchored bar contribute to the anchorage capacity, while stirrups placed transversely to the bar have small or no effect. However, the concrete specimens tested had reinforcing details very different from those in a typical column-slab joint of a slab bridge.

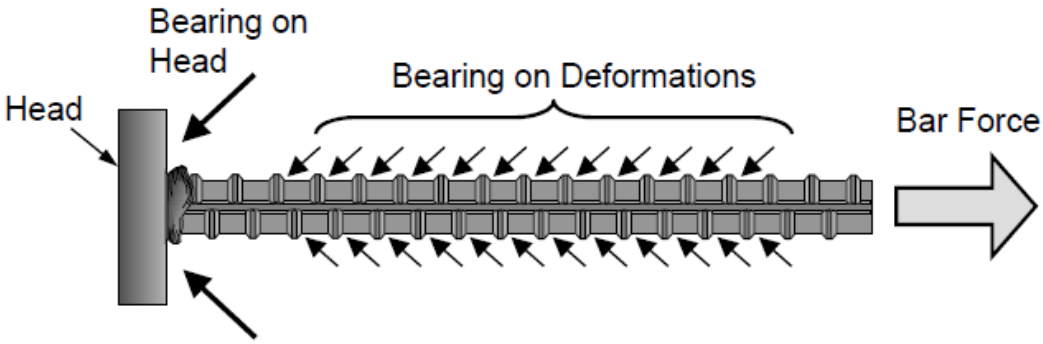

Figure 2.1 – Anchorage of a headed bar (Thompson et al. 2002)

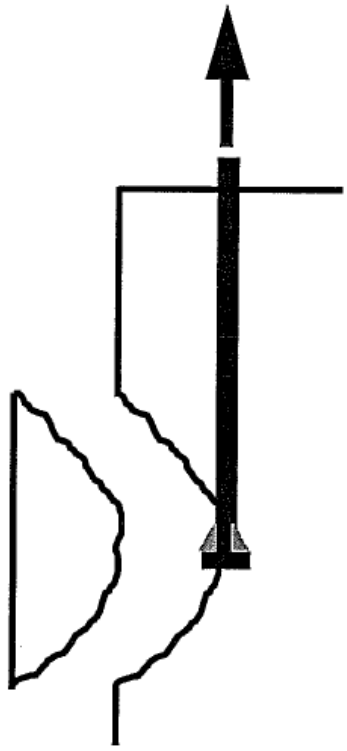

Figure 2.2 – Side-blowout failure (De Vries et al. 1996)

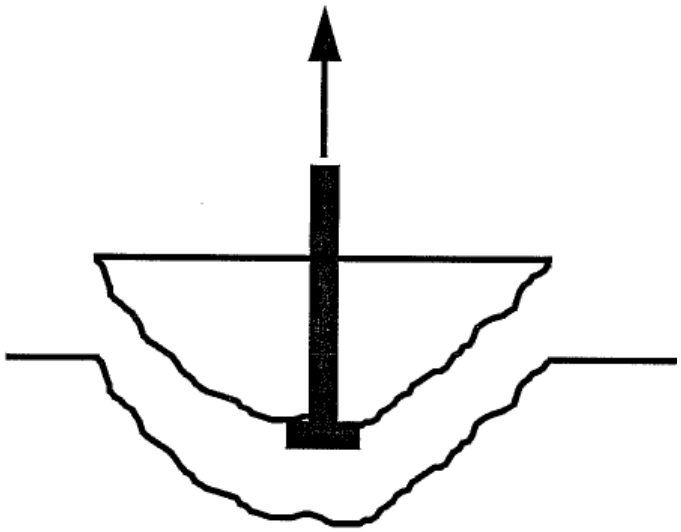

Figure 2.3 – Concrete breakout failure (De Vries et al. 1996)

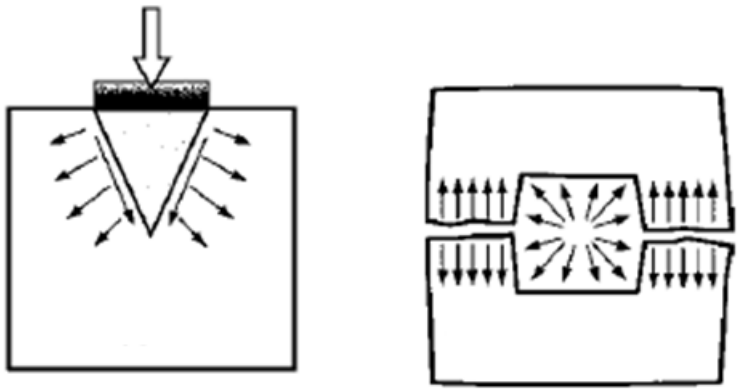

(a) Side view (b) Top view

Figure 2.4 – Bearing failure (Thompson et al. 2002)

Figure 2.5 – Concrete Breakout failure in a shallow embedment test (De Vries et al. 1999)

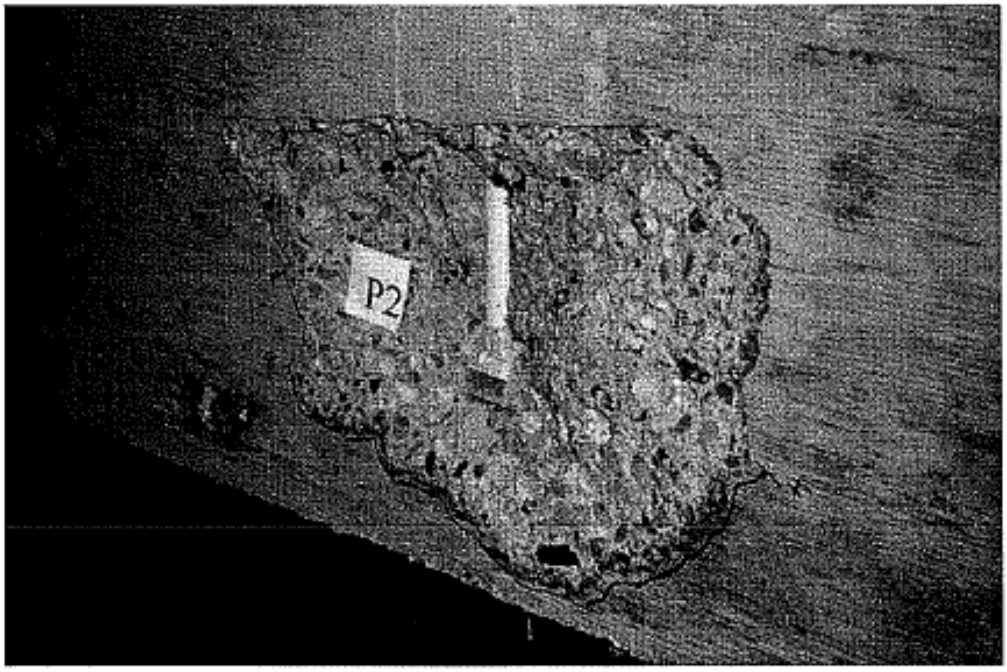

Figure 2.6 – Side-blowout failure in a beam-column joint test (Bashandy 1996)

CHAPTER 3

SLAB-COLUMN ASSEMBLY TEST PROGRAM

In this study, three full-scale slab-column assemblies were tested to assess the minimum development length required for headed longitudinal bars extending from a bridge column into the superstructure of a slab bridge, with the slab-column joint reinforced according to the requirements of Memo To Designer (MTD) 20-7 (Caltrans, October 2014), and in particular, to determine if a development length as low as $10d_b$ can be sufficient. This chapter presents the test program, including the design of the specimens, the test setup, the instrumentation, and the loading protocol. The test results are presented in Chapter 4.

3.1 Test Specimens and Test Setup

The test setup mimicked the loading condition for a slab bridge when it is subjected to a lateral seismic force in the transverse direction, as shown in Figure 3.1. As shown in the figure, the test assembly represented a portion of the bridge. The configuration of a test specimen and the test setup are shown in Figure 3.2. The slab-column assemblies were tested in an upside-down position with two edges of the slab hinge-supported. Each specimen was subjected to quasi-static cyclic lateral displacements in the north-south direction using a 220-kip load capacity, 48-in. stroke, actuator attached to the hammerhead of the column on the south side of the specimen. The other end of the actuator was attached to a strong wall. The hinge supports for the slab were based on the assumption that inflection points developed during the bending of the cap beam were located midway between two adjacent columns when the superstructure was subjected to the lateral seismic force. The point of horizontal application represented the inflection point of column bending. Figure 3.3 shows a picture of the test setup. The total axial compressive stress applied to the base section of the column was 3.5% of the targeted compression strength of the concrete.

It was applied by two post-tensioning rods anchored with a hinge mechanism at the bottom of the slab in the test configuration. This was to simulate the expected gravity load on the column from the superstructure. The locations of these rods were determined so that the applied loads would simulate the distribution of the tributary gravity load on the slab as close as possible. The forces in the post-tensioning rods were controlled by center-hole hydraulic jacks placed on top of the steel beam sitting on the hammer head. The pressure in the center-hole jacks was controlled in the tests so that the vertical load applied on the specimens remained constant. The post-tensioning rods passed through holes in the steel beam and the slab, and were anchored to the bottom of the slab with a hinge mechanism.

The specimens were designed according to the AASHTO LRFD Bridge Design Specifications (AASHTO 2014), and the Caltrans Seismic Design Criteria (SDC) (2013), MTD 20-7 (October 2014) and Bridge Design Aids (BDA) 4-10 (2009). Each of the slab-column assemblies had a 2-ft. diameter cast-in-place column with a height of 12 ft., measured from the bottom surface of the slab (top surface in the specimen) to the elevation at which the lateral load was applied. The main differences among the test specimens were the size of the longitudinal reinforcing bars in the columns and the thickness of the slab at the slab-column joint. Table 3.1 summarizes the design details of Specimens #1, #2 and #3. The specimens were tested in sequence, and the reinforcement details of the second and third specimens were based on the test results obtained from the first specimen.

For Specimen #1, eight No. 9 headed bars were used for the longitudinal reinforcement of the column. The thickness of the slab was 16 in. The embedment length for the headed bars was $9.8d_b$, measured from the bottom surface of the head to bottom surface of the slab considering the upright position of an actual bridge. This was the maximum embedment length practically possible for the 16-in. thick slab with the condition that the head of a bar had to be below the top mat of reinforcement in the slab. A pre-test finite element analysis using a model similar to that presented in Chapter 5 indicated that this length would be sufficient to develop the tensile strength of the headed bars.

Specimen #2 had six No. 10 headed bars for the longitudinal reinforcement of the column. The total cross-sectional area of the longitudinal reinforcement was almost the same as that for Specimen #1. The thickness of the slab was kept at 16 in. The embedment length provided for the headed bars was the same as that in Specimen #1 and is $8.7d_b$ for the No. 10 bars. This specimen was intended to establish the lower limit of the required development length.

Specimen #3 also had six No. 10 headed bars for the longitudinal reinforcement of the column. However, as shown in Figure 3.4, a 3-in. deep drop cap was added to the 16-in. thick slab, providing an embedment length of $11d_b$ for the headed bars. This specimen was intended to check if structural performance could be improved, in terms of the severity of punching cracks in the slab, with the increase of the development length.

3.2 Design Details and Materials

3.2.1 Specimen #1

The steel reinforcement for the column of Specimen #1 is shown in Figure 3.5. The column longitudinal reinforcement consisted of 8 No. 9 bars (with a reinforcement ratio of 1.77 %), and the transverse reinforcement consisted of No. 5 hoops spaced at 3.5 in. on center (with a volumetric reinforcement ratio of 1.77%). The concrete clear cover in the column was 2 in., measured from the outer perimeter of the transverse hoops. The column was connected to a 10 x 8 ft. slab with a thickness of 16 in. The embedment length of the column longitudinal bars in the slab was 11 in., which is $9.8d_b$, measured to the bottom face of the head considering the upright position of the assembly. This length is shorter than the $14d_b$ currently required in Caltrans MTD 20-7 and MTD 20-19 for concrete with a compressive strength of 5,000 psi.

The reinforcement details for the slab are shown in Figure 3.6. The clear concrete cover in the slab was 2 in., measured from the top and bottom most longitudinal bars in the slab. Detailed design drawings for the specimen are provided in Appendix A. The longitudinal slab reinforcement was determined according to BDA 4-10 for a 3-span bridge, with the length of each span equal to 30 ft. and a slab thickness of 16 in. The shear reinforcement was determined according to Section 5.13.3.6 of the AASHTO LRFD Bridge Design Specifications. The slab reinforcement within the effective bending width at a slab-column joint also complied with Caltrans SDC Section 4.3, which requires that the moment and shear capacities of the slab over the effective bending width be greater than the demands caused by the over strength moment capacity of the column. In addition to the longitudinal reinforcement required to carry the over strength of the column, extra longitudinal reinforcement was added within the effective bending width region of the slab according to the requirements of MTD 20-7, which are shown in Table 3.2. Different regions at a slab-column joint, as referred to in the table, are defined in Figure 3.7. As shown, MTD 20-7 requires J-bars in the core region of a joint, stirrups in the outer joint region and the joint perimeter region, horizontal side reinforcement, and a minimum amount of column hoops inside the slab. These reinforcement requirements are to ensure the structural integrity of a joint that is subjected the moment and shear exerted by the column, and are based on the recommendations of Ayoub and Sanders (2010) derived from a strut-and-tie model. However, the original recommendations have been modified to improve the implementation and to prevent breakout failure that could be induced by headed column bars with a reduced development length. Even though not specified in MTD 20-7, all the vertical stirrups and J-bars were hooked around the outermost longitudinal bars in the slab. The effectiveness of these requirements for the latter purpose is the subject of this investigation. These details can be seen in Figure 3.8, where a picture of the slab and column reinforcement during the construction of Specimen #1 is shown. The placement of the heads of the bars above the mat of the longitudinal and transverse reinforcement at the bottom face the slab specimen (top face in the bridge deck) can also be seen in the figure. Finally, the figure clearly shows the concrete cover of 2 in. measured from the longitudinal bars of the top face of the slab (bottom face in the specimen). The same detailing in the reinforcement was

followed for Specimens #2 and #3. Figure 3.9 shows the slab and column reinforcement of Specimen #1 before the concrete cast.

The concrete for the slab had a specified compressive strength of 4,000 psi at 28 days, a slump of 4 in., and a maximum aggregate size of 1 in. The mix design for the slab concrete is shown in Table 3.3. The concrete in the column had a specified compressive strength of 4,500 psi at 28 days, and the same slump and maximum aggregate size as those for the slab concrete. Table 3.4 summarizes the mix design for the column concrete. The concrete in the slab was poured first, and the concrete in the column was poured one week later. The specimens were to be tested when the strength of the concrete in the slab was close to but did not exceed 5,000 psi. It was intended that the strength of the column concrete would be equal to or higher than that of the slab concrete when the specimens were tested. The actual strengths of the concrete measured on the day of each test are presented in Table 3.5. All the reinforcement was Grade 60 complying with the ASTM A706 specifications. The column longitudinal reinforcement (HRC 150) had a full-size head (with a net bearing area of $9A_b$), complying with the ASTM A970 specifications. Results from material tests on the steel reinforcement for Specimen #1 are presented in Table 3.6. The material samples for the column hoops were cut and straightened prior to the test. As a result of the plastic deformation they experienced from bending, the stress-strain curves from the samples did not show a distinct yield plateau but a gradual transition from the elastic regime to the inelastic regime. Hence, the yield strength for the hoops is defined with the 0.2% offset strain method as shown in Figure 3.10.

As shown in Table 3.5, the concrete strength for the column was much lower than the expected. On the day of the test, the compressive strength was only 3,200 psi. This could be attributed to an over-compensation of water content in the concrete mix because of the small amount of concrete delivered in the truck as compared to that for a normal construction project. To avoid this problem, a larger amount of concrete was ordered for casting the subsequent specimens. The lower concrete strength could compromise the ductility of the column and might also slightly reduce its moment capacity, thus reducing the load demand on the slab-column joint. To circumvent this problem, external rings of steel straps were

added in the lower 4-ft. region of the column as exterior confinement, as shown in Figure 3.3. The straps were of Grade 50 steel, and were 1-in. wide with a thickness of 3/16 in. They were spaced at 4 in. on center. The rings were fabricated in halves and welded together at the site. Their inner diameter was 0.5 in. larger than the diameter of the column. A fluid grout with a specific compressive strength of 2,800 ksi was injected into the gaps between the column and the rings. The testing of three coupon samples from the steel straps showed a yield strength of 54 ksi and a tensile strength70 ksi.

3.2.2 Specimen #2

The steel reinforcement for the column of Specimen #2 is shown in Figure 3.11. Specimen #2 differed from Specimen #1 only in the longitudinal reinforcement in the column. Its longitudinal reinforcement consisted of 6 No. 10 bars (with a reinforcement ratio of 1.68 %). Figure 3.12 shows the plan view of the slab reinforcement for Specimen #2, while detailed design drawings are provided in Appendix A. The slab of Specimen #2 had the same thickness (16 in.) and the same reinforcement as that of Specimen #1, except that it had four additional vertical stirrups at positions next to the column cage, as shown in Figure 3.12. These four vertical stirrups were not required according to MTD 20-7 but were deemed useful as observed from the test of Specimen #1. The embedment length of the column longitudinal bars was 11 in., which is $8.7d_b$ for the No. 10 bars.

The concrete mix designs for Specimen #2 were the same as those for Specimen #1. The actual strengths of the concrete on the day of the test are presented in Table 3.5. For this specimen, both the slab and column concrete reached the desired strength even though the column concrete was a little weaker. All the reinforcement was Grade 60 complying with the ASTM A706 specifications. The strengths of the steel reinforcement from material tests are presented in Table 3.6.

3.2.3 Specimen #3

Specimen #3 had the same column design as Specimen #2 but differed in the slab design. It had a 16-in.-thick slab with a 3-in. deep drop cap. With the addition of the drop cap, the embedment length was 14 in., which is $11d_b$ for the No. 10 bars. The plan view of Specimen #3, along with the south and east elevation views are shown in Figure 3.13. The reinforcement for the drop-cap region was determined according to MTD 20-7. Figure 3.14 shows a plan view of the steel reinforcement for the slab. Detailed design drawings are provided in Appendix A. Figure 3.15 shows a picture of the slab and column reinforcement of Specimen #3 before the concrete cast.

The concrete mix designs specified for this specimen were the same as those for the other two specimens. The actual strengths of the concrete measured on the day of the test are provided Table 3.5. It should be noted that the slab concrete reached a compressive strength of 4,500 psi, which was a little lower than the targeted. All the reinforcement was Grade 60 complying with the ASTM A706 specifications. The strengths of the steel reinforcement from material tests are presented in Table 3.6.

3.3 Instrumentation

Electrical resistance strain gages were attached to selected column and slab reinforcement of the specimens. Strain gages were placed at different elevations in selected column longitudinal bars near the north and south faces of the specimen (which were loaded in the north-south) to monitor the strain distributions along these bars, including the strains along their embedment length in the joint region. The strain gages were placed on the longitudinal ribs of the bars to avoid disturbing the transverse ribs, which could affect the bond characteristics.

Displacement and rotation transducers were used to measure the lateral displacement of the column and the rotations of the slab. Vertical displacement transducers were mounted near the base of the column to measure the rotation of the column base with respect to the slab caused by bar slip.

For Specimens #2 and #3, two vertical transducers were placed underneath the slab to measure the vertical displacements of the top surface of the slab (bottom surface face in the specimen) at the positions of the two extreme longitudinal bars at the north and south faces of the column. These displacements were caused by the punching force of the headed bars as the rotation of the slab was extremely small. Detailed instrumentation plans for the specimens are provided in Appendix A.

3.4 Loading protocol

The test setup is shown in Figure 3.2 and Figure 3.3. In each test, the column was subjected to a constant vertical load of 70 kips using the two post-tensioned rods. Together with the self-weight of the column and the hammer head, this load subjected the base section of the column to an axial stress equal to 3.5% of the targeted compressive strength of the column concrete (which was 5,000 psi).

With the slab hinge-supported, the top of the column of each specimen was subjected to fully reverse lateral displacement cycles. The loading protocol is shown in Figure 3.16(a). Initially, the specimen was subjected to four fully-reversed force-controlled load cycles, with load amplitudes of 25, 50, 75, and 100% of the lateral load, F_y', that corresponds to the theoretical first yield of the longitudinal reinforcement at the base of the column. The specimen was then subjected to fully-reversed displacement-controlled load cycles with increasing ductility demands of 1, 2, 3, 4, and so forth, until the lateral load resistance dropped significantly. There were two cycles at each ductility level. The ductility demand is defined as $\mu = \Delta / \Delta_y$, in which Δ is the lateral displacement of the specimen at the level of the centerline of the horizontal actuators, and Δ_y is the effective yield displacement. As shown in Figure 3.16(b), Δ_y is defined as the displacement at the intersection of the secant line passing through the origin and the point $\left(\Delta_y', F_y'\right)$, which corresponds to the theoretical first yield of the column longitudinal bars, with the horizontal line passing through the theoretical ultimate load, F_y. Hence, it can be calculated as

$$\Delta_y = \frac{F_y}{F_y'} \Delta_y' \tag{3.1}$$

To determine the loading protocol, F_y' and F_y were estimated from finite element analyses using models that will be described in Chapter 5, and Δ_y' was taken as the average of the absolute maximum displacements measured in both loading directions in Cycle 4 of the test, in which the theoretical first yield was reached.

Table 3.1 – Design details of slab-column specimens

	Specimen #1	Specimen #2	Specimen #3
Column diameter	24 in.	24 in.	24 in.
Confined core diameter	20 in.	20 in.	20 in.
Column height	12 ft.	12 ft.	12 ft.
Column longitudinal bars	8 No. 9	6 No. 10	6 No. 10
Long. steel ratio	1.77 %	1.68 %	1.68 %
Column hoops	No. 5 @ 3.5 in.	No. 5 @ 3.5 in.	No. 5 @ 3.5 in.
Transverse steel ratio	1.77 %	1.77 %	1.77 %
Slab thickness at slab-column joint	16 in.	16 in.	19 in.
Embedment length of long. bars	11 in. ($9.8d_b$)	11 in. ($8.7d_b$)	14 in. ($11d_b$)

Table 3.2 – Slab reinforcement in the slab-column joint region per MTD 20-7 (October 2014)

Description	Requirement	Specimen #1	Specimen #2	Specimen #3
Area of flexural reinforcement in the longitudinal and the transverse directions within effective width	$A_{cap}^{top}, A_{cap}^{bot}$ = [Flexural reinf. required + additional reinf.] Addit. reinf. = $0.25 \times A_{st}$ for drop cap Addit. reinf. = $0.35 \times A_{st}$ for flat slab	No. 8 @ 6 in. (longitudinal) No. 8 @ 6 in. (transverse)	No. 8 @ 6 in. (longitudinal) No. 8 @ 6 in. (transverse)	No. 8 @ 6 in. (longitudinal) No. 7 @ 6 in. (transverse)
J-bars in the core zone of joint region	$A_s^{j-bar} = 0.35 \times A_{st}$	9 No. 5	9 No. 5	9 No. 5
Total area of vertical stirrups in Joint region	$A_s^{jv} = 1.15 \times A_{st}$	36 No. 5	40 No. 5*	40 No. 5*
Total area of vertical stirrups in Joint Perimeter	$A_s^{jvp} = 1.15 \times A_{st}$	32 No. 5	32 No. 5	32 No. 5
Horizontal ties	$A_s^{jh} = 0.1 \times A_{st}$	8 No. 3	8 No. 3	8 No. 3
Horizontal side reinforcement	$A_s^{sf} \geq \begin{cases} 0.1 \times A_{cap}^{top} \\ or \\ 0.1 \times A_{cap}^{bot} \end{cases}$	4 No. 4	4 No. 4	4 No. 4
Transverse column reinf. extended into slab	$A_{s,joint}^{v} \geq 0.18 \times A_{st}$	3 No. 5 hoops	3 No. 5 hoops	3 No. 5 hoops

*Slightly more than that required by MTD 20-7.

Table 3.3 – Concrete mix design for the slab of slab-column specimens

Specified compressive strength = 4,000 psi		
Material	Quantity	Proportion of Aggregate (%)
Cement	560 lbs./yd^3	-
Flyash	118 lbs./yd^3	-
1'' x #4 Agg.	1344 lbs./yd^3	44
3/8'' x #8 Agg.	351 lbs./yd^3	11
Fine Agg.	1286 lbs./yd^3	45
Water (w/c)	38.1 gl./yd^3 (0.471)	-
WRDA-64 (admixture)	25 oz./yd^3	-
Air content	2 %	-

Table 3.4 – Concrete mix design for the column of slab-column specimens

Specified compressive strength = 4,500 psi		
Material	Quantity	Proportion of aggregate (%)
Cement	560 lbs./yd^3	-
Flyash	118 lbs./yd^3	-
1'' x #4 Agg.	1223 lbs./yd^3	42
3/8'' x #8 Agg.	445 lbs./yd^3	15
Fine Agg.	1240 lbs./yd^3	43
Water (w/c)	39 gl./yd^3 (0.448)	-
WRDA-64 (admixture)	21 oz./yd^3	-
Air content	2 %	-

Table 3.5 – Compressive and tensile strengths of concrete on the day of test

Specimen	Region	Compressive strength of concrete (ksi)	Splitting tensile strength of concrete (ksi)
#1	Column	3.2[1]	0.46
	Slab	5.0	0.35
#2	Column	4.8	0.41
	Slab	4.9	0.45
#3	Column	5.0	0.43
	Slab	4.5	0.43

[1]To compensate for the low concrete strength, the column was externally confined with Grade 50 steel rings; fluid grout with a specified compressive strength of 2,800 ksi was injected between the column and the rings. The low concrete strength could be attributed to an over-compensation of water content in the mix.

Table 3.6 – Yield and tensile strengths of steel reinforcement

Specimen	Reinforcement	Bar size	Yield strength, ksi	Tensile strength, ksi
#1	Column longitudinal bars	No. 9	69.0	99.5
	Column hoops	No. 5	67.5 [1]	91.2
	Slab longitudinal bars	No. 8	66.5	91.5
	Vertical ties in slab	No. 5	67.5	96.0
#2	Column longitudinal bars	No. 10	64.5	94.2
	Column hoops	No. 5	69.6 [1]	92.2
	Slab longitudinal bars	No. 8	68.2	98.2
	Vertical ties in slab	No. 5	61.0	85.0
#3	Column longitudinal bars	No. 10	71.1	90.1
	Column hoops	No. 5	64.0 [1]	97.9
	Slab longitudinal bars	No. 7	64.5	96.5
	Slab longitudinal bars	No. 8	67.6	97.5
	Vertical ties in slab	No. 5	63.2	90.1

[1]Stress at 0.002 plastic strain.

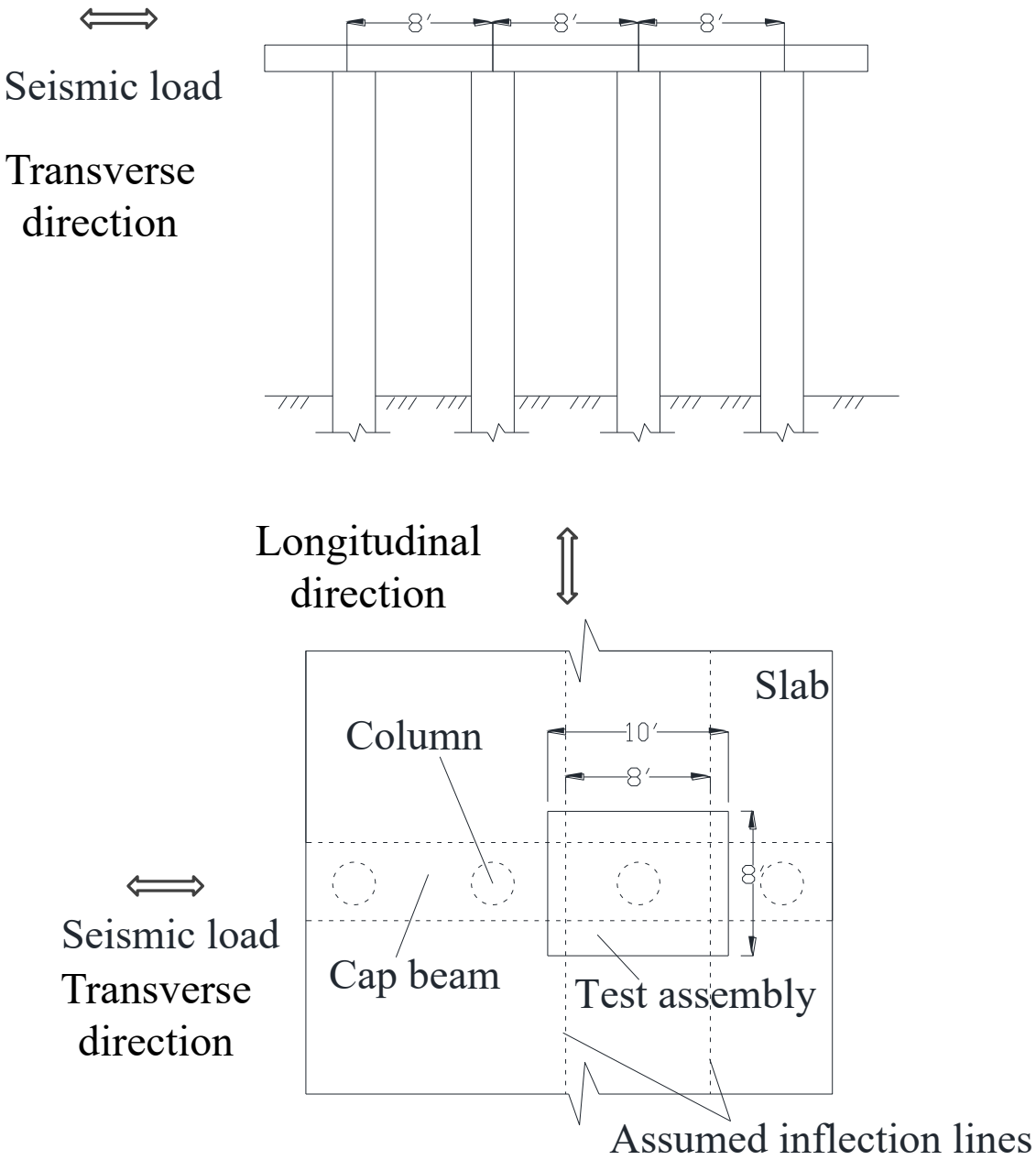

Figure 3.1 – Slab-column assembly of a slab bridge

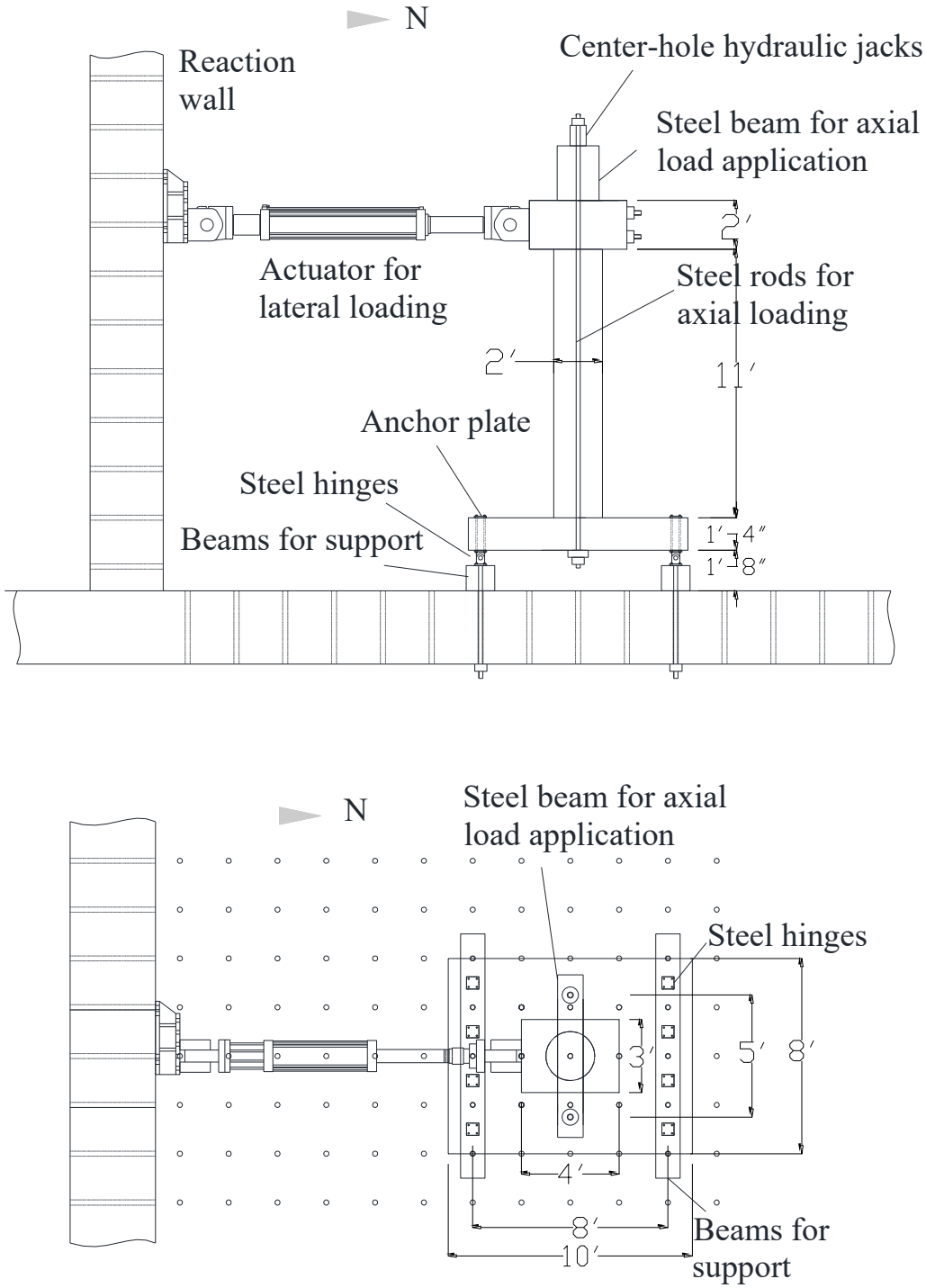

Figure 3.2 – Test setup for a slab-column assembly

Figure 3.3 – Picture of test setup (Specimen #1)

Figure 3.4 – Slab with drop cap in Specimen #3

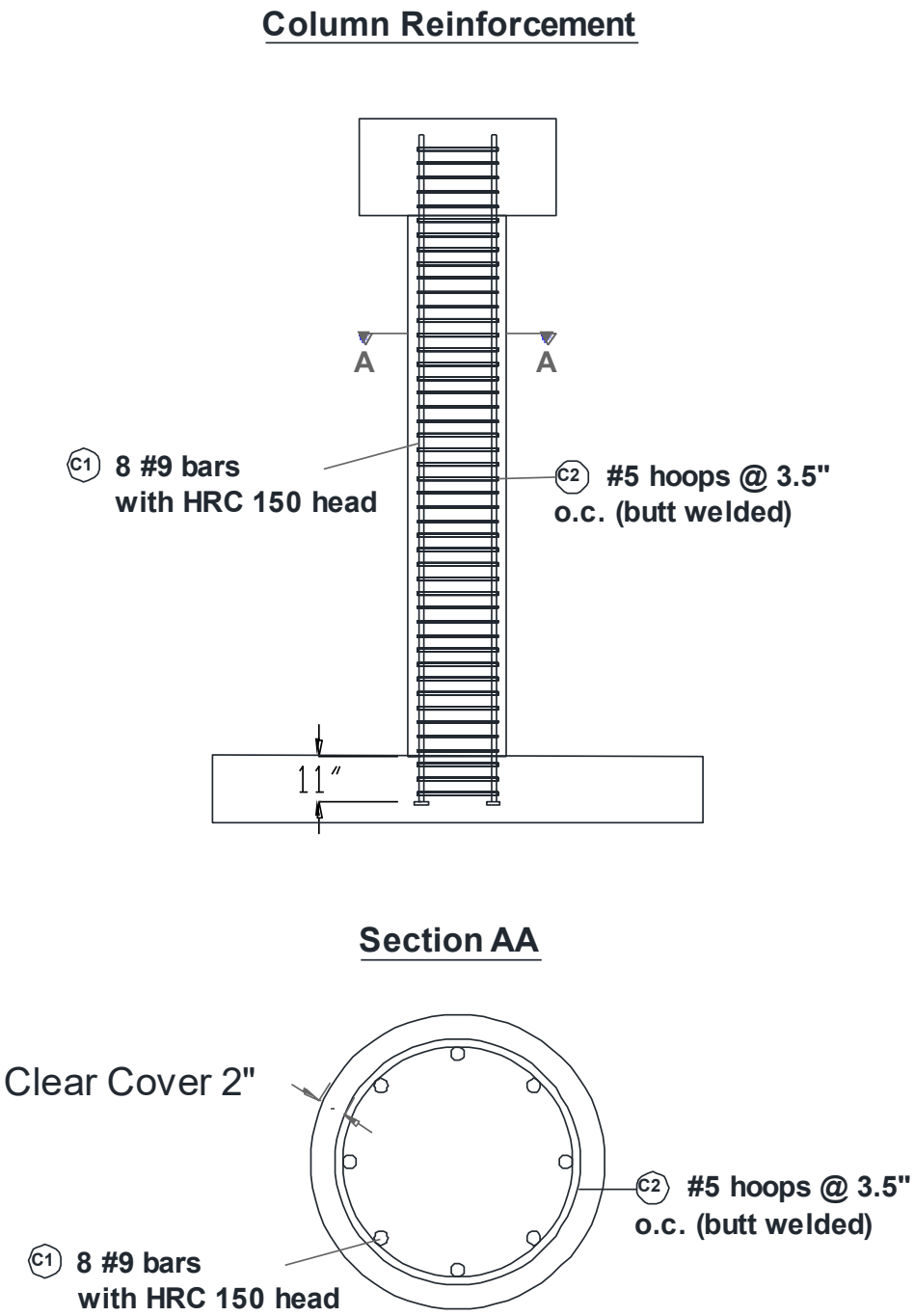

Figure 3.5 – Column reinforcement for Specimen #1

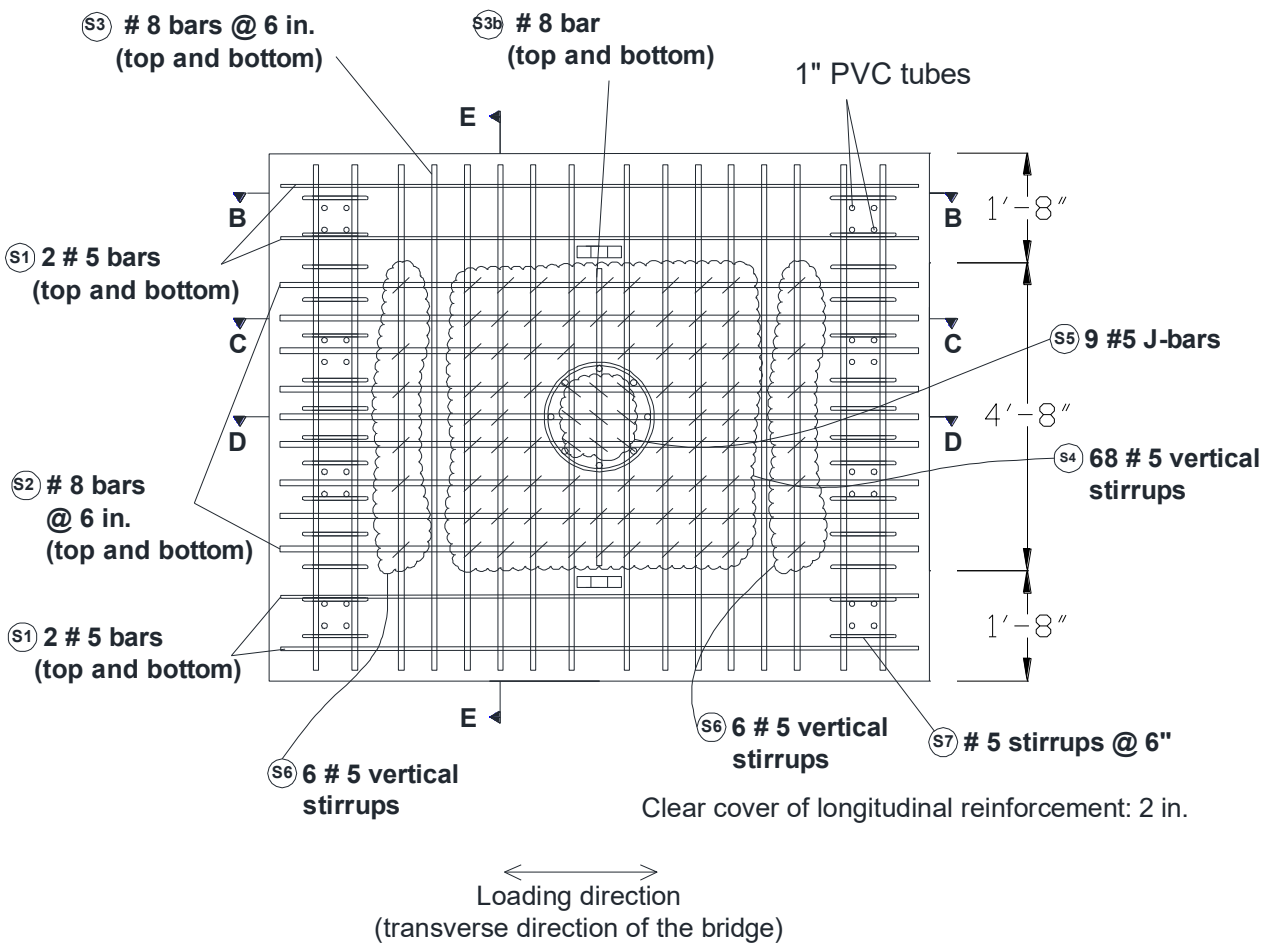

Figure 3.6 – Plan view of slab reinforcement for Specimen #1

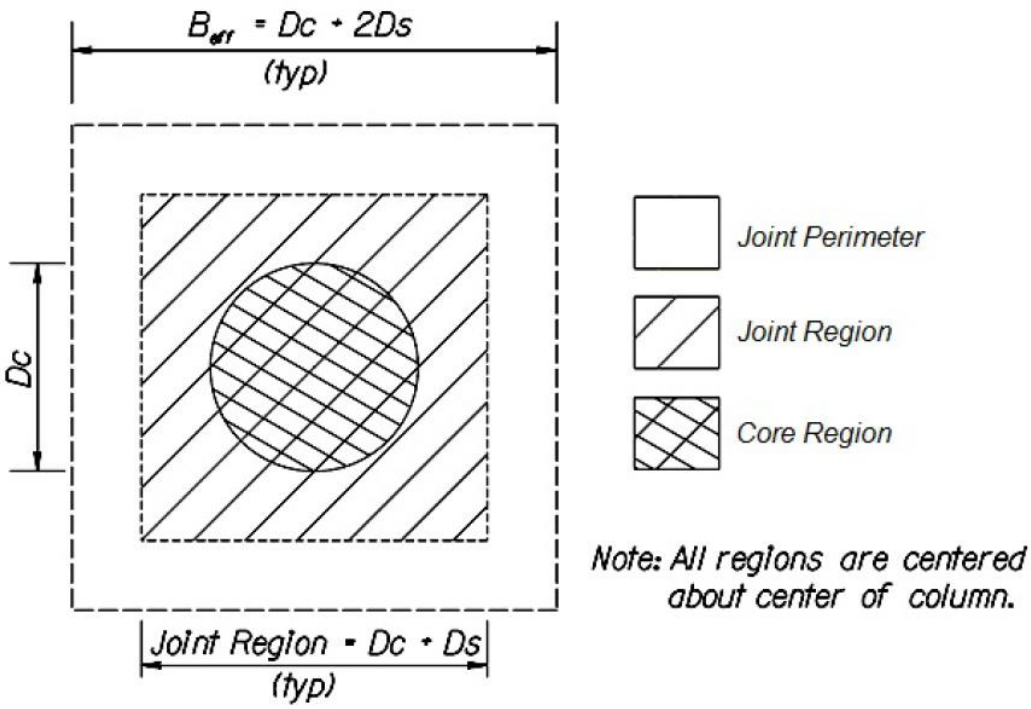

Figure 3.7 –Regions in a slab-column joint defined in MTD 20-7(October 2014)

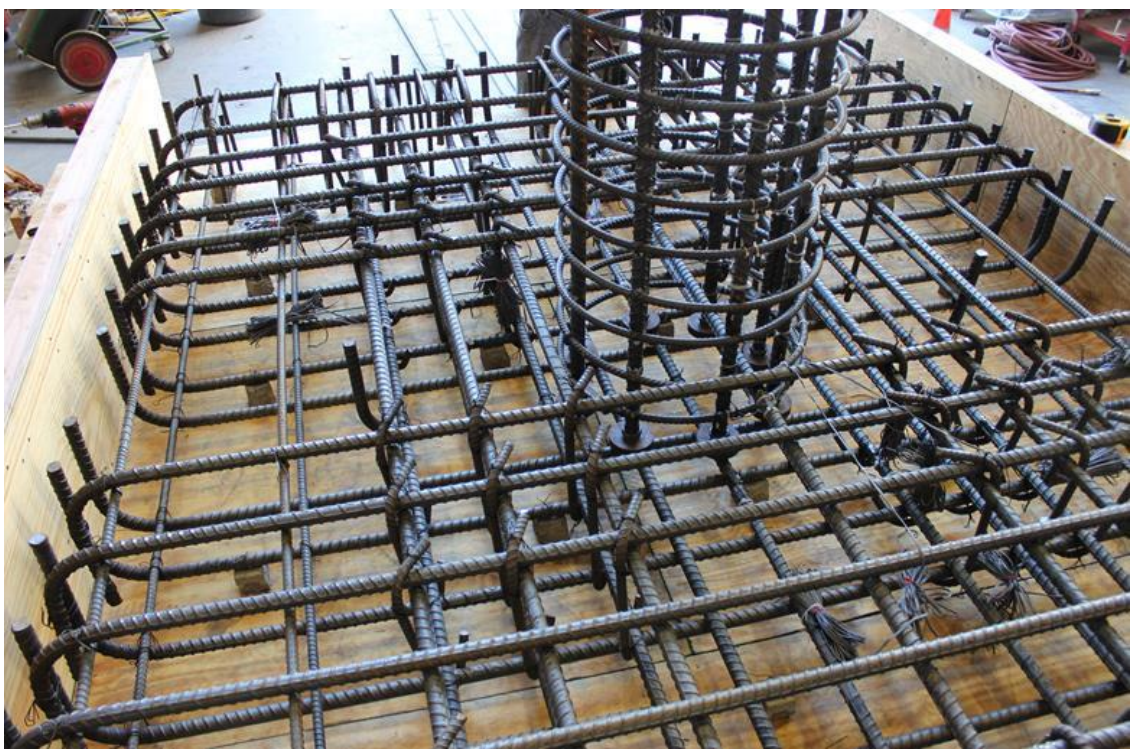

Figure 3.8 – Picture of the slab and column reinforcement of Specimen #1 during construction

Figure 3.9 – Picture of the slab and column reinforcement of Specimen #1 prior to cast

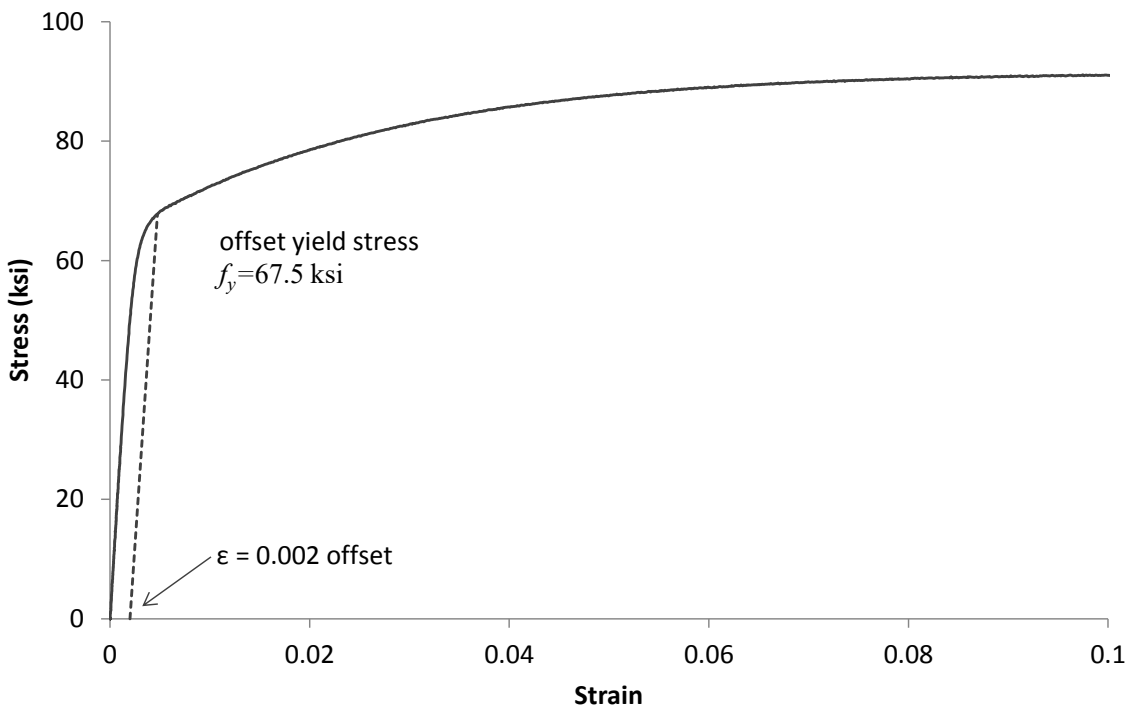

Figure 3.10 – Stress-strain curve for material sample of column hoops in Specimen #1

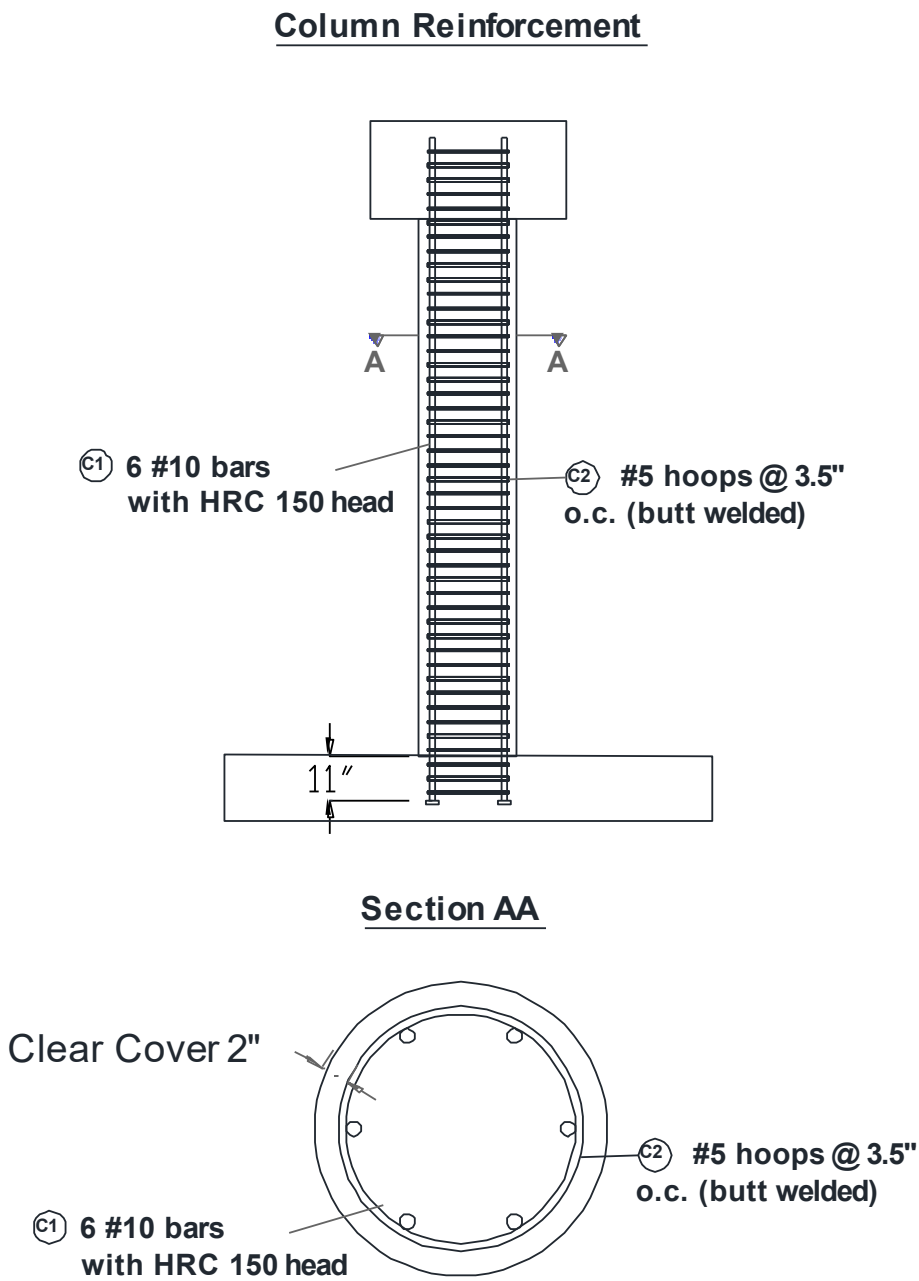

Figure 3.11 – Column reinforcement for Specimen #2

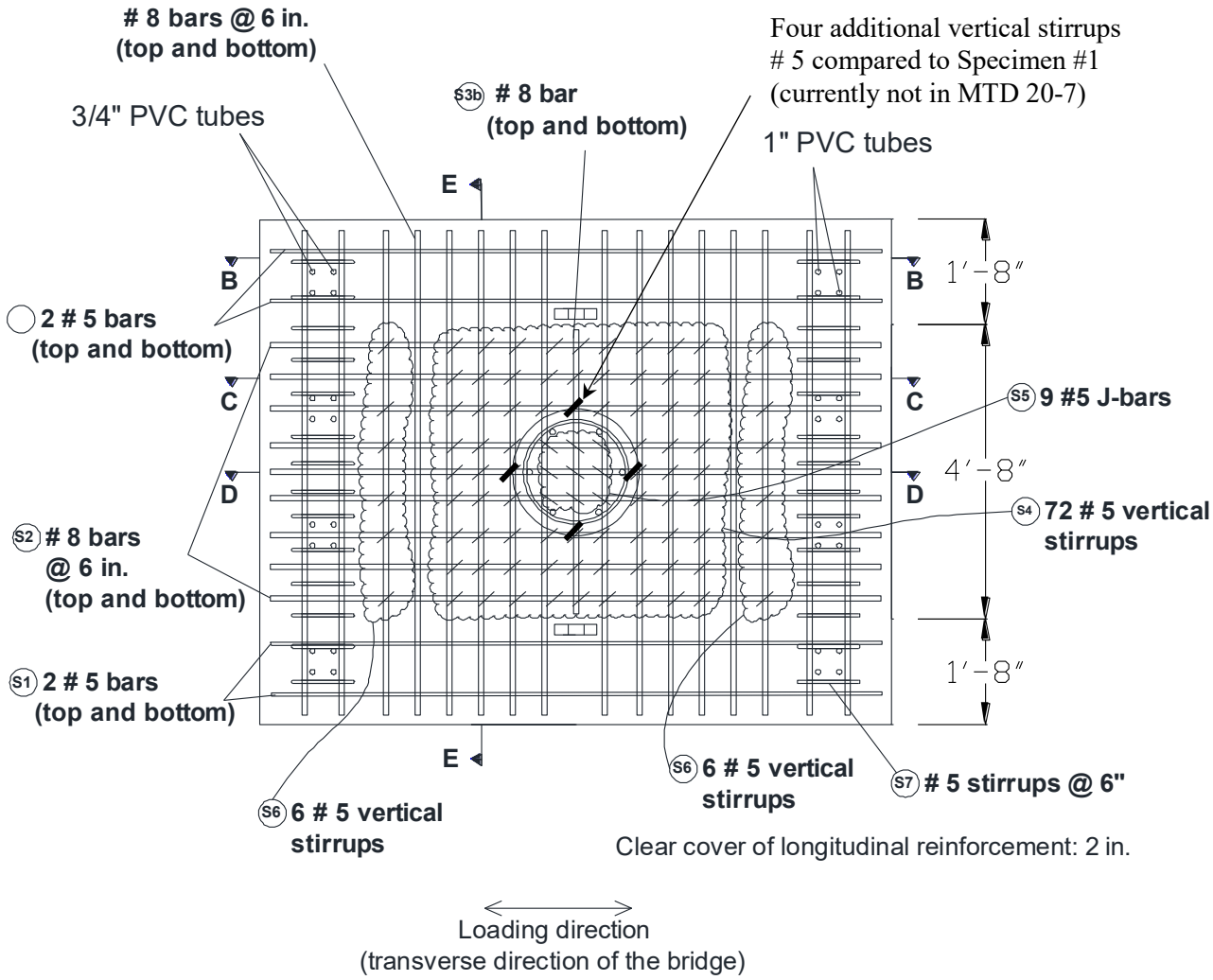

Figure 3.12 – Plan view of slab reinforcement for Specimen #2

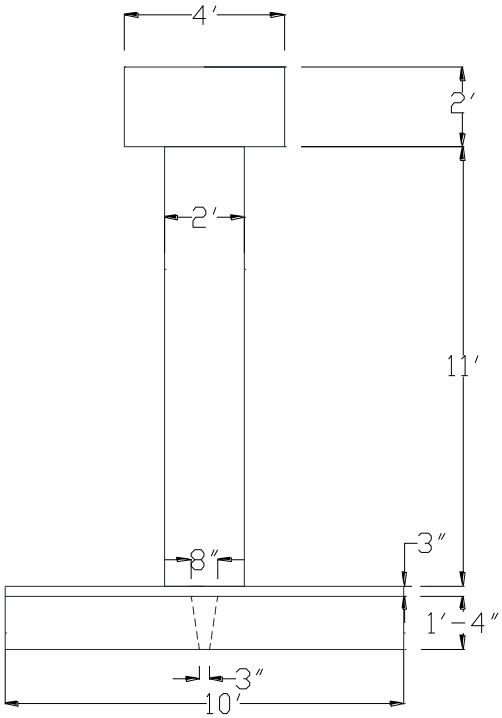

(a) Elevation view AA (east)

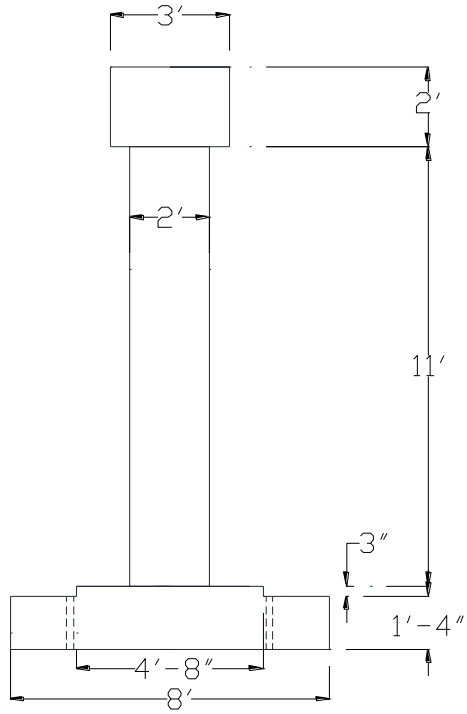

(b) Elevation view BB (south)

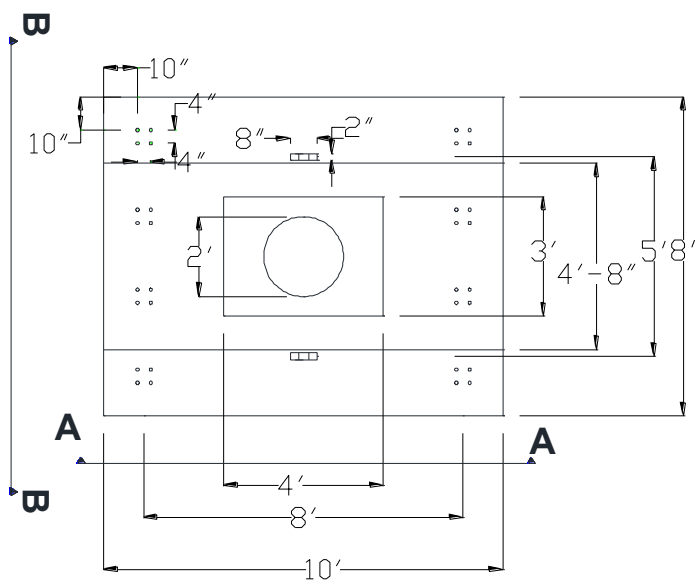

(c) Plan view

Figure 3.13 – Plan and elevation views for Specimen #3

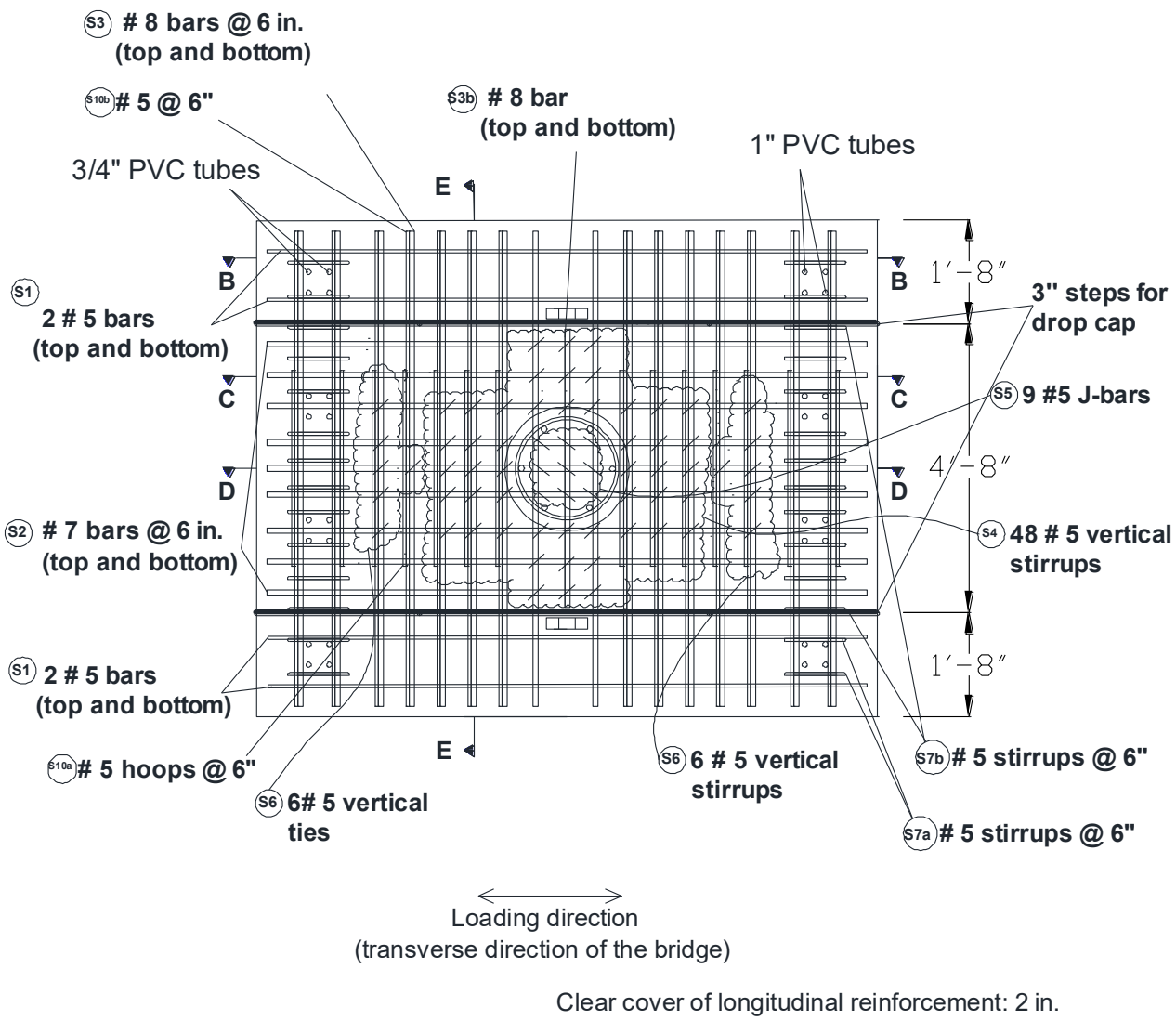

Clear cover of longitudinal reinforcement: 2 in.

Figure 3.14 – Plan view of slab reinforcement for Specimen #3

Figure 3.15 – Picture of slab and column reinforcement of Specimen #3 prior to casting

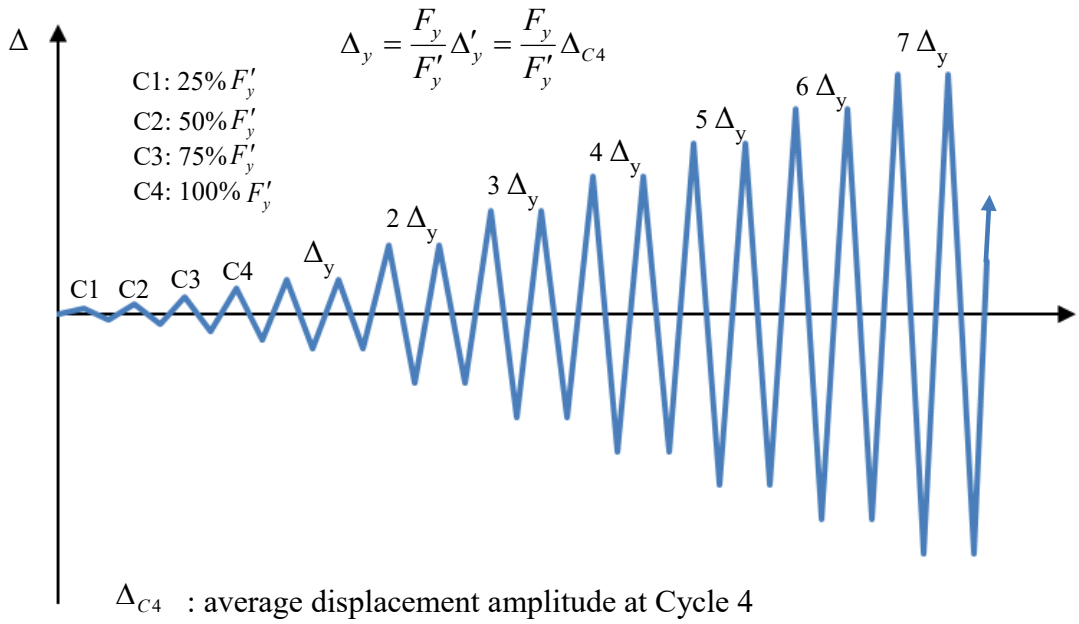

(a) loading history

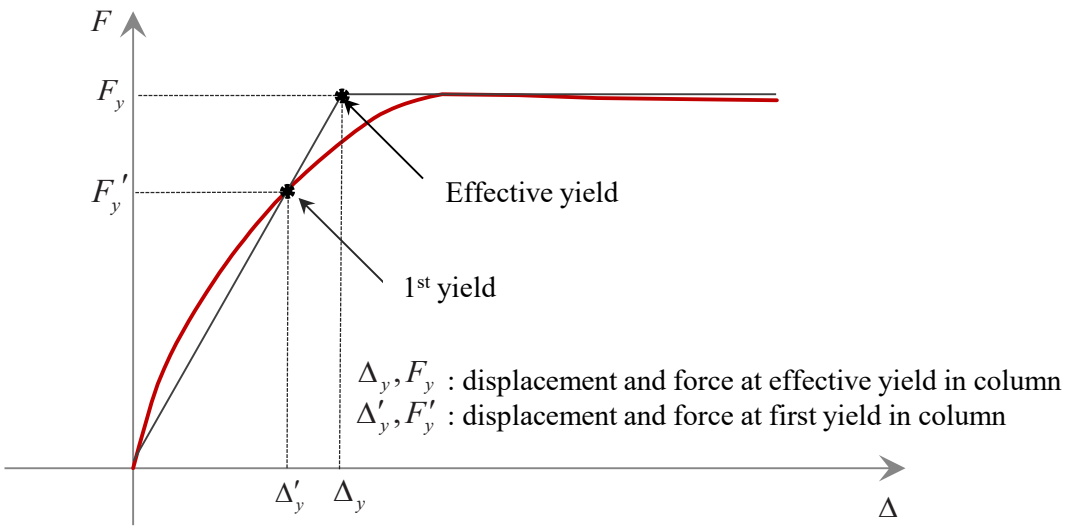

(b) first yield and effective yield

Figure 3.16 – Loading protocol

CHAPTER 4

SLAB-COLUMN ASSEMBLY TEST RESULTS

This chapter presents the results and findings from the tests of the three slab-column assemblies. The lateral load-vs.-displacement curves for the specimens, the main test observations, the deformations of the columns and slabs, and strains in the reinforcing bars are presented and compared.

4.1 General Observations and Lateral Load-vs.-Displacement Response

The lateral load-vs.-drift ratio curves for Specimens #1 and #2 are presented and compared in Figure 4.1. The horizontal component of the force exerted by the post-tensioning rods has been corrected for in these curves. The drift ratio is defined as the lateral displacement of the column measured at the point of lateral load application divided by the height of the column (12 ft.) measured from the top surface of the slab to the point of load application in the test configuration. Hence, the drift ratio also includes the slab deformation. The positive direction of loading and displacement is defined to be towards the north.

The lateral load capacity attained by Specimen #1 was 36 kips, while that of Specimen #2 was 35 kips. Specimen #1 had a longitudinal reinforcement ratio $\rho_l = 1.77\%$, while Specimen #2 had $\rho_l = 1.68\%$. As shown in Figure 4.1, Specimen #2 exhibited more rapid load degradation than Specimen #1. This can be attributed to the external confinement applied to the column of Specimen #1, which helped to alleviate the crushing of concrete at the compression toes.

The maximum displacement and ductility demand reached in each loading cycle are summarized in Table 4.1 and Table 4.2. The ductility values presented here are calculated with the effective yield displacement, Δ_y, defined in Eq. 3.1. However, instead of using the theoretical values, the actual displacement and force at the first yield and the actual maximum lateral force measured in the test are used to calculate the effective yield displacement for each specimen. The effective yield displacement

calculated for Specimen #1 is $\Delta_y = 2.5$ in. The test of Specimen #1 was stopped after the ductility demand had reached 6 to avoid possible damage to the vertical post-tensioning rods. Due to the high drift level, these rods were slightly bent near their anchorage on the slab. A hinge mechanism was thus introduced to the rod anchorages in the subsequent tests. Figure 4.2 shows the lateral deformation of Specimen #1 at ductility 6. This corresponds to a drift ratio of 10.4%.

For Specimen #2, the effective yield displacement calculated is $\Delta_y = 2.0$ in. During the 2nd cycle of positive drift at ductility 6, concrete spalling was observed at the top surface of the slab (bottom surface in the specimen), with big concrete pieces coming off. The spalling was limited to the cover concrete and was caused by the punching action of the headed bars when they were in compression. The test was stopped at that point, due to the significant drop of the lateral load resistance in the following load reversal, as it can be seen in Figure 4.1. The maximum drift ratio attained was 8.3 %. The smaller embedment length ($8.7d_b$) of the headed bars in Specimen #2, as compared to $9.8d_b$ in Specimen #1, resulted in more severe deterioration of the bar anchorage and the more significant load drop in the later cycles due to bar slip. It can also be noted from Figure 4.1 that the hysteresis curves for Specimen #2 are more pinched because of the more significant slip of the headed bars within the slab.

Figure 4.3 compares the lateral load-vs.-drift ratio curves for Specimens #2 and #3. The columns in Specimens #2 and #3 had the same longitudinal and transverse reinforcement, which resulted in the same lateral load capacities. However, the headed bars in Specimen #3, which had a 3-in. drop cap in addition to a 16-in. slab, had an embedment length of $11d_b$, which is the largest among the three specimens. The effective yield displacement calculated for Specimen #3 is $\Delta_y = 2.0$ in., which is the same as that for Specimen #2. As shown in Figure 4.1 and Figure 4.3, the higher embedment length in Specimen #3 resulted in less pinched hysteresis curves. However, the rate of degradation of the peak load in each cycle for Specimen #3 appears to be the same as that for Specimen #2 till the ductility demand of 6 was reached. This load degradation was caused by the crushing of concrete in the compression toes of the column. Compared to Specimen #2, Specimen #3 was subjected to two additional displacement cycles

at ductility 7. At that point, the test was ended to avoid possible damage to the vertical post-tensioning rods. The damage at the top surface of the slab (bottom surface in the specimen) of Specimen #3 was very mild, compared to that observed in Specimen #2.

4.2 Detailed Test Observations

For all three specimens, flexural cracks started to be visible in the lower half of the columns, in the test configuration, during Cycle 2, at a lateral load that was about 50% of the force predicted by analysis to cause the first yield of the longitudinal bars. At Cycle 4, when the load approached the theoretical first yield, flexural cracks were formed almost along the whole height of the columns, as shown in Figure 4.4 for Specimens #1 and #2. The same observations also stand for Specimen #3. Up to Cycle 4, no cracks were observed in the slabs. Observations obtained in latter cycles are presented below. For all three specimens, plastic hinges eventually developed at the bottom of columns in the test configuration, which had the slab-column assembly in the upside-down position.

4.2.1 Specimen #1

Figure 4.5 shows the evolution of damage near the bottom of the column in Specimen #1. Crushing of the concrete cover started in Cycle 6(a), which was the 1st cycle of ductility 2, as shown in Figure 4.5(a) and Figure 4.5(b). Concrete cover spalling and large flexural cracks were observed in the 1st cycle of ductility 5, as shown in Figure 4.5(c) and Figure 4.5(d). However, the spalling of concrete was not severe because of the external steel confinement. This is reflected in the small load degradation exhibited by the lateral load-vs.-drift ratio curve presented in Figure 4.1. Figure 4.6 shows the hoop strains in the two steel straps closest to the base of the column. The straps were located 4 in. and 8 in. away from the column base. As shown, the straps yielded in tension, with the lowest one experiencing larger strains. This shows that they were fully engaged in the confinement action.

Figure 4.7 shows the evolution of damage in the slab of Specimen #1. Flexural cracks were observed at the bottom face of the slab (top face in the specimen) in the 1st cycle of ductility 1. In Cycle 7a, corresponding to a ductility demand of 3, additional cracks, radiating from the column, appeared at the bottom face of the slab (top face in the specimen). These cracks extended towards the east and west edges of the slab, as the displacement applied to the column increased. The crack pattern at the bottom face of the slab (top face in the specimen), at the end of the test, is shown in Figure 4.8. At the top face of the slab (bottom face in the specimen), punching cracks could be observed in the 2nd cycle of ductility 3, as shown in Figure 4.7(c). The punching cracks were formed as the heads of the bars under compression pushed against concrete. The punching cracks were marked and measured after the end of the test. Relative vertical displacements were observed across punching cracks. After the end of the test, the residual punching crack displacements in the north and south region were 0.12 in. and 0.2 in., respectively. The punching crack displacement is defined as the differential vertical displacement of the slab surface across a punching crack measured with a micrometer. Figure 4.9 shows the crack pattern at the end of the test, with the locations of the column and the heads of the longitudinal bars marked. As shown in the figure, two large punching cracks were formed outside the column perimeter, at a maximum distance of 10 in. Cracks crossing the footprints of the column and the bar heads were also observed. After the test, concrete pieces between large punching cracks were removed with the use of mechanical tools, and some fracture surface was exposed, as shown in Figure 4.10. The average inclination of the fracture surface radiating from a bar head varies between 20° and 40°.

4.2.2 Specimen #2

Crushing of concrete started near the base of the column of Specimen #2 in the 2nd cycle of ductility 2, as shown in Figure 4.11(a). This was followed by a noticeable drop of the lateral resistance of the column as shown in the lateral load-vs.-drift ratio curve in Figure 4.1. Figure 4.11(b) through Figure 4.11(d) show the evolution of damage near the base of the column, where severe concrete cover spalling

was observed. In the last cycle at ductility 6, the transverse reinforcement was exposed due to the cover spalling, as shown in Figure 4.11(d).

The evolution of damage at the bottom face of the slab (top face in the specimen) is shown in Figure 4.12. In the 2nd cycle of ductility 1, cracks, radiating from the column, started to form at the bottom face of the slab (top face in the specimen). These cracks propagated in the following cycles, extending towards the west and east sides of the slab, as shown in Figure 4.12(a) and Figure 4.12(b). At Cycles 8a and 8b, corresponding to ductility 4, column pullout cracks were observed at the bottom face of the slab (top face in the specimen), 2 to 4 in. away from the column. Figure 4.12(c) and Figure 4.12(d) show these pullout cracks during the 1st cycle of ductility 5.

Figure 4.13 shows the evolution of damage at the top face of the slab (bottom face in the specimen). Punching cracks started to form during the 2nd cycle of ductility 1. In every subsequent cycle, existing cracks propagated and new cracks were formed. Figure 4.13(a) shows the punching cracks at the top face of the slab (bottom face in the specimen) in the 2nd cycle of ductility 3. In that cycle, the maximum punching crack displacement measured was 0.012 in. Figure 4.13(b) shows severe punching cracks on the north side of the slab in the 2nd cycle of ductility 5. In that cycle, the maximum punching crack displacement of the cracked slab surface measured was 0.26 in. In the 1st cycle of ductility 6, the punching crack displacement increased even more and concrete spalling was observed, as shown in Figure 4.13(c). In the 2nd cycle of ductility 6, concrete pieces came off, as shown in Figure 4.13(d). At that point, the test was ended.

Figure 4.14 shows the extensive damage at the top face of the slab (bottom face in the specimen) at the end of the test. Part of the concrete cover on the north side came off, while another part with an area larger than the footprint of the column was detached. Figure 4.15 shows the top face of the slab before and after removing the loose concrete pieces. The loose concrete pieces were removed with no effort and a clear fracture surface was exposed. Some vertical stirrups and longitudinal bars in the slab were exposed as shown in Figure 4.15(b). The average inclination of the fracture surface was between 10° and 15°.

4.2.3 Specimen #3

Similar to Specimen #2, crushing of concrete near the base of the column of Specimen #3 was observed during the 2nd cycle of ductility 2, as shown in Figure 4.16(a). This was responsible for the subsequent drop of the lateral resistance of the column as shown in Figure 4.3. Figure 4.16(b) shows the damage near the base of the column during the 1st cycle of ductility 4. The column of Specimen #3 experienced more severe cover spalling near the base as compared to Specimen #2 (see Figure 4.11(b)). This can be attributed to the less slip of the headed longitudinal bars within the joint region of the slab of Specimen #3, which resulted in more severe bar deformation in the plastic-hinge region. Figure 4.16(c) and Figure 4.16(d) show the evolution of damage in the column up to the 2nd cycle of ductility 7. The transverse hoops and the longitudinal bars in the column were exposed due to the cover spalling, which extended to a height of 15 in. from the column base.

The evolution of damage at the bottom face of the slab (top face in the specimen) is shown in Figure 4.17. In the 1st cycle of ductility 2, cracks radiating from the column towards the west and east sides of the slab were observed, as shown in Figure 4.17(a). During the 2nd cycle of ductility 4, severe column pullout cracks were observed at the bottom face of the slab (top face in the specimen) around the column, as shown in Figure 4.17(b). In the following cycle of ductility 5, the pullout cracks became wider, as shown in Figure 4.17(c). During the last cycle at ductility 7, the pullout cracks had some interior fracture surface exposed as shown in Figure 4.17(d). Figure 4.18 shows the exposed fracture surface around the column after pieces of concrete had been removed.

Figure 4.19 shows the evolution of damage at the top face of the slab (bottom face in the specimen). Some minor punching cracks were formed during the 1st cycle of ductility 4, as shown in Figure 4.19(a). For later cycles, existing cracks propagated and new ones were formed, as shown in Figure 4.19(b) and (c). The maximum punching crack displacement (relative displacement across a crack) measured was 0.021 in., and it was reached during the 2nd cycle of ductility 6, with no further increase in the subsequent cycles of ductility 7. The punching crack pattern at the top face of the slab (bottom face in

the specimen) after the test is shown in Figure 4.19(d). The damage due to the punching of the headed bars was very minor.

The vertical displacements of the top surface of the slab (bottom surface in the specimen) of Specimens #2 and #3, measured by displacement transducers at the positions of the headed bars on the extreme north and south sides of the column, are plotted against the column displacement, expressed in terms of the ductility level, in Figure 4.20 and Figure 4.21. It can be observed that Specimen #2 had much larger displacements than Specimen #3. During the cycles of ductility 6, the vertical displacements in Specimen #2 increased significantly, which is consistent with the severe punching cracks observed.

4.3 Global Lateral Deformations

The lateral displacement of the column had contributions from (1) the rotation of the slab due to bending, (2) the rotation of the column at its base caused by the strain penetration of the column longitudinal bars into the anchorage region in the slab, as well as the pullout and punching mechanisms of the column longitudinal bars in the slab-column joint, (3) the flexural deformation of the column, and (4) the shear deformation of the column. Figure 4.22 through Figure 4.24 show the lateral displacements along the columns at the peaks of different cycles for Specimens #1, #2 and #3. During the tests, the slab rotation and base rotation of the columns were monitored. The flexural and shear deformations of the columns were not measured, but the summed displacement due to these two mechanisms has been calculated by subtracting the displacements contributed by the slab deformation and the base rotation of the columns from the total displacement measured at the top. For the aspect ratio of the columns, the contribution of the shear deformation is expected to be negligible. Table 4.4 through Table 4.6 show the contributions of the aforementioned mechanisms to the lateral displacements at the top of the columns of Specimens #1, #2 and #3. The contribution of the slab rotation was negligible for all three specimens. Figure 4.25 through Figure 4.27 show the lateral load-vs.-slab rotation curves for Specimens #1, #2 and #3. The rotations were measured at the midspan of the slab. It can be seen that the slab rotation was more

or less linearly proportional to the load. However, some minor change in stiffness can be observed for Specimens #1 and #2. This can be attributed to cracking in the slabs.

In the 5th cycle with ductility 1, column deformation was the major contributor of the lateral displacement, accounting for 77% of the total displacement for Specimen #1, 72% for Specimen #2, and 82% for Specimen #3, while the remaining displacement was contributed by the rotation at the column base. The contribution of the base rotation increases in the subsequent cycles reaching 42% for Specimens #1, 50% for Specimen #2, and 34% for Specimen #3. Specimen #3 had the least column base rotation because of the adequate embedment length for the headed bars.

4.4 Strains in Column Longitudinal Bars

The strain variations along the longitudinal bars close to the north and south faces of the columns were measured by strain gages. Figure 4.28 and Figure 4.29 show the strain variations in Bars 1 and 5 (placed at the extreme locations) for Specimen #1, along the lower part of the column and inside the slab. In these plots, a solid line corresponds to the bar in tension, and a dashed line to the bar in compression. Figure 4.30 and Figure 4.31 plot the strains at the gage locations within the embedment length of Bars 1 and 5,against the ductility demand. A number of strain gages were damaged in later cycles, as indicated by the missing data points in the figures. The measurements taken at 10 in. below the top face of the slab in the test configuration show that the yield strain penetrated the entire embedment length during the 1st cycle of ductility 5 as the top face of the bar heads (in the inverted T orientation) was located at a depth of 11 in. below the slab-column interface. Bars 1 and 5 reached a maximum tensile strain of about 0.03 before the strain gages failed. This indicates that an embedment length of $9.8d_b$ was sufficient to develop not only the yield strength of the headed bars, but also strain hardening. The large strain reversals shown in the plots indicate that the bars also developed large compressive stresses.

The strains along the Bars 1 and 4 in Specimen #2 are presented in Figure 4.32 through Figure 4.35. The observations for the strains in Specimen #2 are very similar to those for Specimen #1. Even

with an embedment length as small as $8.7d_b$, the headed bars were able to develop the tensile yield strain and strain levels larger than 0.01, beyond which strain hardening is expected to occur. The measurement taken from Bar 1 at 10 in. below the top face of the slab shows that yielding penetrated the entire embedment length at the 1st cycle of ductility 4. The similar reading from Bar 4 shows that the yield strain was exceeded at the 2nd cycle of ductility 4. Specimen #2 had bar yielding penetrated to the heads one to two cycles earlier than Specimen #1.

Figure 4.36 through Figure 4.39 show the strains in Bars 1 and 4, for Specimen #3. The bars yielded in tension and developed large tensile strains in the strain-hardening regime. As shown in Figure 4.39, up to ductility 5, Bar 4 had not reached the tensile yield strain at the gage location that was 13 in. below the top face of the slab (1 in. above the head surface) in the test configuration. The gage was damaged after this ductility level. For this bar, the gage reading that was taken 9 in. below top face of the slab barely reached the yield strain at ductility 5. However, at the depth of 9 in., Bar 1 reached a tensile strain much larger than the yield strain, as shown in Figure 4.38.

In all three specimens, the bars developed their yield strength and reached strain hardening. Specimens #1 and #2, which had development lengths of $9.8d_b$ and $8.7d_b$, respectively, had tensile yielding penetrating all the way to the heads of the longitudinal bars close to the north and south faces of the columns. Specimen #3, which had an embedment length of $11d_b$, had much smaller tensile strains developed near the heads, indicating that the headed bars were better developed compared to those in Specimens #1 and #2.

4.5 Strains in J-bars

Figure 4.40 shows the strains developed in the J-bars placed in the core region of the slab-column joint of Specimen #1. The strain measurements were taken at the mid-height of the J-bars (as shown in Figure A.23). It can be seen that the J-bars developed tensile strains close to the yield level. These bars

were always subjected to tension with comparable strain levels when the column was pushed towards the north or the south (i.e., regardless of the fact that the longitudinal headed bars next to the J-bars were subjected to tension or compression). This indicates that the J-bars were engaged to resist both the pullout and punching forces exerted by the headed bars after diagonal breakout cracks developed in the joint region of the slab. Similar tensile strains were measured in the J-bars of Specimen #2, as shown in Figure 4.41. However, the strain level was a little lower than that for Specimen #1.

The strains in the J-bars of Specimen #3 are shown in Figure 4.42. The strains in the J-bars, except for J4 (placed at the center), barely reached half of the yield strain. This indicates that the J-bars in Specimen #3 were not engaged as much as those in Specimens #1 and #2, in which the deterioration of the anchorage of the headed bars in the slabs was much more severe.

4.6 Strains in Vertical Stirrups

Figure 4.43 shows the strains in the 1st row of vertical stirrups next to the column steel cage for Specimen #1. The strain measurement was taken at the mid-height of the stirrups. These stirrups exhibited a similar behavior as the J-bars, developing tensile strains when the adjacent column longitudinal bars were subjected to tension or compression. They developed strains up to 0.0015 (less than 75% of the yield strain). Figure 4.44 shows the strains in the 1st row of vertical stirrups next to the column steel cage for Specimen #2. Both Specimens #2 and #3 had four additional vertical stirrups, V4, V7, V10, and V13, placed in the first rows, which were not required according to MTD 20-7 (October 2014). Stirrup V4 developed a strain level close the yield strain, while V7, V10 and V13 reached a maximum strain around 0.0015. The rest of the vertical stirrups in the 1st row developed strains up to 0.001, which was a little less than those in Specimen #1. This indicates that V4, V7, V10, and V13 can take a large share of the pullout and punching forces exerted by the headed bars when the column is displaced in the respective directions.

Figure 4.45 shows the strains in the 1st row of vertical stirrups in Specimen #3. The strains measured are much smaller than those in Specimens #1 and #2. This can be attributed to the better development of the headed bars in Specimen #3.

Figure 4.46 through Figure 4.48 show the strains in the 2nd row of vertical stirrups for Specimens #1, #2 and #3. In all three specimens, the strains developed were very small, reaching values of about 25% of the yield strain. This indicates that the vertical stirrups farther away from the slab-column joint will not be as actively engaged as those adjacent to the headed longitudinal bars.

4.7 Strains in Longitudinal Bars in Slabs

Figure 4.49 through Figure 4.51 plot the strains in the longitudinal bars at the bottom face of the slab (top face in the specimen), against the ductility demand, at a section close to the north face of the columns, for Specimens #1, #2 and #3. For all three specimens, the strains in the longitudinal bars remained within the elastic regime, not exceeding 0.001. It is interesting to note that the bars did not experience the expected compressive strains for a section subjected to positive and negative bending moments. However, the tensile strains do appear to be smaller when the columns were displaced towards north (the positive direction), especially for Specimen #3. This behavior can be attributed to the proximity of the measurement locations to the column-joint region, which is subjected to a complex distribution of forces.

Figure 4.52 through Figure 4.54 plot the strains in the longitudinal bars at the top face of the slabs (bottom face in the specimen) against the ductility demand, at a section close to the north face of the columns, for Specimens #1, #2 and #3. For Specimen #1, in which moderate punching cracks were observed at the top face of the slab (bottom face in the specimen), the strains in the longitudinal bars remained within the elastic regime with a maximum of 0.0012. For Specimen #2, where the top face of the slab experienced significant damage due to the punching action of the headed bars, Bar B3 experienced a maximum compressive strain of -0.012 during the last cycle of ductility 6, exceeding the

yield level. Up to ductility 5, the strain in Bar B3 remained within the elastic regime. Only during the last two cycles at ductility 6, the bar yielded in compression. This is probably due to the fact that it experienced significant bending deformation caused by the punching action of the headed bars. For Specimen #3, in which very limited damage was observed at the top face of the slab (bottom face of the specimen), the strains developed in the longitudinal bars were small, as shown in Figure 4.54.

4.8 Conclusions

The test results have shown that an embedment length of $8.7d_b$ (Specimen #2) was able to develop the tensile yield strength of the headed bars and the plastic moment capacity of the column. However, the severe anchorage deterioration of the headed bars led to more pinched hysteretic load-displacement curves, as compared to the other two cases with higher embedment lengths. Furthermore, the top face of the slab (bottom face in the specimen) was severely damaged by the punching action of the headed bars. Specimen #1, which had an embedment length of $10d_b$, had moderate punching cracks and a better hysteretic load-displacement behavior. Specimen #3, which had an embedment length of $11d_b$, exhibited the most satisfactory behavior with very minor punching cracks.

The J-bars adjacent to the headed bars within the column cage, and the vertical stirrups right outside the column cage played a significant role in restraining breakout cracks and punching cracks when the headed bars were subjected to tension and compression. The vertical stirrups in the 2nd row and farther away from the column cage did not develop any significant stress during the tests. The specifications for J-bars and vertical stirrups in MTD 20-7 appear to be adequate to restrain breakout and punching cracks in the slab for an embedment length of $10d_b$. Nevertheless, it is recommended that MTD 20-7 be revised to include four additional stirrups adjacent to the column cage, as for Specimens #2 and #3. When probably restrained by the J-bars and vertical stirrups, the mat of longitudinal and transverse

bars at the top face of the slab (bottom face in the specimen) can resist the punching action of the headed bars. Therefore, the bar heads should be below the top mat of reinforcement in the bridge slab.

Table 4.1 – Loading Protocol for Specimen #1

Cycle no.	Drift (in.)	Ductility demand
1	0.2	0.1
2	0.6	0.2
3	1.1	0.4
4	1.8	0.7
5a, 5b	2.5	1
6a, 6b	5.0	2
7a, 7b	7.5	3
8a, 8b	10.0	4
9a, 9b	12.5	5
10a, 10b	15.0	6

Table 4.2 – Loading Protocol for Specimen #2

Cycle no.	Drift (in.)	Ductility demand
1	0.1	0.05
2	0.5	0.25
3	1.0	0.5
4	1.5	0.75
5a, 5b	2.0	1
6a, 6b	4.0	2
7a, 7b	6.0	3
8a, 8b	8.0	4
9a, 9b	10.0	5
10a, 10b	12.0	6

Table 4.3 – Loading Protocol for Specimen #3

Cycle no.	Drift (in.)	Ductility demand
1	0.1	0.05
2	0.5	0.25
3	1.0	0.5
4	1.5	0.75
5a, 5b	2.0	1
6a, 6b	4.0	2
7a, 7b	6.0	3
8a, 8b	8.0	4
9a, 9b	10.0	5
10a, 10b	12.0	6
11a, 11b	14.0	7

Table 4.4 – Contributions of different deformation sources to the column drift in Specimen #1

Cycle no. (drift)	Rotation of the slab (%)	Column base rotation (%)	Flexural and shear deformations of column (%)
5a (+ 2.5 in.)	2	24	74
5a (- 2.5 in.)	0	26	74
6a (+ 5.0 in.)	2	27	71
6a (- 5.0 in.)	0	27	73
8a (+ 10.0 in.)	2	30	68
8a (- 10.0 in.)	0	33	68
9a (+ 12.5 in.)	2	33	65
9a (- 12.5 in.)	0	35	65
10a (+ 15.0 in.)	2	38	60
10a (- 15.0 in.)	0	40	60
10b (+ 15.0 in.)	1	40	58
10b (- 15.0 in.)	0	42	58

Table 4.5 – Contributions of different deformation sources to the column drift in Specimen #2

Cycle no. (drift)	Rotation of the slab (%)	Column base rotation (%)	Flexural and shear deformations of column (%)
5a (+ 2.0 in.)	1	27	72
5a (- 2.0 in.)	0	29	71
6a (+ 4.0 in.)	1	35	64
6a (- 4.0 in.)	0	40	60
8a (+ 8.0 in.)	0	42	58
8a (- 8.0 in.)	0	40	60
9a (+ 10.0 in.)	0	45	55
9a (- 10.0 in.)	0	41	59
10a (+ 12.0 in.)	1	48	51
10a (- 12.0 in.)	0	44	56
10b (+ 12.0 in.)	1	50	49
10b (- 12.0 in.)	-	-	-

Table 4.6 – Contributions of different deformation sources to the column drift in Specimen #3

Cycle no. (drift)	Rotation of the slab (%)	Column base rotation (%)	Flexural and shear deformations of column (%)
5a (+ 2.0 in.)	0	19	81
5a (- 2.0 in.)	0	18	82
6a (+ 4.0 in.)	0	24	77
6a (- 4.0 in.)	1	25	74
8a (+ 8.0 in.)	0	22	78
8a (- 8.0 in.)	1	27	72
9a (+ 10.0 in.)	0	21	79
9a (- 10.0 in.)	0	30	70
10a (+ 12.0 in.)	0	16	84
10a (- 12.0 in.)	1	33	66
11a (+ 14.0 in.)	0	15	85
11a (- 14.0 in.)	1	34	65

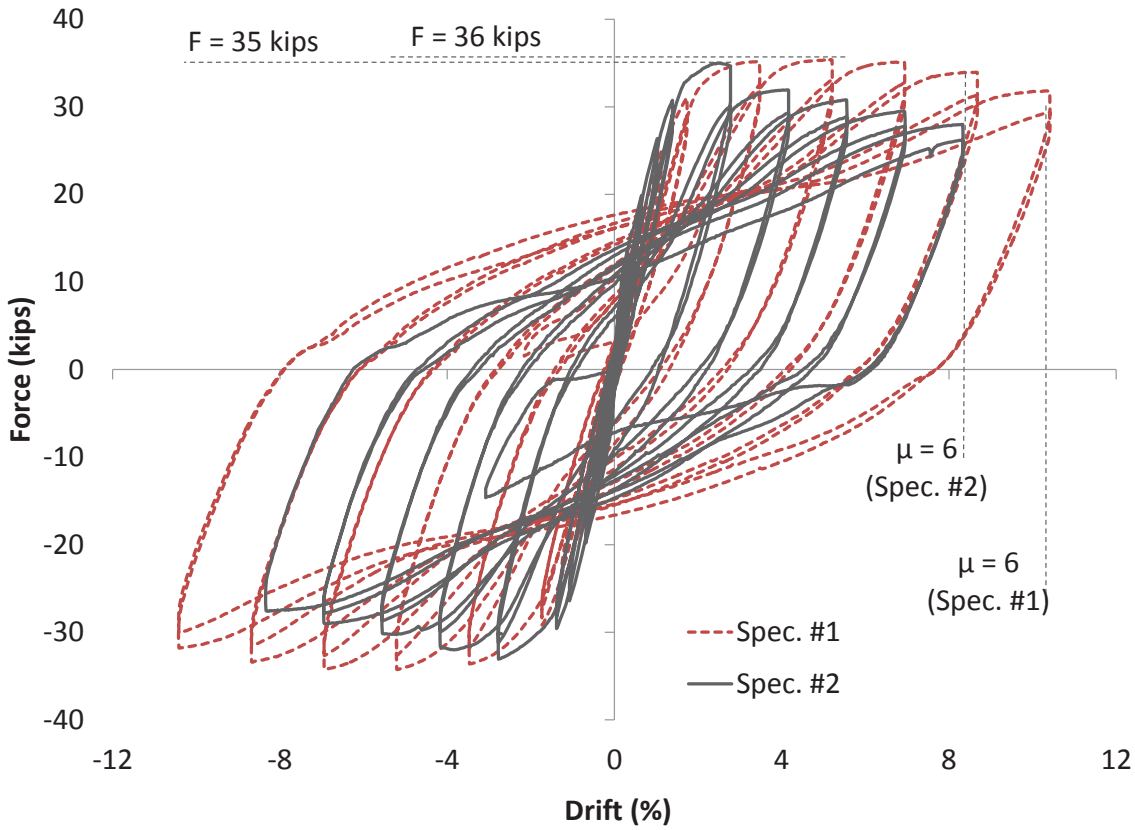

Figure 4.1 – Lateral force-vs.-drift ratio for Specimens #1 and #2

Figure 4.2 – Deflected shape of Specimen #1 at ductility 6

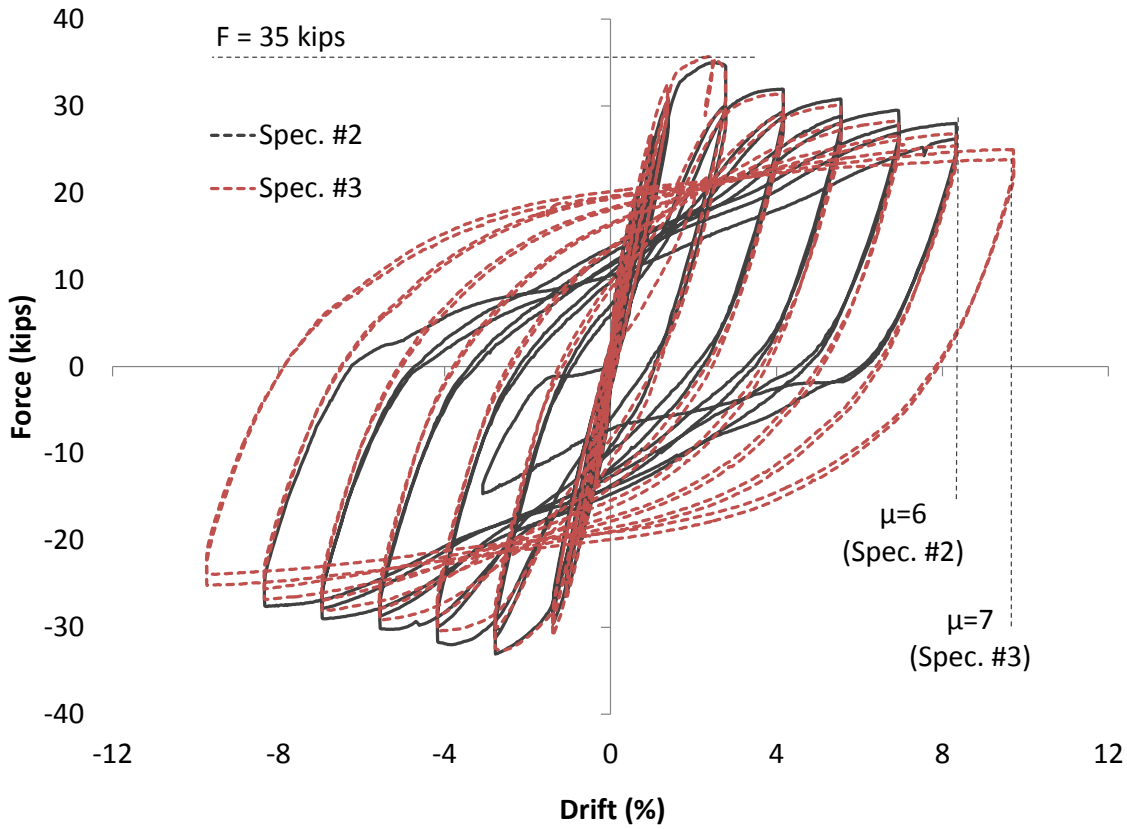

Figure 4.3 – Lateral force-vs.-drift ratio for Specimens #2 and #3

(a) Specimen #1 (b) Specimen #2

Figure 4.4 – Flexural cracks at the south face of the columns of Specimens #1 and #2 at Cycle 4 (1st yield)

(a) north face at Cycle 6a (μ = 2)

(b) south face at Cycle 6a (μ = 2)

(c) north face at Cycle 9a (μ = 5)

(d) south face at Cycle 9a (μ = 5)

Figure 4.5 – Evolution of damage at the bottom of the column of Specimen #1

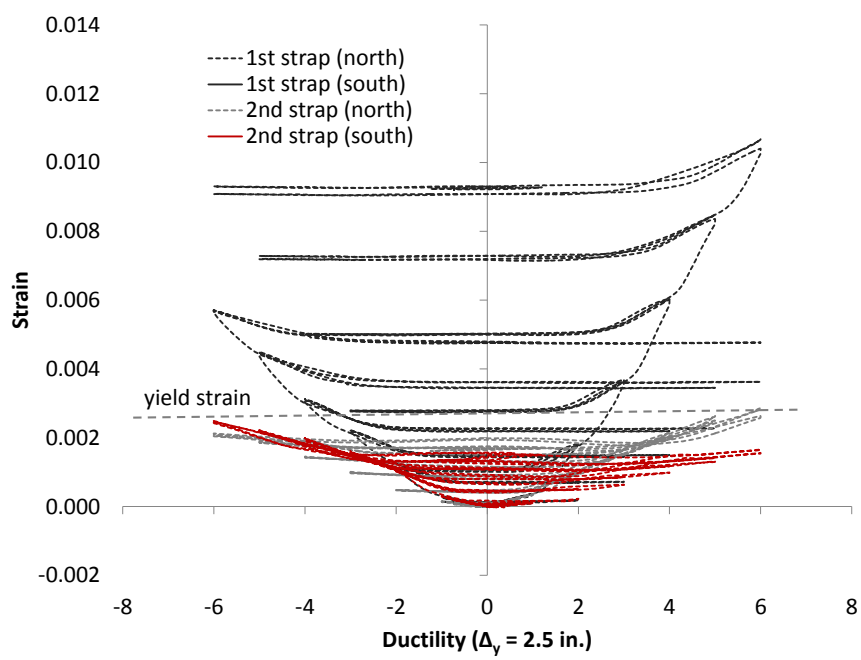

Figure 4.6 – Strains in confining steel straps around the column of Specimen #1

(a) Cycle 5a (μ = 1)

(b) Cycle 7a (μ = 3)

(c) Cycle 7b (μ = 3)

(d) Cycle 10a (μ = 6)

Figure 4.7 – Evolution of damage in the slab of Specimen #1

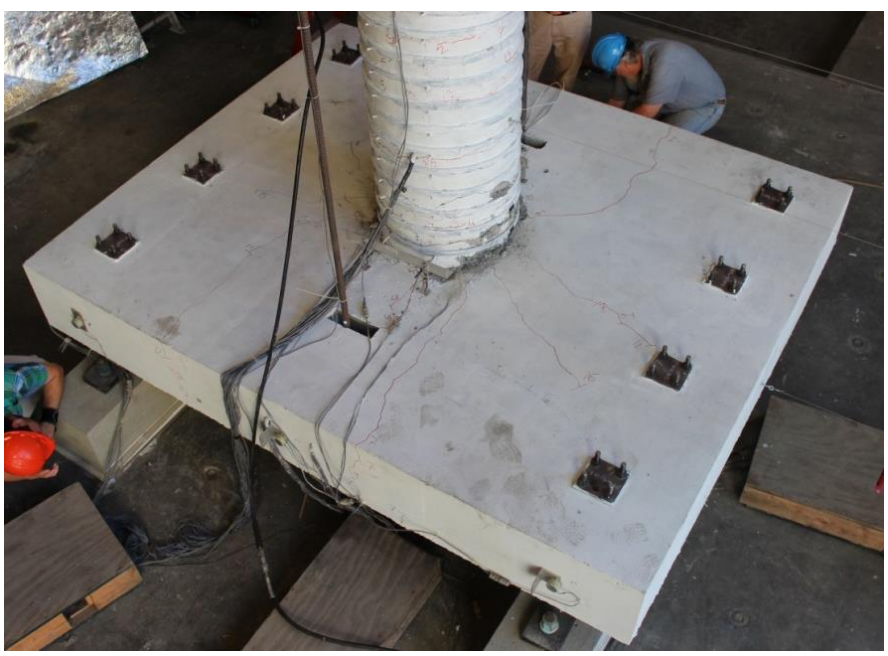

Figure 4.8 – Damage at the bottom face of the slab (top face in the specimen) of Specimen #1 at the end of testing

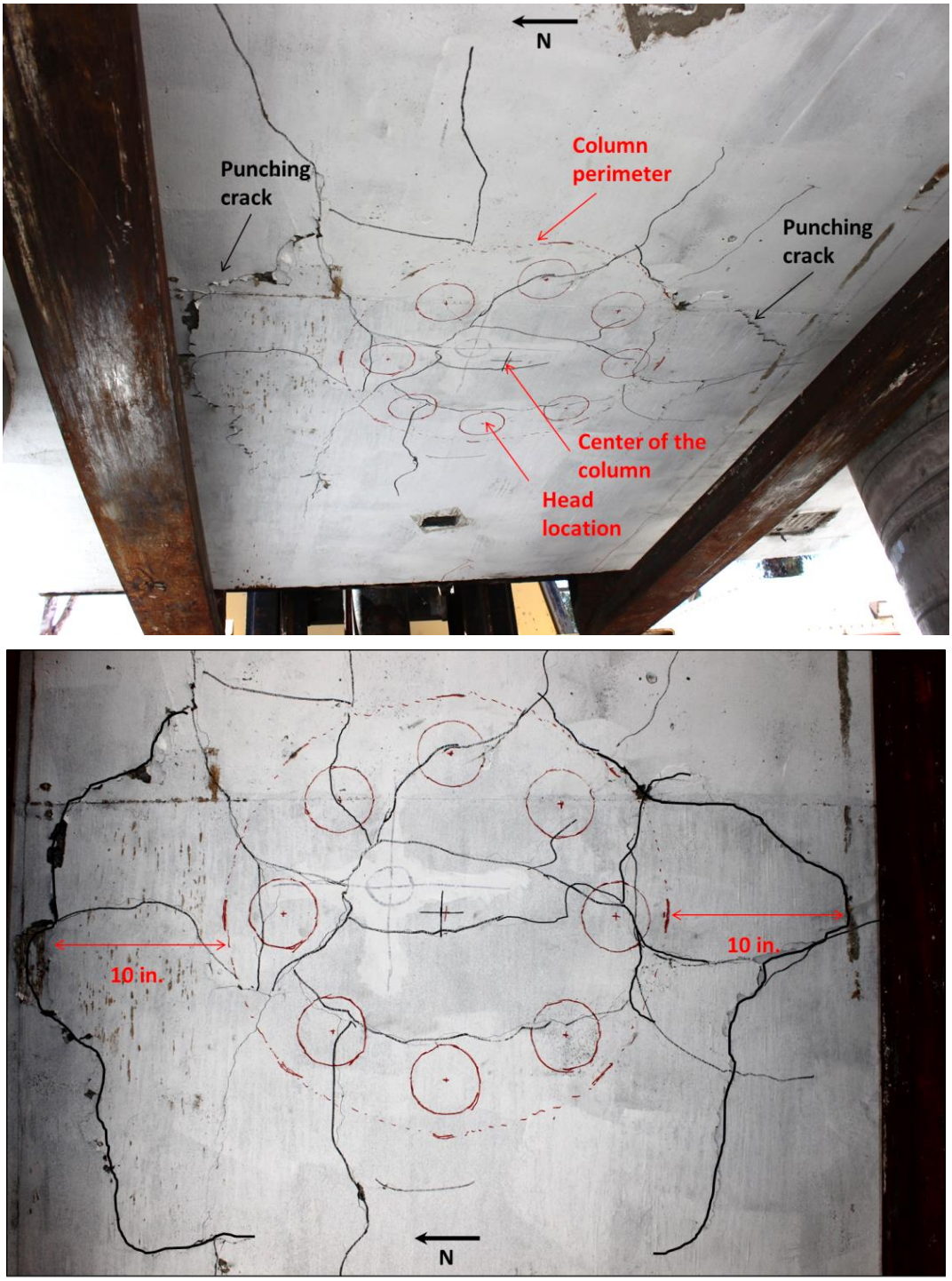

Figure 4.9 – Crack pattern at the top face of the slab (bottom face in the specimen) after the testing of Specimen #1

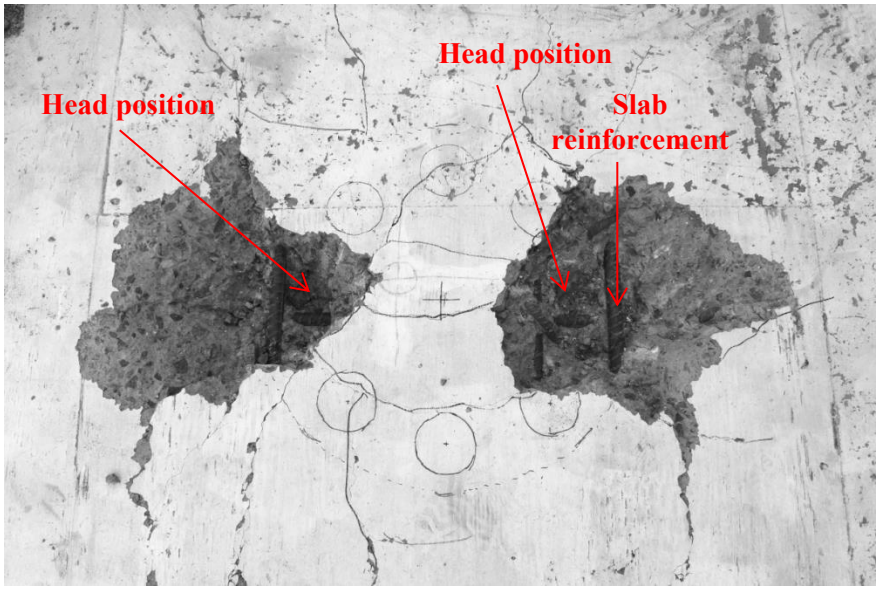

Figure 4.10 – Exposure of fracture surface at the top face of the slab (bottom face in the specimen) of Specimen #1

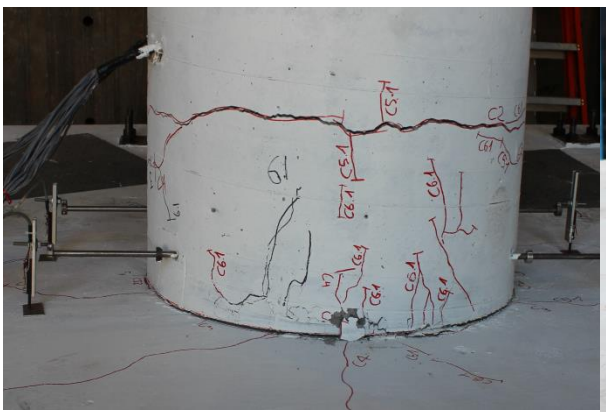

(a) north face at Cycle 6b (μ = 2)

(b) west face at Cycle 8a (μ = 4)

(c) east face at Cycle 10a (μ = 6)

(d) north face at Cycle 10a (μ = 6)

Figure 4.11 – Evolution of damage at the bottom of the column of Specimen #2

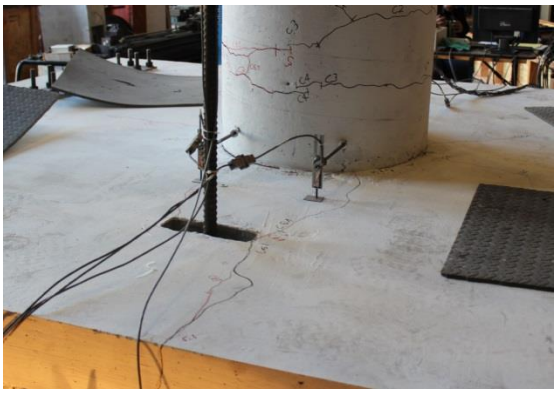

(a) west face at Cycle 6a (μ = 2)

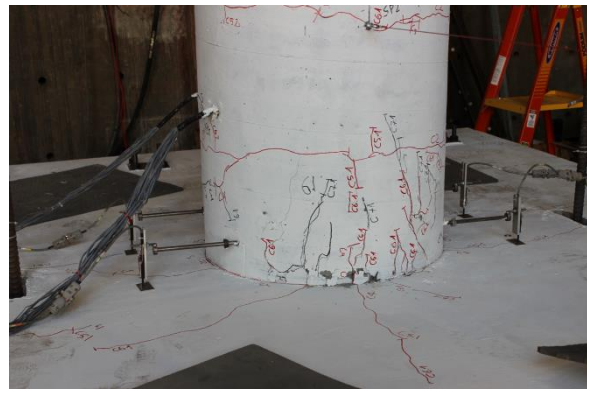

(b) north face at Cycle 7a (μ = 3)

(c) east face at Cycle 9a (μ = 5)

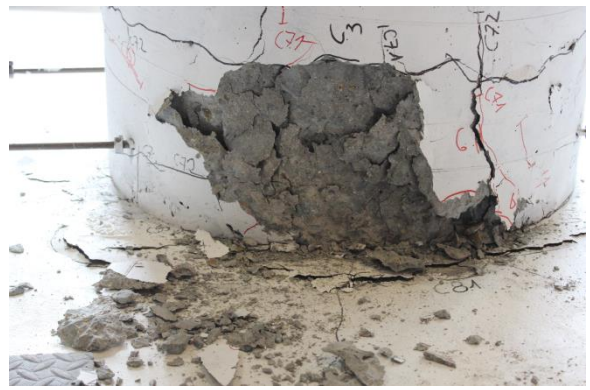

(d) north face at Cycle 9a (μ = 5)

Figure 4.12 – Evolution of damage at the bottom face of the slab (top face in the specimen) of Specimen #2

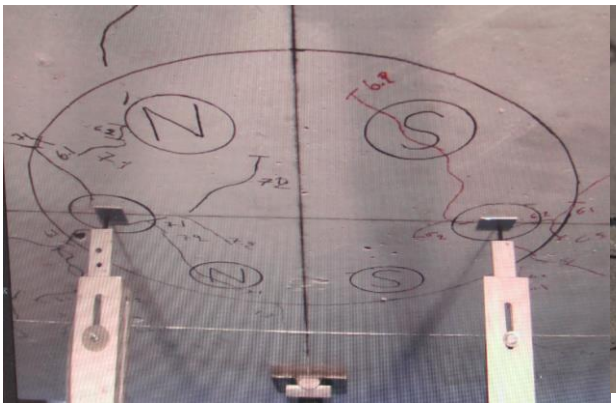

(a) Cycle 7b (μ = 3)

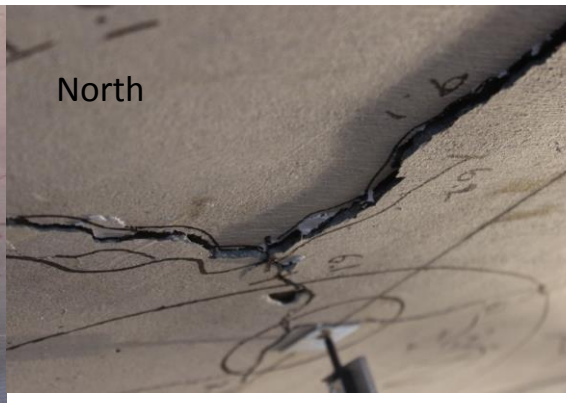

(b) Cycle 9b (μ = 5)

(c) Cycle 10a (μ = 6)

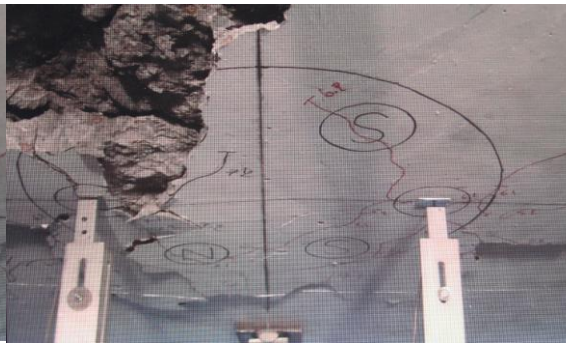

(d) Cycle 10b (μ = 6)

Figure 4.13 – Evolution of damage at the top face of the slab (bottom face in the specimen) of Specimen #2

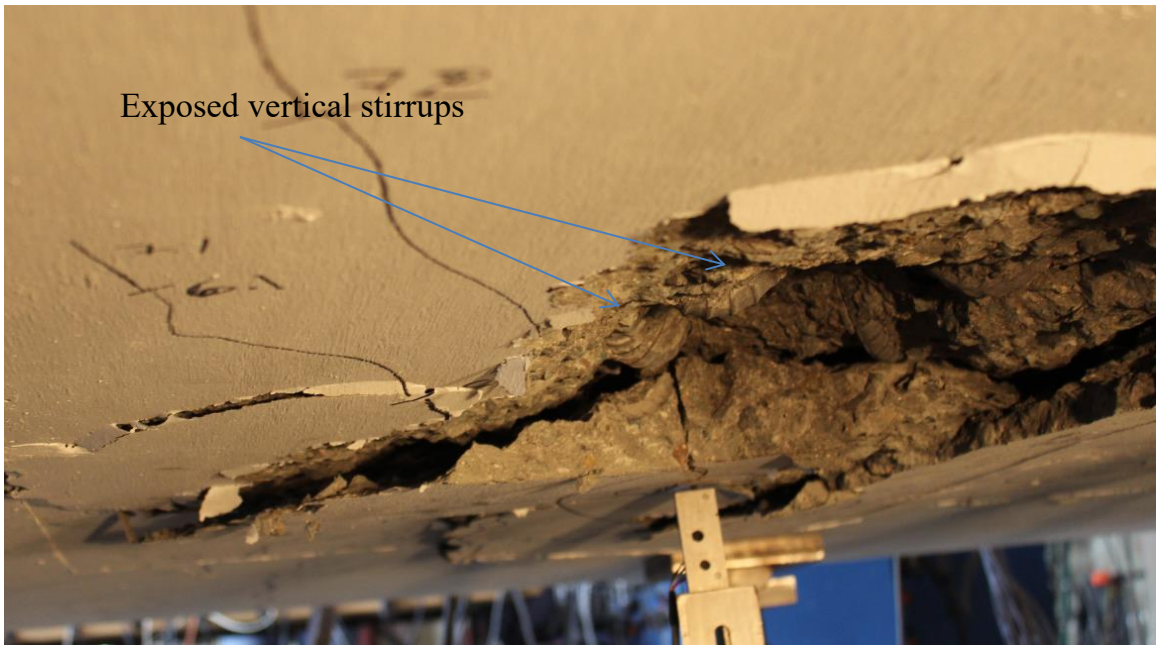

(a) North region

(b) South region

Figure 4.14 – Damage at the top face of the slab (bottom face in the specimen) of Specimen #2 at the end of testing

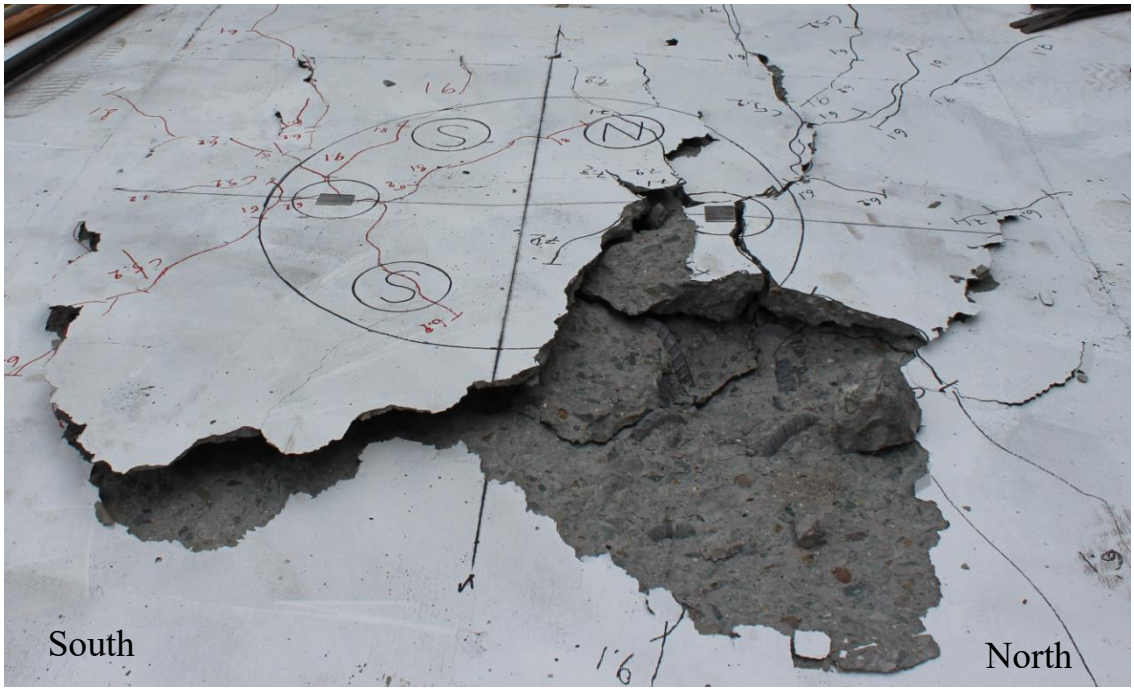

(a) Before removing loose concrete pieces

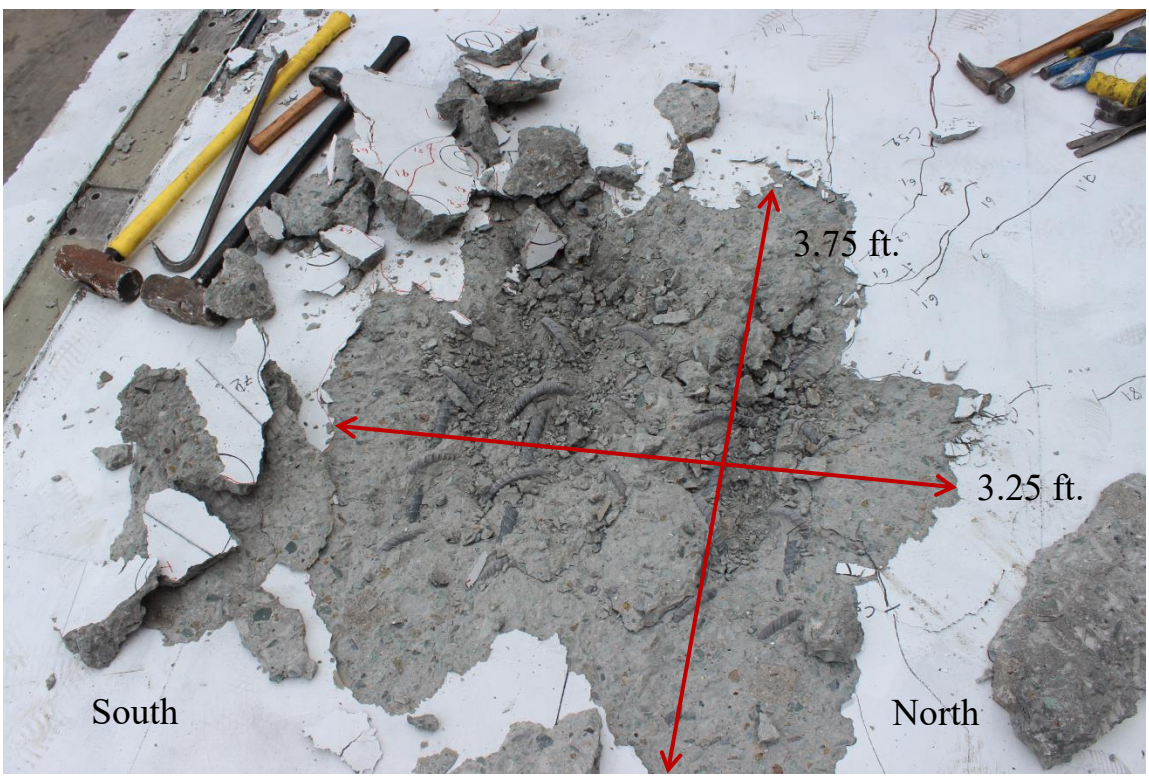

(b) After removing loose concrete pieces

Figure 4.15 – Exposure of fracture surface at the top face of the slab (bottom face in the specimen) of Specimen #2

(a) north face at Cycle 6b (μ = 2) (b) west face at Cycle 8a (μ = 4)

(c) north face at Cycle 10b (μ = 6) (d) south face at Cycle 11b (μ = 7)

Figure 4.16 – Evolution of damage at the base of the column of Specimen #3

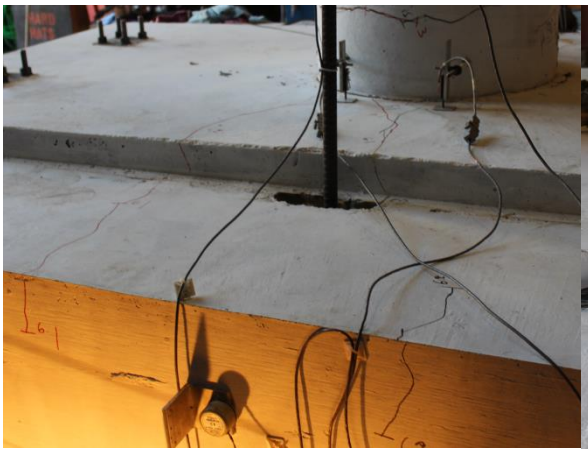

(a) west face at Cycle 6b (μ = 2)

(b) east face at Cycle 8a (μ = 4)

(c) east face at Cycle 9a (μ = 5)

(d) north face at Cycle 11b (μ = 7)

Figure 4.17 – Evolution of damage at the bottom face of the slab (top face in the specimen) of Specimen #3

Figure 4.18 – Damage at the slab-column interface after the testing of Specimen #3

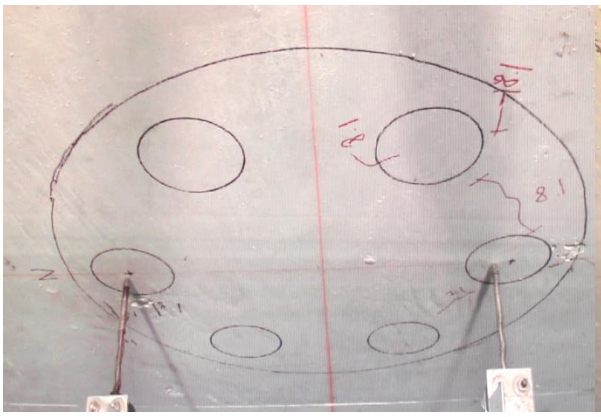

(a) Cycle 8a (μ = 4)

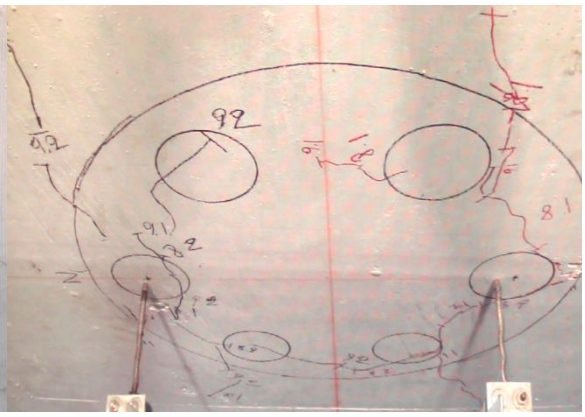

(b) Cycle 10b (μ = 6)

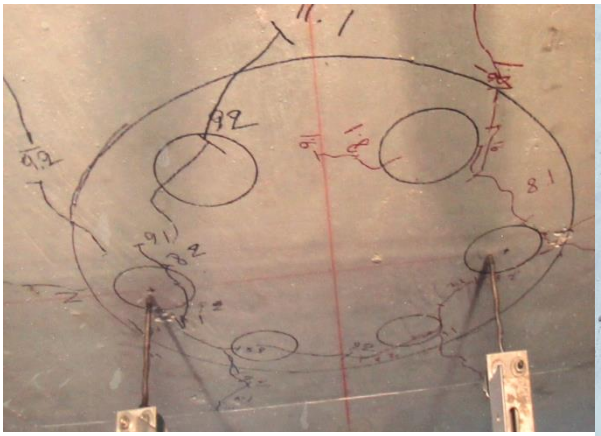

(c) Cycle 11b (μ = 7)

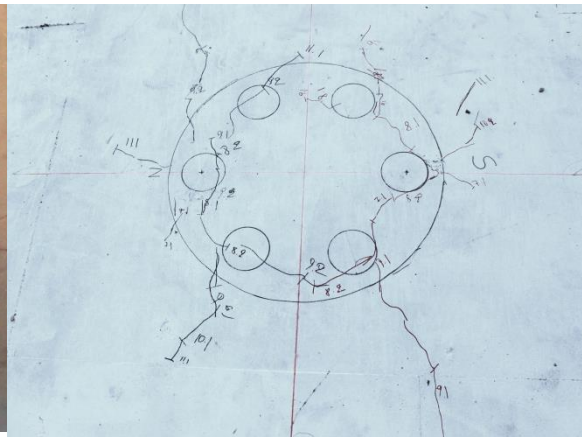

(d) After the end of the test

Figure 4.19 – Evolution of damage at the top face of the slab (bottom face in the specimen) of Specimen #3

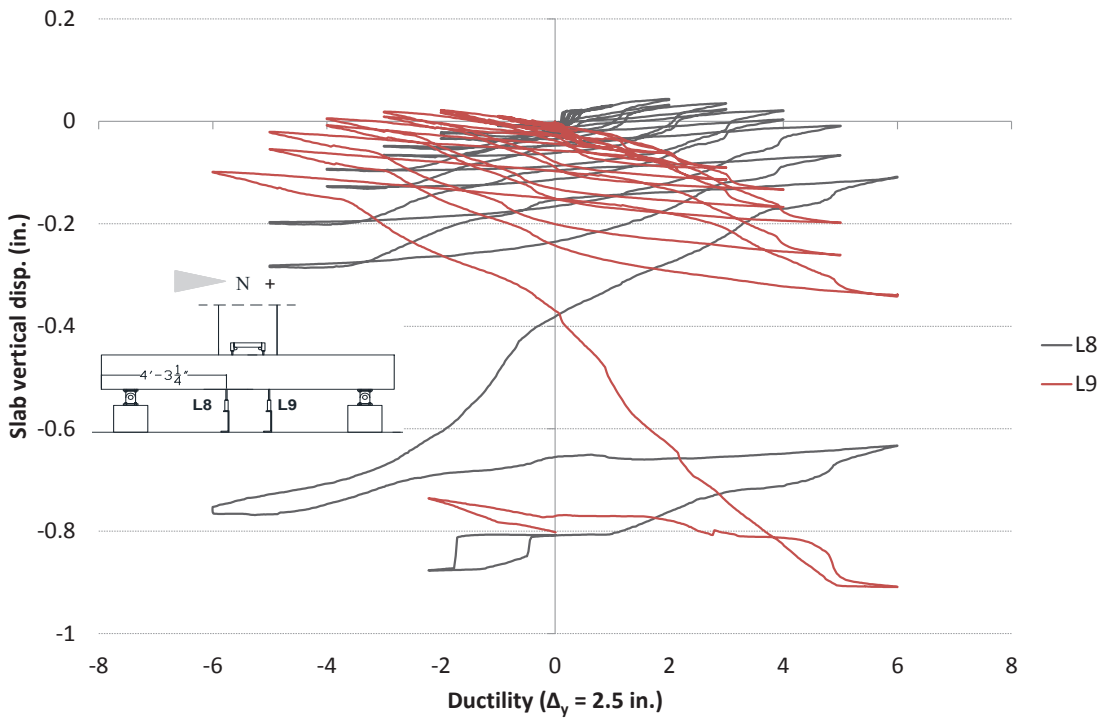

Figure 4.20 – Vertical displacement of the top face of the slab (bottom face in the specimen) of Specimen #2

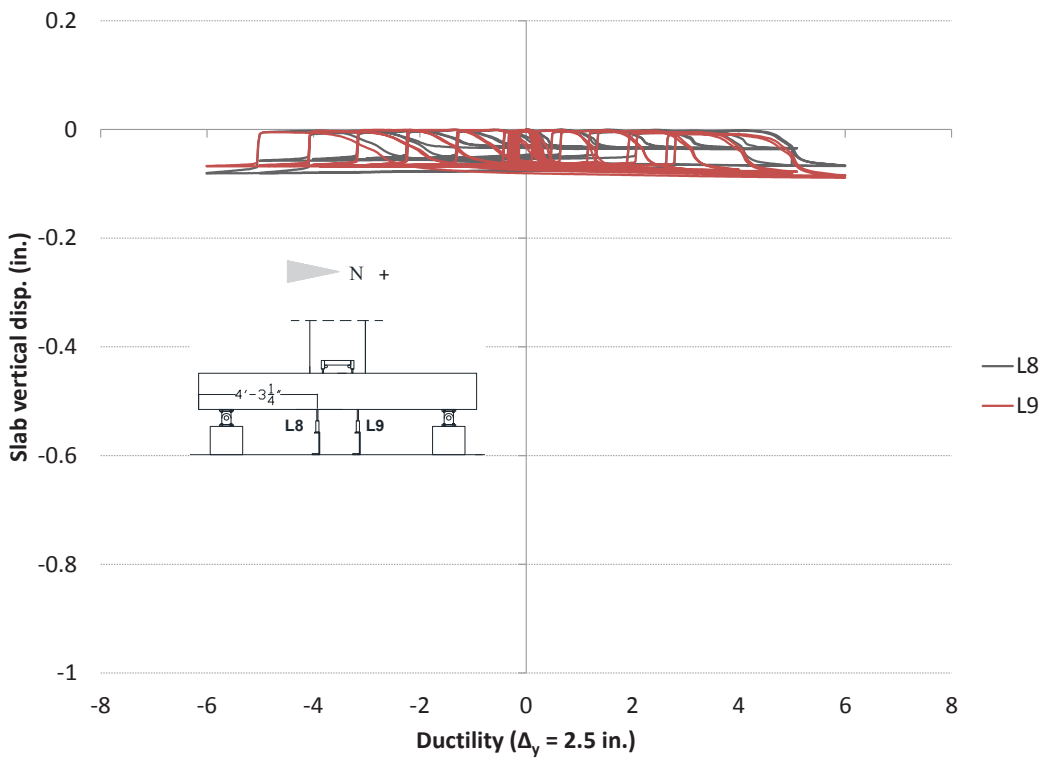

Figure 4.21 – Vertical displacement of the top face of the slab (bottom face in the specimen) of Specimen #3

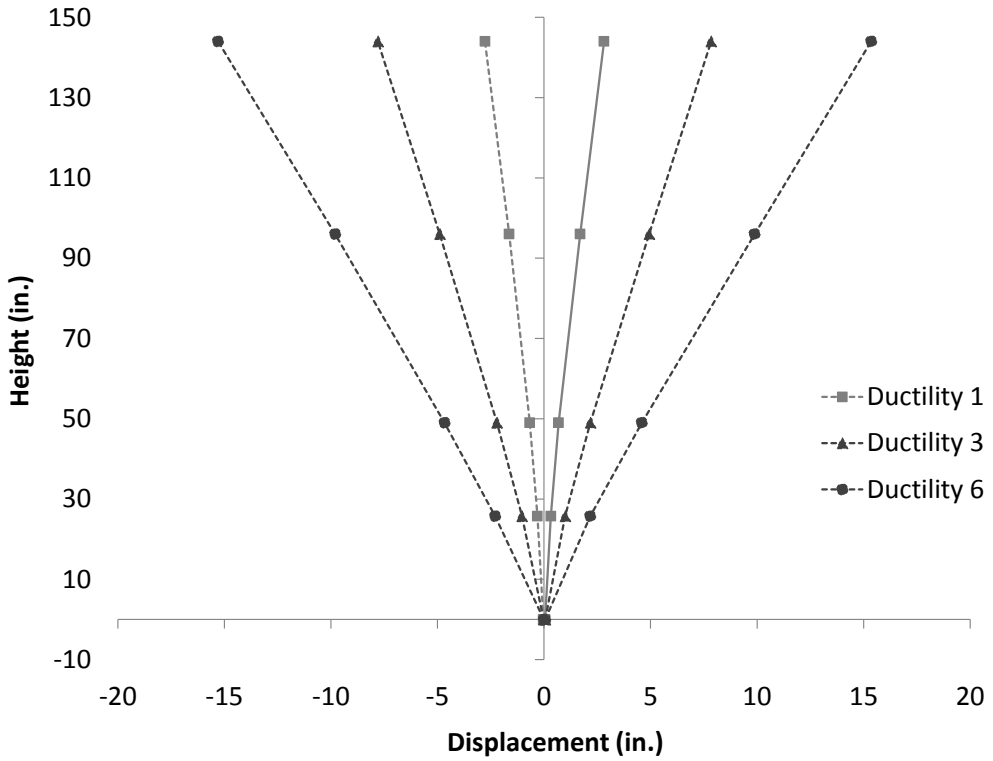

Figure 4.22 – Lateral displacement of the column of Specimen #1

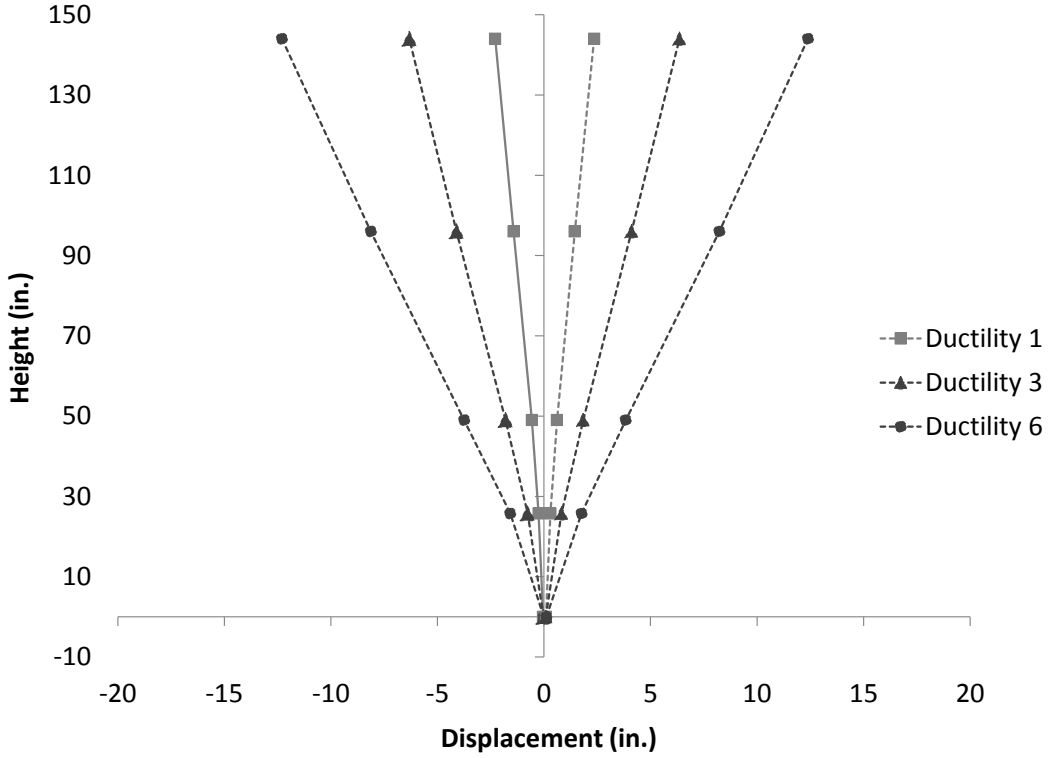

Figure 4.23 – Lateral displacement of the column of Specimen #2

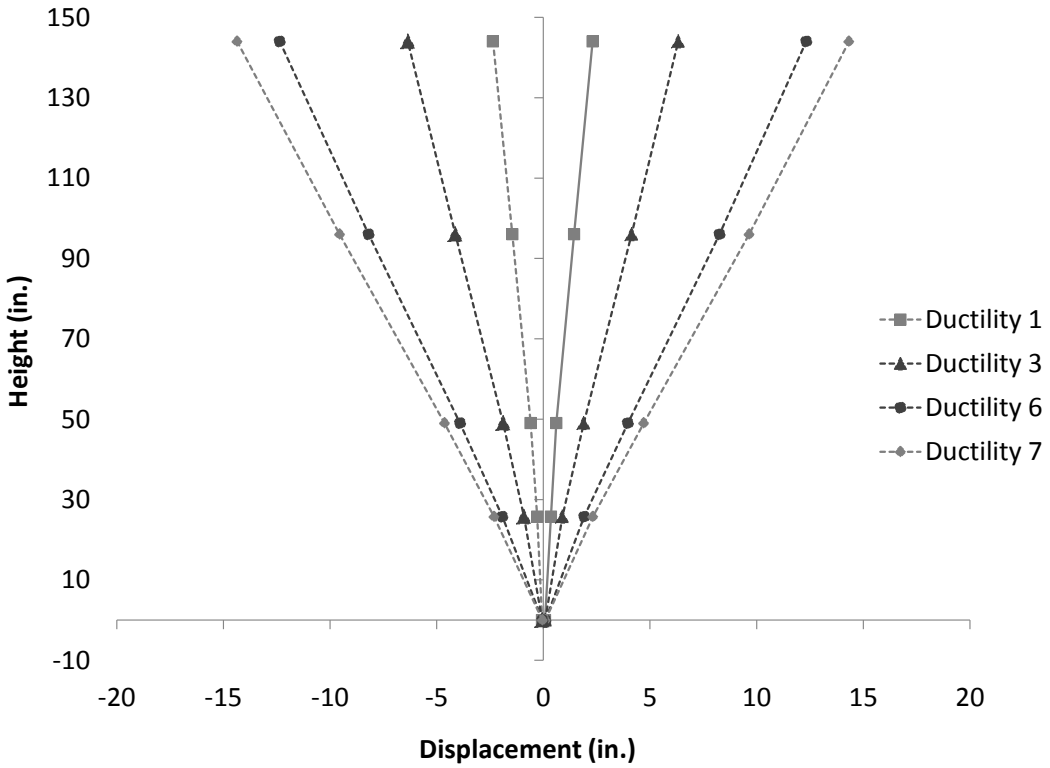

Figure 4.24 – Lateral displacement of the column of Specimen #3

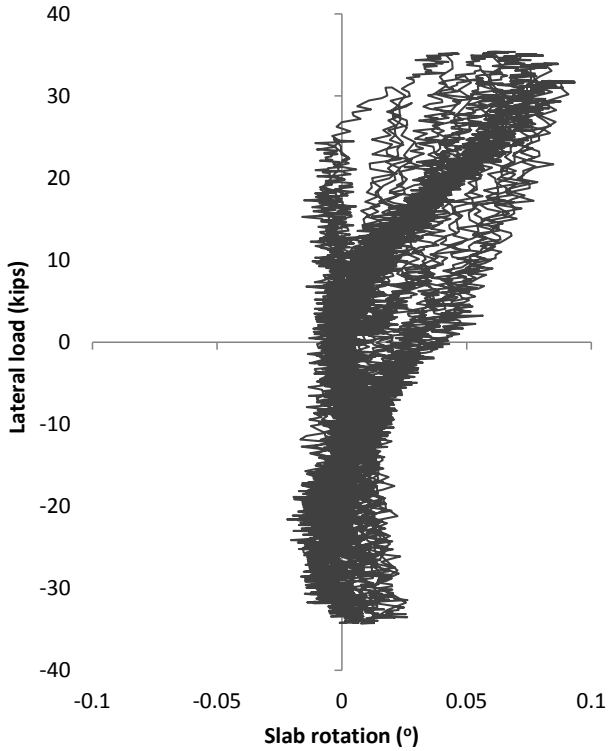

Figure 4.25 – Lateral load-vs.-slab rotation (at center) curves for Specimen #1

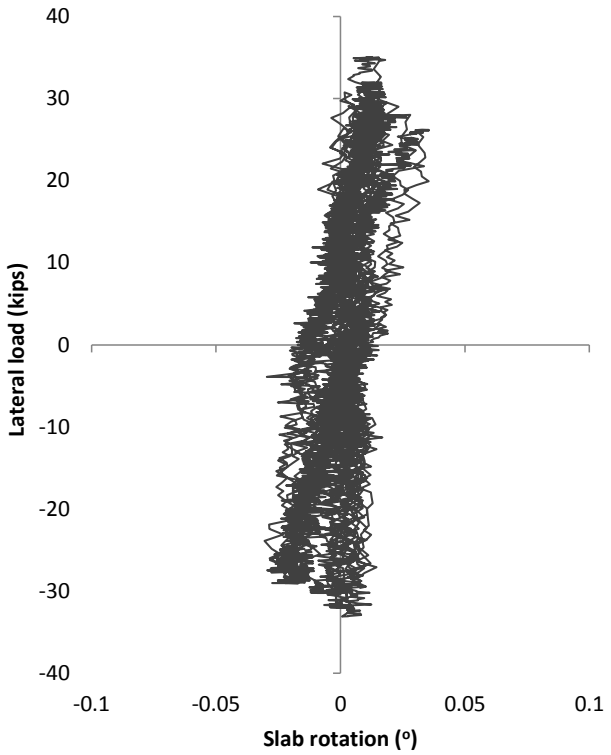

Figure 4.26 – Lateral load-vs.-slab rotation (at center) curves for Specimen #2

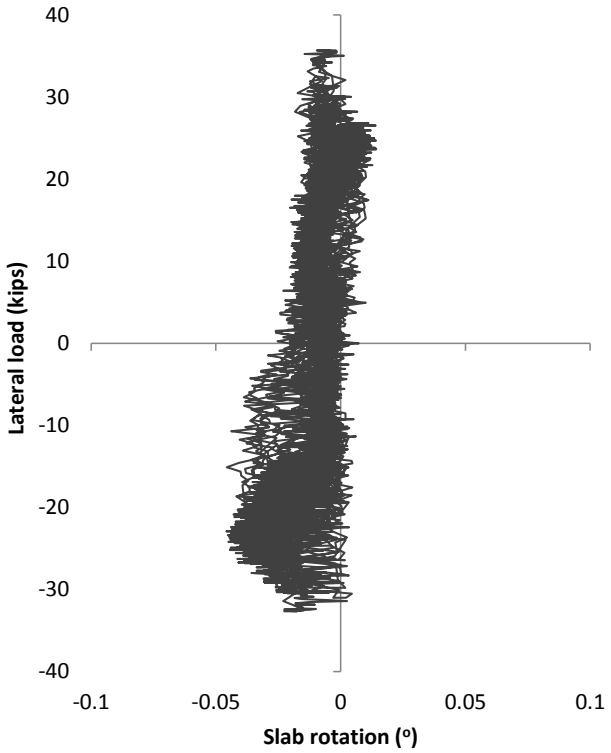

Figure 4.27 – Lateral load-vs.-slab rotation (at center) curves for Specimen #3

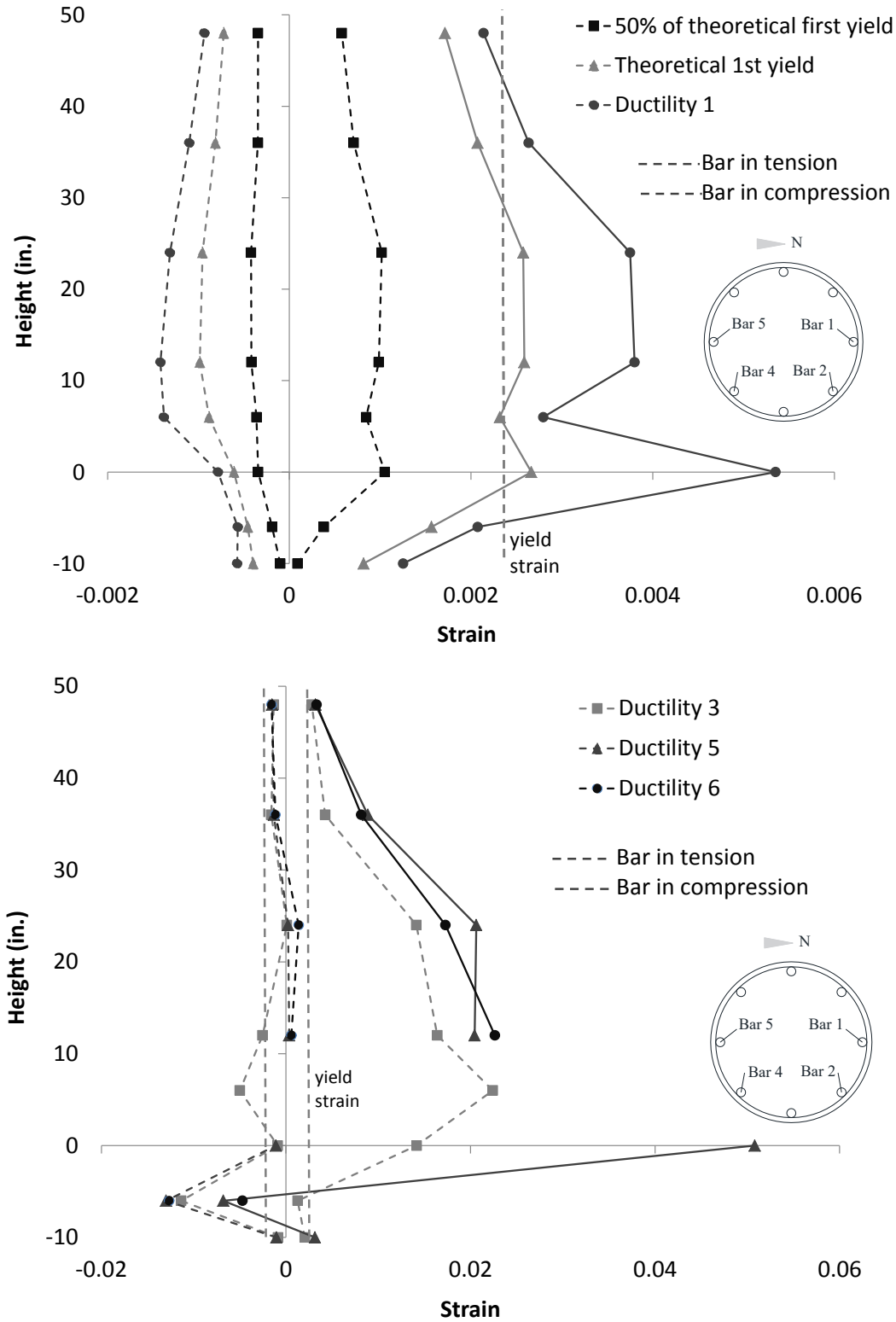

Figure 4.28 – Strains along Bar 1 in Specimen #1

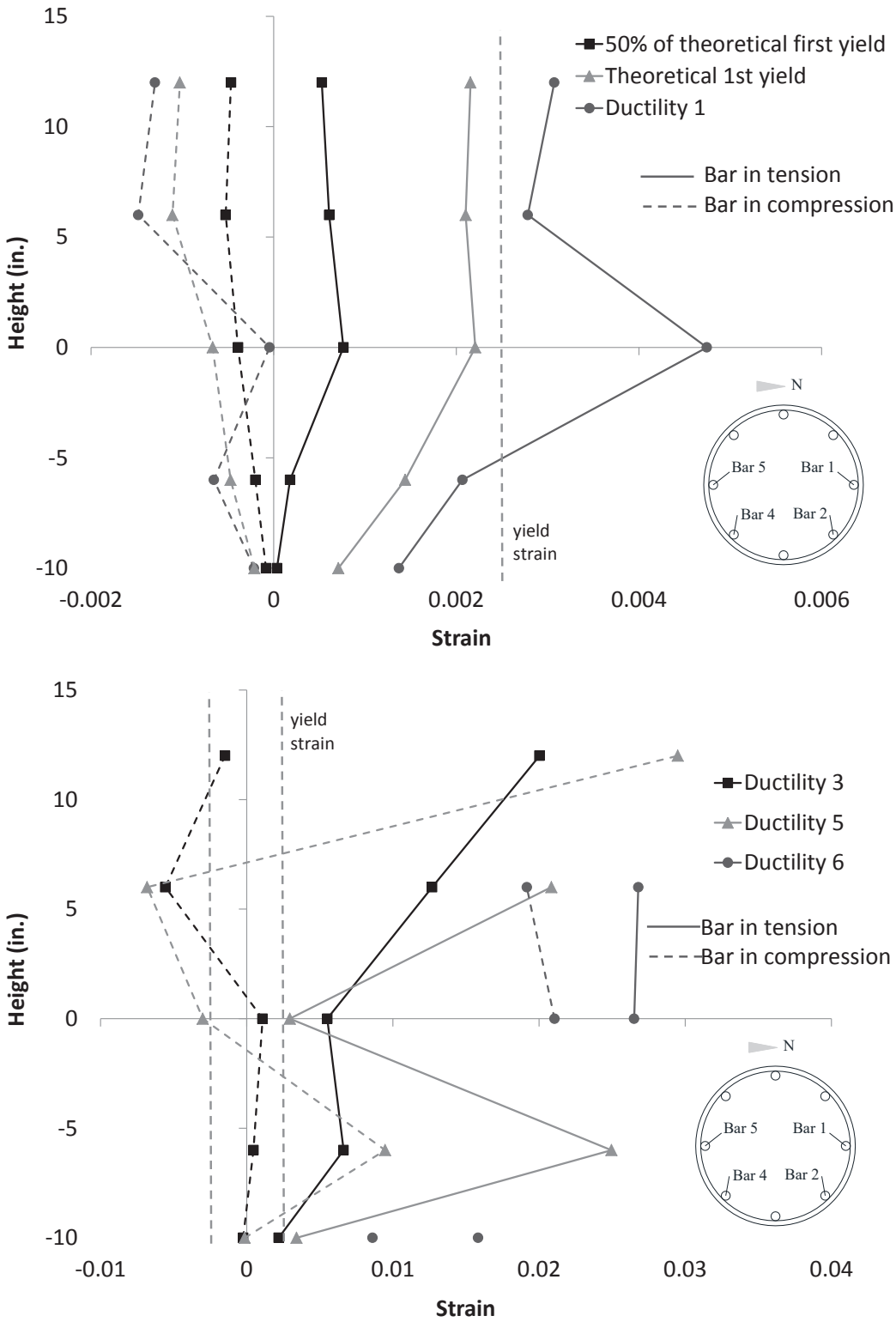

Figure 4.29 – Stains along Bar 5 in Specimen #1

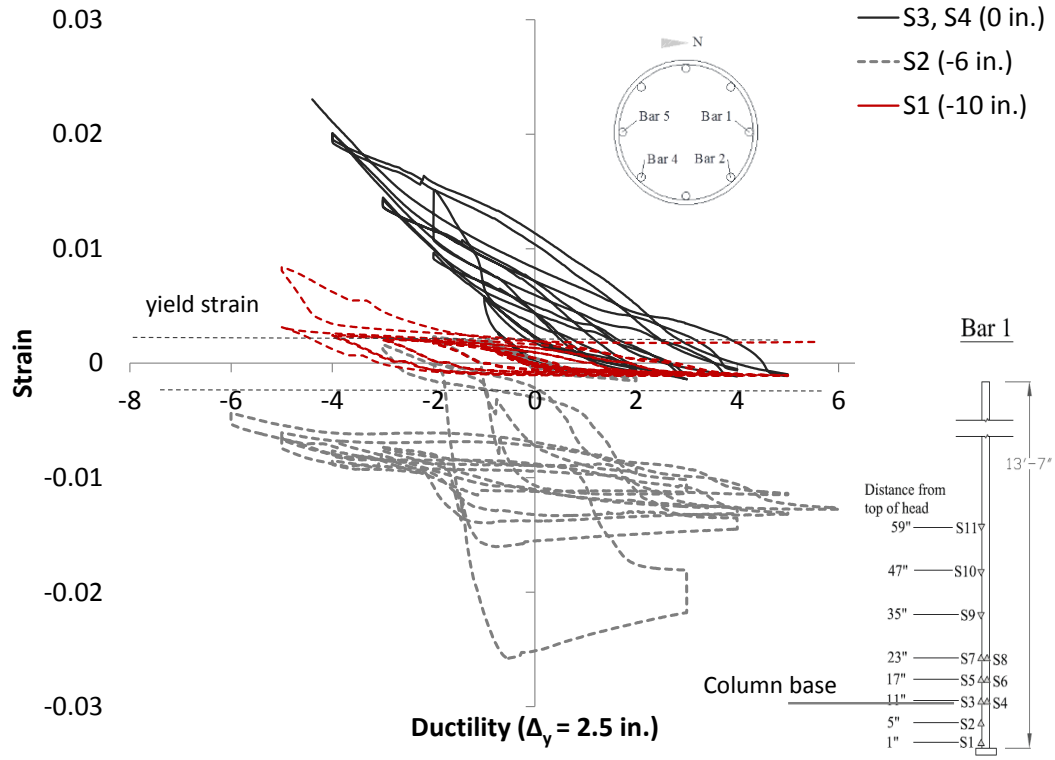

Figure 4.30 – Strain-vs.-ductility curves for Bar 1 in the slab-column joint of Specimen #1

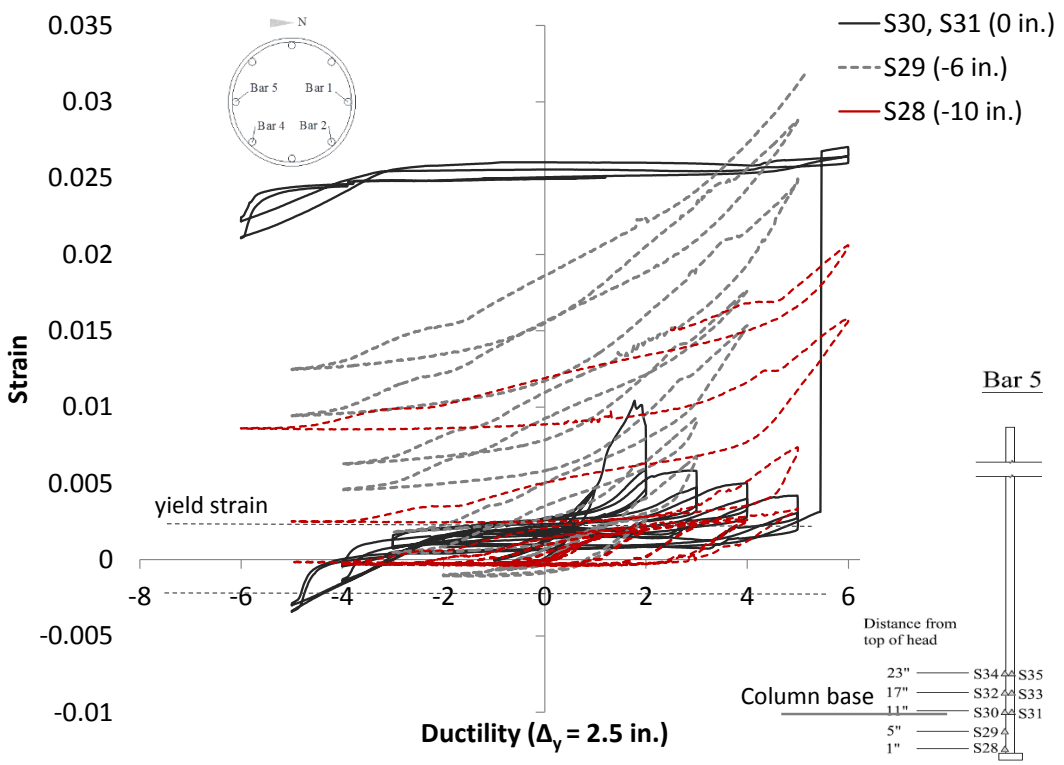

Figure 4.31 – Strain-vs.-ductility curves for Bar 5 in the slab-column joint of Specimen #1

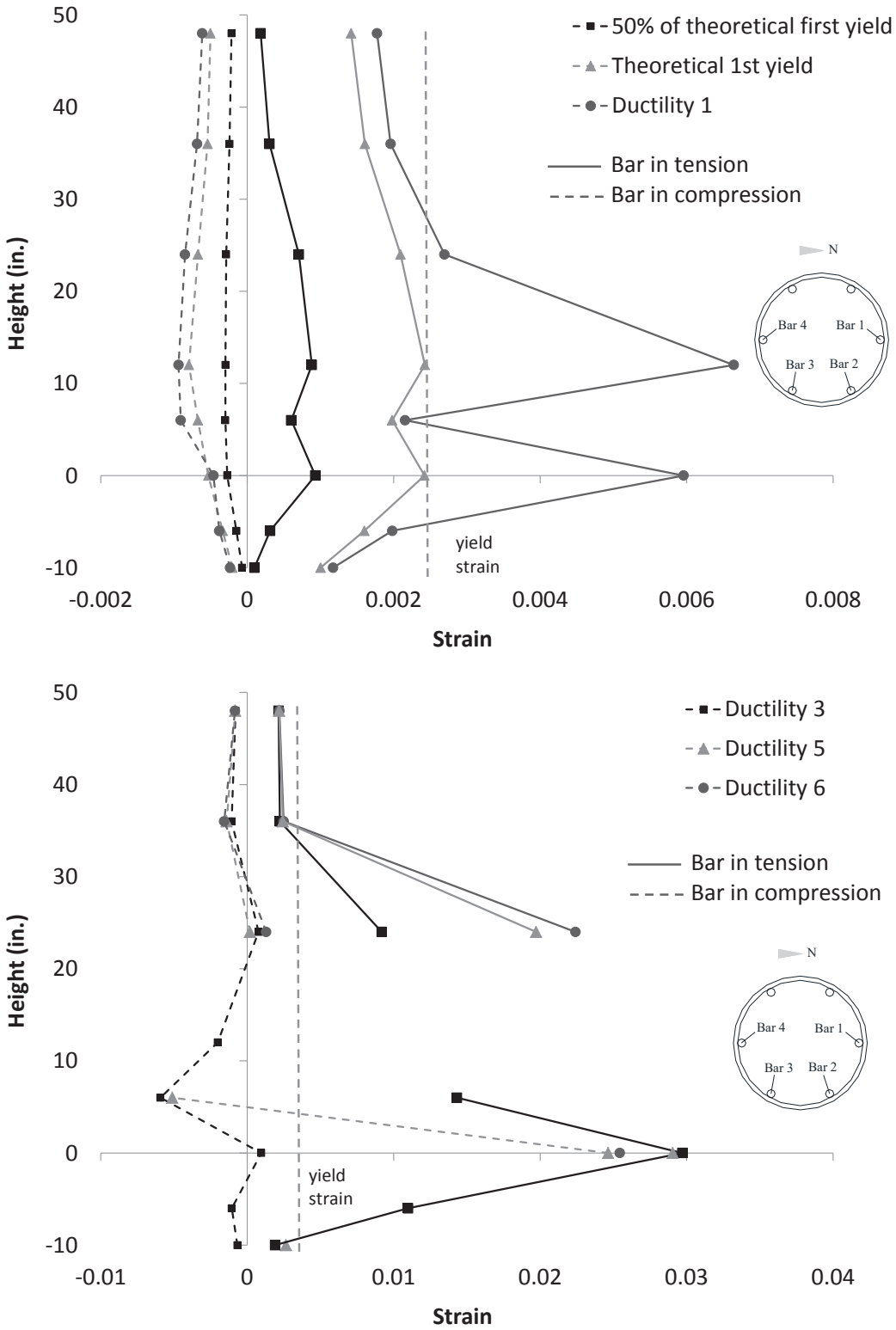

Figure 4.32 – Strains along Bar 1 in Specimen #2

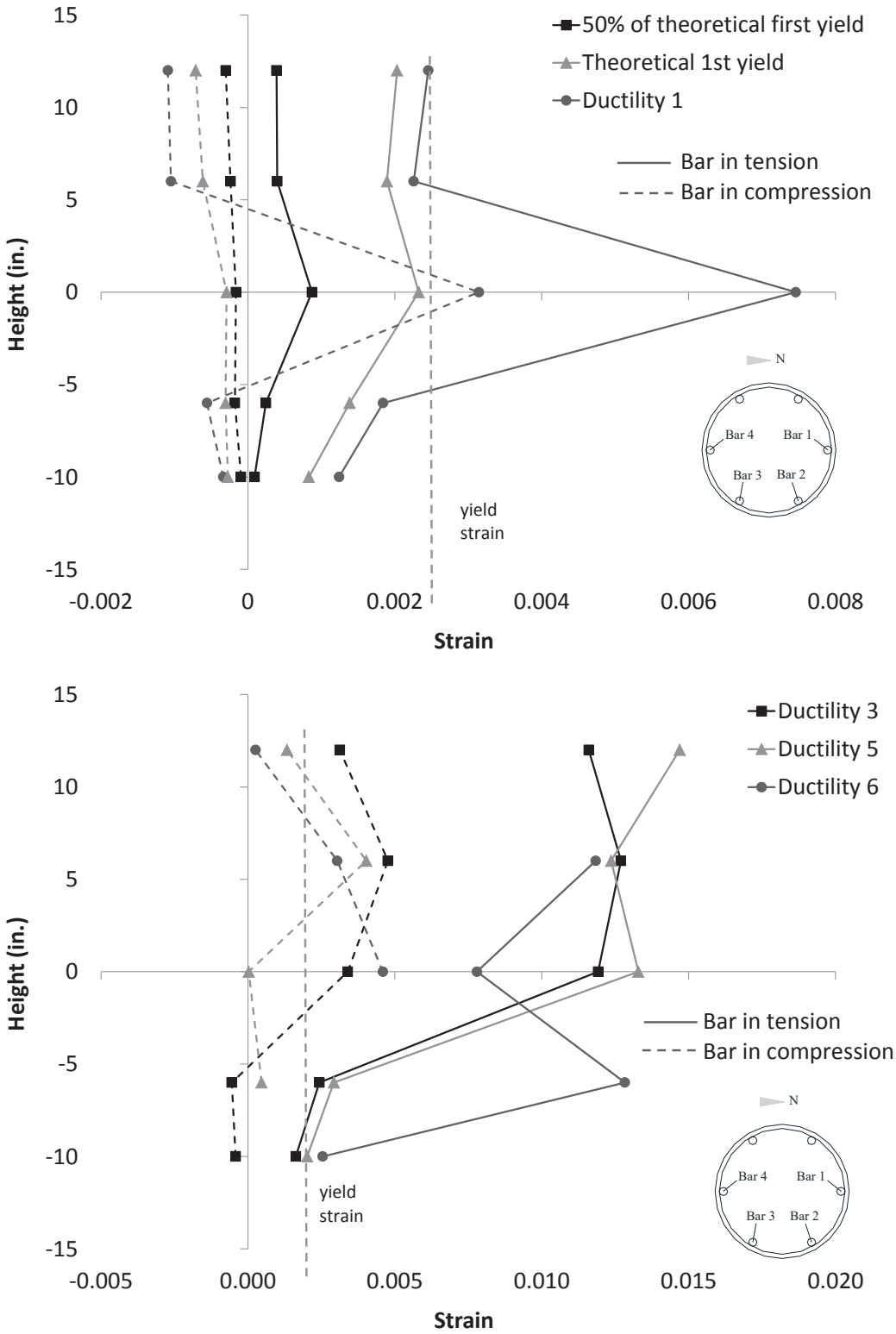

Figure 4.33 – Strains along Bar 4 in Specimen #2

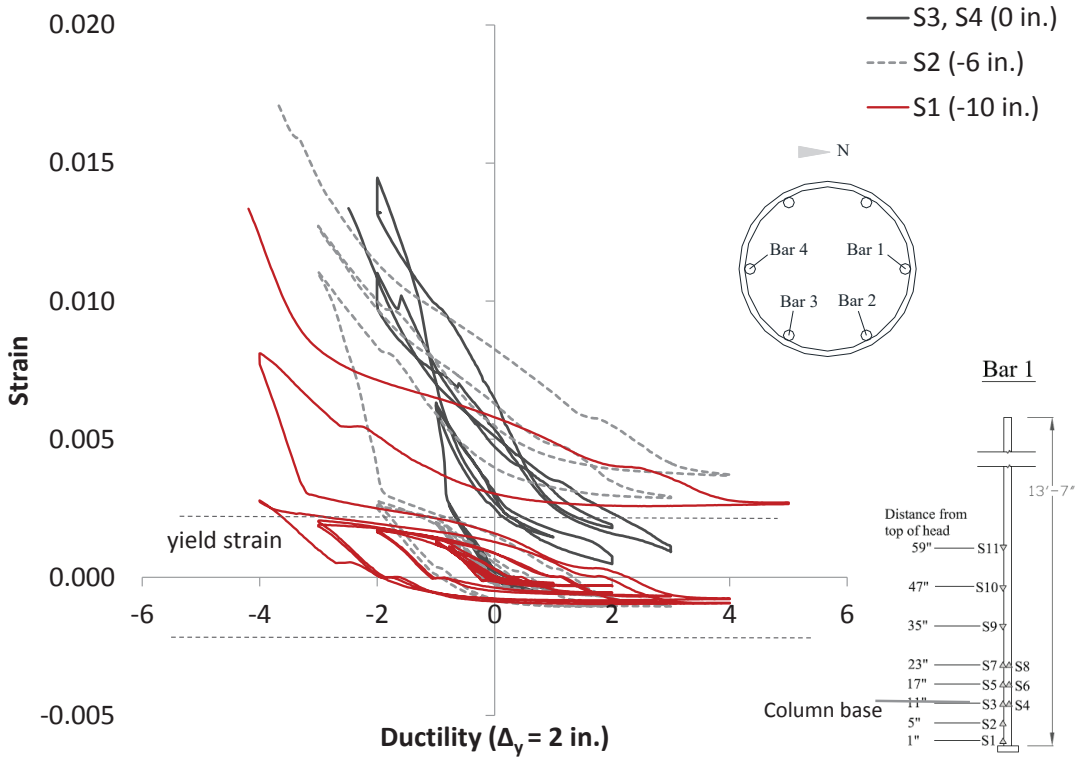

Figure 4.34 – Strain-vs.-ductility curves for Bar 1 in the slab-column joint of Specimen #2

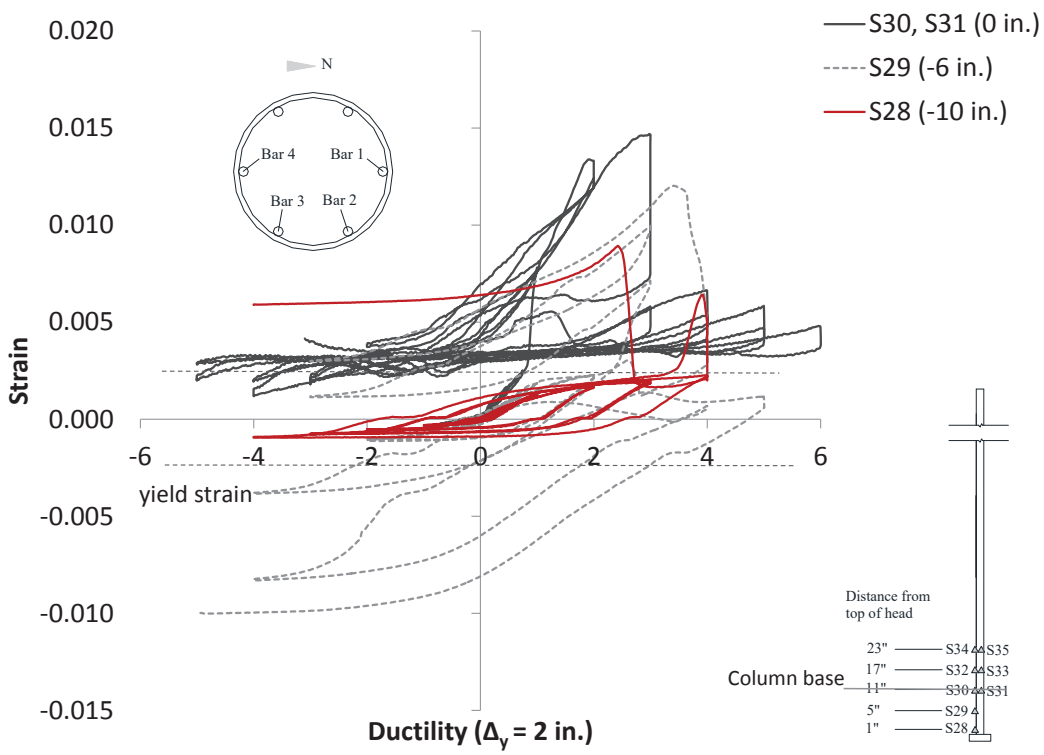

Figure 4.35 – Strain-vs.-ductility curves for Bar 4 in the slab-column joint of Specimen #2

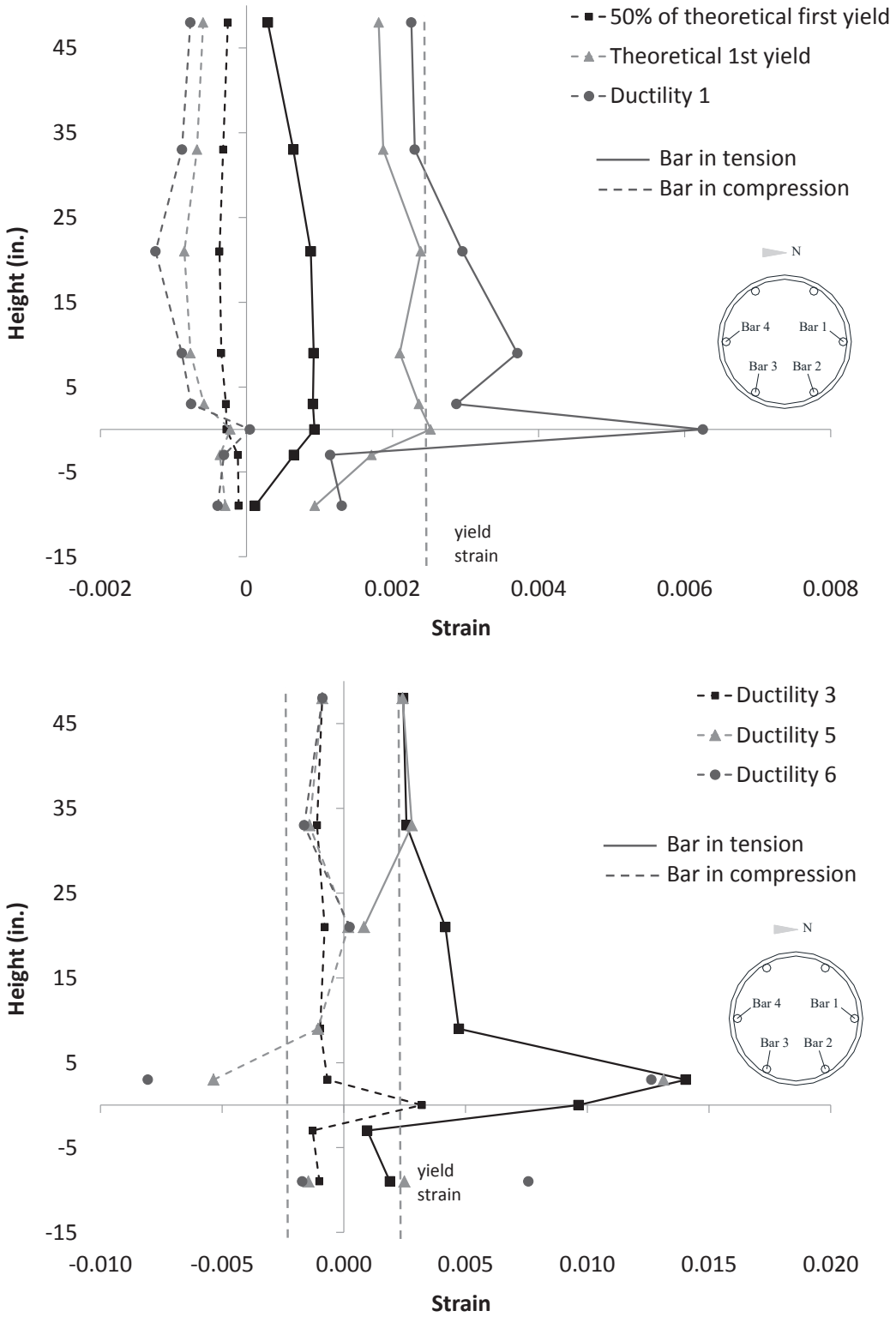

Figure 4.36 – Strains along Bar 1 in Specimen #3

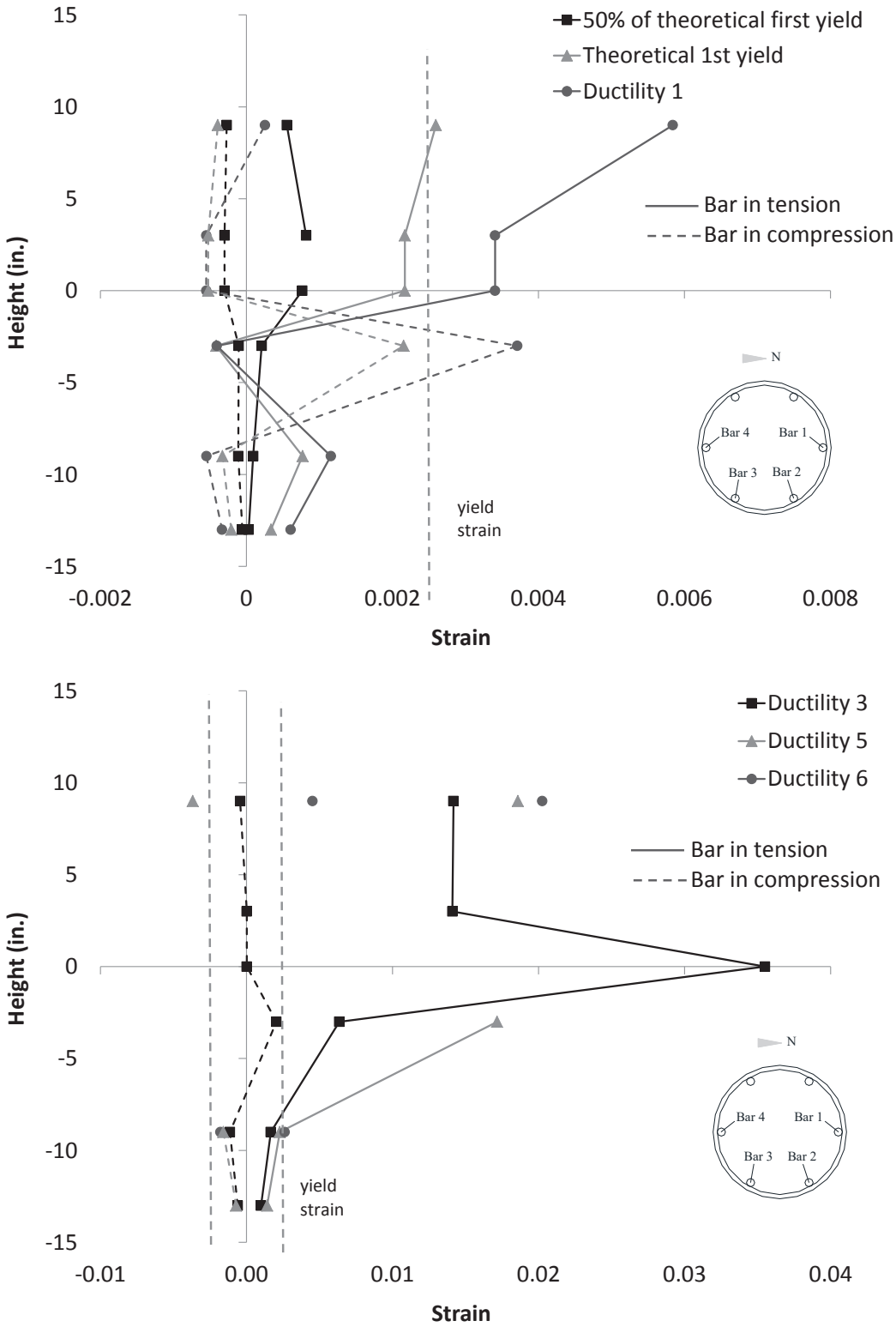

Figure 4.37 – Strains along Bar 4 in Specimen #3

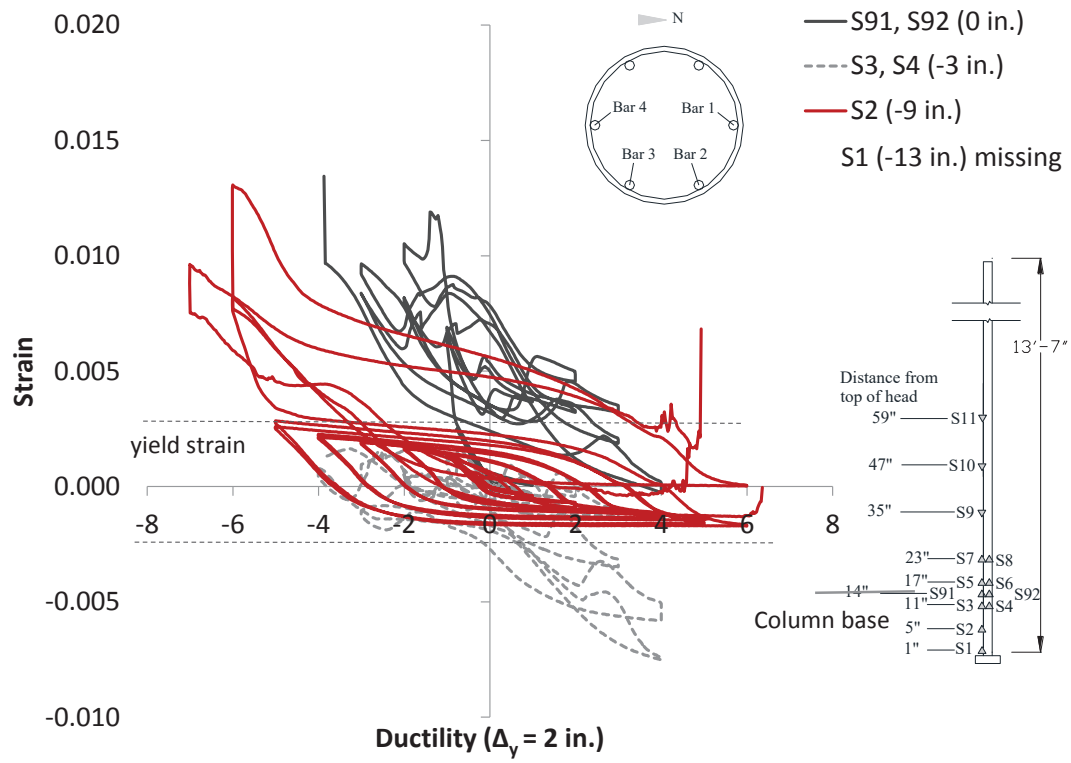

Figure 4.38 – Strain-vs.-ductility curves for Bar 1 in the slab-column joint of Specimen #3

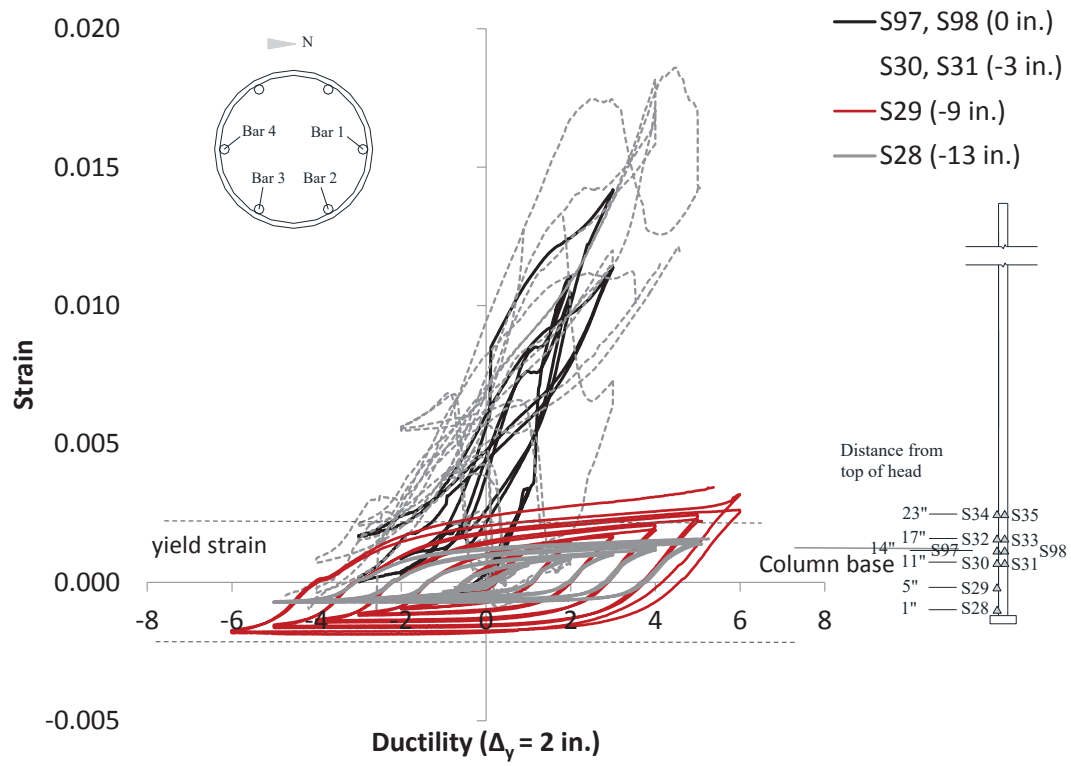

Figure 4.39 – Strain-vs.-ductility curves for Bar 4 in the slab-column joint of Specimen #3

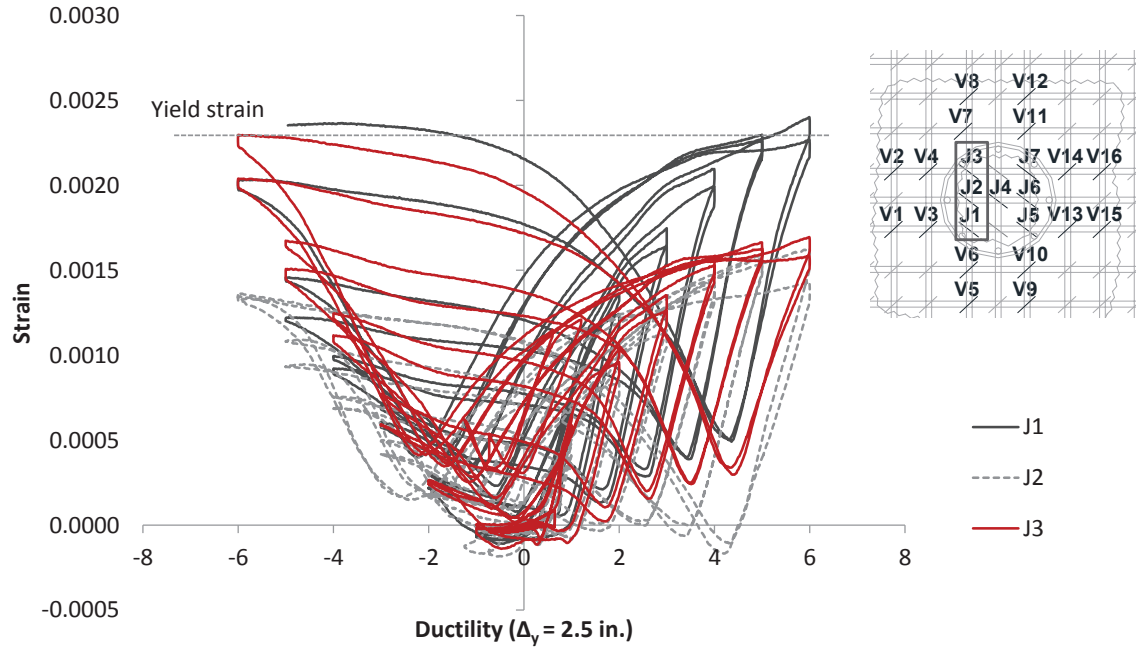

(a) J-bars on the south side

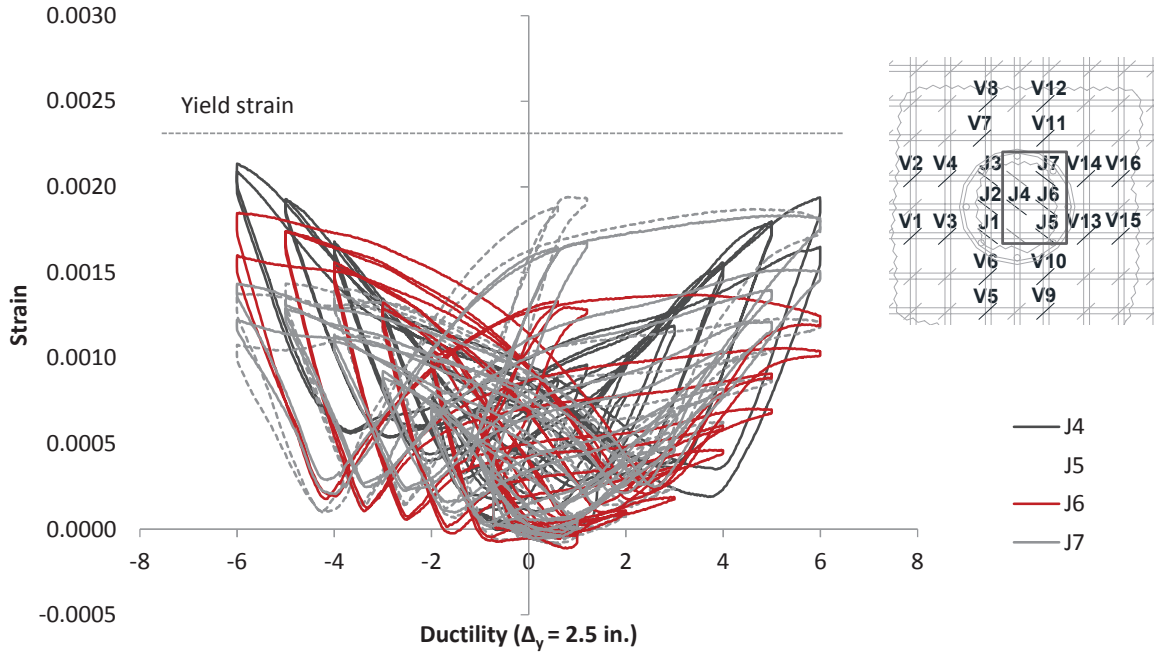

(b) J-bars at the center and on the north side

Figure 4.40 – Strains in J-bars of Specimen #1

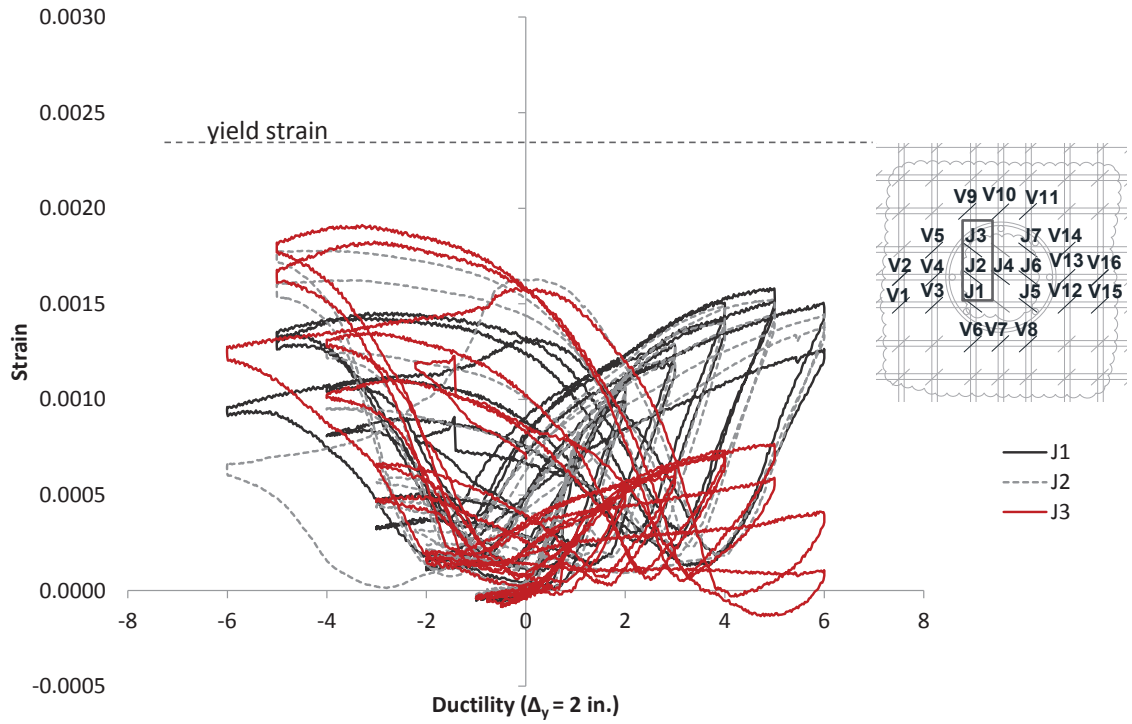

(a) J-bars on the south side

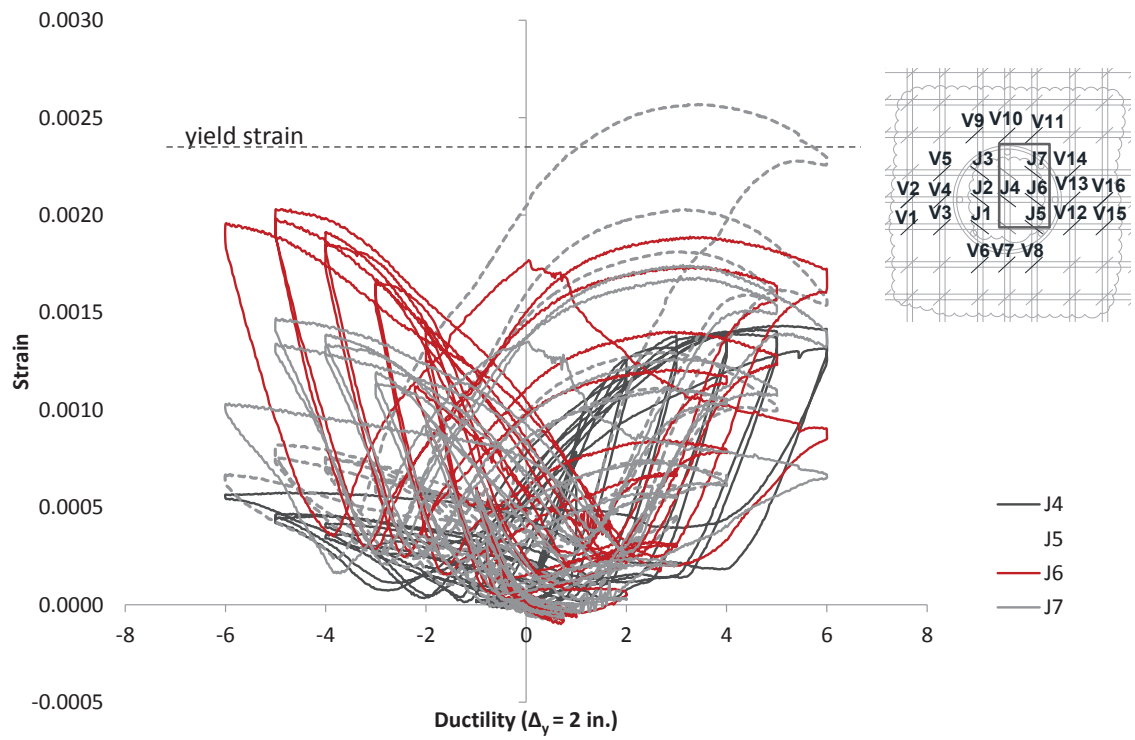

(b) J-bars at the center and on the north side

Figure 4.41 – Strains in J-bars of Specimen #2

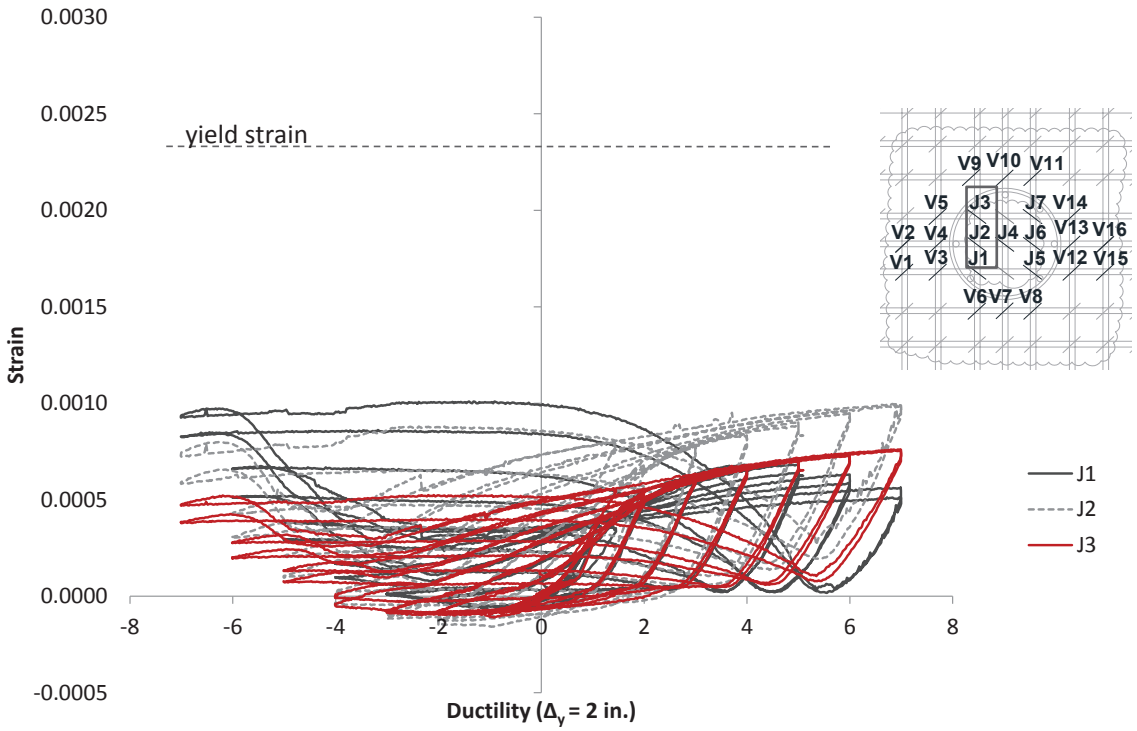

(a) J-bars on the south side

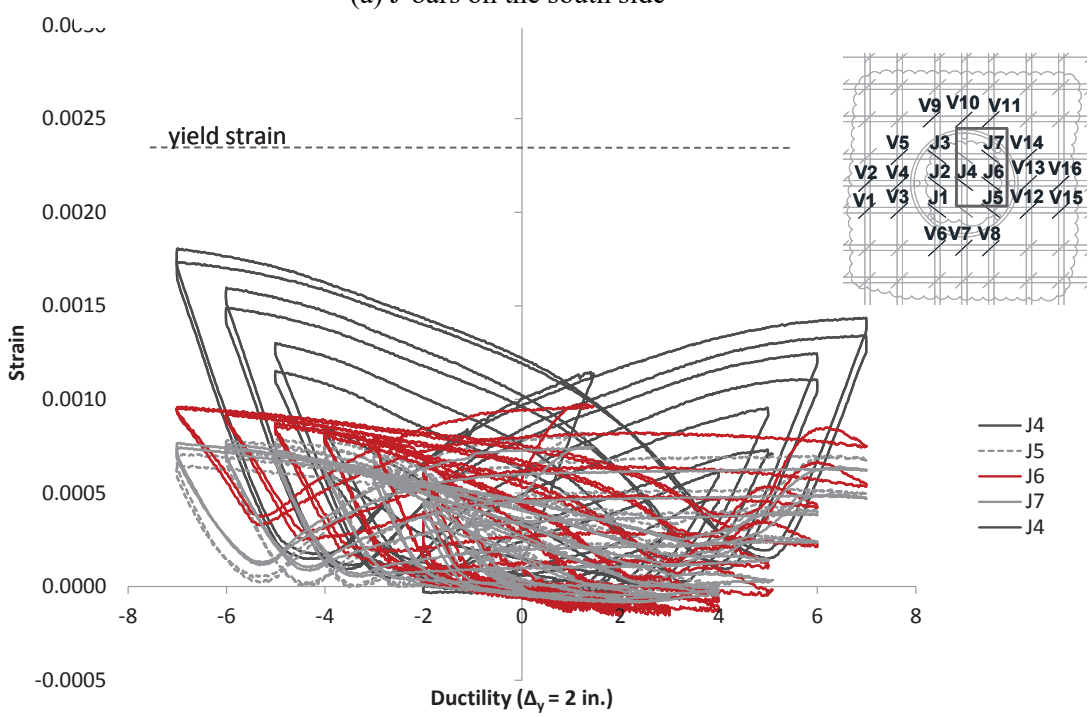

(b) J-bars at the central and on the north side

Figure 4.42 – Strains in J-bars of Specimen #3

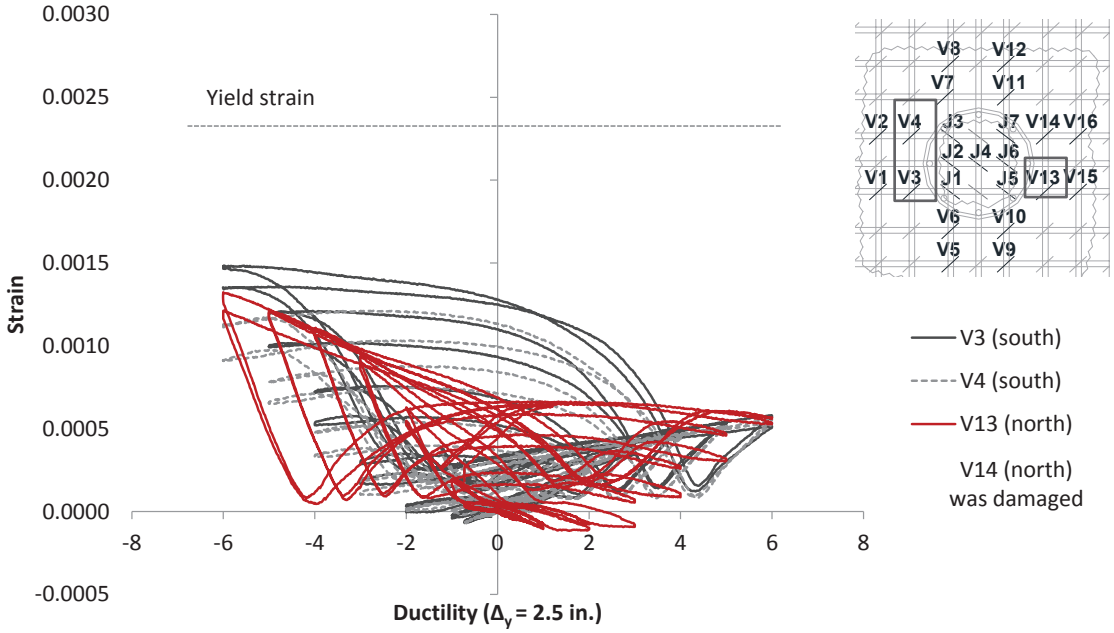

(a) south and north faces

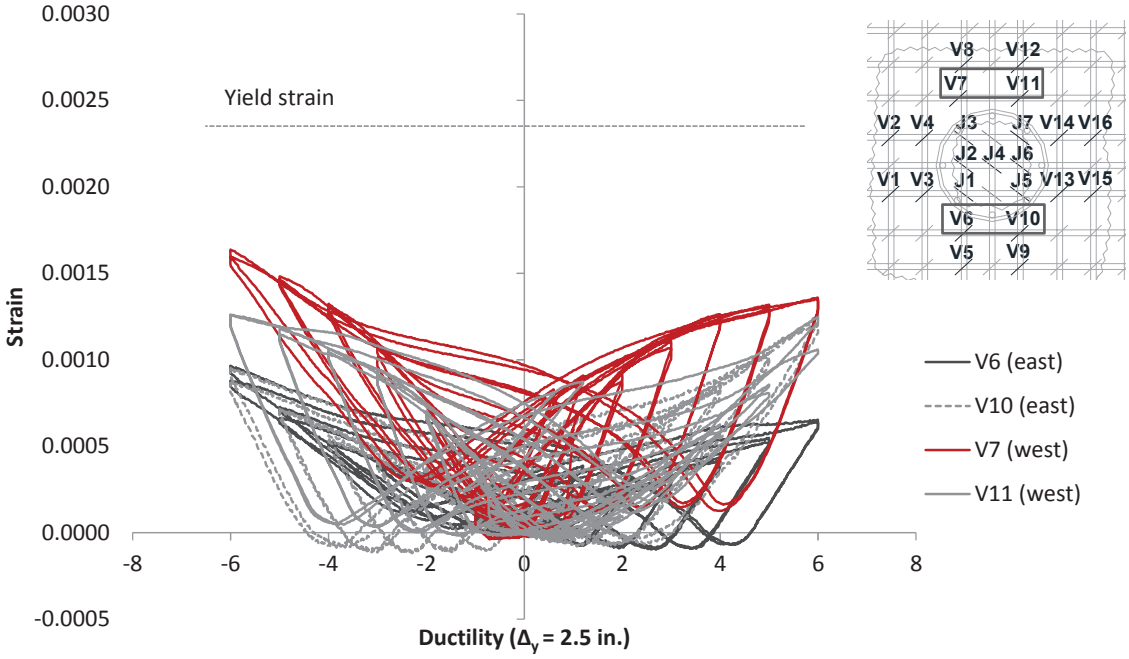

(b) east and west faces

Figure 4.43 – Strains in the 1st row of vertical stirrups of Specimen #1

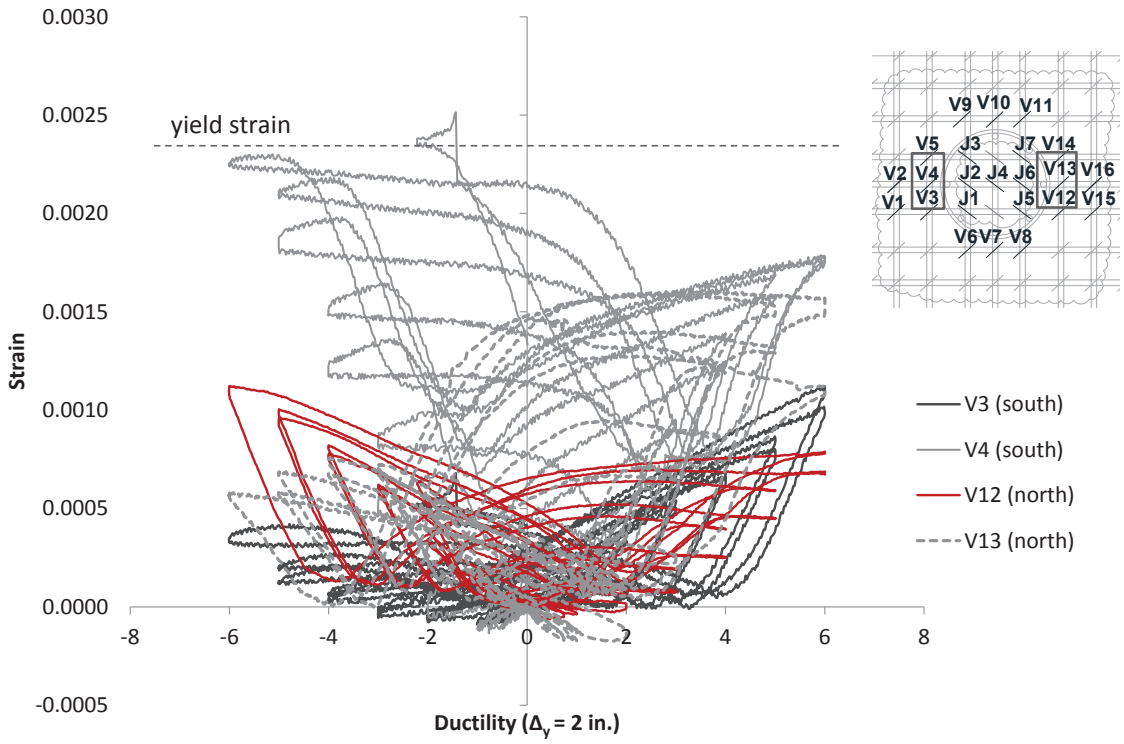

(a) south and north faces

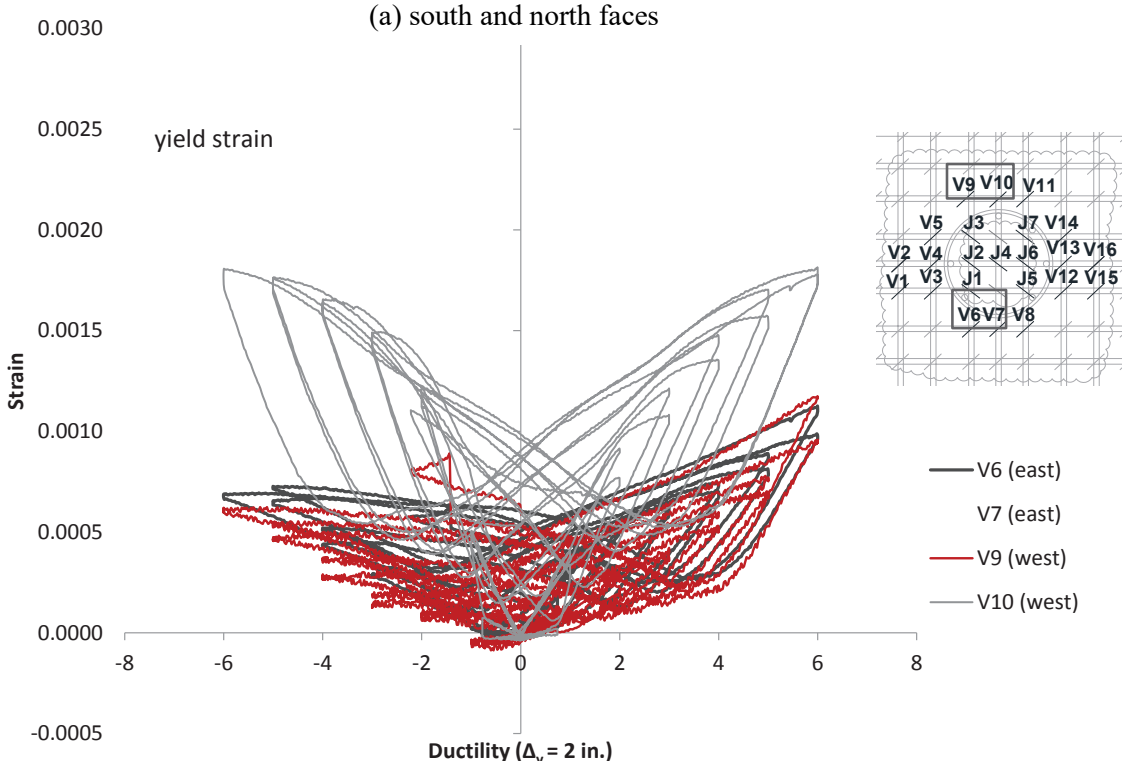

(b) east and west faces

Figure 4.44 – Strains in the 1st row of vertical stirrups of Specimen #2

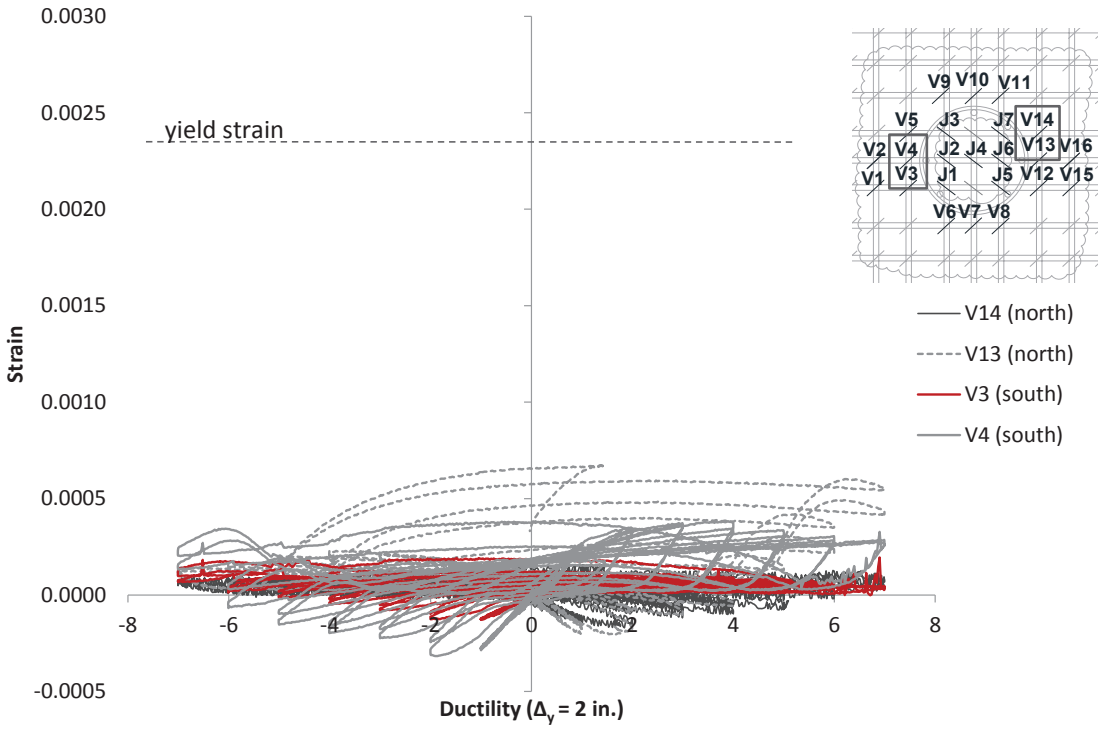

(a) south and north faces

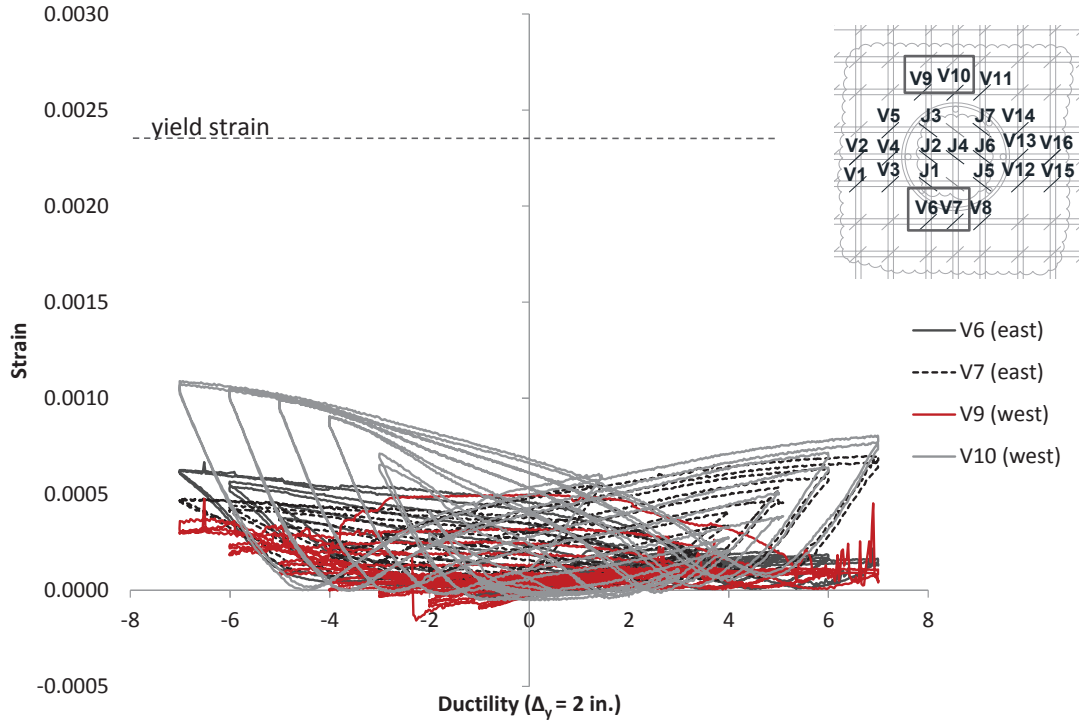

(b) east and west faces

Figure 4.45 – Strains in the 1st row of vertical stirrups of Specimen #3

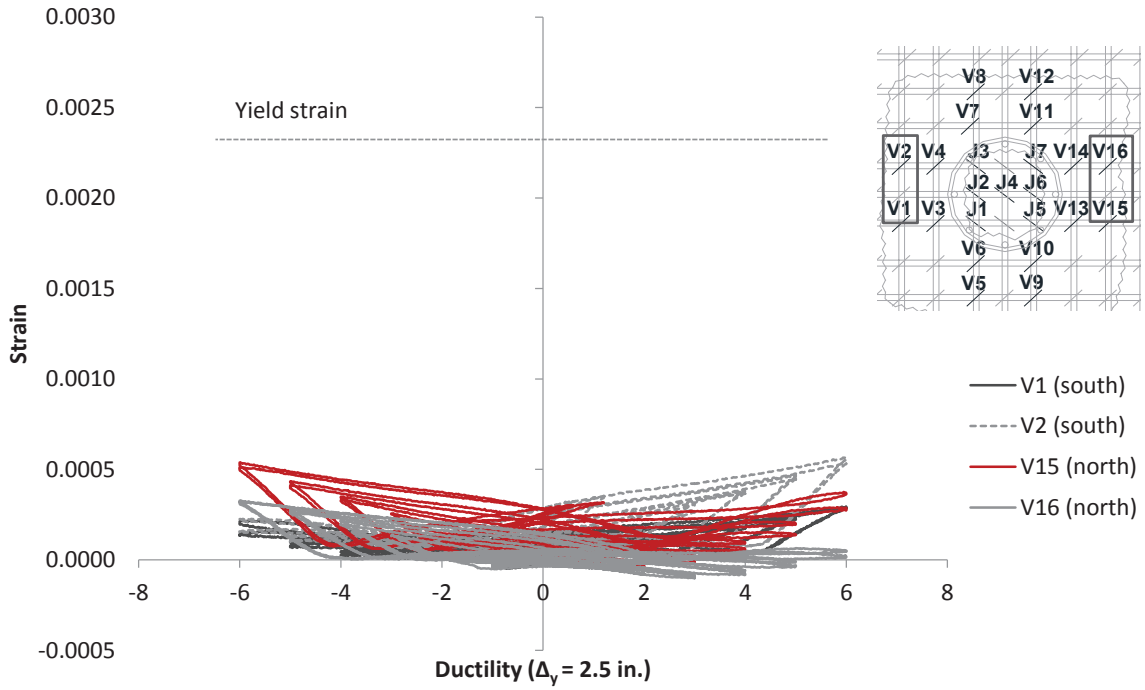

(a) south and north faces

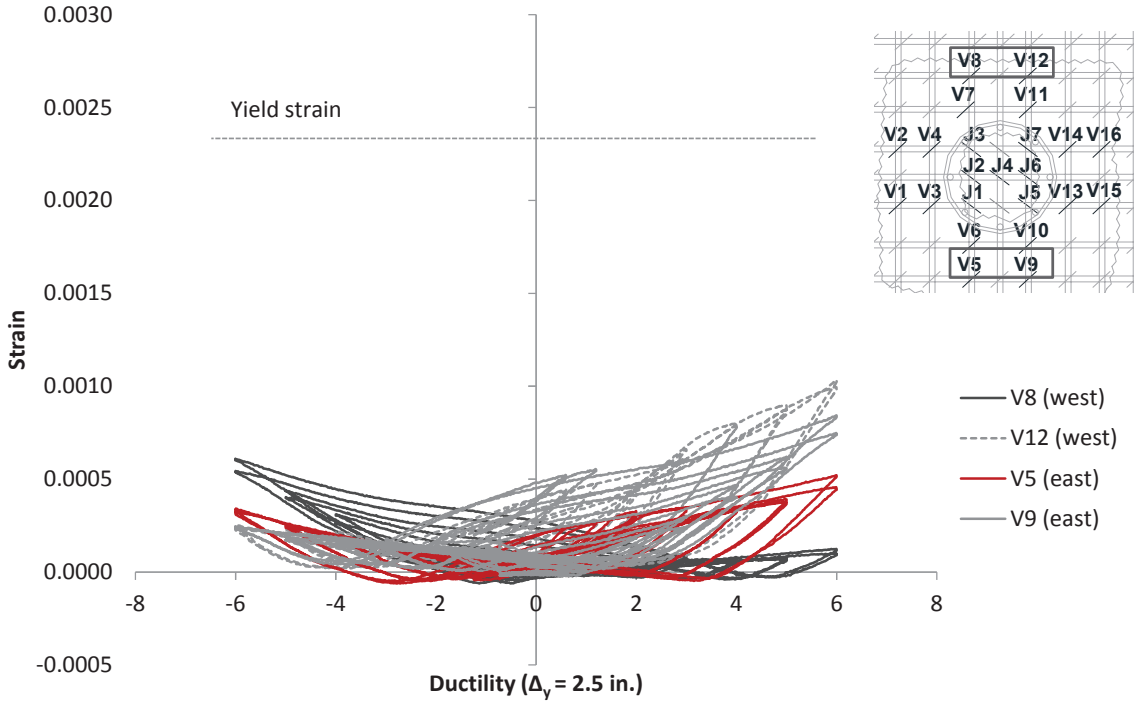

(b) east and west faces

Figure 4.46 – Strains in the 2nd row of vertical stirrups of Specimen #1

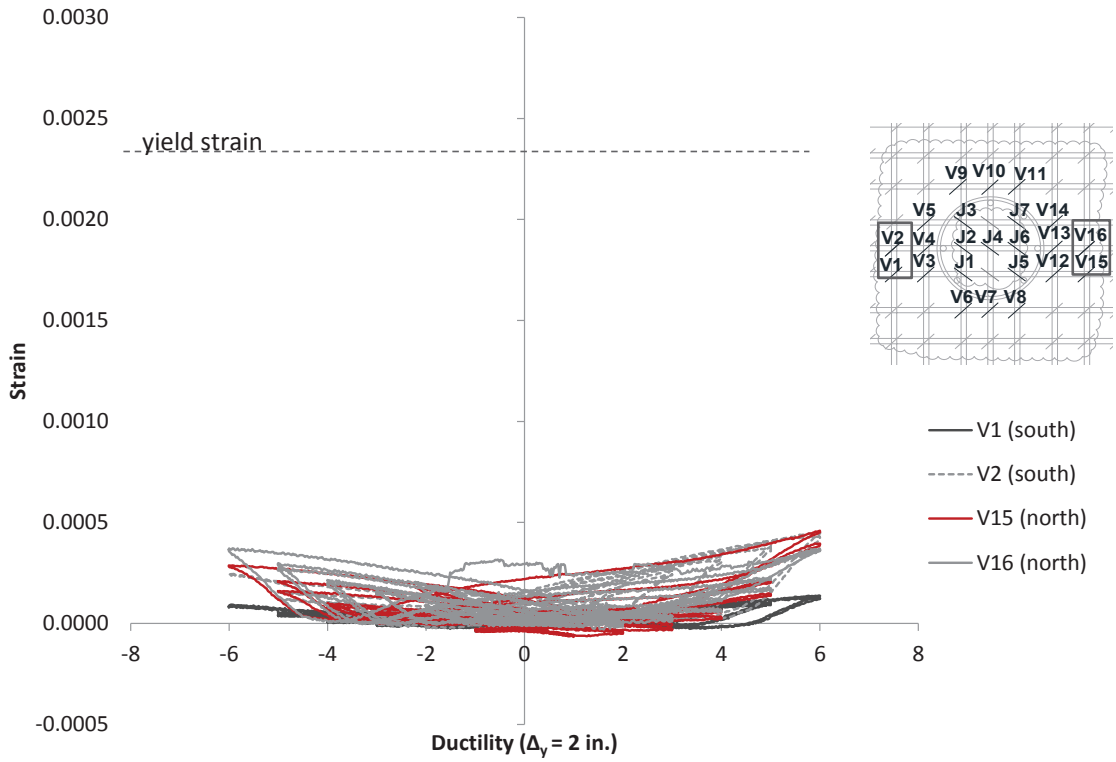

Figure 4.47 – Strains in the 2nd row of vertical stirrups of Specimen #2

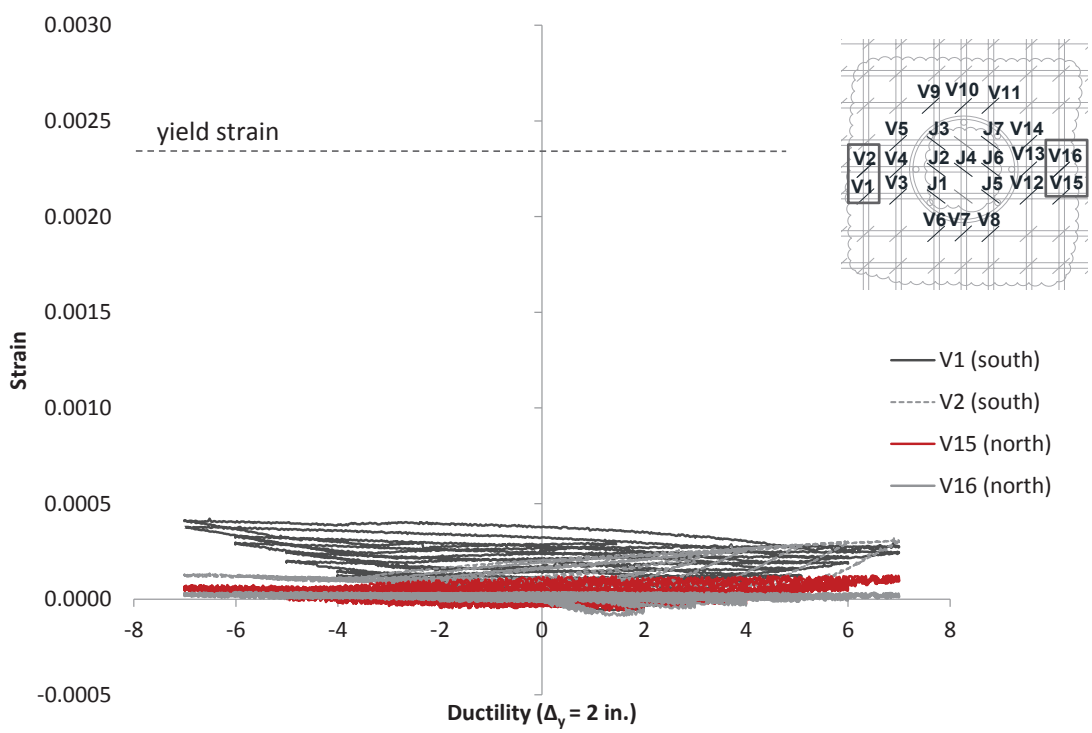

Figure 4.48 – Strains in the 2nd row of vertical stirrups of Specimen #3

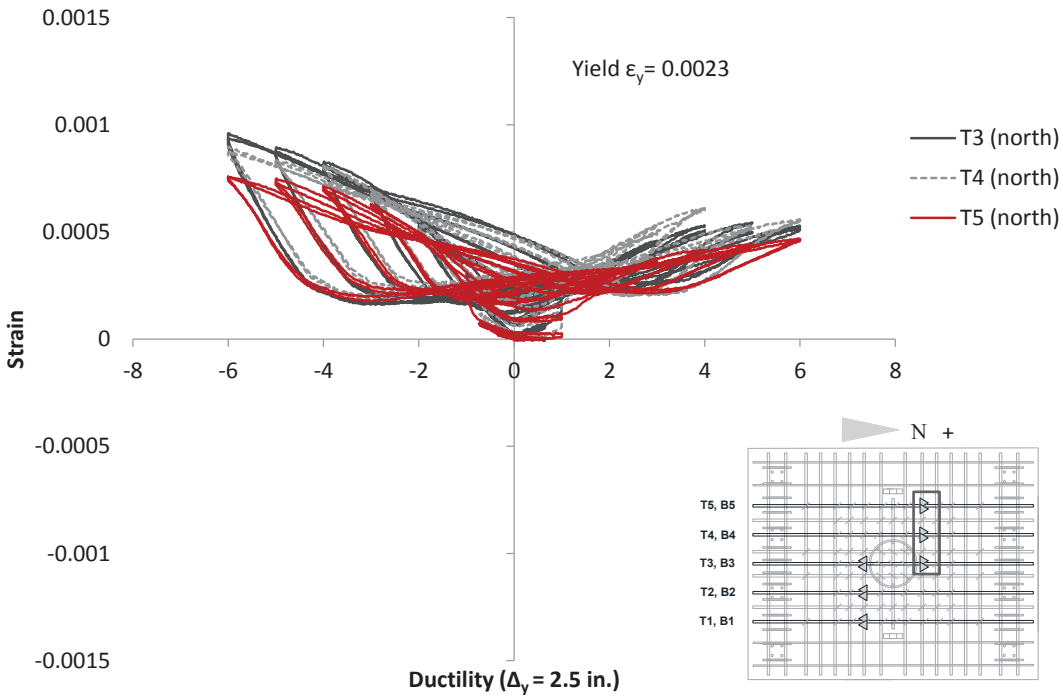

Figure 4.49 – Strains in longitudinal bars at the bottom face of the slab (top face in the specimen) of Specimen #1

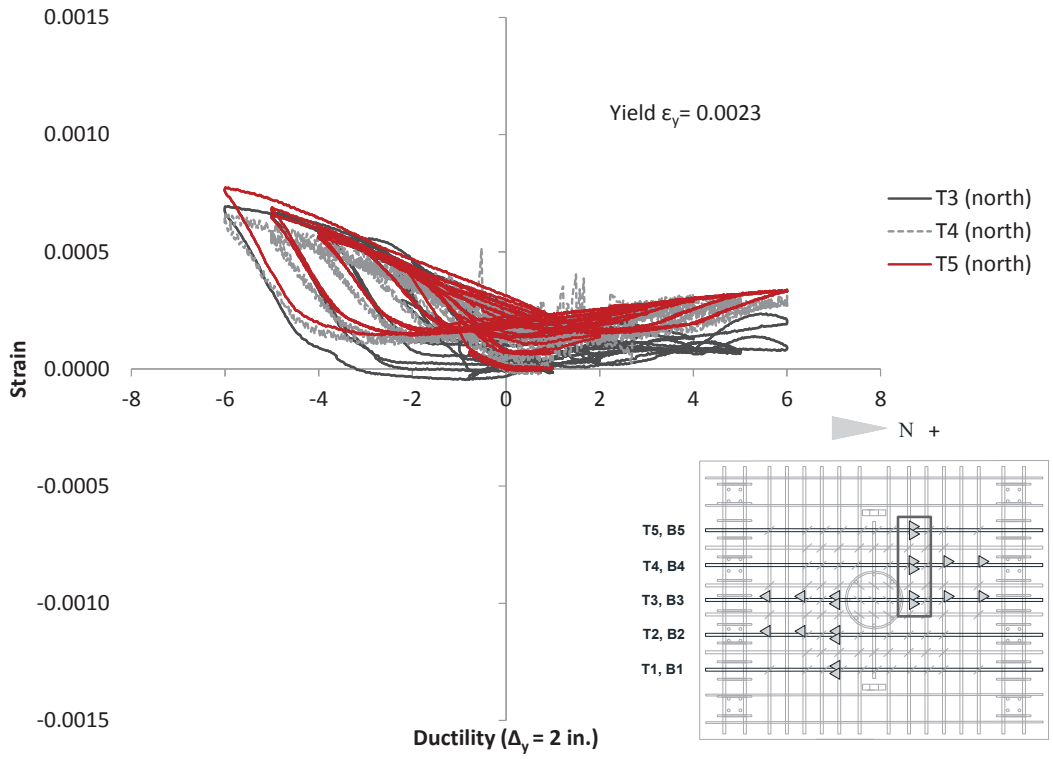

Figure 4.50 – Strains in longitudinal bars at the bottom face of the slab (top face in the specimen) of Specimen #2

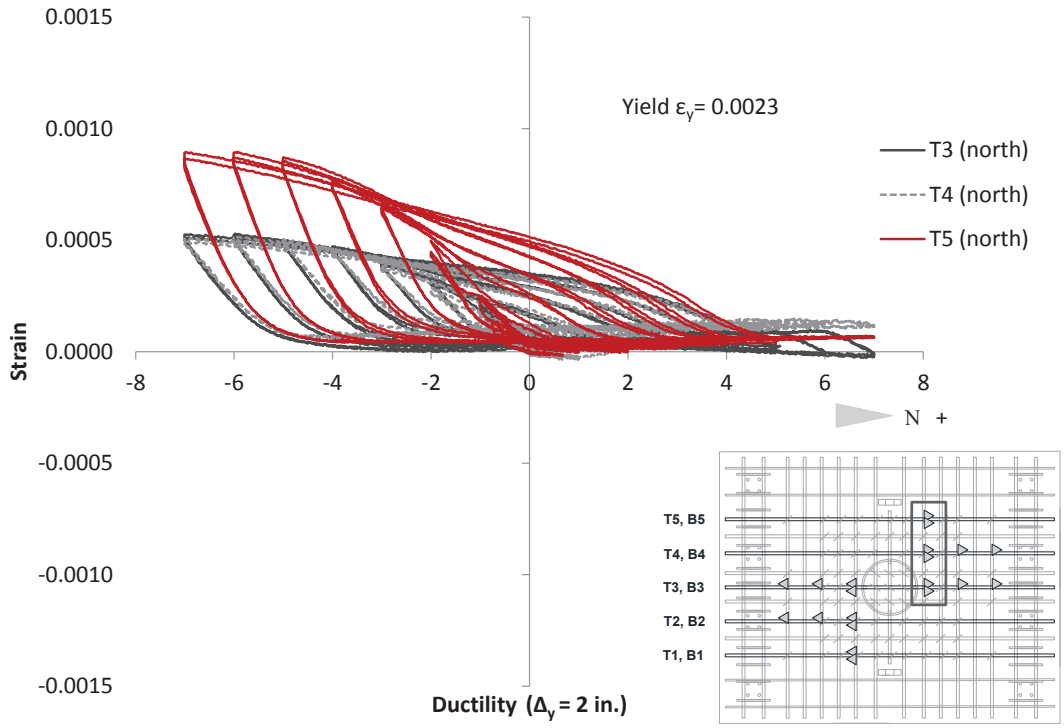

Figure 4.51 – Strains in longitudinal bars at the bottom face of the slab (top face in the specimen) of Specimen #3

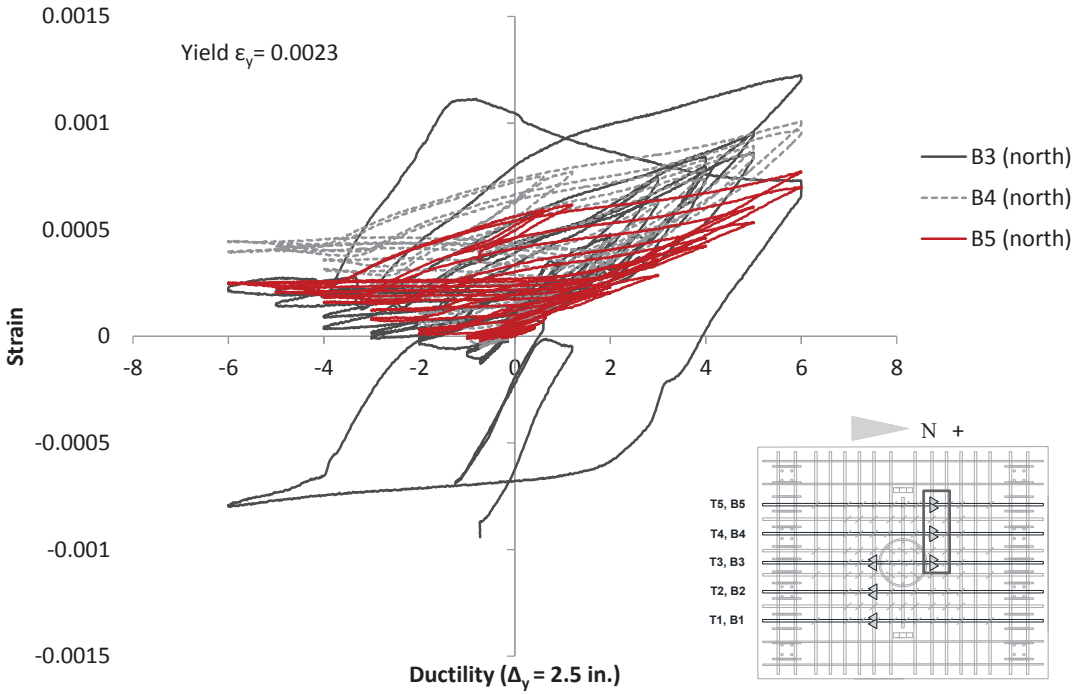

Figure 4.52 – Strains in longitudinal bars at the top face of the slab (bottom face in the specimen) of Specimen #1

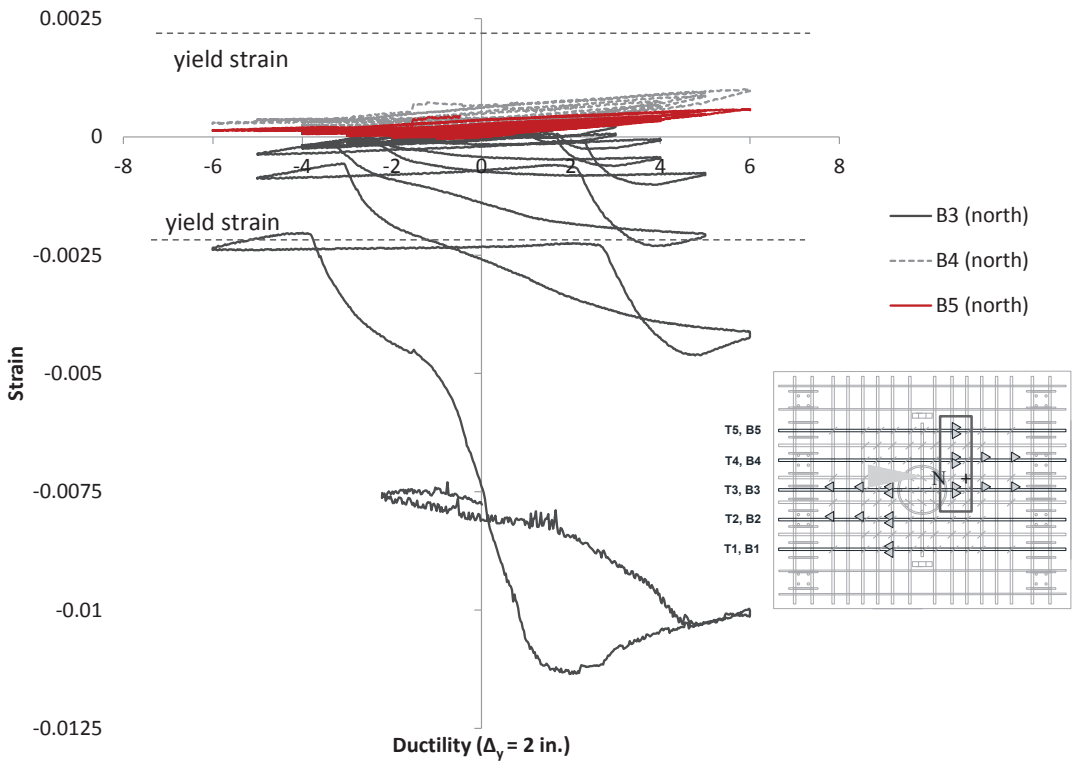

Figure 4.53 – Strains in longitudinal bars at the top face of the slab (bottom face in the specimen) of Specimen #2

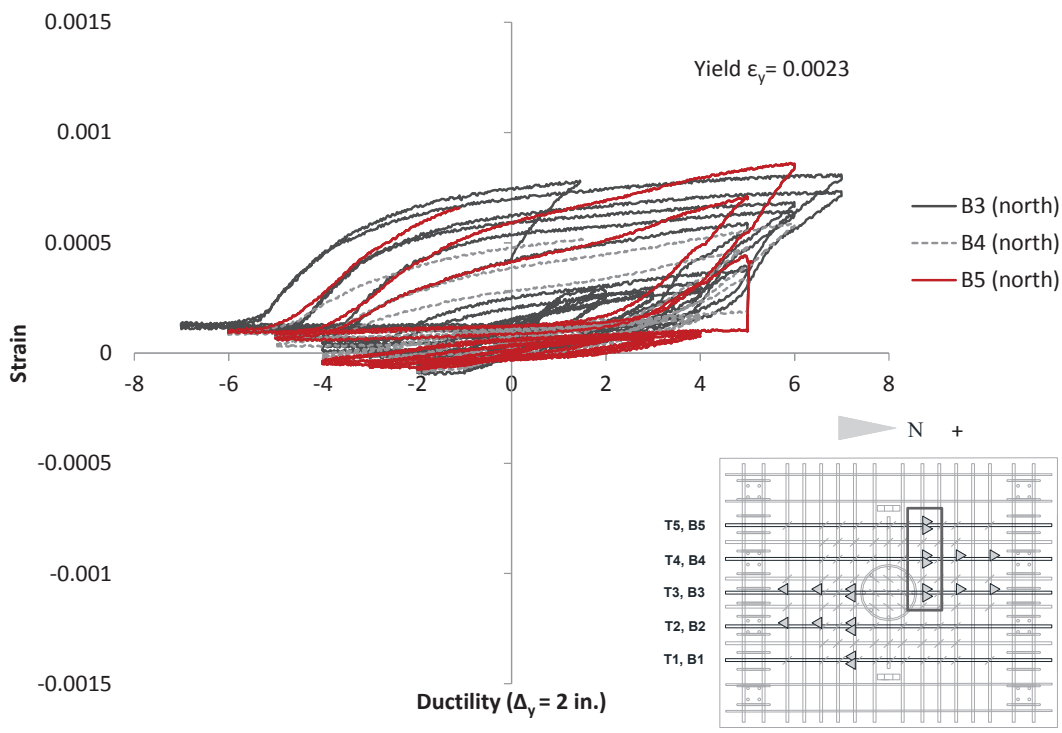

Figure 4.54 – Strains in longitudinal bars at the top face of the slab (bottom face in the specimen) of Specimen #3

CHAPTER 5

FINITE ELEMENT ANALYSIS OF SLAB-COLUMN ASSEMBLIES

Finite element (FE) models have been developed to study the anchorage of headed bars in concrete, and have been verified with experimental data from pullout tests. The column-slab assemblies that were tested in this study have been modeled with the FE method. In this chapter, the FE models are presented, and the numerical results are compared with experimental data.

5.1 Finite Element Analysis of Pullout Tests on Headed Bars

A three-dimensional FE model developed to evaluate the anchorage capacity of headed bars is presented in Figure 5.1. It is used to simulate the tests of De Vries et al. (1996) and Choi et al. (2002). The concrete blocks in the former tests were unreinforced, while those in the latter had horizontal and vertical bars as shown in Figure 5.1. The finite element analyses (FEA) are performed with the program Abaqus (Simulia 2012).

For the modeling of concrete, two different constitutive models have been employed. They are the damaged-plasticity (D-P) model, available in Abaqus, and the microplane model developed by Caner and Bazant (2013a). These two models have been described, calibrated, and validated with experimental data by Papadopoulos and Shing (2015). The microplane model can adequately simulate the opening and closing of cracks in concrete, while the D-P model cannot. The microplane model is also able to capture the influence of confinement on the post-peak behavior of concrete in a more accurate manner.

For model calibration, the compressive strength of concrete is obtained from material test data in the respective experimental studies. Table 5.1 shows the values selected for the key material parameters

in the D-P model for all the analyses presented in this chapter. For different levels of confinement, the D-P requires different uniaxial stress-strain relations as input, which is explained in Papadopoulos and Shing (2015). The key material parameters for the microplane model for the simulation of the pullout tests are shown in Table 5.2. The calibration of the microplane model is explained in more detail in Papadopoulos and Shing (2015). Both the D-P model and the microplane model are calibrated to have the same uniaxial compressive strength and tensile strength for the given test.

The headed bar is modeled with beam elements and an elasto-plastic law with linear kinematic hardening. The tri-linear stress-strain curve for the steel model with a yield stress of 80 ksi and an ultimate stress of 95 ksi is plotted in Figure 5.2. The yield strength and ultimate strength are based on the respective tensile test data. The bar head is modeled with solid elements and elastic steel properties. A contact condition is imposed between the head and the concrete. The interaction between the bar and the surrounding concrete is modeled with a bond-slip interface element, developed and implemented in Abaqus by Murcia-Delso and Shing (2015). This model accounts for bond deterioration caused by bar yielding in tension and by cyclic loading. The bond-slip model is calibrated based on the compressive strength of the concrete (f_c') and the diameter of the bars (d_b) as discussed in Murcia-Delso and Shing (2015).

The ability of the FE model to predict the anchorage capacity and failure mode for headed bars has been verified with bar pullout tests conducted by De Vries et al. (1996), and Choi et al. (2002). The main characteristics of the test specimens, and the results of the tests and the FEA, with the D-P model and the microplane model for concrete, are given in Table 5.3.

De Vries et al. (1996) conducted pullout tests of bars with shallow embedment lengths. The concrete is unreinforced. Three of their test specimens have been analyzed with a FE model. A picture of a specimen and the corresponding FE model are shown in Figure 5.3. Only one quarter of the specimen is modeled, given the double symmetry in the tests. Specimens T1B1 and T1B3 had an unbonded bar of diameter 0.79 in., embedded $1.8d_b$ and $5.7d_b$, respectively, in a concrete slab with a compressive strength

of 12,000 psi, while Specimen T1B7 had an unbonded bar of diameter 1.38 in., embedded $6d_b$ in a concrete slab of the same compressive strength. The FEA can satisfactorily differiantiate the anchorage load capacities for the different specimens tested by De Vries et al. (1996).

Choi et al. (2002) conducted pullout tests of bars embedded in concrete blocks with horizontal bars and vertical ties, which contributed to the increase of the anchorage load capacity. The test specimens modeled here had a No. 5 bar embedded in an RC beam with an 11.8 in. x 5.7 in. cross-section and No. 3 horizontal bars and vertical stirrups, which are modeled by truss elements, assigned an elasto-plastic material law with a yield stress of 61 ksi. The specimens had different spacings of the vertical stirrups. Only one quarter of the test specimen has been modeled, given the double symmetry of the tests. Figure 5.4 shows the maximum principal strains developed in the FE model of specimen C16-6DB-1A, which had vertical stirrups spaced at $3d_b$, while Figure 5.5 shows the maximum principal strains of specimen C16-6DB-1D, which had vertical stirrups spaced at $9d_b$. The FEA with the D-P model and the microplane model satisfactorily reproduce the breakout failure, with the development of splitting cracks and a cone-shaped failure surface, as shown in the figures. The anchorage load capacities from the FEA and the tests are summarized in Table 5.3.

5.2 Finite Element Analysis of Column-Slab Assemblies

The column-slab assemblies, tested in this study and presented in Chapter 4, have also been modeled with FE. Three-dimensional FE models were developed to simulate the structural behavior of the column-slab assemblies. Initially, the FE models were used for the pre-test assessment of the performance of the slab-column assemblies and to assist the development of the loading protocols for the tests presented in Chapter 3. Once the FE models were validated by the test results and were further refined, they were used to obtain detailed information, such as strains in the column and slab reinforcement, bond stresses between concrete and steel, and punching crack displacements at the top face of the slab (bottom face in the specimen).

5.2.1 Finite Element Model

Figure 5.6 shows the FE model of Specimen #1. Specimens #2 and #3 have been modeled in the same way. Geometric nonlinearity is considered in the FEA. Only half of the specimen is represented in the model by taking advantage of the symmetry of the specimen about the applied lateral load.

Figure 5.7 shows the FE model of the reinforcement cage of Specimen #1. The column longitudinal bars are modeled with beam elements and are assigned the stress-strain law developed by Papadopoulos and Shing (2015), which is based on the Menegotto-Pinto model and accounts for low-cycle fatigue (LCF) of reinforcing bars. The values of the material parameters for the longitudinal reinforcement are summarized in Table 5.4. Bond slip between the longitudinal bars and concrete is considered, using the bond-slip model of Murcia-Delso and Shing (2015). The heads of the bars are modeled with solid elements and elastic steel properties are assigned to them. They are connected to the bars.

The lateral reinforcement in the column is modeled with truss elements and is assigned an elasto-plastic constitutive law with linear kinematic hardening. The slab longitudinal bars are modeled with beam elements, while the vertical bars are modeled with truss elements. Both of them are assigned the elasto-plastic law for steel with linear kinematic hardening. A yield stress of 65 ksi and an ultimate stress of 95 ksi at strain 0.1 are assigned, based on average values of the material test data.. A perfect bond with concrete is considered for the slab reinforcement and the lateral reinforcement in the column.

Concrete is modeled with solid elements and both the damaged-plasticity (D-P) and microplane constitutive models have been employed to model the concrete in the column-slab assembly. With the D-P model, contact conditions are introduced to at the column-to-slab interface as well as between the bar heads and concrete to better simulate the opening and closing of cracks during cycling loading, as shown in Figure 5.8. The compressive strengths of concrete, as shown in Table 5.5, are based on the material test data. The other material parameters for the D-P model are the same as those summarized in Table 5.1. With the microplane model, there is no need to introduce contact conditions as it can accurately capture

the tensile unloading and reloading stiffness of cracked concrete. The microplane model has been calibrated to have the compressive strengths shown in Table 5.5. It also has the same tensile strengths as the D-P model. Table 5.6 presents the values of the model parameters that will result in the desired strengths.

Both models adequately simulate the behavior of the slab-column assemblies under lateral loading. However, the microplane model provides more accurate results than the D-P model. For this reason, this report presents detailed results for the microplane model only.

For Specimen #1, the steel straps, installed on the outer perimeter of the column to compensate for the lower-than-expected compressive strength of concrete, are also modeled, as shown in Figure 5.8. They are modeled with solid elements and are assigned the elasto-plastic steel law, with a yield stress of 55 ksi and an ultimate stress of 70 ksi at strain 0.1, based on material test data. Figure 5.9 shows the FE model of Specimen #3, whose slab geometry is slightly different from that of Specimens #1 and #2, with a 3-in. drop cap in the slab.

5.2.2 Lateral Load-vs.-Displacement Response

5.2.2.1 Specimen #1

Figure 5.10 shows the lateral load-vs.-drift ratio curves for Specimen #1 from the FEA with the D-P model and the microplane model, along with the experimental result. The numerical result with the D-P model matches the test result sufficiently well. The hysteresis curves from the FEA show a slightly higher strength and a better energy-dissipation capability than the test data. The relatively ductile behavior of Specimen #1, due to the confining steel straps placed at the bottom of the column, is well reproduced in the FEA.

The hysteresis curves obtained with the microplane model closely match the experimental result, in terms of the lateral load capacity, the strength degradation, and the pinching of the hysteresis loops.

The microplane model is able to better capture the pinching of the hysteresis loops as compared to the D-P model.

5.2.2.2 Specimen #2

Figure 5.11 shows the lateral load-vs.-drift ratio curves for Specimen #2 from the FEA with the D-P model and the microplane model, along with the experimental result. Both models are able to capture the experimental result well. The D-P model appears to over-estimate the strength but better capture the pinching phenomenon probably related to the deterioration of the anchorage of the headed bars.

5.2.2.3 Specimen #3

Figure 5.12 shows the lateral load-vs.-drift ratio curves for Specimen #3 from the FEA with the D-P model and the microplane model, along with the experimental result. Both models are able to capture the shape of the hysteresis curves well with the D-P again slightly over-estimates the strength.

5.2.3 Vertical Displacement underneath the Test Slabs

5.2.3.1 Specimen #1

During the test of Specimen #1 $\left(l_e = 9.8d_b\right)$, the vertical displacement at the bottom face of the slab was not monitored by displacement transducers. However, it was clearly observed that it experienced some damage caused by the punching of the headed bars, as discussed in Chapter 4. At the end of the test, the vertical displacement of the top face of the slab (bottom face of the specimen), at the position of the headed bar placed at the extreme south side was measured to be between 0.3 and 0.4 in. Figure 5.13 shows the vertical displacement of the top face of the slab (bottom face in the specimen) at the same position, as obtained from the FEA with the microplane model.. The analysis predicts a maximum vertical displacement of 0.3 in.

The deformed shapes of the FE models with the D-P model and the microplane model, at the 2nd cycle of ductility 6, are shown in Figure 5.14. The vertical deformation of the slab surface due to the

punching of the headed longitudinal bars is not too noticeable, which is consistent with the experimental observations.

5.2.3.2 Specimen #2

During the test of Specimen #2 $\left(l_e = 8.7d_b\right)$, the damage at the top face of the slab (bottom face in the specimen) due to the pinching of the headed bars was significant, resulting in the severe spalling of the concrete during the second cycle of ductility 6. Figure 5.15 plots the vertical displacement of the top face of the slab (the bottom face of the specimen), at the position of the headed bar placed at the extreme south side, against the column displacement (in terms of the ductility level) for the test and the analysis with the microplane model. The numerical result matches the test well. Figure 5.16 shows the deformed shapes of the FE models of Specimen #2. The punching deformations are well captured by the FE models.

5.2.3.3 Specimen #3

Figure 5.17 shows the vertical displacement of the top face of the slab for Specimen #3 $\left(l_e = 11d_b\right)$. The numerical result matches the experimental result well. The vertical displacement due to the punching of the headed bars is extremely limited, indicating the benefit of the increased embedment length for the headed bars. The deformed shapes of the FE models for Specimen #3, at ductility 7, are presented in Figure 5.18. The numerical result is consistent with the very limited damage at the top face of the slab (bottom face in the specimen) observed in the test.

5.2.4 Strains in Column Longitudinal Bars

Figure 5.19 shows the strain variations along the headed bar on the extreme north side of the column of Specimen #1. The numerical results (with the microplane model) are compared to those measured in the test. Some of the strain gages were damaged as the ductility demand on the column increases, resulting in missing strain data in the plots. Near the slab-column interface, the analysis

overestimates the strains in the bar. Away from there, the analysis results satisfactorily match the strains measured in the test.

The strains along the embedment length of the headed bar inside the slab are predicted by the FEA sufficiently well up to a ductility demand of 1. As the ductility demand increases, the strains are overestimated in the FEA. The yield strain penetrated all the way to the head of the bar in the test of Specimen #1, which has also been captured in the analysis.

Figure 5.20 and Figure 5.21 plot the strains in the headed bar on the extreme north side obtained from the analysis and the test of Specimens #2 and #3. Due to the damage of the strain gages in later cycles, no experimental readings were available. The numerical results match the test results sufficiently well with similar observations as those for Specimen #1.

The analyses show that the strain developed close to the head of the bar in Specimen #3 at high ductility demands of 3, 5, and 6 is much smaller than that in Specimen #2, as shown in Figure 5.20 and Figure 5.21 . This indicates that the headed bars in Specimen #3 are better developed than those in Specimen #2.

The better development of the headed bars and the less severe anchorage deterioration in Specimen #3, as compared to Specimen #2, can also be seen in Figure 5.22 and Figure 5.23. Each figure presents the axial forces in the longitudinal bar at the elevation of the slab-column interface and at its head, as well as the total bond force along the embedment length, obtained in the analyses of Specimens #2 and #3. The total bond force is calculated as the difference in the bar forces at the aforementioned locations. When the headed bar is in tension, the bond force is maintained in Specimen #3 $\left(l_e = 11 d_b\right)$ as the ductility demand increases, while it drops significantly in Specimen #2 $\left(l_e = 8.7 d_b\right)$. Moreover, at higher ductility demand levels (4, 5, and 6), when the bar in Specimen #2 is reloaded in tension, the force-displacement curves show some pinching and then a sudden increase in resistance, as shown in Figure 5.22, which can be attributed to the punching failure of the concrete next to the bar head causing the

disengagement and reengagement of bearing action of the bar head as the bar slips back and forth. This is not observed for Specimen #3.

When the bar is in compression, the bond force in Specimen #3 is maintained up to ductility 5, while it drops significantly in Specimen #2. For both specimens, a maximum compressive force of about 82 kips is developed at the head of the bar. This indicates that 82 kips is the borderline punching force that can induce the punching failure of the concrete layer below the bar head in the specimen. The ability of Specimen #3 to maintain the bond force up to a large ductility demand, due to the larger bar embedment length, can avert the punching failure.

For Specimen #3, bar elements, presenting the headed bars in the column above the slab-column interface, experience significant bending deformations due to buckling when the ductility demand exceeds 5. Due to this, the forces in the headed bars embedded in the slab drop; so is the bond force. However, during the test of Specimen #3, no evidence of bar buckling was observed, even though the concrete spalling at the base of the column was more severe in Specimen #3 than that in Specimen #2.

5.2.5 Strains in J-Bars

Figure 5.24 shows the strains in J-bars, J5 and J7, placed in the core region of the slab-column joint in Specimen #1 $\left(l_e = 9.8d_b\right)$. The strains from the analysis (with the microplane model) and the test are plotted together. Since only half of the slab-column assembly is modeled assuming a perfect symmetry, J7 and J5 should have the same behavior. The J-bars are modeled with truss elements and are embedded in concrete with perfect bond (i.e., without bond-slip elements). The end nodes of the J bars and vertical stirrups are connected to the nodes of the top and bottom longitudinal bars in the slab, assuming that the hooks provided perfect anchorage. Considering the modeling assumptions and the uncertainty in the locations of cracks in the slab, the numerical data match the experimental findings reasonably well. The strains developed in the J-bars reach values close to the yield strain.

It should be mentioned that the test data were obtained from strain gages attached at the middle height of the J-bars. The strains from the FEA, as shown in Figure 5.24, are obtained from the middle truss element (out of three) representing the modeled J-bar. The element near the top face of the slab (bottom face in the specimen) develops a maximum tensile strain of 0.008, exceeding the yield strain (which is 0.0023).

For Specimen #2 $\left(l_e = 8.7d_b\right)$, the strains in the same J-bars are shown in Figure 5.25. The numerical data are in accordance with the test measurements. The strains developed in Specimen #2 $\left(l_e = 8.7d_b\right)$ slightly exceed the yield strain, larger than those in Specimen #1. This more significant engagement of the J-bars is attributed to the more severe anchorage deterioration of the headed bars in Specimen #2, as compared to Specimen #1.

The strains in the J-bars of Specimen #3 $\left(l_e = 11d_b\right)$, which had the largest embedment length for the headed bars and experienced the least severe anchorage deterioration among the three specimens, are shown in Figure 5.26. The analysis matches the test well. The strains in Specimen #3 $\left(l_e = 11d_b\right)$ are quite smaller than those in Specimen #2.

5.2.6 Strains in Vertical Stirrups

The analyses capture the variation of the stirrup strain with the stirrup location in a specimen as well as the variation of the maximum strain in a stirrup from one specimen to the other. Figure 5.27 shows the strains in V13, a vertical stirrup in the 1st row next to the column cage, obtained from the FEA (microplane) and the test of Specimen #1. The vertical stirrups are modeled in the same way as the J-bars. Considering uncertainties in concrete cracking and the bond-slip behavior of reinforcing bars, the numerical results match the experimental measurements reasonably well. Similar to the test results, the analyses show that the vertical stirrups in the 1st row adjacent to the column develop more significant tensile strains than the other stirrups, because the former are more engaged in resisting the punching and

bearing actions of the headed bars. Figure 5.28 shows the strains in vertical stirrup V13, obtained from the FEA and the test of Specimen #2. The numerical results match the test sufficiently well, with the maximum strain slightly exceeding 0.0015. Figure 5.29 shows the strains in V13 from the FEA and the test of Specimen #3. The maximum strain developed in V13 in Specimen #3 is 0.0006, significantly smaller than that in Specimen #2 (Figure 5.28). This indicates that the 1st row of vertical stirrups in Specimen #3 is not engaged as much as that in Specimen #2, consistent with the better anchorage and less slip of the headed bars in Specimen #3.

Figure 5.30 through Figure 5.32 show the strains developed in the stirrups in the 2nd row away from the column cage for Specimens #1, #2, and #3, obtained from the FEA and the tests. For all three specimens, the strains developed are significantly smaller than the yield strain. The numerical results match the measurements in the tests reasonably well.

5.2.7 Strains in Longitudinal Bars in Slabs

Figure 5.33 through Figure 5.35 show the strains (average strain over the section of the beam element) in the longitudinal bar, T3, at the top face of the slab of Specimens #1, #2 and #3 (bottom face in a real bridge), obtained from the FEA and the tests. The numerical results (with microplane model) match the tests reasonably well, with strains way below the yield level. In the negative displacement direction, the numerical results adequately match the experimental measurements, reaching a maximum strain of about 0.001. For the positive direction, the FEA results show a more linear behavior of the bar. However, both the test and the numerical results show that the bar tends to be in tension most of the time when the column was displaced towards the positive direction. This contradicts the direction of the bending moment induced on the slab, and can be attributed to the strut action developed in the short-span slab.

Figure 5.36 shows the strains developed in the longitudinal bar, B3, placed at the bottom face of the slab of Specimen #2, from the test and the FEA. Only the reading from one of the two gages is plotted, because the other gage was damaged. For the numerical result, the strain is taken at a point that

can be subjected to the most severe compression in the cross-section of the beam element due to bending. The comparison shows that the longitudinal bar was subjected to significant bending caused by the punching of the headed bars in the test.

Figure 5.37 shows the strain (averaged strain from two gages) developed in longitudinal bar B3 near the column cage obtained in the test of Specimen #3, and the average strain obtained from the FEA at a similar location. The longitudinal bar develops only elastic strains, since no significant punching force from the headed bars was observed. Figure 5.38 shows how the longitudinal bars at the bottom face of the specimen are deformed in the FEA of Specimens #2 and #3. It can be seen that the mat of longitudinal and transverse bars in the slab, the J-bars, and the vertical stirrups are engaged to resist the punching action of the headed bars. This is much more significant in Specimen #2 than in Specimen #3.

5.2.8 Effectiveness of Slab Vertical Reinforcement to the Development of Headed Bars

Two additional FEA of Specimen #3 have been conducted with variations in the amount of the vertical stirrups and J-bars in the slab. In one case, identified as Specimen #3B, all the J-bars and vertical stirrups have been removed, and in the second, identified as Specimen #3C, only the J-bars and the 1st row of vertical stirrups closest to the column cage have been retained, while all the other vertical stirrups have been removed.

Figure 5.39 compares the lateral load-vs.-top drift curves for Specimens #3 and #3B. It can be seen that while the lateral load capacity of the column can be developed in Specimen #3B, the hysteresis loops are more pinched, indicating some significant deterioration of the anchorage capacity of the headed bars. Furthermore, the drop of the lateral load resistance with increasing drift amplitude is slightly larger in Specimen #3B than in Specimen #3. Figure 5.40 shows the deformed meshes for Specimens #3 and #3B. The damage at the bottom face of the slab in Specimen #3B is obvious while Specimen #3 does not show noticeable damage.

Figure 5.41 compares the lateral load-vs.-top drift curves for Specimens #3 and #3C. It can be seen that the two specimens have almost the same behavior. Figure 5.42 shows the deformed meshes of Specimens #3 and #3C. Again, the difference between the two cases is not noticeable. This comparison shows that the vertical stirrups in the 2nd row and farther away the column cage have little influence on the behavior of a slab-column joint provided the headed bars are adequately developed with a minimum development length of $11d_b$.

5.2.9 Influence of Concrete Cover Thickness

An additional FEA of Specimen #2 has been conducted by changing the embedment length of the headed bars. Specimen #2, which had $8.7d_b$ embedment length, experienced severe punching damage at the top face of the slab (bottom face in the specimen). To investigate the influence of the concrete cover above the bar head, the headed bars in Specimen #2 are moved away from the bottom face of the specimen (top face in the bridge slab) by $2d_b$ reducing the embedment length to $6.7d_b$, while increasing the distance of the bar heads from the nearest slab surface by $2d_b$. This is referred to as Specimen #2B.

Figure 5.43 compares the lateral load-vs.-top drift curve for Specimens #2B with that for Specimen #2. The two specimens exhibit a very similar behavior. Even with a development length of $6.7d_b$, the lateral load capacity of the column is developed. The hysteresis curves for Specimen #2B are less pinched than those for Specimen #2. This can be attributed to the increased concrete cover, which provides more resistance to the punching forces of the bars and thereby reduces the punching damage. Figure 5.44 shows the deformed meshes for Specimens #2 and #2B. It is clearly observed that the punching damage at the bottom of the slab is much less severe in Specimen #2B.

Figure 5.45 plots the strains developed in vertical stirrup V13, placed in the 1st row next to the column cage, for Specimens #2 and #2B. By reducing the embedment length for the headed bars, V13 develops larger strains when the adjacent headed bar is in tension (in the negative displacement direction), indicating its more active engagement to resist the tension in the bar. When the adjacent bar is loaded in

compression (in the positive displacement direction), V13 develops smaller strains. This can be attributed to the additional concrete cover, which helps to resist punching forces. However, further experimental investigation is required to verify the numerical findings.

5.3 Conclusions

The FE models produce results consistent with the experimental data and observations. For the slab reinforcing details and thickness considered in this study, the FEA have shown that the slab can sustain a punching force of 82 kips from a bar head without punching failure. Furthermore, the analyses have confirmed the experimental observation that the vertical stirrups in the slab farther away from the first row next to the column cage have little contribution to the resistance of the punching and bearing forces of the headed bars. Finally, the analyses have indicated that if there is not enough room to provide an adequate embedment length of $11d_b$, it may be advantageous to reduce the embedment length and increase the distance of the bar head from the slab surface to reduce or avoid punching damage.

Table 5.1 – Key parameters of the D-P model for concrete

Parameter	Description	
f_c' (ksi)	Compressive strength	From material test data
f_t' (ksi)	Tensile strength	$f_t' = 8\sqrt{f_c'}$
G_f^I (lb/in)	Fracture energy	2.9
ζ_{b0}/ζ_{c0}	Controls biaxial compressive strength	0.12
ψ	Dilation angle	20°
ε	Eccentricity	0
K_c	Controls shape of yield surface	1
w_c	Compression recovery factor	0
w_t	Tension recovery factor	1

Table 5.2 – Key parameters of the microplane model for pullout tests

Test	k_2, k_3	E (ksi)	k_1 (x10^{-4})	f_c' (ksi), ε_p
De Vries et al.	1, 1	15,700	1.65	12, 0.0015
Choi et al.	1, 1	7,380	1.65	5.7, 0.0015

Table 5.3 – Numerical results for pullout tests

Test	Specimen	d_b (in.)	f_y (ksi)	f_u [1] (ksi)	l_e (d_b)	Vertical ties	f_c' (ksi)	P_{test} (kips) & failure mode	P_{FEA} D-P (kips)	P_{FEA} microplane (kips)
De Vries et al.	T1B1	0.79	80	95	1.8	-	12.0	17.0 Concrete breakout	10.0	18.5
	T1B3	0.79	80	95	5.7	-	12.0	46.0 Bar fracture	43.0[2]	46.0
	T1B7	1.38	78	95	6.0	-	12.0	110.0 Concrete breakout	108.0	140.0[3]
Choi et al.	C16-6DB-1A	0.63	61	85[4]	6.0	No. 3 stirrups, $s_{tr} = 3d_b$	5.7	18.9 Concrete breakout	14.7	18.9
	C16-6DB-1C	0.63	61	85[4]	6.0	No. 3 stirrups, $s_{tr} = 6d_b$	5.7	18.0 Concrete breakout	13.3	18.4
	C16-6DB-1D	0.63	61	85[4]	6.0	No. 3 stirrups, $s_{tr} = 9d_b$	5.7	17.5 Concrete breakout	13.0	18.0
	Specimen without ties	0.63	61	61[3]	6.0	-	5.7	-	8.3	9.4

[1]The strain at ultimate stress of steel was assumed as $\varepsilon_u = 0.12$
[2]FEA with D-P failed by concrete breakout
[3]FEA with microplane model failed by bar fracture
[4]The ultimate stress of rebars is not documented in the study of Choi et al.

Table 5.4 – Steel material parameters for column longitudinal reinforcement

Parameter	Description	Specimen #1	Specimen #2	Specimen #3
f_y' (ksi)	Yield stress	69	65	65
E (ksi)	Elastic Stiffness		29000	
ε_f'	LCF coefficient	0.0645	0.0656	0.0656
c	LCF coefficient	0.2534	0.2518	0.2518

Table 5.5 – Compressive strengths of concrete (in ksi) for slab-column specimens

	Specimen #1	Specimen #2	Specimen #3
Slab	5.0	4.9	4.5
Column	3.2	4.8	5.0

Table 5.6 – Calibration of the microplane model for the slab-column assemblies

Specimen		Concrete	k_2, k_3	E (MPa)	k_1 (x10^{-4})	f_c' (ksi), ε_p
#1	Slab	Confined	Default	40,620	0.5	5.0, 0.0015
		Unconfined	1, 1	44,800	1.65	5.0, 0.0015
	Column	Confined	Default	26,000	0.5	3.2, 0.0015
		Unconfined	1, 1	28,670	1.65	3.2, 0.0015
#2	Slab	Confined	Default	39,810	0.5	4.9, 0.0015
		Unconfined	1,1	43,910	1.65	4.9, 0.0015
	Column	Confined	Default	39,900	0.5	4.8, 0.0015
		Unconfined	1, 1	43,010	1.65	4.8, 0.0015
#3	Slab	Confined	Default	36,560	0.5	4.5, 0.0015
		Unconfined	1, 1	40,320	1.65	4.5, 0.0015
	Column	Confined	Default	40,625	0.5	5.0, 0.0015
		Unconfined	1, 1	44,800	1.65	5.0, 0.0015

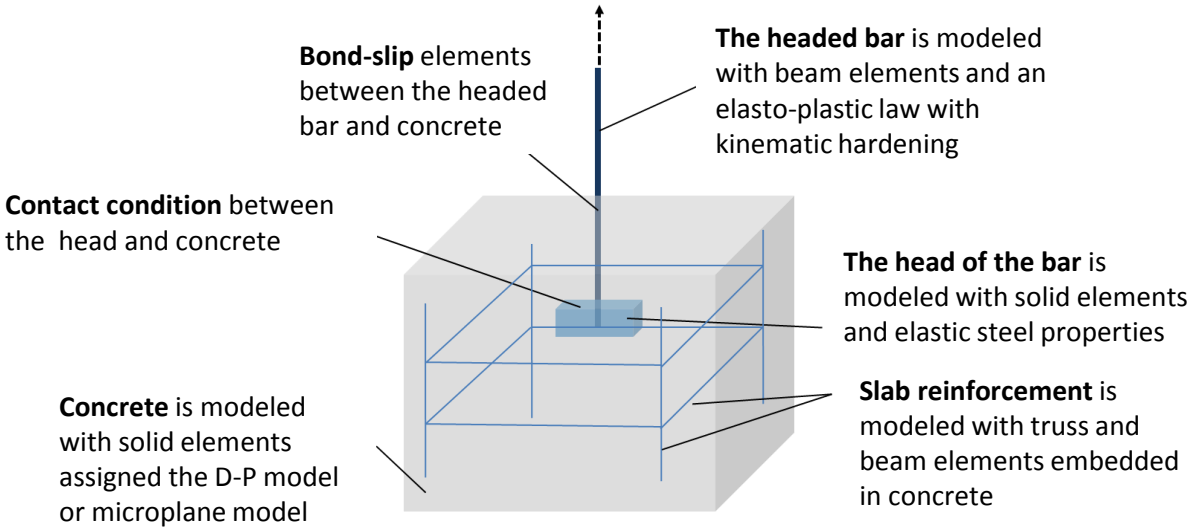

Figure 5.1 – FE model for pullout tests

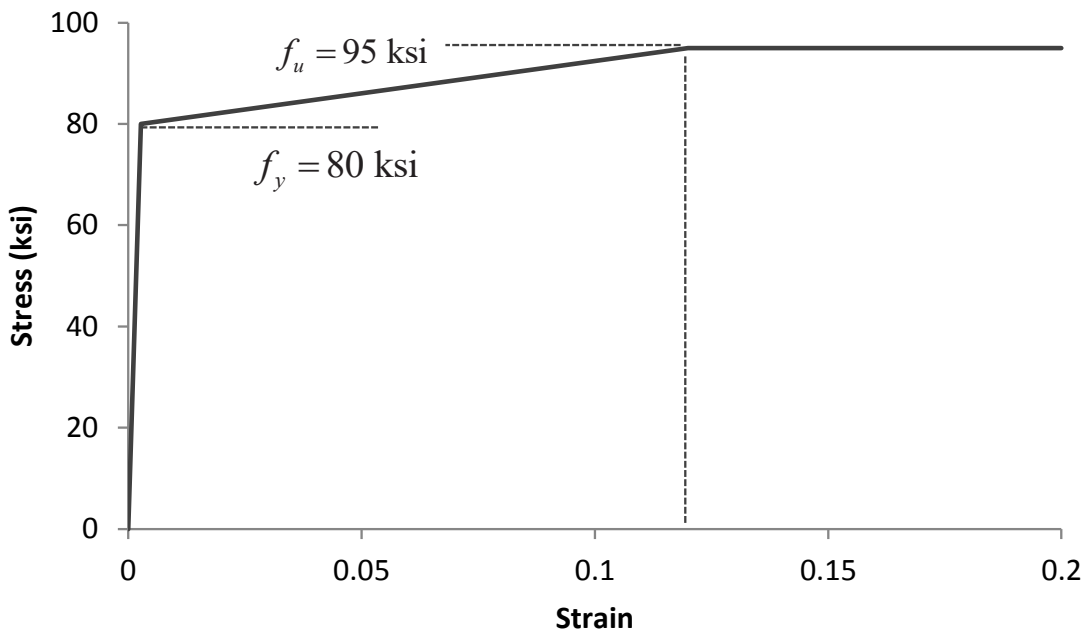

Figure 5.2 – Stress-strain curve for steel model

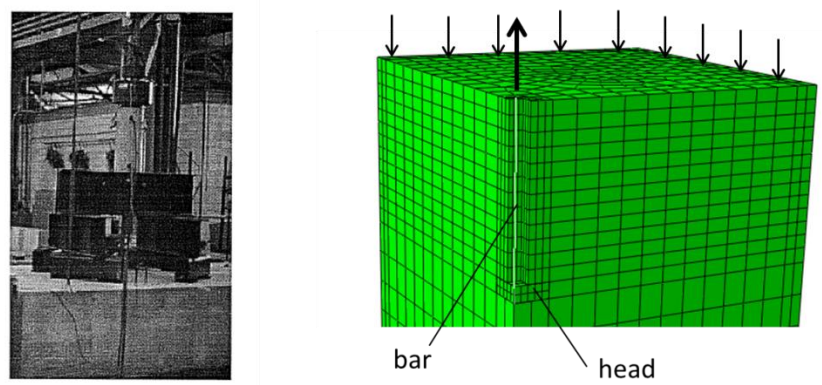

(a) Test specimen and setup (b) FE model of ¼ of a test specimen

Figure 5.3 – Tests by De Vries et al. (1996)

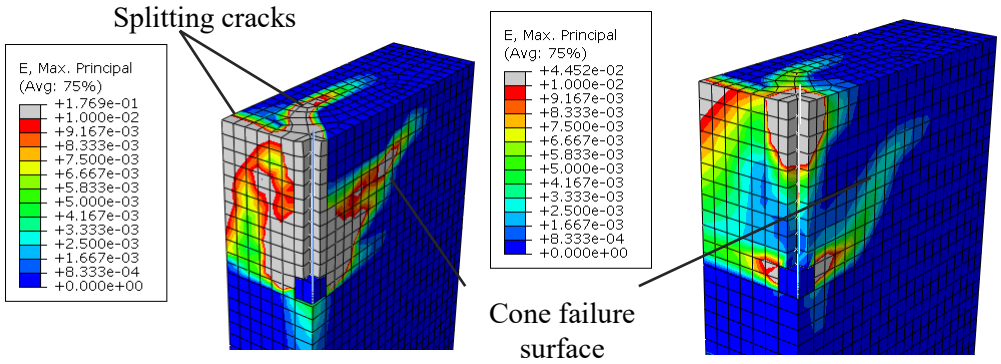

(a) D-P model (b) Microplane model

Figure 5.4 – Maximum principal strains in FE model of Specimen C16-6DB-1A by Choi et al. (2002)

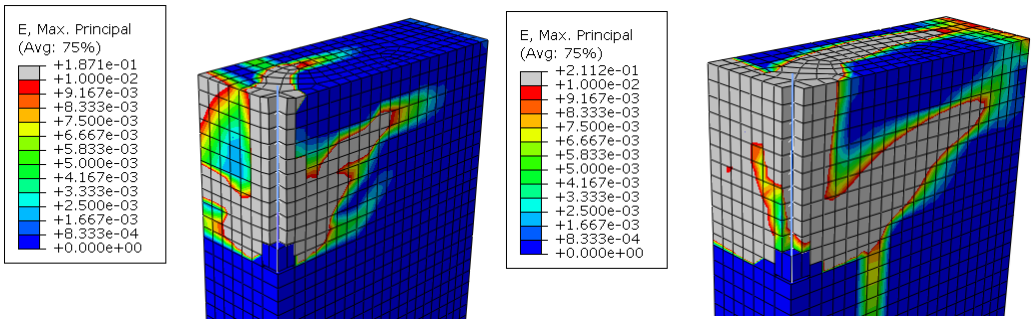

(a) D-P model (b) Microplane model

Figure 5.5 – Maximum principal strains in FE model of Specimen C16-6DB-1D by Choi et al. (2002)

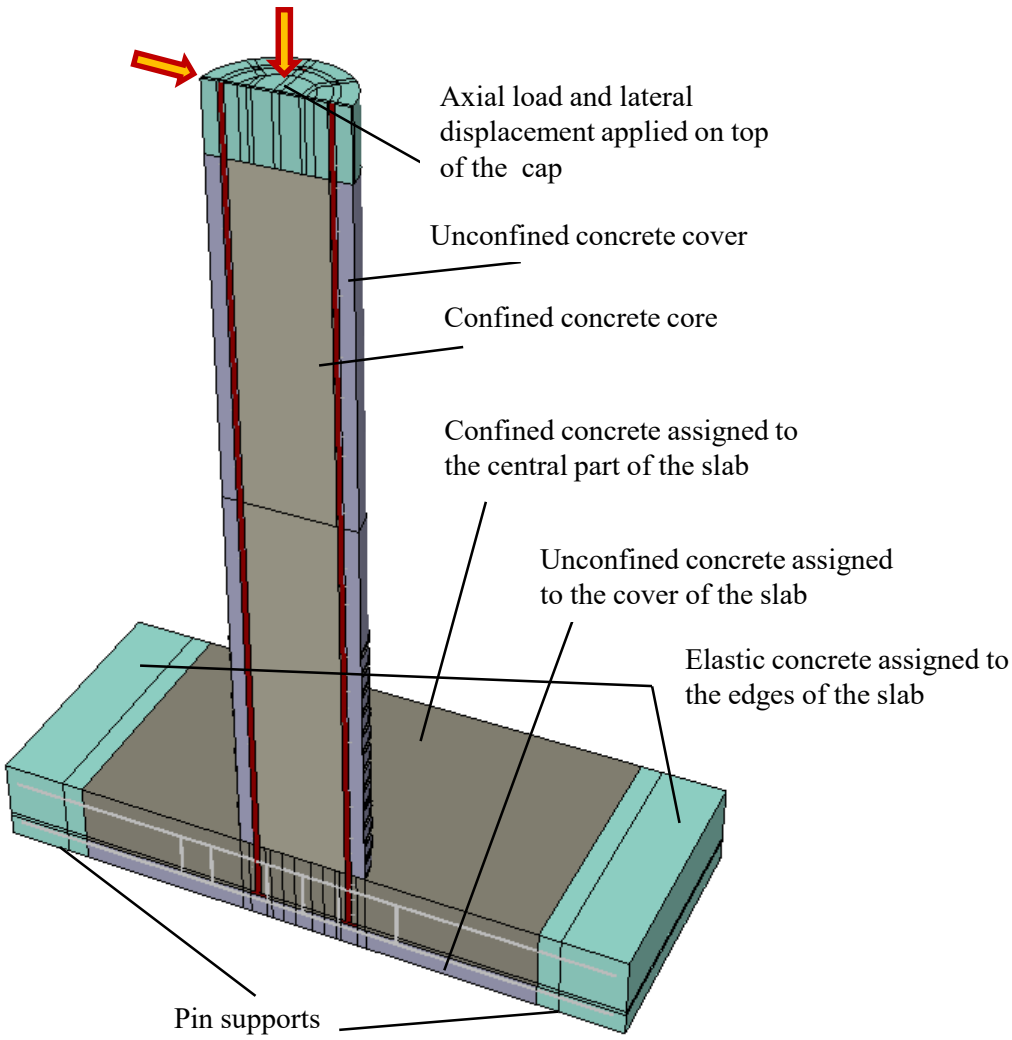

Figure 5.6 – FE model of slab-column Specimen #1

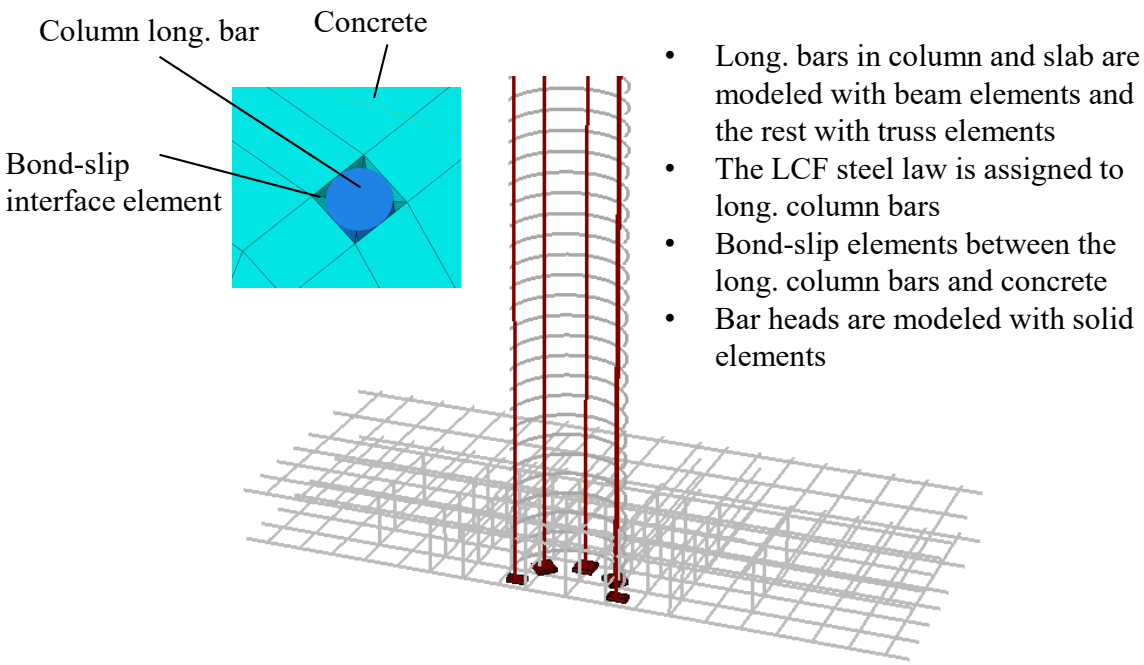

Figure 5.7 – FE assembly for reinforcement cage of Specimen #1

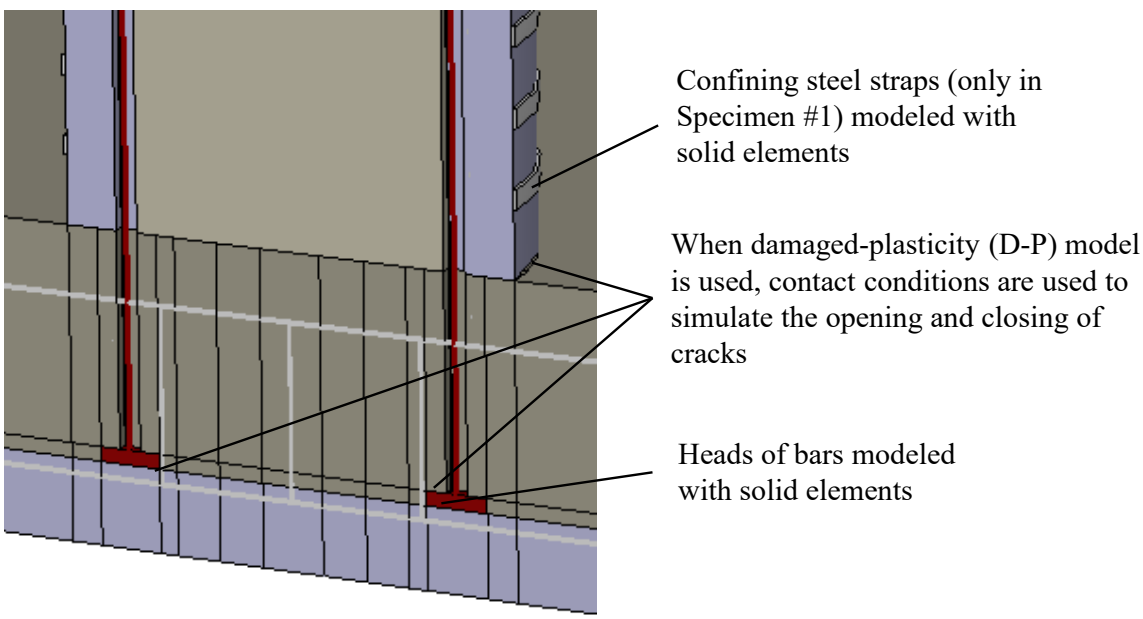

Figure 5.8 – Close-up details for the FE model of Specimen #1

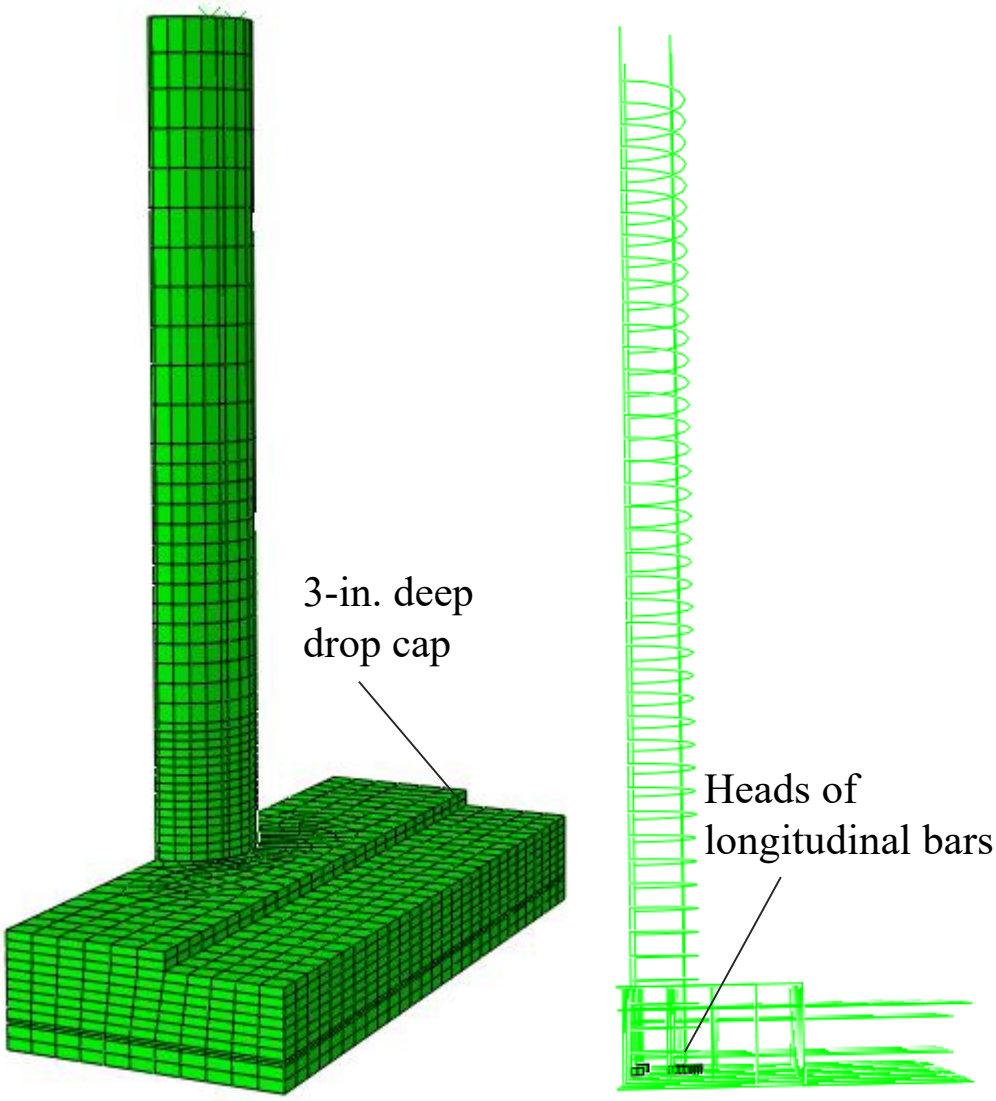

(a) Slab-column assembly

(b) Reinforcement cage

Figure 5.9 – FE model of Specimen #3

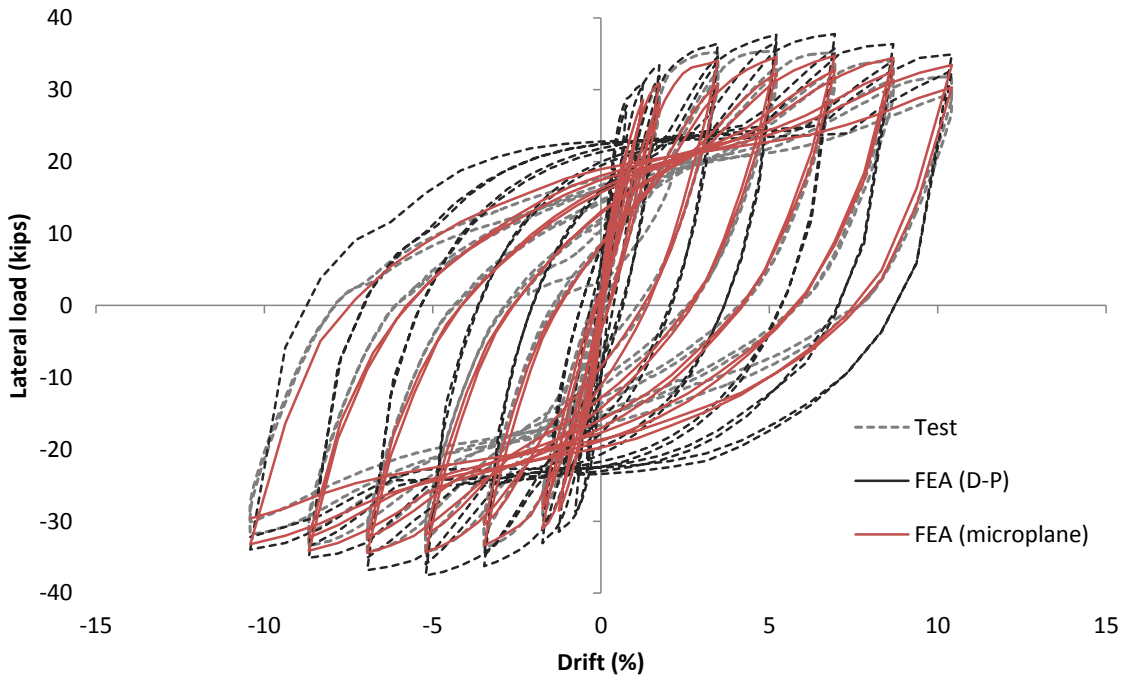

Figure 5.10 – Lateral load-vs.-top drift curves from test and FEA of Specimen #1

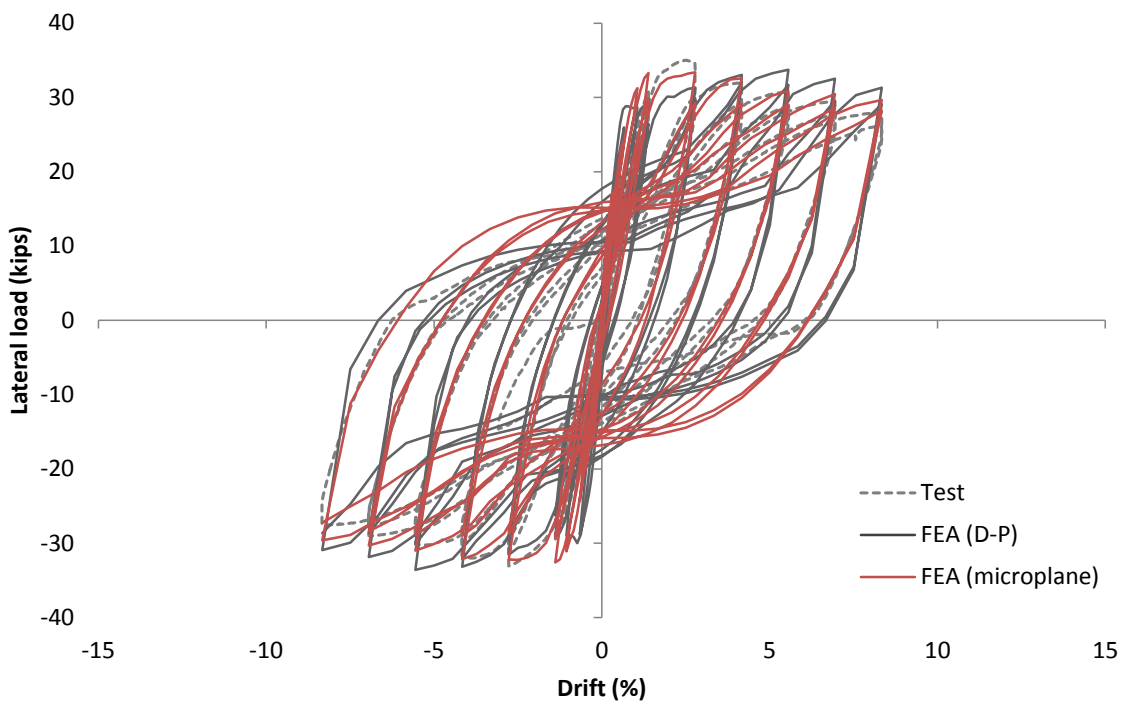

Figure 5.11 – Lateral load-vs.-top drift curves from test and FEA of Specimen #2

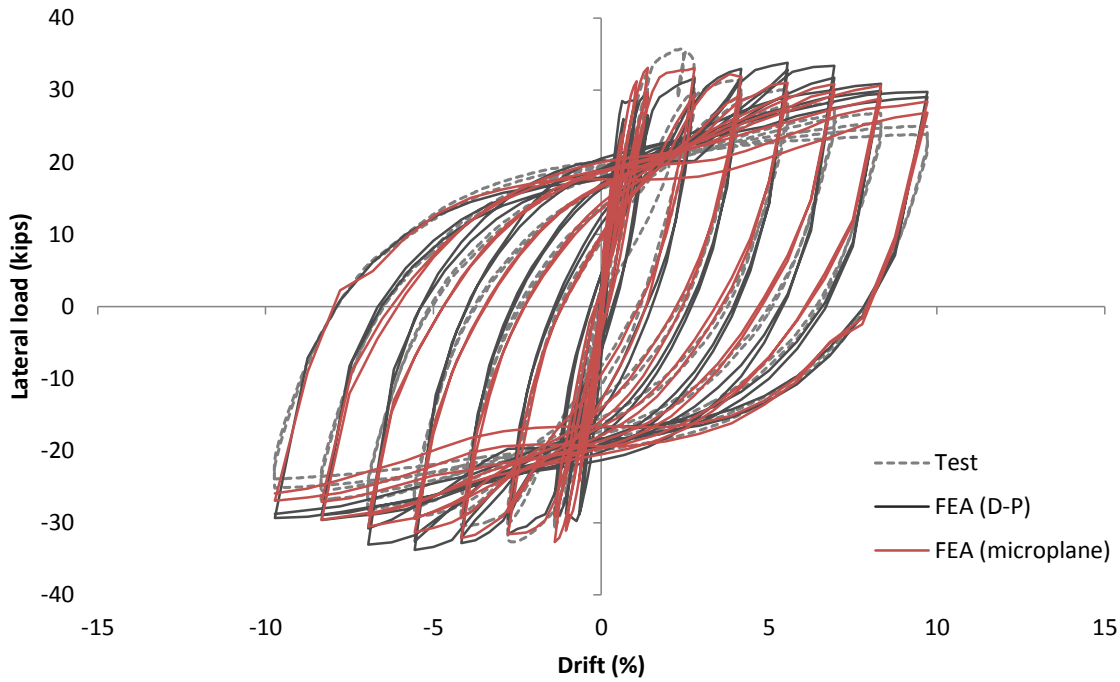

Figure 5.12 – Lateral load-vs.-top drift curves from test and FEA of Specimen #3

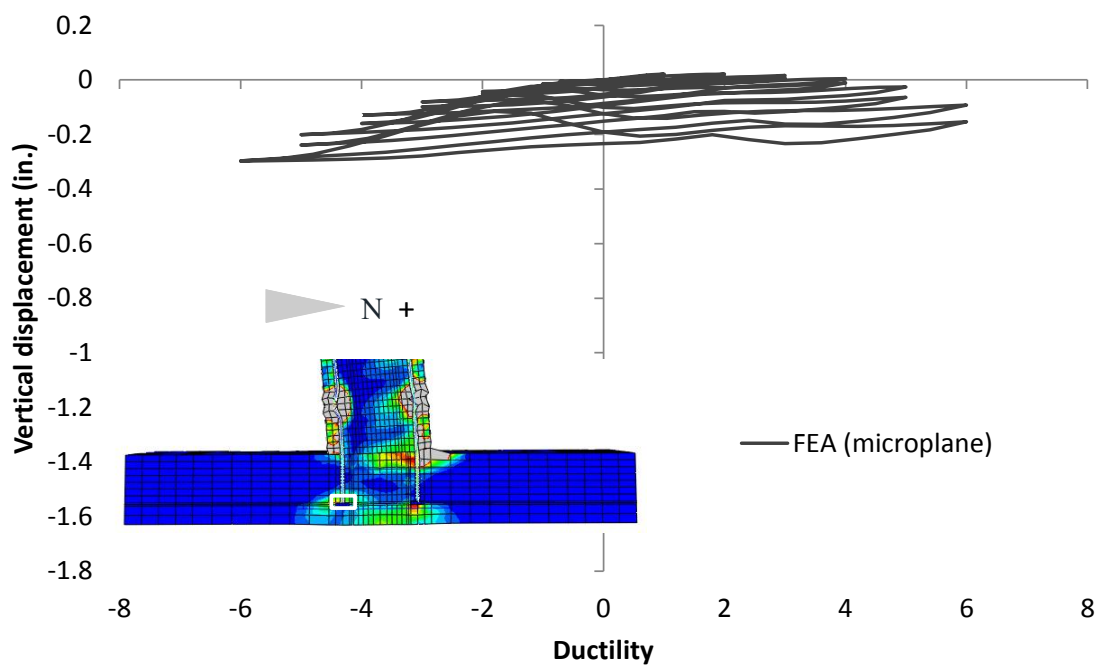

Figure 5.13 – Vertical displacement of the top face of the slab (bottom face in the specimen) at the position of the headed bar on the south side of Specimen #1 $\left(l_e = 9.8d_b\right)$

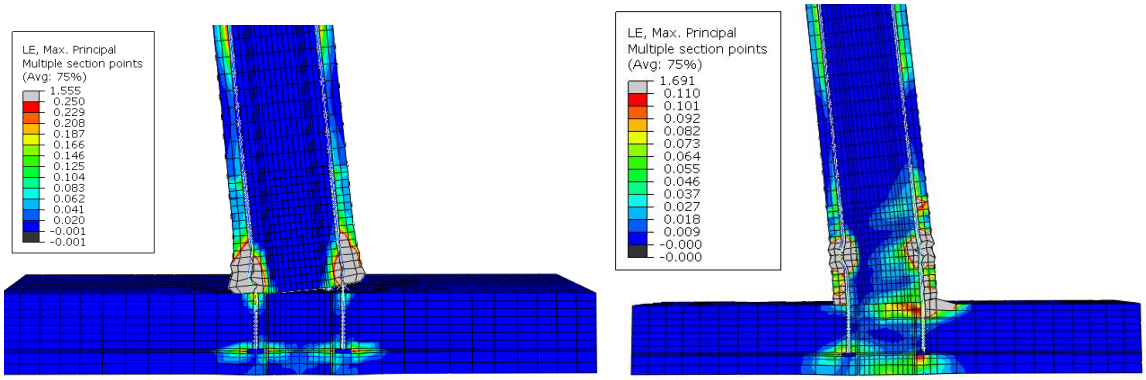

(a) FEA with D-P model (b) FEA with microplane model

Figure 5.14 – Deformed FE mesh for Specimen #1 $\left(l_e = 9.8d_b\right)$

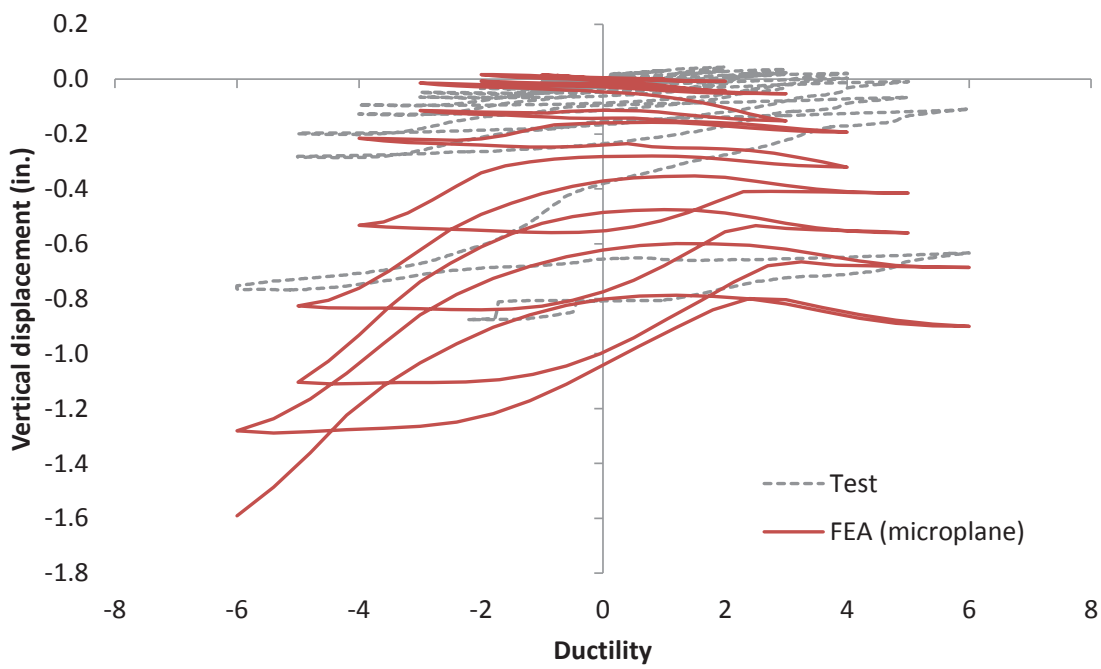

Figure 5.15 – Vertical displacement of the top face of the slab (bottom face in the specimen) at the position of the headed bar on the south side of Specimen #2 $\left(l_e = 8.7d_b\right)$

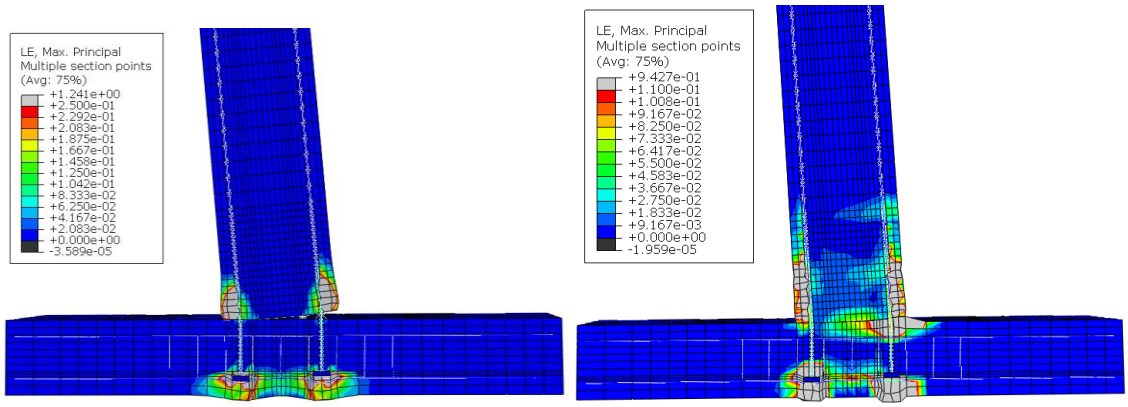

(a) FEA with D-P model (b) FEA with microplane model

Figure 5.16 – Deformed FE mesh for Specimen #2 $\left(l_e = 8.7 d_b\right)$

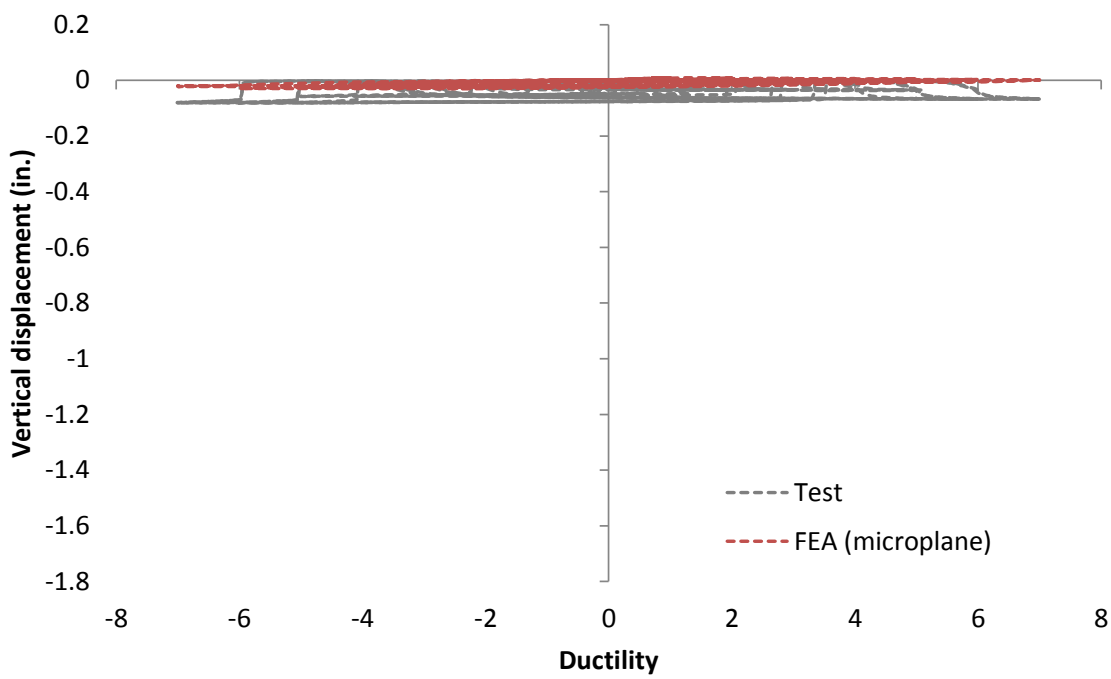

Figure 5.17 – Vertical displacement of the top face of the slab (bottom face in the specimen) at the position of the headed bar on the south side of Specimen #3 $\left(l_e = 11 d_b\right)$

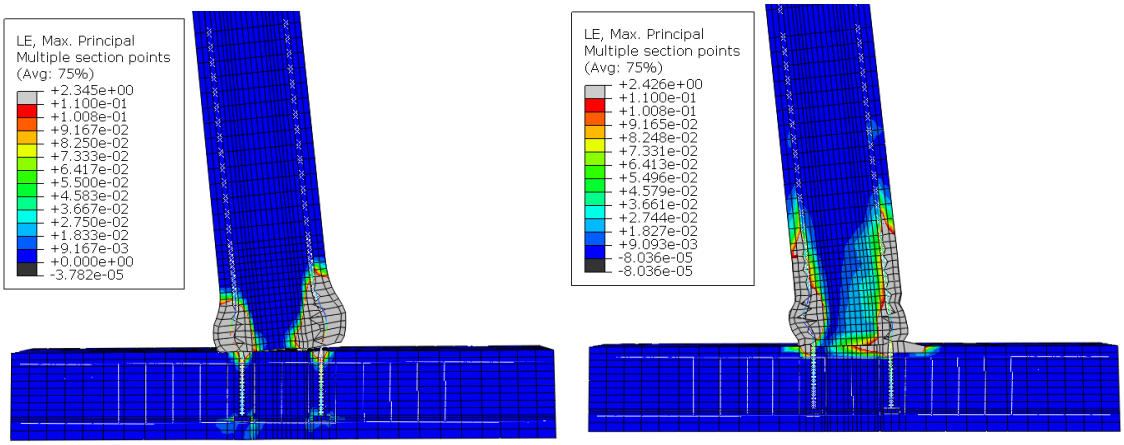

(a) FEA with D-P model (b) FEA with microplane model

Figure 5.18 – Deformed FE mesh for Specimen #3 $\left(l_e = 11 d_b\right)$

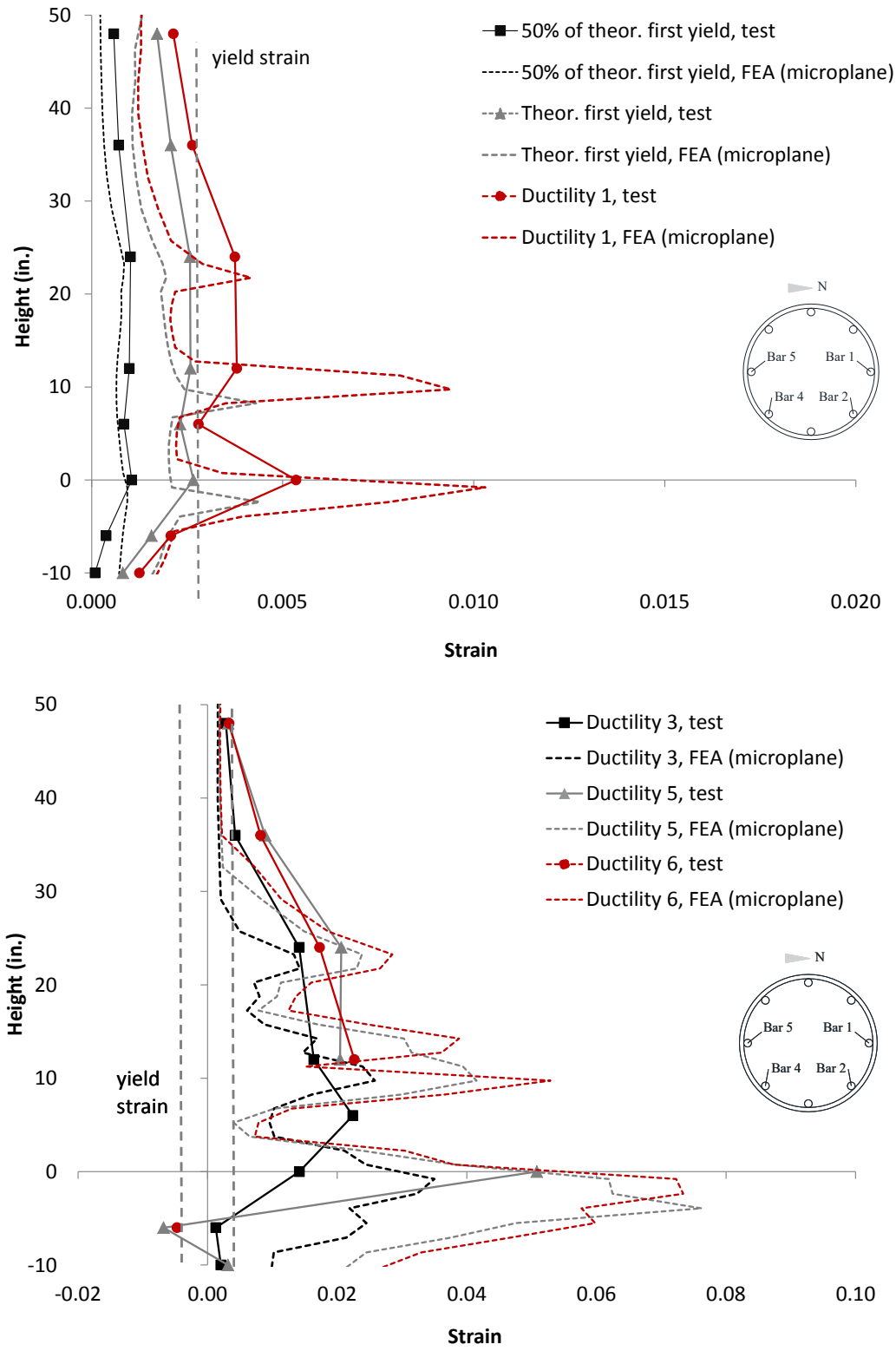

Figure 5.19 – Strains in longitudinal Bar 1 from FEA (microplane) of Specimen #1

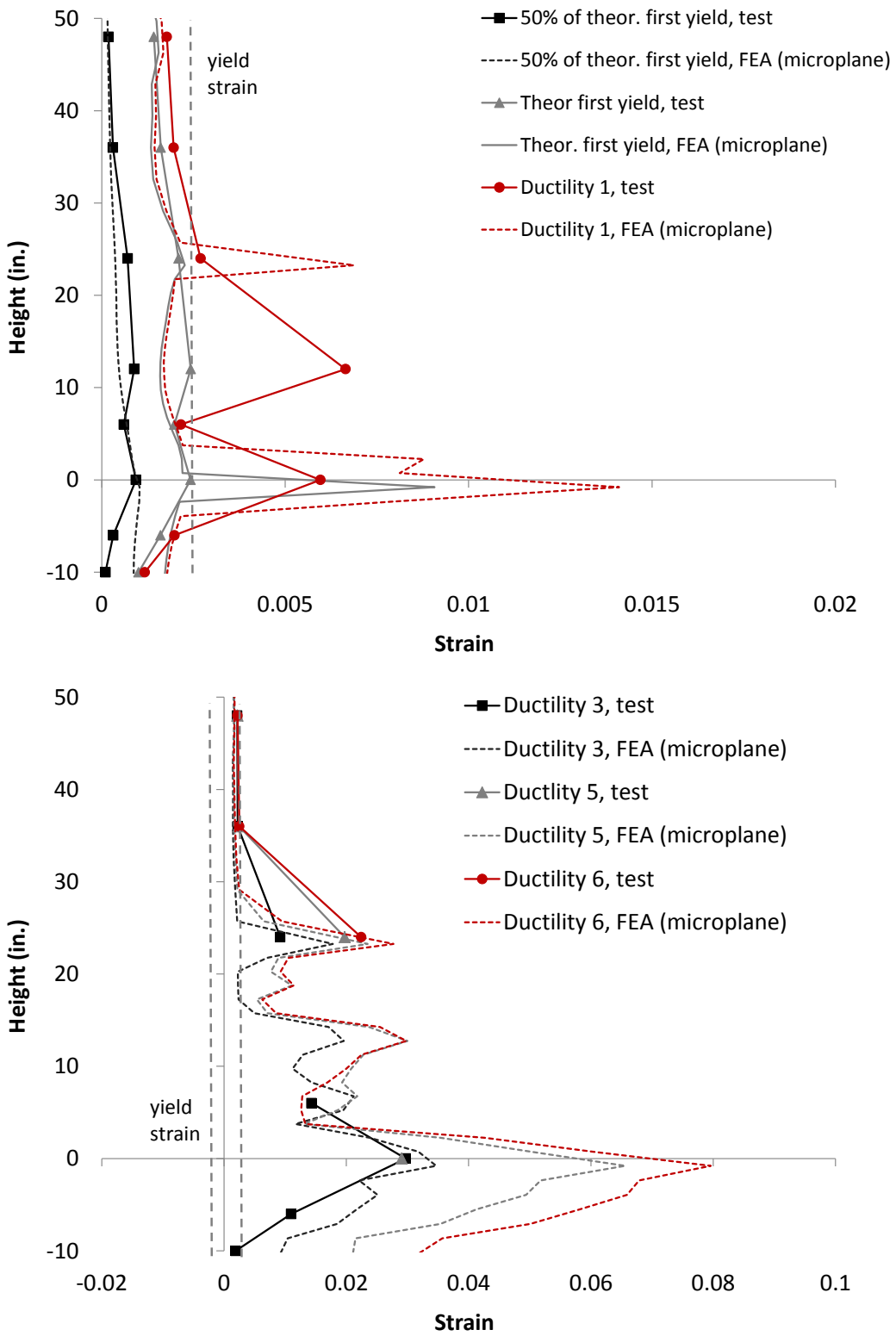

Figure 5.20 – Strains in longitudinal Bar 1 from FEA (microplane) of Specimen #2

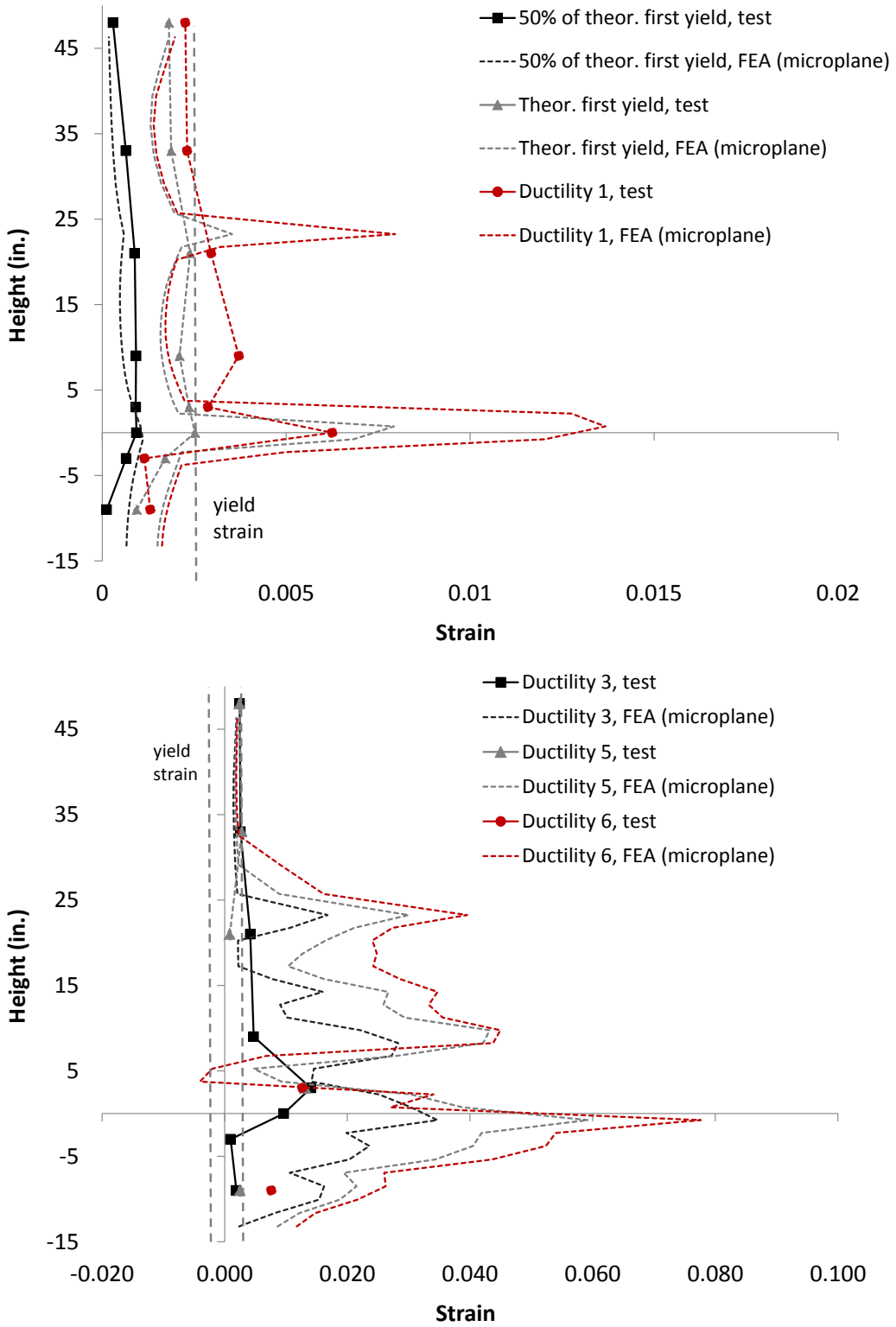

Figure 5.21 – Strains in longitudinal Bar 1 from FEA (microplane) of Specimen #3

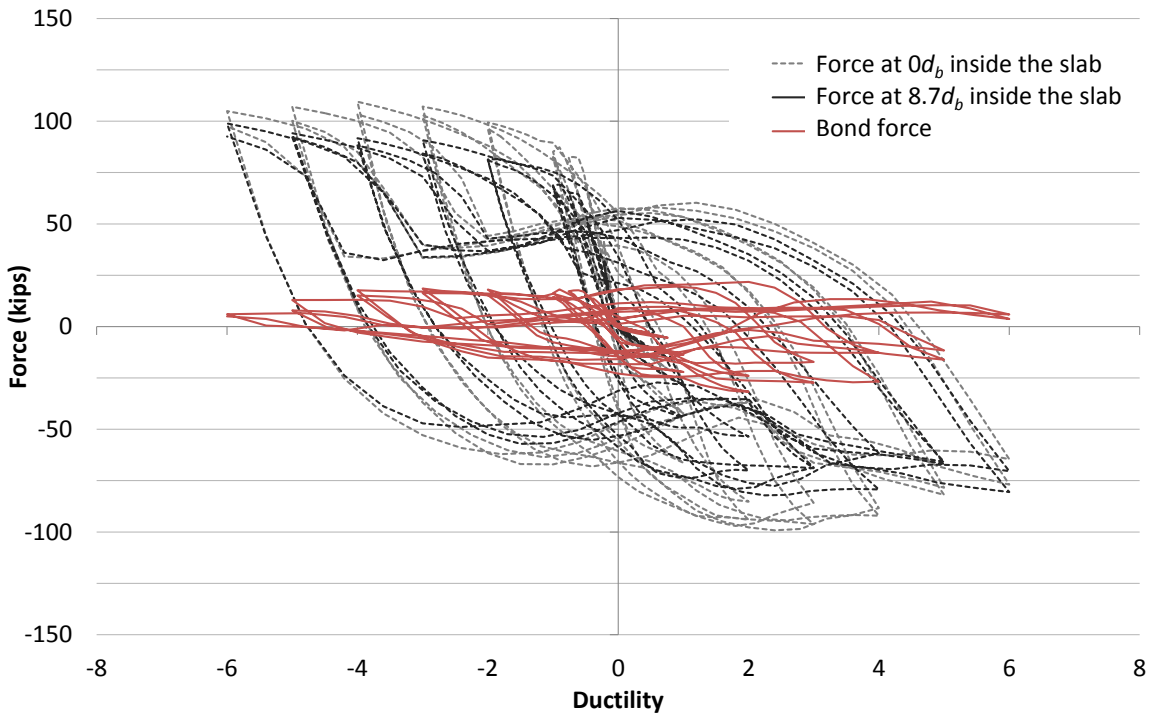

Figure 5.22 – Forces in longitudinal Bar 1 from FEA (microplane) of Specimen #2

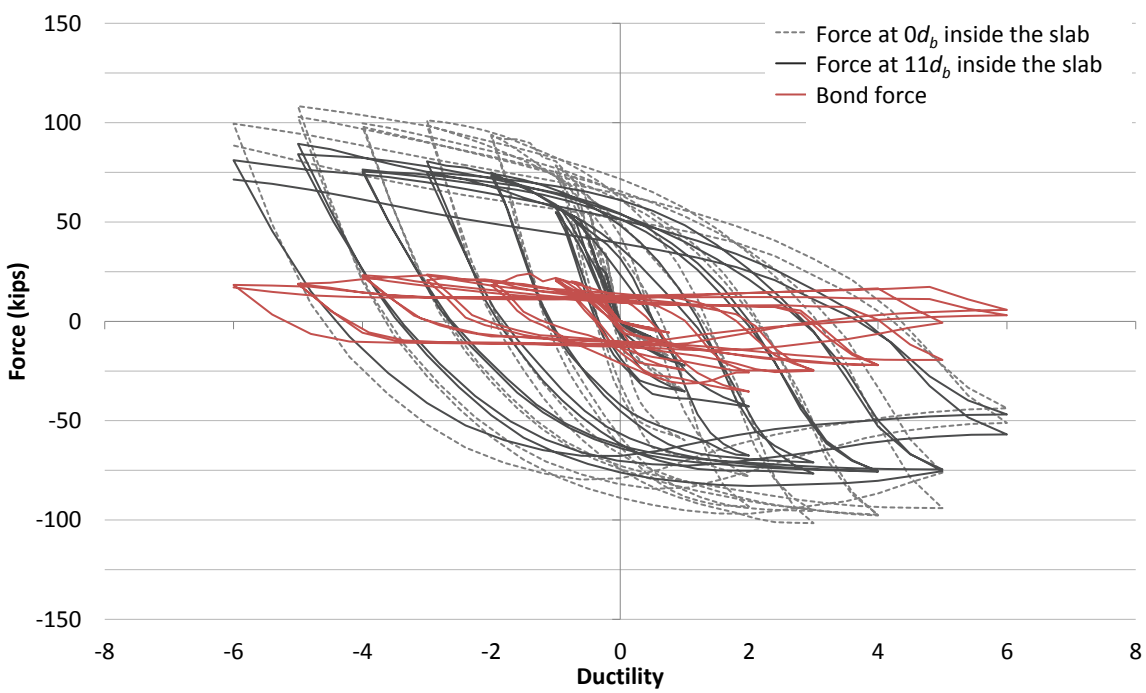

Figure 5.23 – Forces in longitudinal Bar 1 from FEA (microplane) of Specimen #3

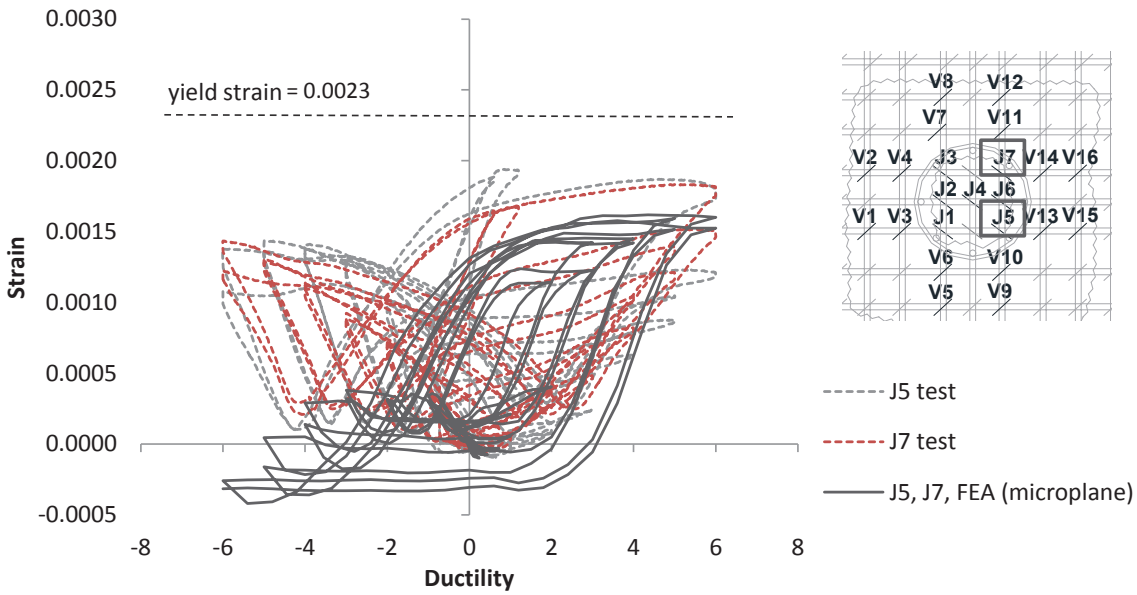

Figure 5.24 – Strains in J-bars of Specimen #1

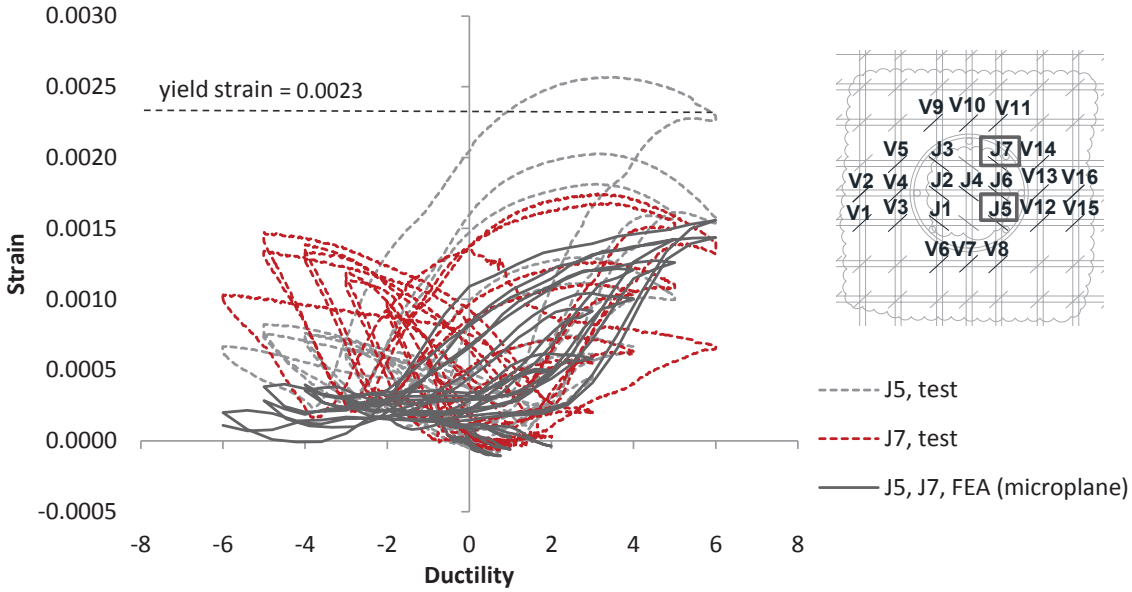

Figure 5.25 – Strains in J-bars of Specimen #2

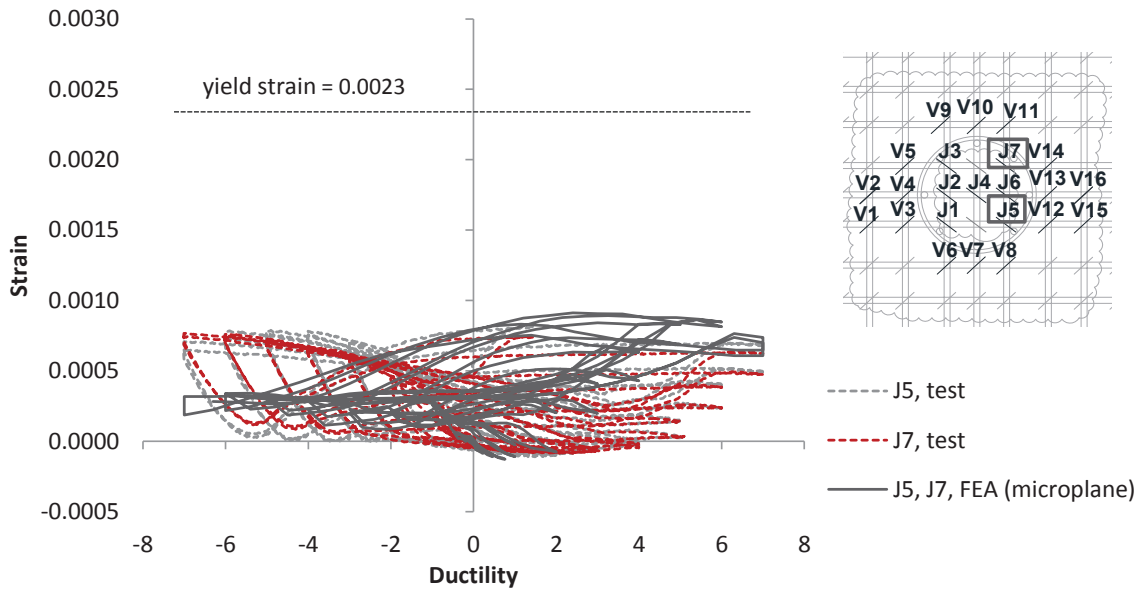

Figure 5.26 – Strains in J-bars of Specimen #3

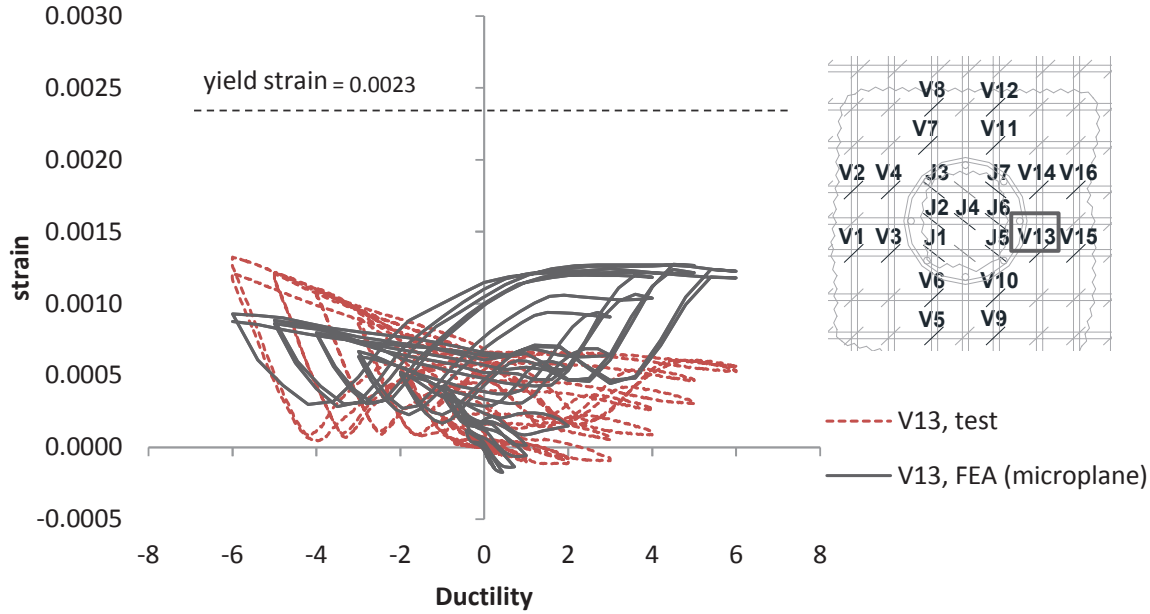

Figure 5.27 – Strains in a vertical stirrup in the 1st row in the slab of Specimen #1

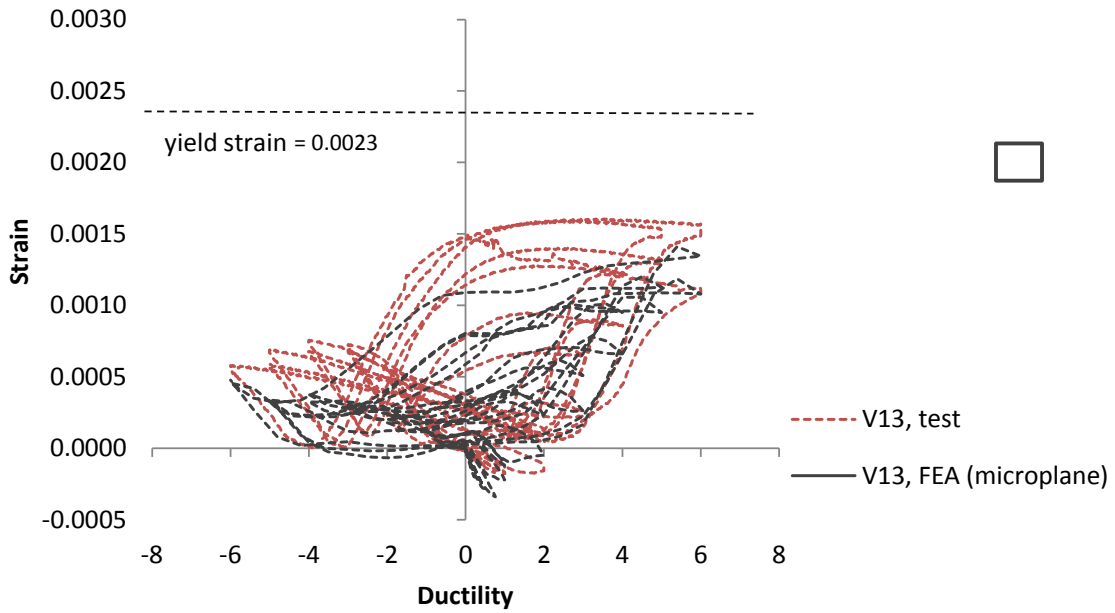

Figure 5.28 – Strains in a vertical stirrup in the 1st row in the slab of Specimen #2

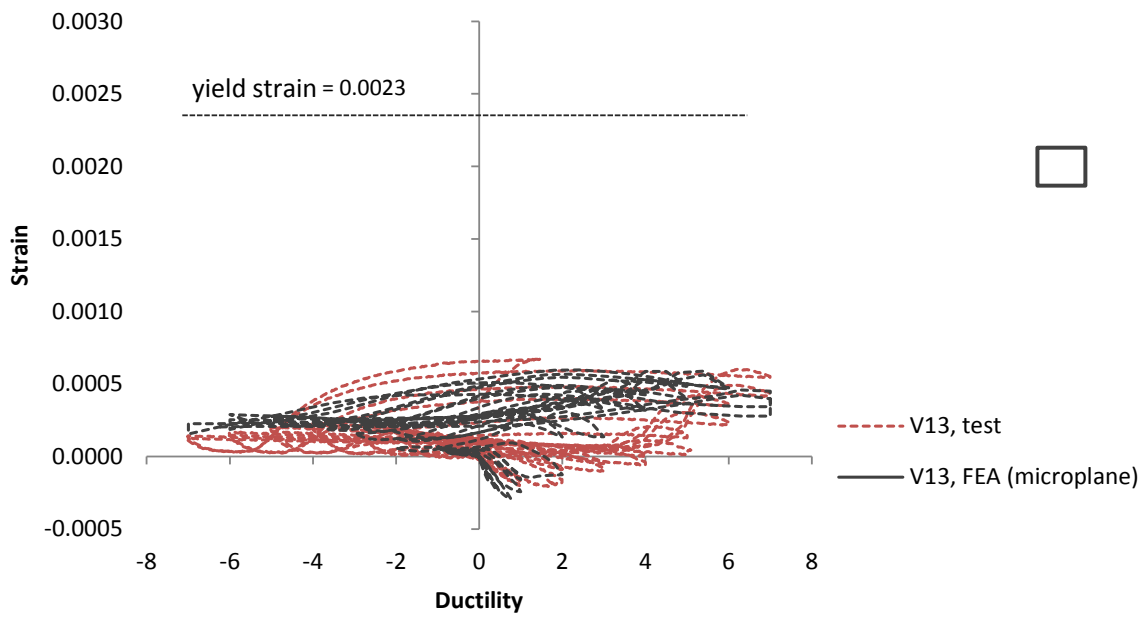

Figure 5.29 – Strains in a vertical stirrup in the 1st row in the slab of Specimen #3

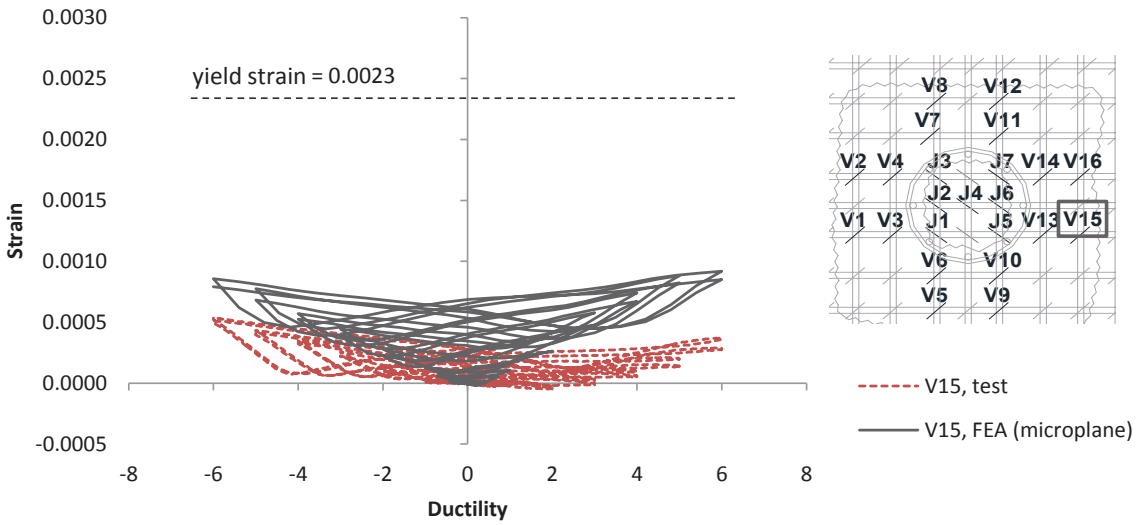

Figure 5.30 – Strains in a vertical stirrup in the 2nd row in the slab of Specimen #1

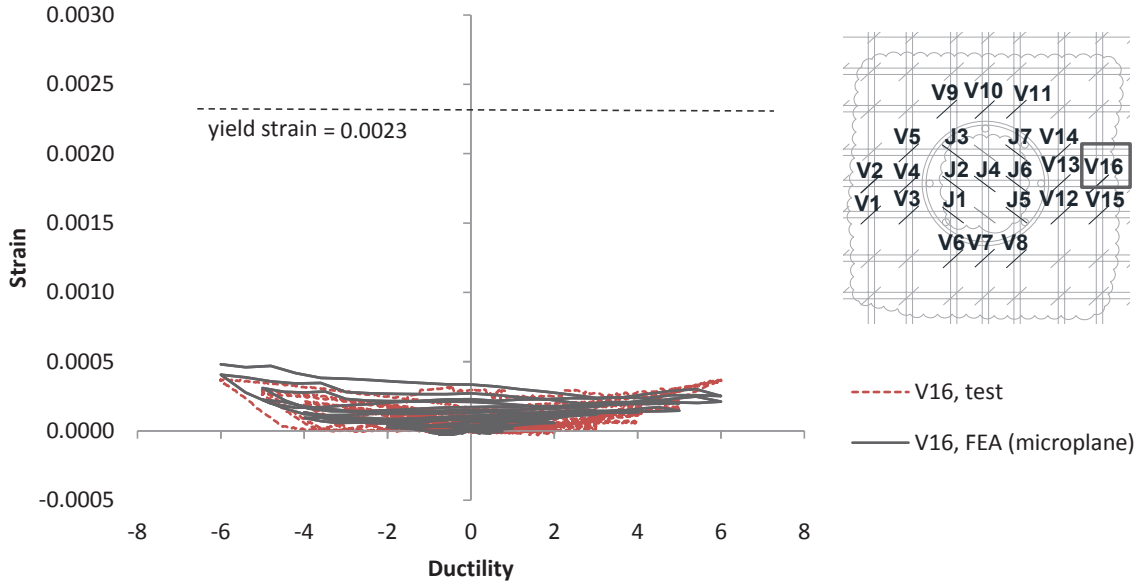

Figure 5.31 – Strains in a vertical stirrup in the 2nd row in the slab of Specimen #2

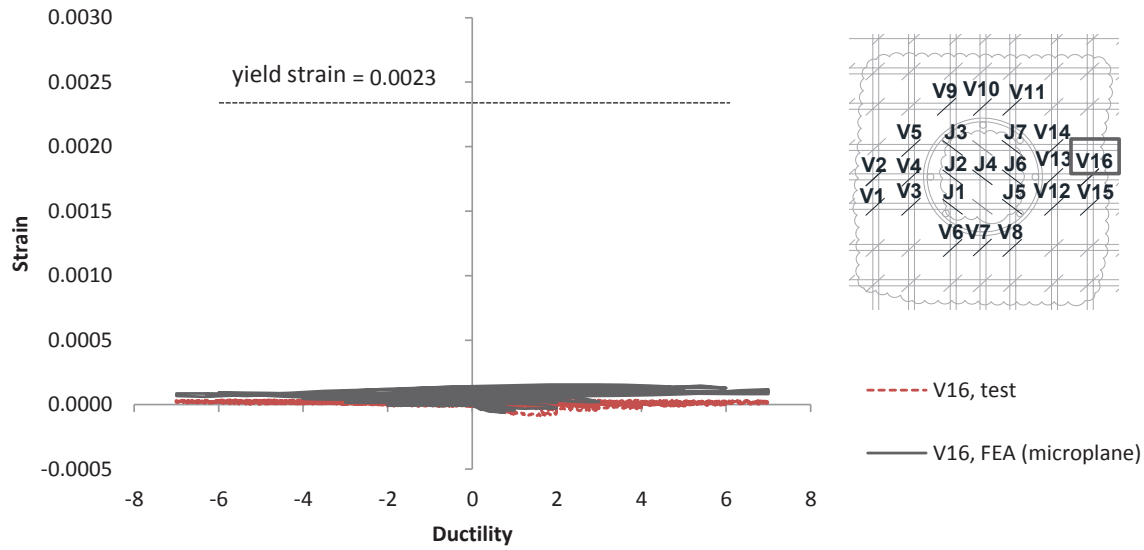

Figure 5.32 – Strains in a vertical stirrup in the 2nd row in the slab of Specimen #3

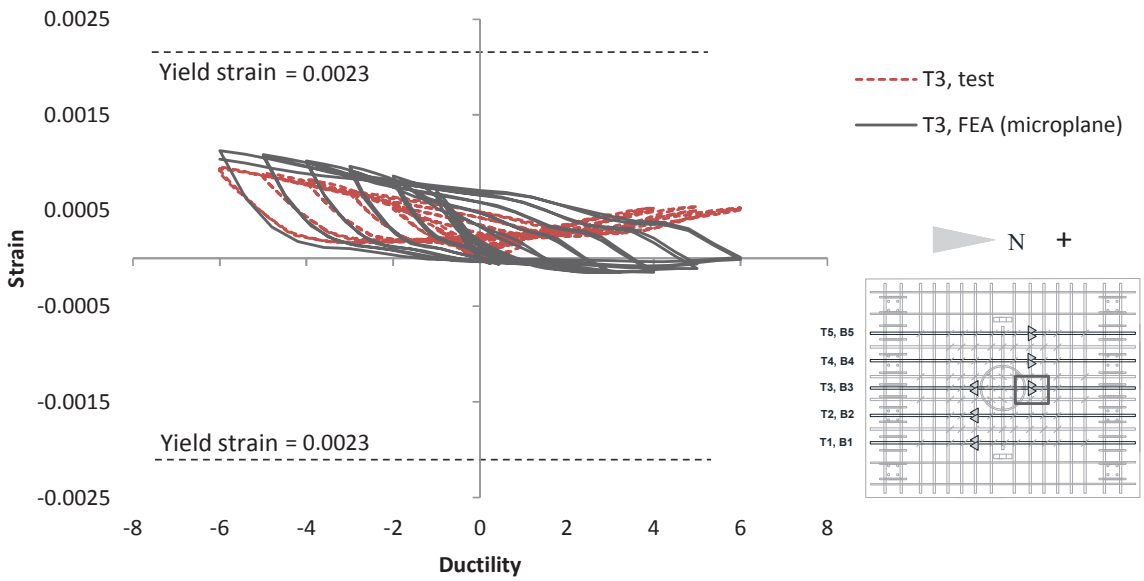

Figure 5.33 – Strains in the top longitudinal bar T3 in the slab of Specimen #1

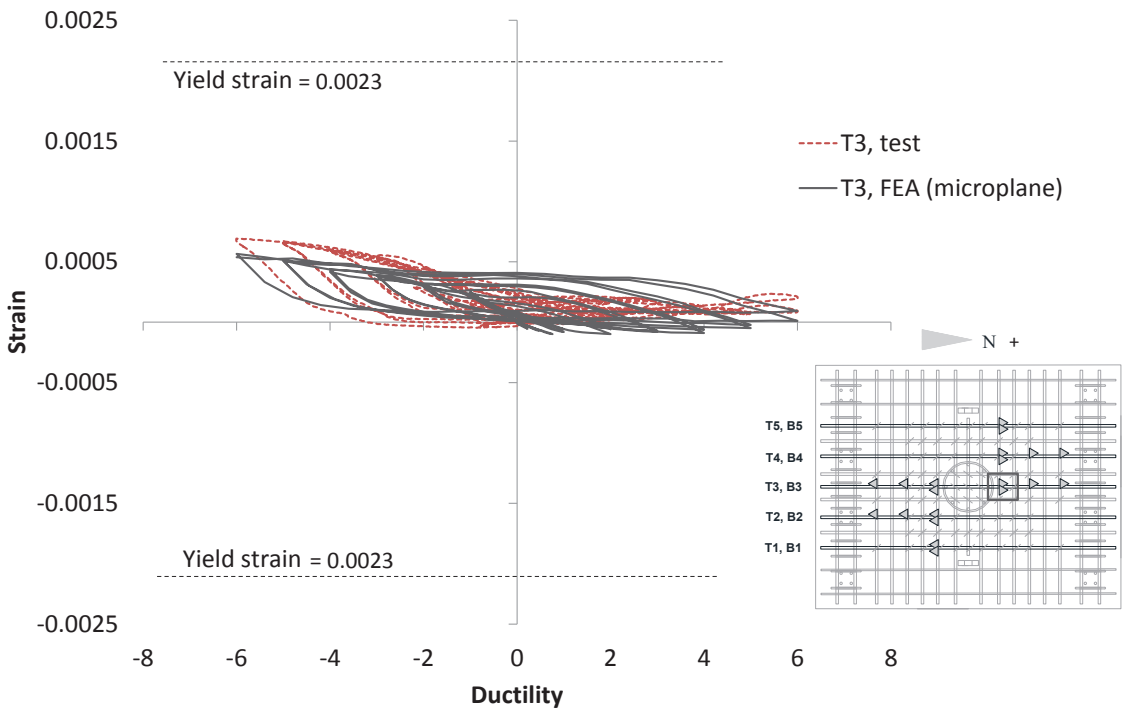

Figure 5.34 – Strains in the top longitudinal bar T3 in the slab of Specimen #2

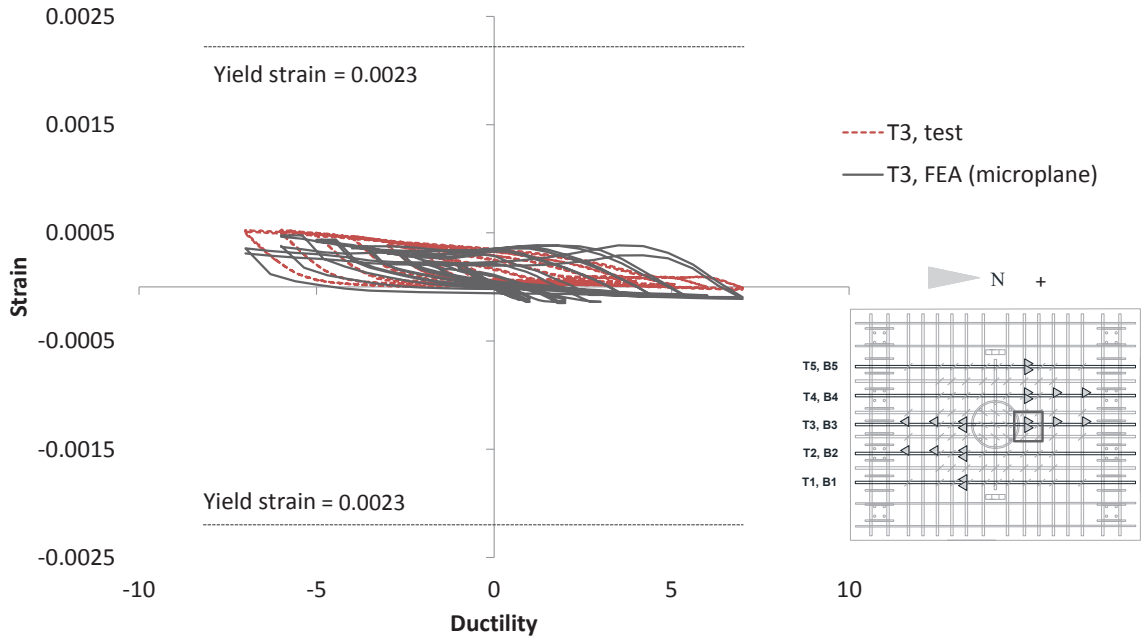

Figure 5.35 – Strains in the top longitudinal bar T3 in the slab of Specimen #3

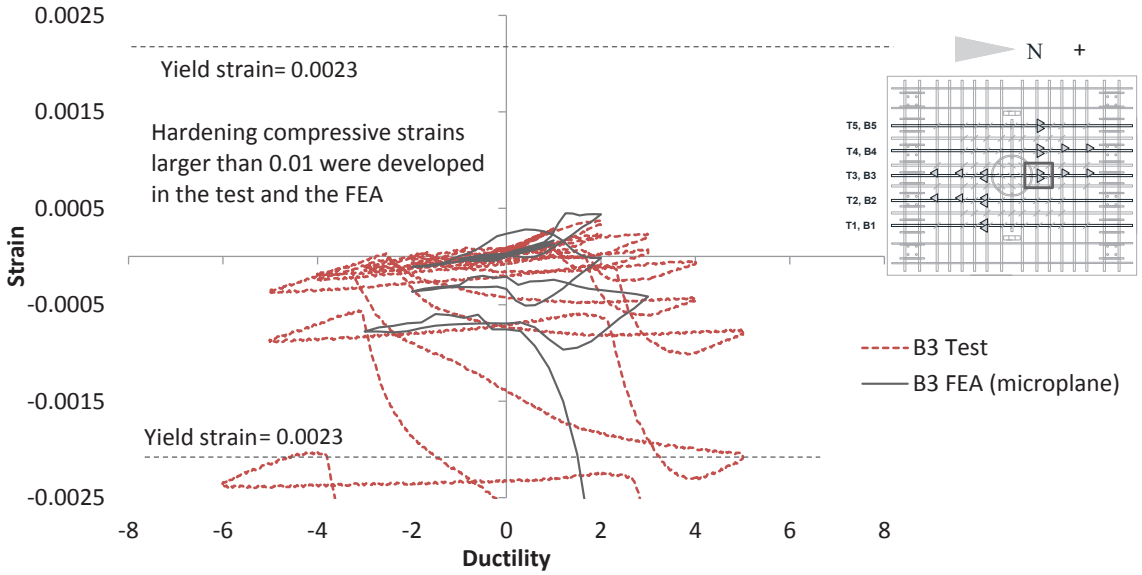

Figure 5.36 – Strains in the bottom longitudinal bar B3 in the slab of Specimen #2

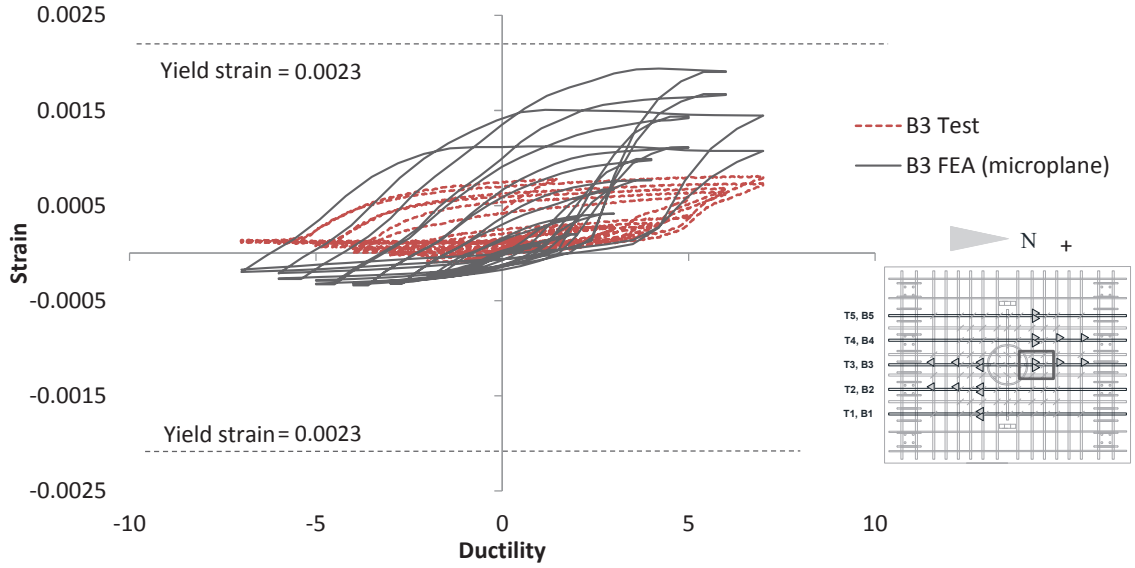

Figure 5.37 – Strains in the bottom longitudinal bar B3 in the slab of Specimen #3

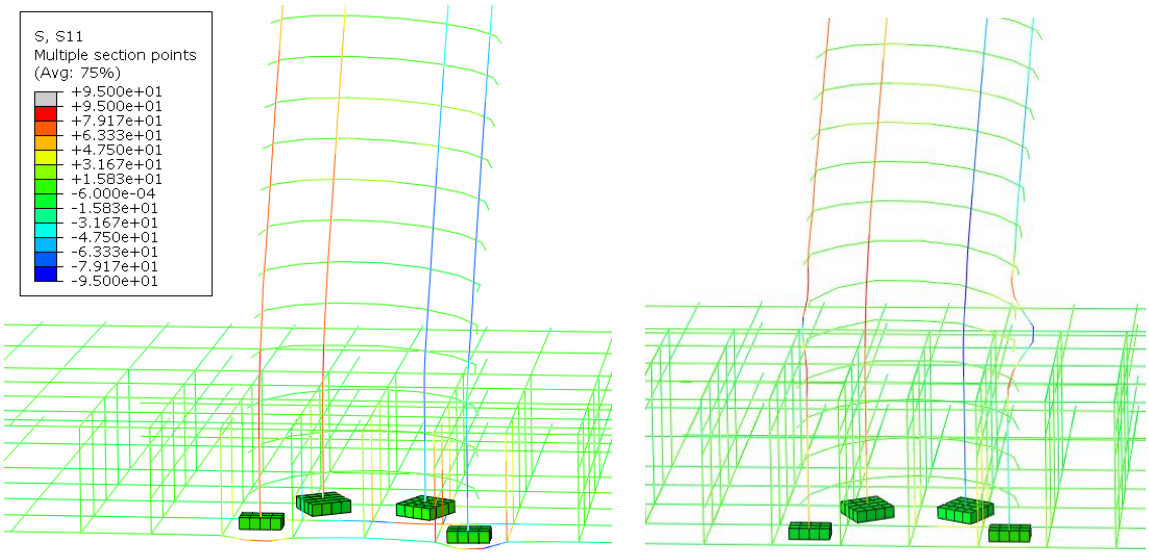

(a) Specimen #2 (b) Specimen #3

Figure 5.38 – Deformed column and slab reinforcement from the FEA with the microplane model

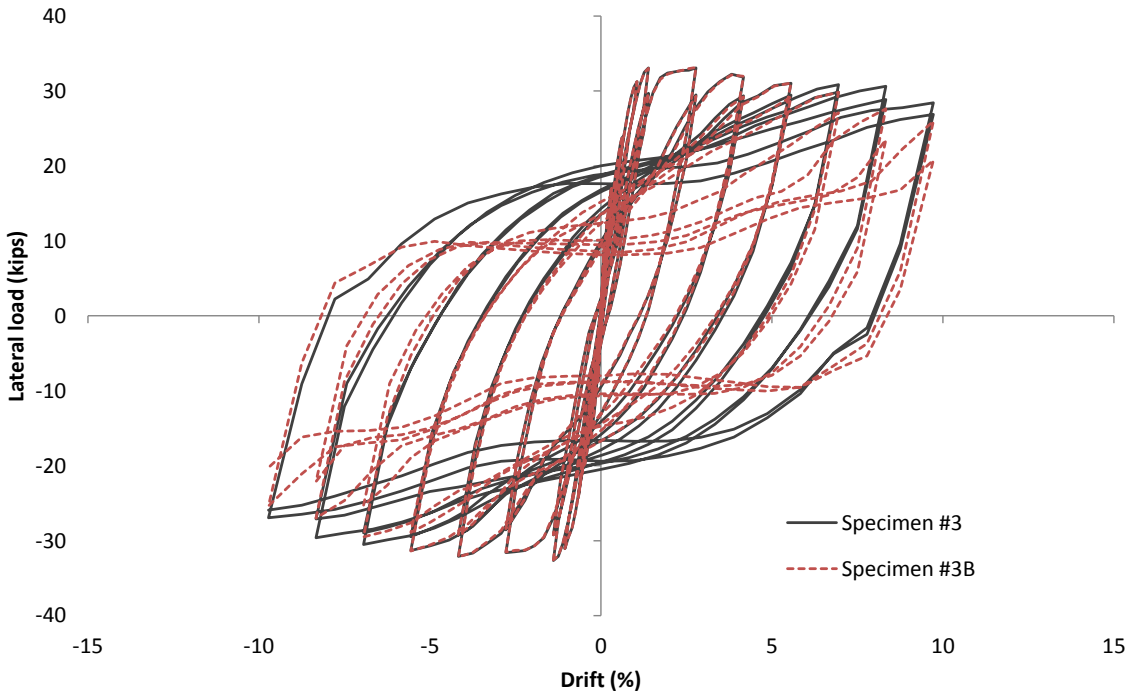

Figure 5.39 – Lateral load-vs.-top drift curve from the FEA of Specimen #3B

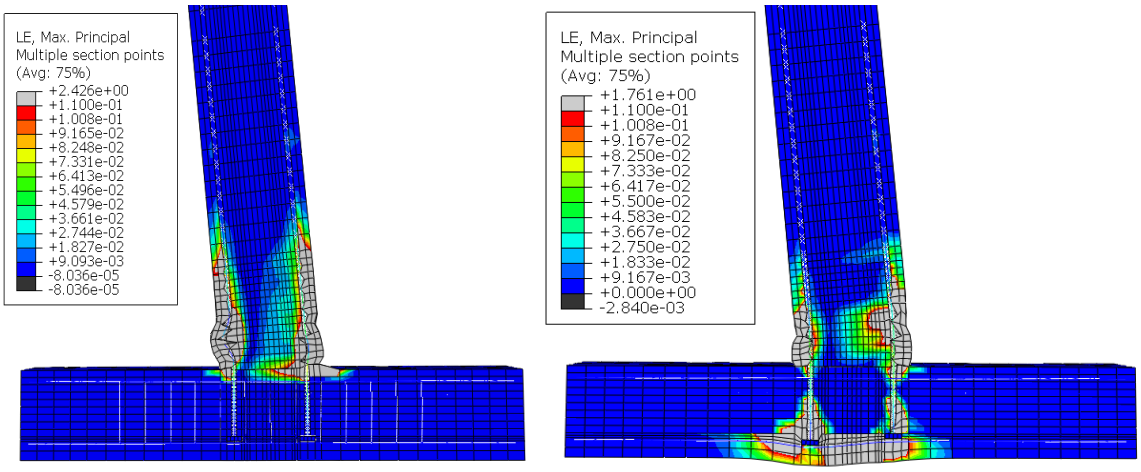

(a) Specimen #3 (b) Specimen #3B (no J-bars and vertical stirrups)

Figure 5.40 – Deformed FE mesh for Specimens #3 and #3B $\left(l_e = 11d_b\right)$

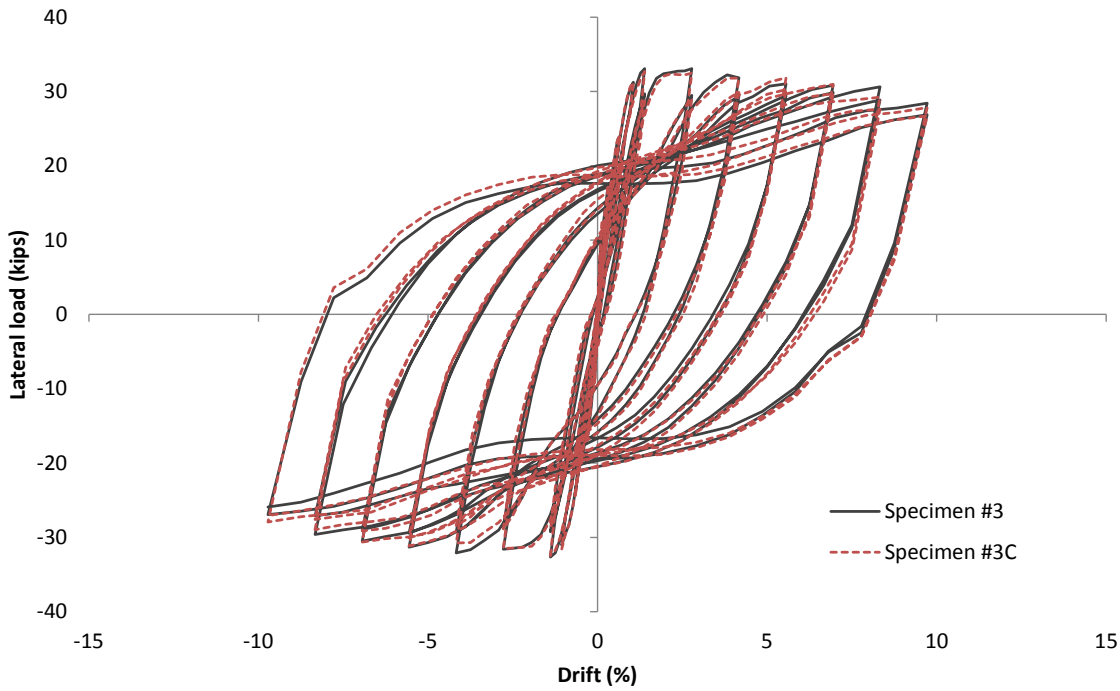

Figure 5.41 – Lateral load-vs.-top drift curve from the FEA of Specimen #3C

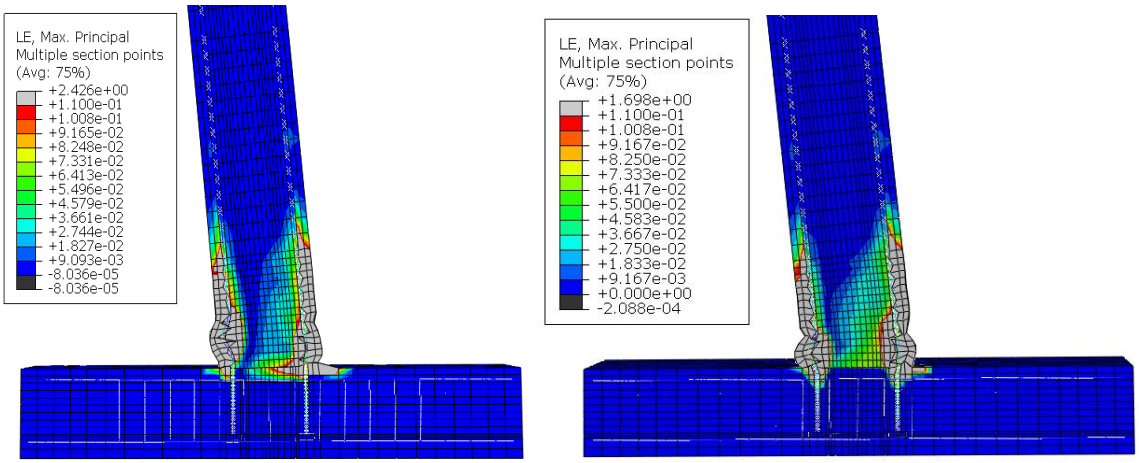

(a) Specimen #3

(b) Specimen #3C
(with J-bars and one row of vertical stirrups)

Figure 5.42 – Deformed FE mesh for Specimens #3 and #3C $\left(l_e = 11 d_b\right)$

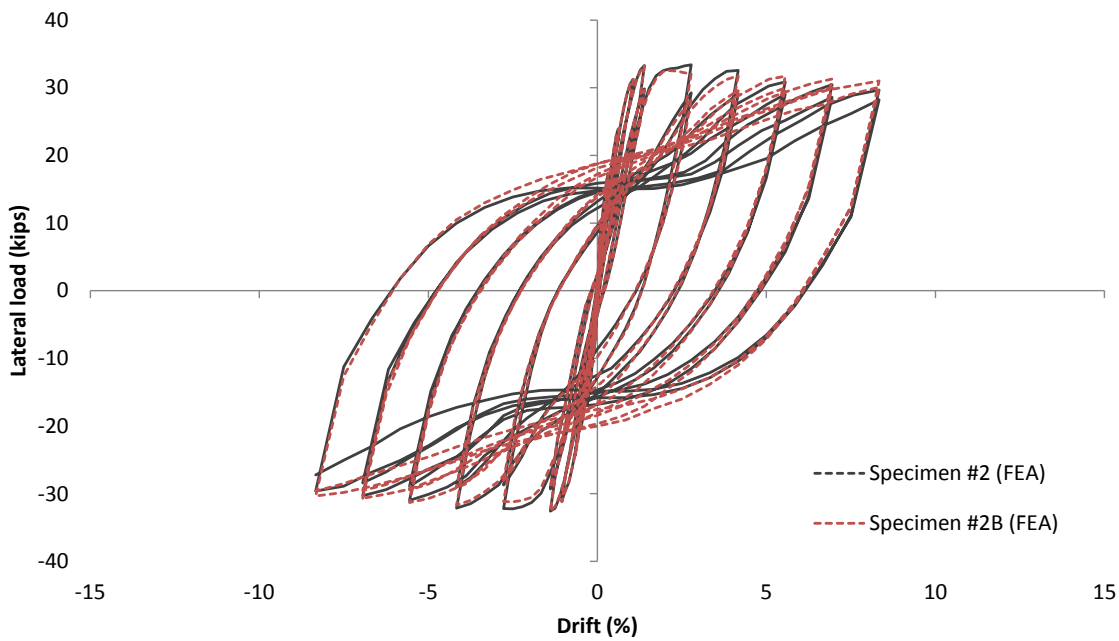

Figure 5.43 – Lateral load-vs.-top drift curve from the FEA of Specimen #2B

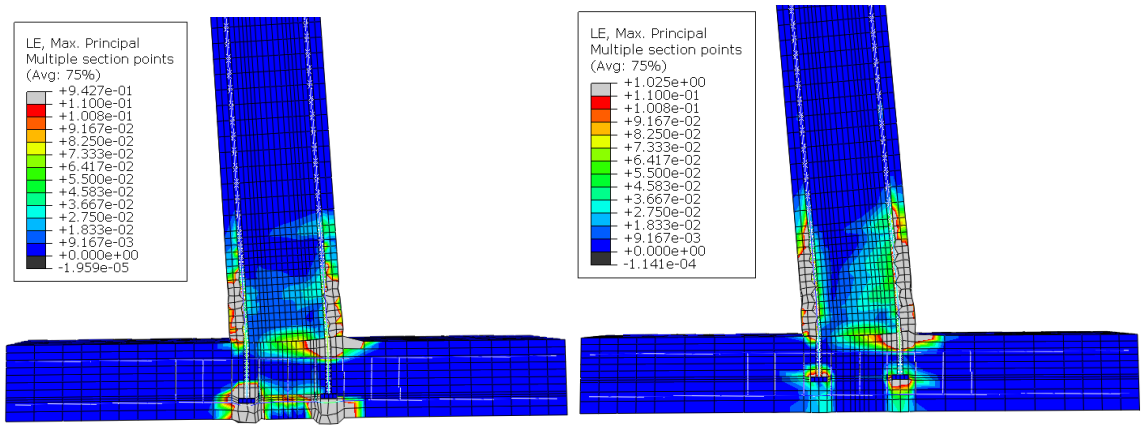

(a) Specimen #2

(b) Specimen #2B
(headed bars moved $2d_b$ upward)

Figure 5.44 – Deformed FE meshes for Specimens #2 and #2B

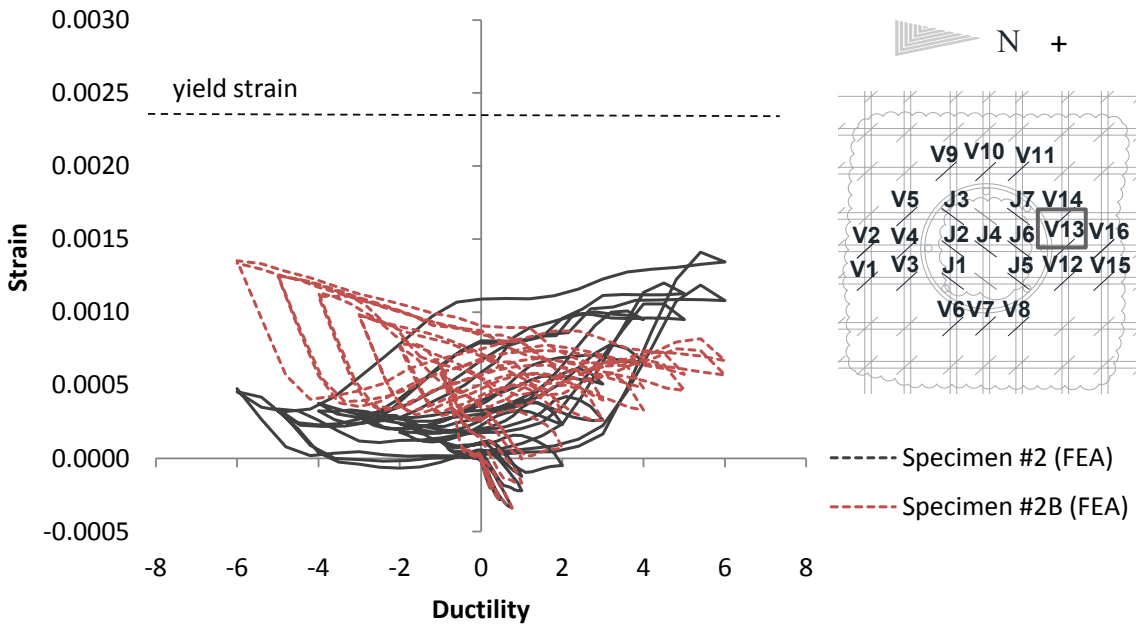

Figure 5.45 – Strains in vertical stirrup, V13, in the slab of Specimens #2 and #2B

CHAPTER 6

SUMMARY AND CONCLUSIONS

6.1 Summary

This report presents an experimental and numerical study on the development of headed bars anchored in slab-columns joints of RC slab bridges. Three full-scale slab-column assemblies were tested under lateral quasi-static loading. The specimens were designed to comply with the AASHTO LRFD Bridge Design Specifications (AASHTO 2014), SDC (Caltrans 2013), and BDA 4-10 (Caltrans 2009). The reinforcement in the slab-column joints of the specimens also complied with the specifications in MTD 20-7 (Caltrans, October 2014). Each specimen had a 24-in.-diameter column and a 16-in.-thick slab. The column had a height of 12 ft., measured from the bottom face of the slab (top face in the specimen) to the elevation at which the lateral load was applied. Specimen #1 had an embedment length of $9.8d_b$ for the headed bars, Specimen #2 had $8.7d_b$, and Specimen #3 had $11d_b$. A 3-in deep drop cap was added to the slab in Specimen #3 in order to provide an increased embedment length in the slab-column joint. The reinforcing steel was Grade 60 and the concrete had a target compressive strength of 5,000 psi.

Along with the experimental study, three-dimensional nonlinear finite element (FE) models have been developed to analyze the performance of the slab-column assemblies before and after the tests. They are also used in a parametric study to evaluate additional design variables that were not considered in the tests.

6.2 Observations

For Specimen #2, which had an embedment length of $8.7d_b$, the tensile yield strength of the headed bars and the plastic moment capacity of the column were developed in the test. However, the anchorage of the headed bars deteriorates significantly, leading to more pinched hysteretic load-displacement curves, as compared to the other two specimens with higher embedment lengths. Moreover, the top face of the slab (bottom face in the specimen) was severely damaged by the punching action of the headed bars. Specimen #1, which had an embedment length of $10d_b$, had moderate punching cracks and a better hysteretic load-displacement behavior than Specimen #2. Specimen #3, which had an embedment length of $11d_b$, exhibited satisfactory performance with very minor punching cracks. The average compressive strength of the concrete cylinders for the slab of Specimen #3 was 4.5 ksi. Hence, since the expected concrete strength for a bridge structure is not likely to be less than 4.5 ksi, $11d_b$ can be taken as the minimum embedment length required for headed bars in slab bridges. However, because of the lack of experimental data, an embedment length shorter than $11d_b$ should be discouraged even if the expected concrete strength is higher than 4.5 ksi.

The J-bars in the slab-column joints, and the vertical stirrups in the slabs right outside the column cage were effectively engaged to restrain breakout cracks and punching cracks when the headed bars were subjected to tension and compression. However, the demand on the J-bars and stirrups was smaller for Specimen #3, which had the highest embedment length. The vertical stirrups in the 2nd row and farther away from the column cage did not develop any significant strains during the tests.

The finite element analyses have accurately reproduced the response of the slab-column assemblies under lateral loading. The analyses support the experimental observation that the vertical stirrups in the 2nd row and farther away from the column cage have little contribution to the resistance of the punching and bearing action of the headed bars. Moreover, the analyses have indicated that the performance of Specimen #2 can be improved by reducing the embedment length of the headed bars to

$6.7d_b$ and increasing the distance of the bar heads from the top face of the slab (bottom face in the specimen) by the same amount. The reduced development length can still allow the plastic moment capacity of the column to develop, while the increased concrete cover can reduce the damage induced by the punching action of the bars.

6.3 Conclusions and Recommendations

This study has shown that for slab concrete with an expected compressive strength of 4.5 ksi and Grade-60 steel, an embedment length of $11d_b$ is adequate for headed bars in slab-column joints designed according to MTD 20-7 (Caltrans, October 2014). For a 16-in. slab with No. 9 headed bars as depicted in Figure 1.1, the required embedment length can be provided either by increasing the slab thickness or by adding a drop cap. Based on the test data, it is recommended that MTD 20-7 be modified to include four additional stirrups adjacent to the column cage, as it was done for Specimens #2 and #3. Furthermore, the amount of vertical stirrups in the 2nd row and farther away from the column cage can be reduced. Their quantity can be determined according to the shear strength required for the slab. The bar heads should be below the top mat of reinforcement in the deck slab.

Both the experimental and numerical investigations have indicated that the performance of the slab-column assemblies was mainly compromised by the punching cracks rather than the breakout failure caused by bar tension. Embedment lengths of $8.7d_b$ and $9.8d_b$ were able to develop the moment capacity of the columns but resulted in moderate to severe punching cracks in the cover concrete of the slabs. They also resulted in severe deterioration of the anchorage of the headed bars and more pinched lateral column force-vs.-column displacement hysteresis curves. This alludes to the possibility that an embedment length less than $11d_b$ can be sufficient to develop the tensile strength of headed bars if punching damage can be controlled. Indeed, it has been shown by FEA that if there is not enough room to provide an adequate embedment length of $11d_b$, it may be advantageous to reduce the embedment length and increase the

distance of the bar head from the slab surface to reduce or avoid punching damage. Additional experimental study is recommended to verify this numerical observation.

APPENDIX A: DESIGN DRAWINGS OF SLAB COLUMN ASSEMBLIES

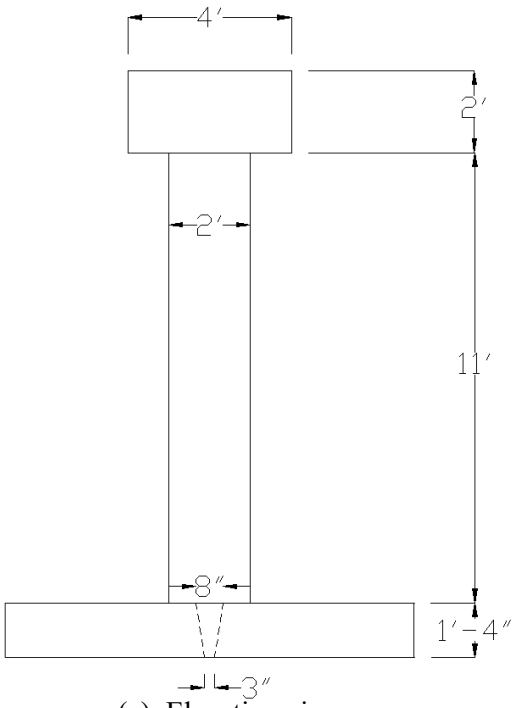

(a) Elevation view

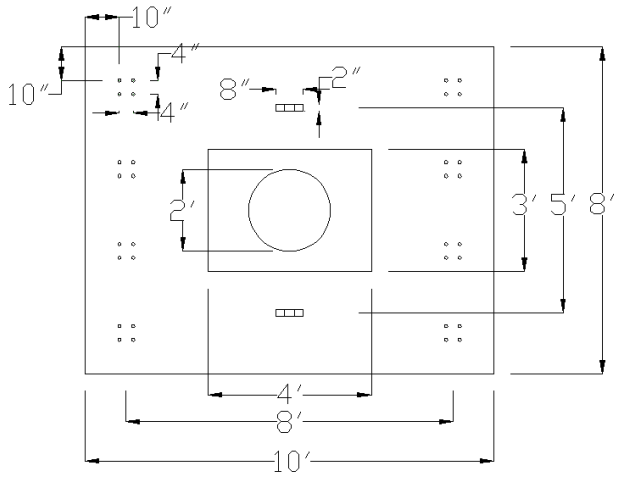

(b) Plan view

Figure A.1 – Plan and elevation views for Specimen #1

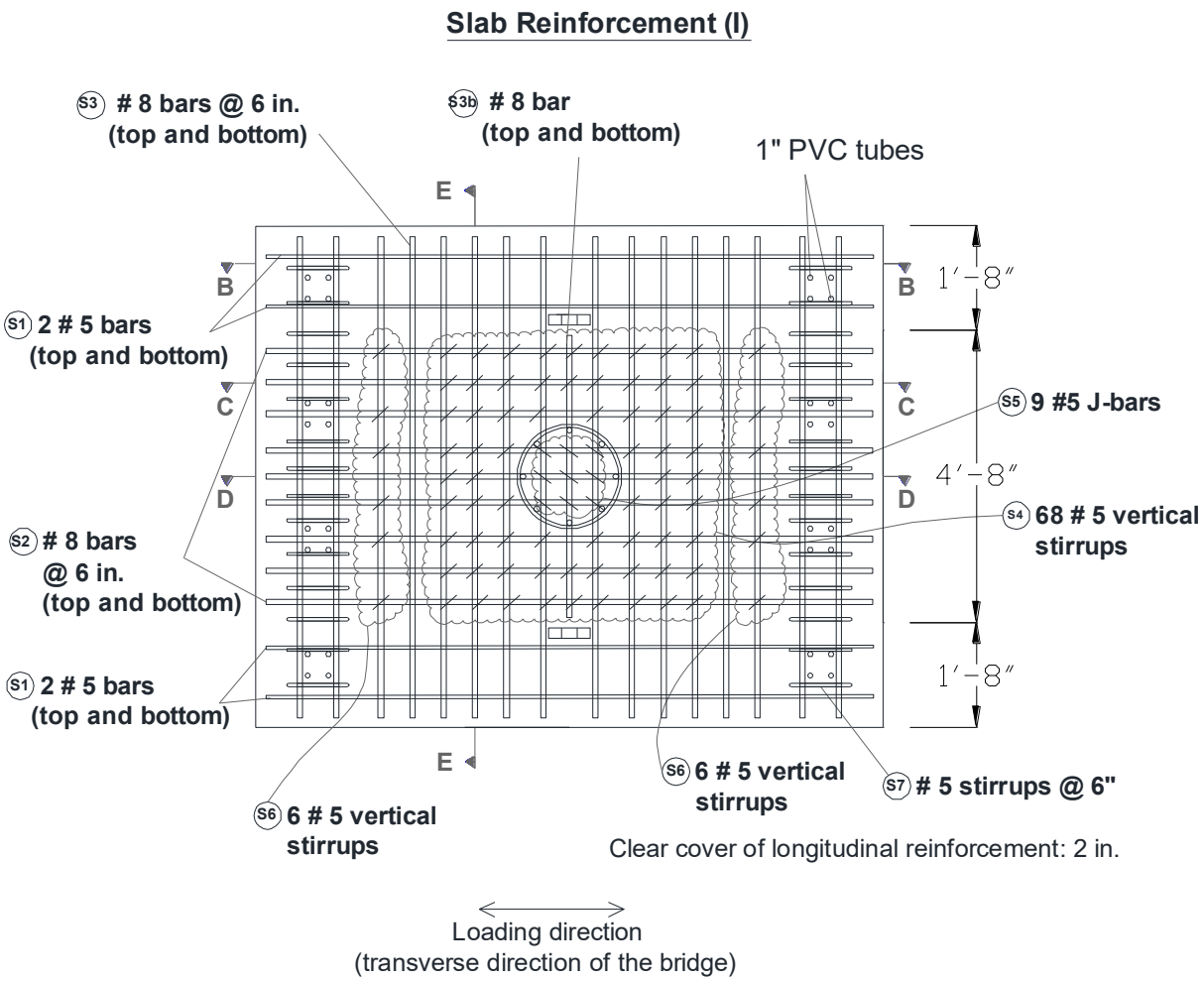

Figure A.2 – Plan view of slab reinforcement for Specimen #1

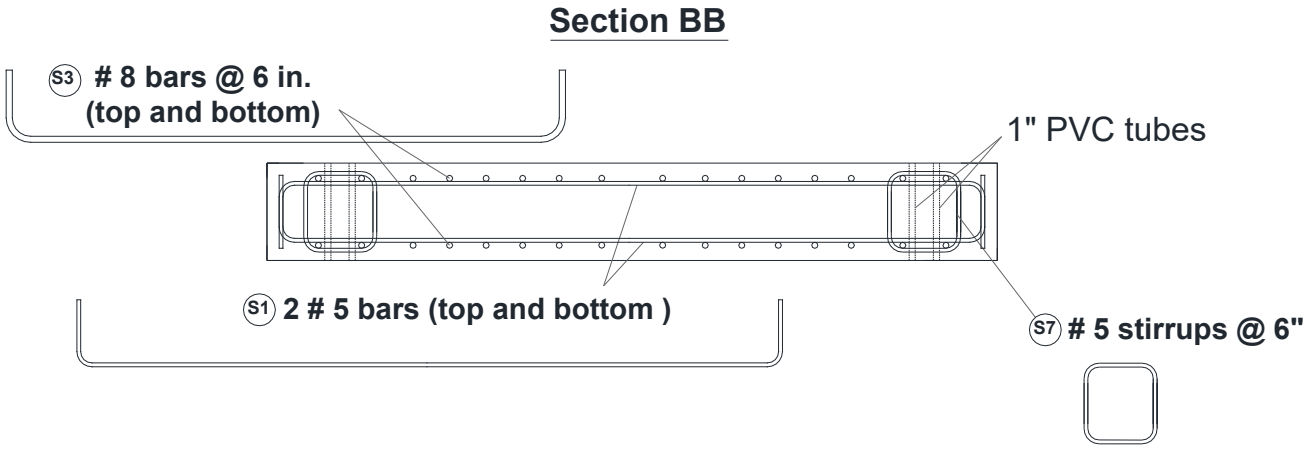

Figure A.3 – Elevation view of slab reinforcement at Section BB for Specimen #1

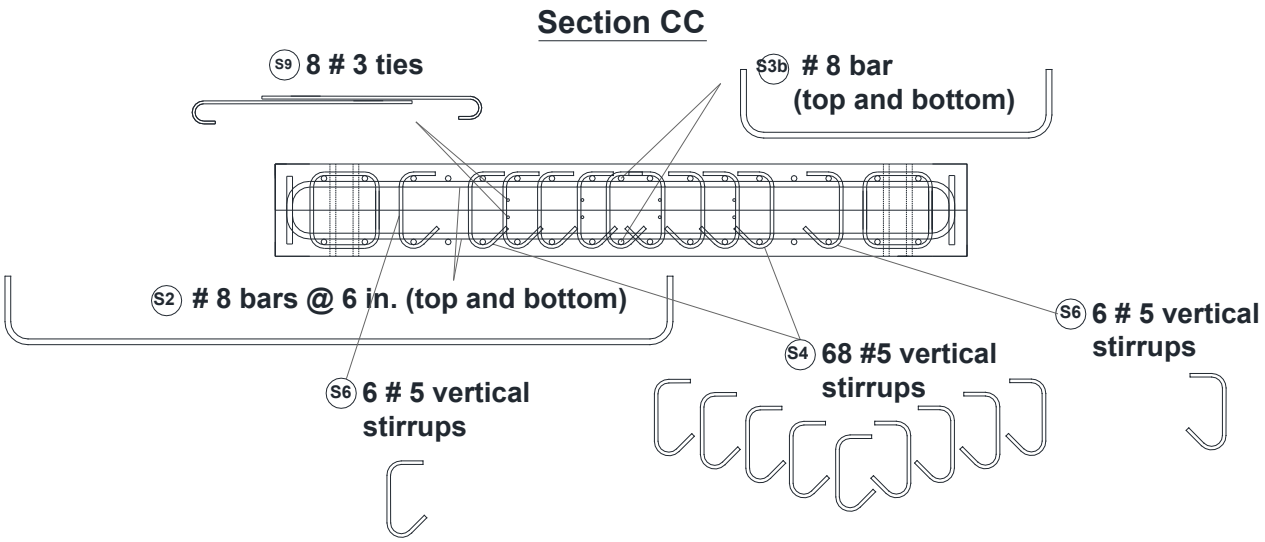

Figure A.4 – Elevation view of slab reinforcement at Section CC for Specimen #1

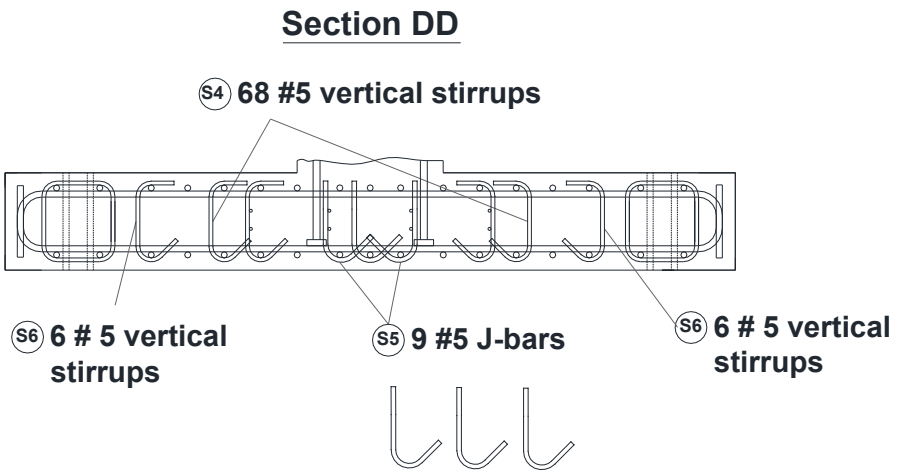

Figure A.5 – Elevation view of slab reinforcement at Section DD for Specimen #1

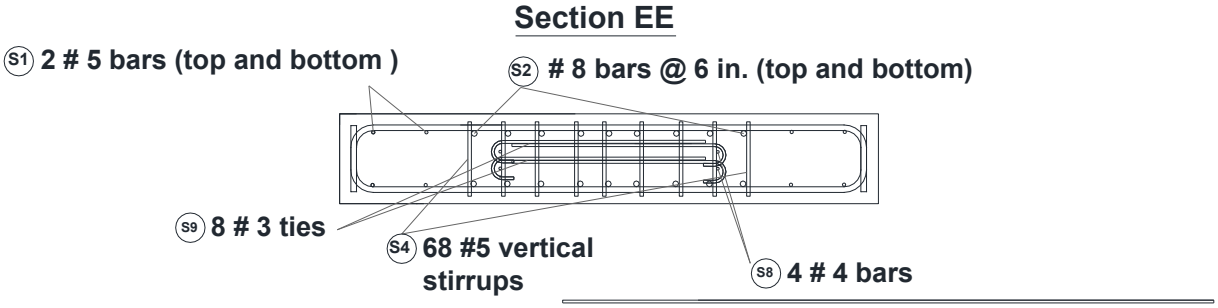

Figure A.6 – Elevation view of slab reinforcement at Section EE for Specimen #1

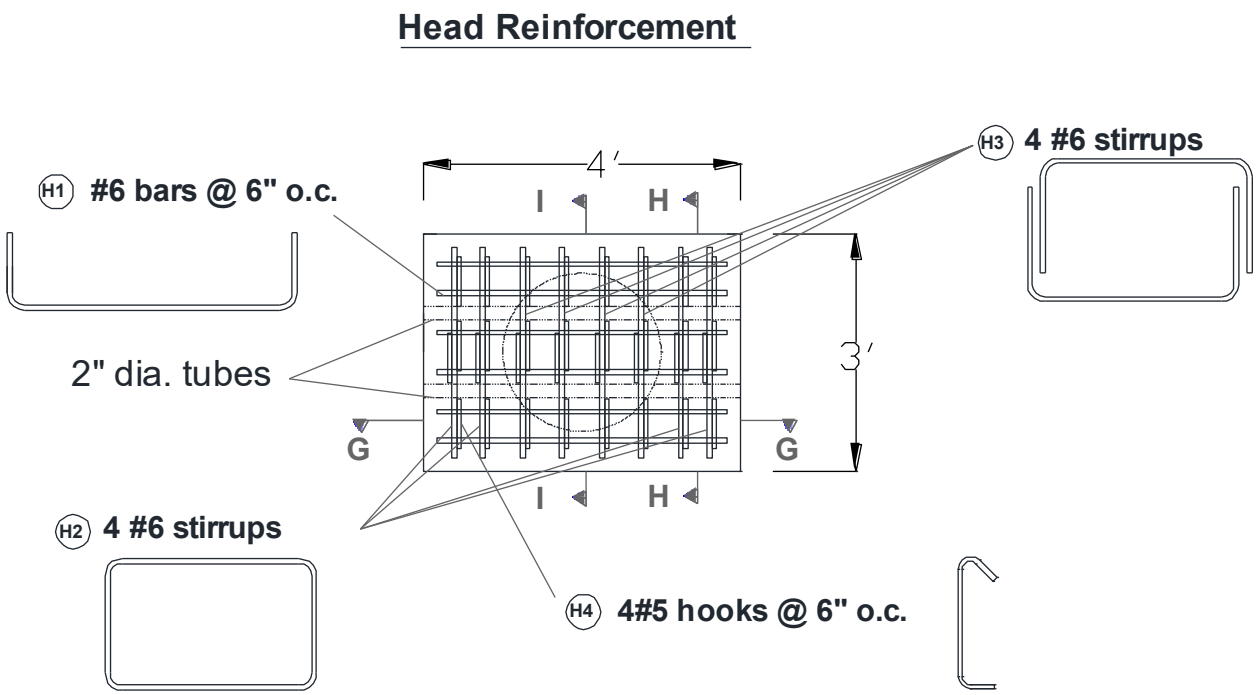

Figure A.7 – Plan view of head reinforcement for Specimen #1 (same for Specimens #2 and #3)

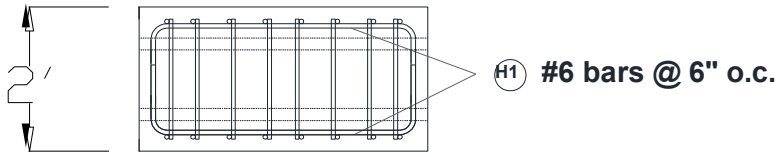

(a) Section GG

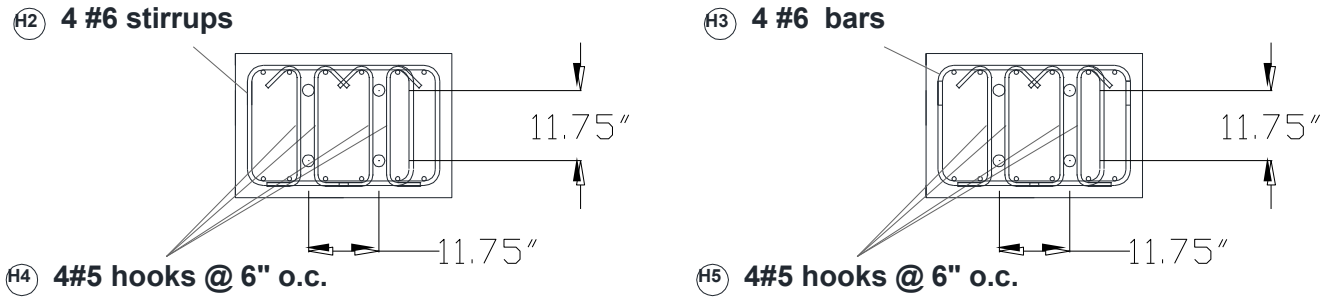

(b) Section HH (c) Section II

Figure A.8 – Elevation views of head reinforcement at different sections for Specimen #1 (same for Specimens #2 and #3)

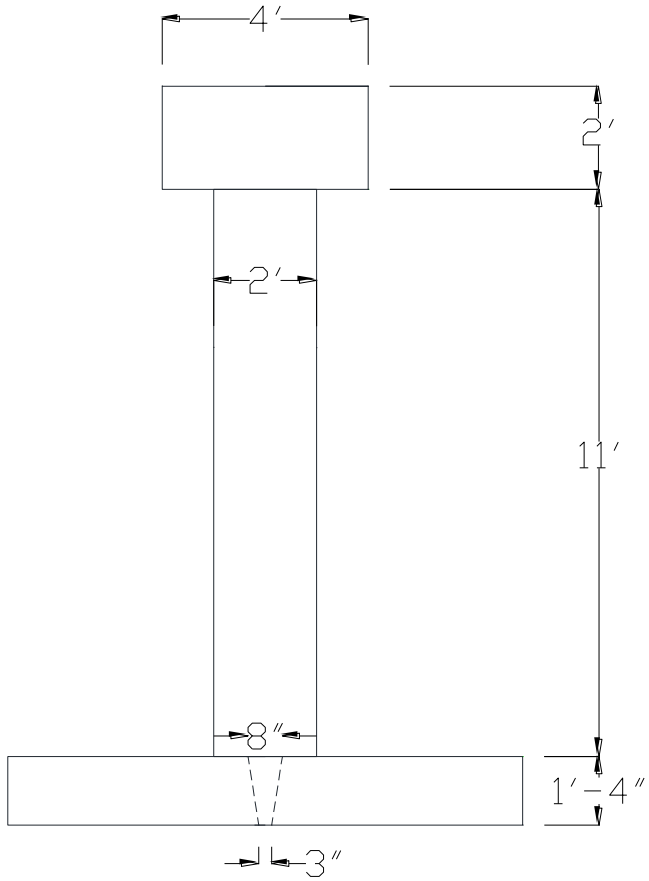

(a) Elevation view

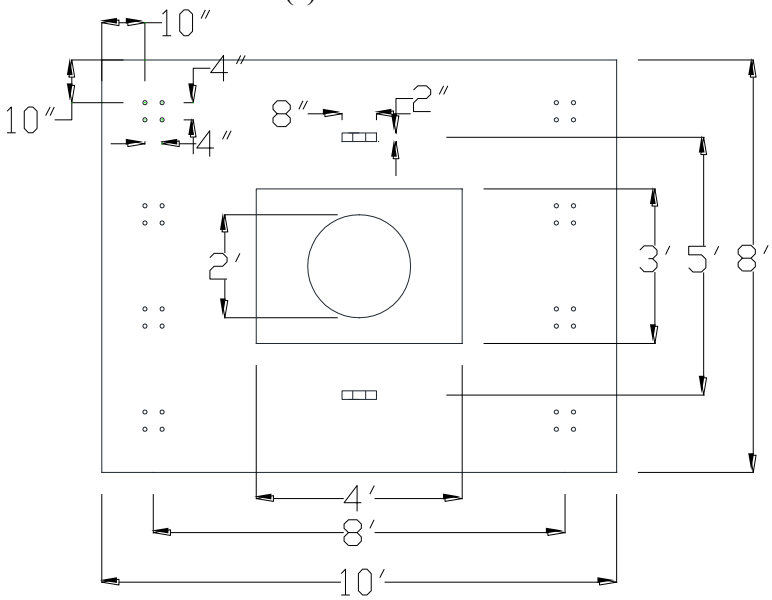

(b) Plan view

Figure A.9 – Plan and elevation views for Specimen #2

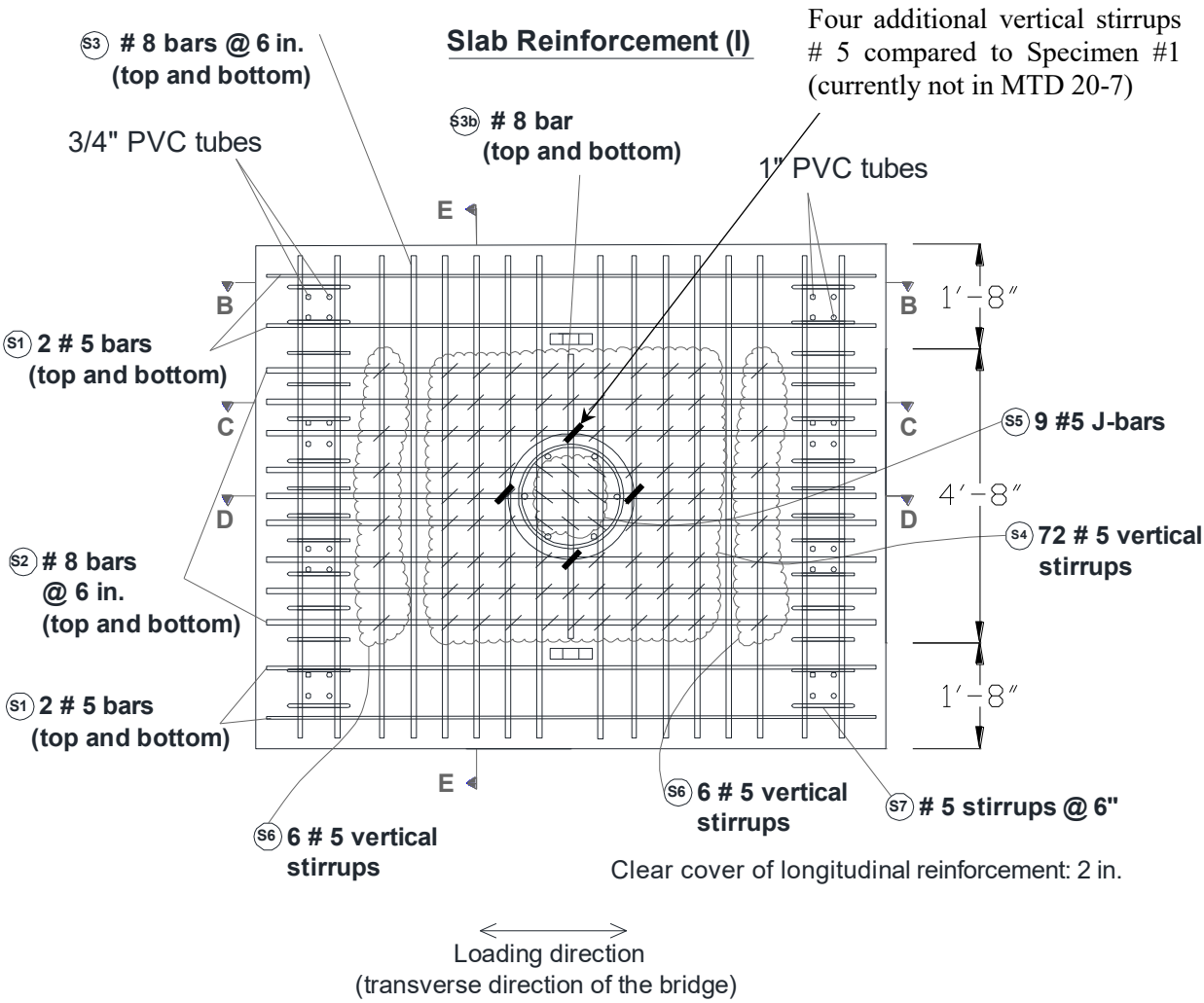

Figure A.10 – Plan view of slab reinforcement for Specimen #2

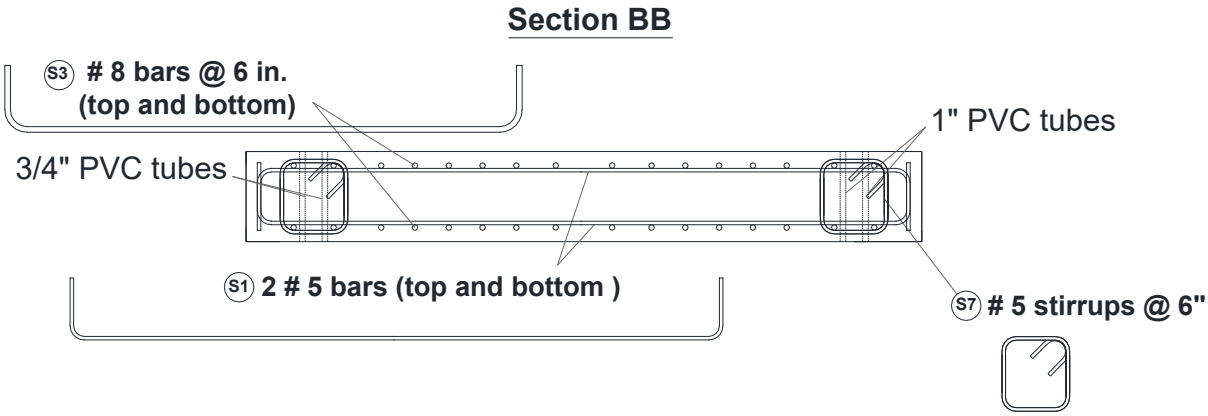

Figure A.11 – Elevation view of slab reinforcement at Section BB for Specimen #2

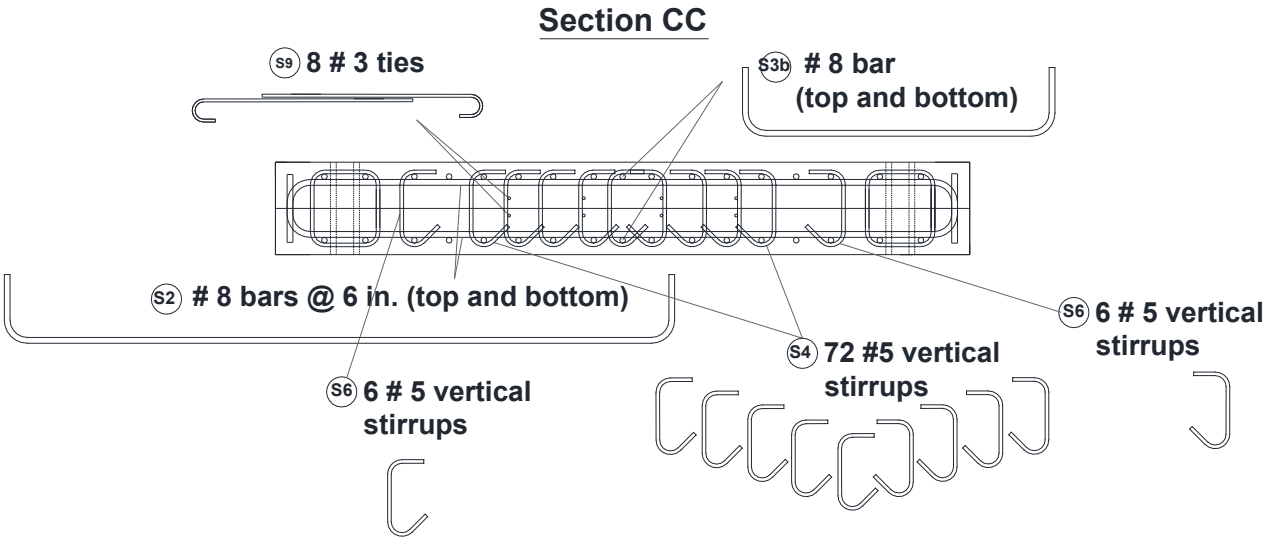

Figure A.12 – Elevation view of slab reinforcement at Section CC for Specimen #2

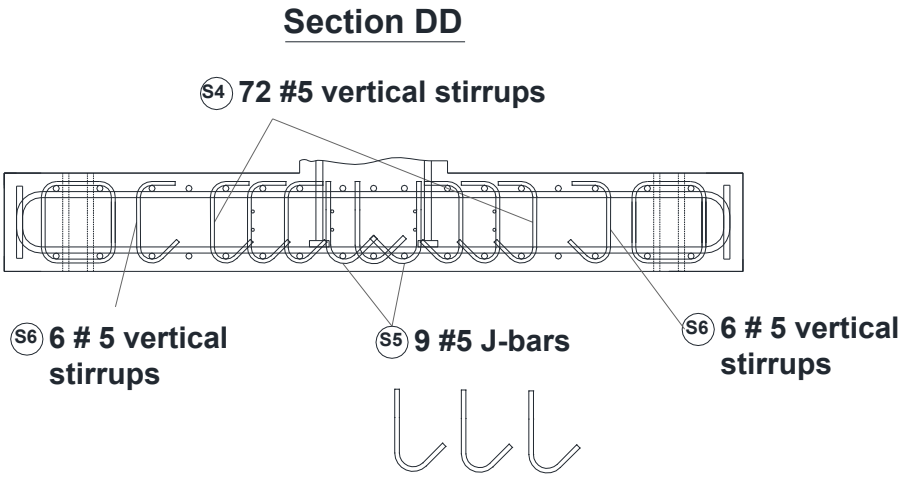

Figure A.13 – Elevation view of slab reinforcement at Section DD for Specimen #2

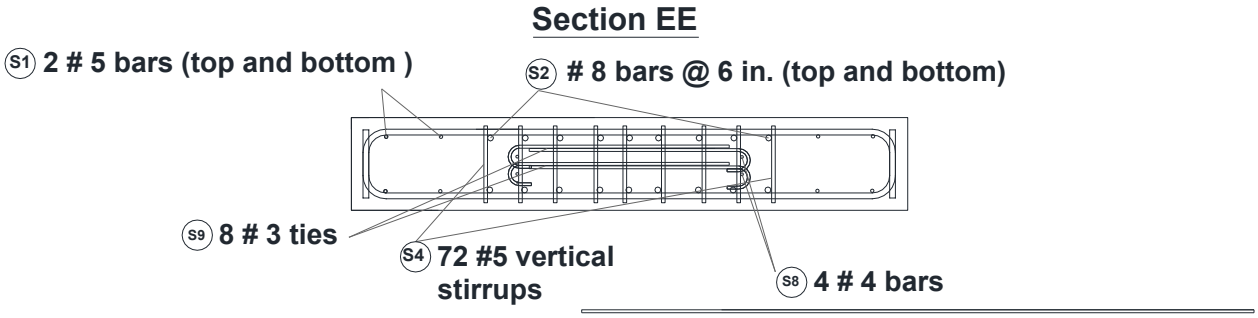

Figure A.14 – Elevation view of slab reinforcement at Section EE for Specimen #2

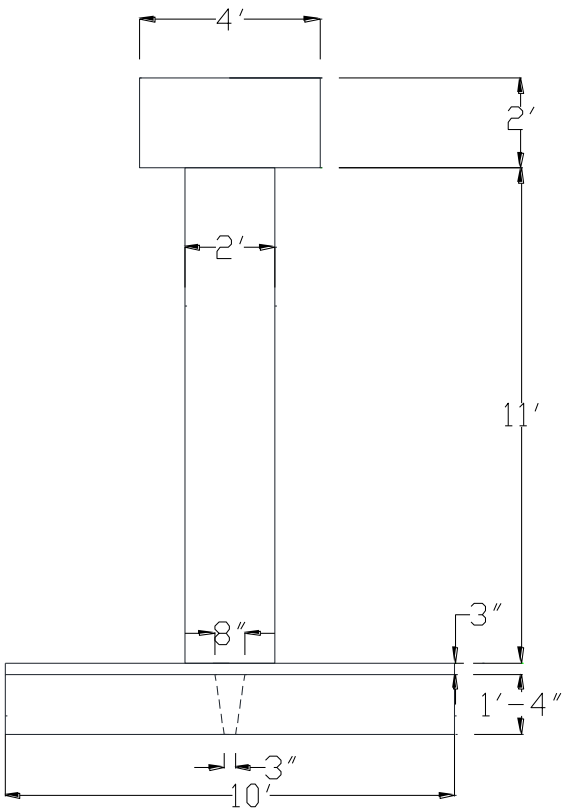

(a) Elevation view AA (east)

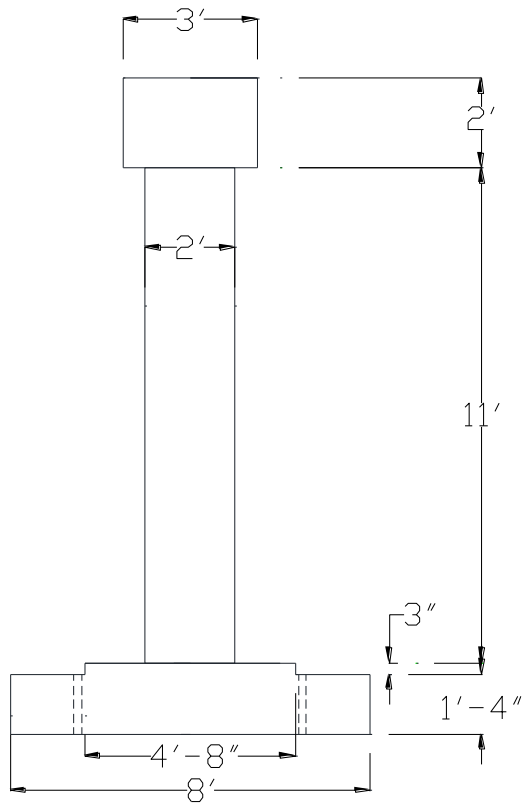

(b) Elevation view BB (south)

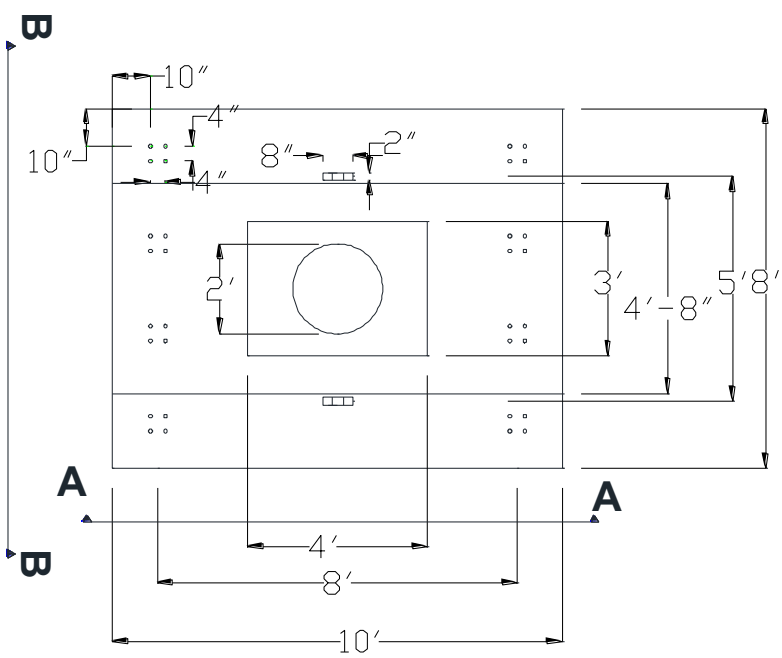

(c) plan view

Figure A.15 – Plan and elevation views for Specimen #3

Column Reinforcement

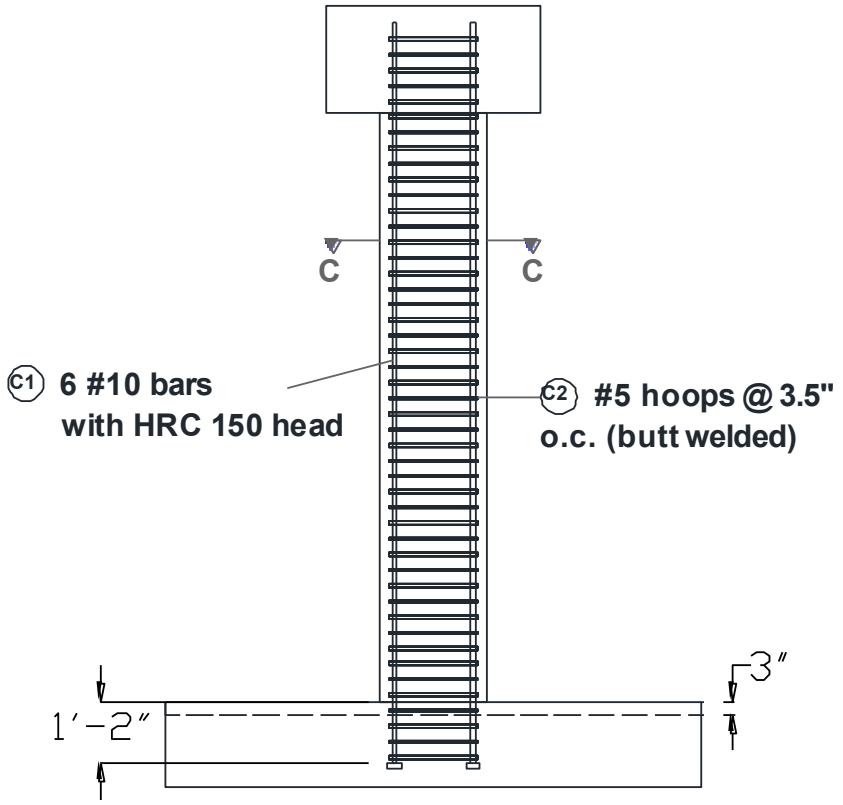

Section CC

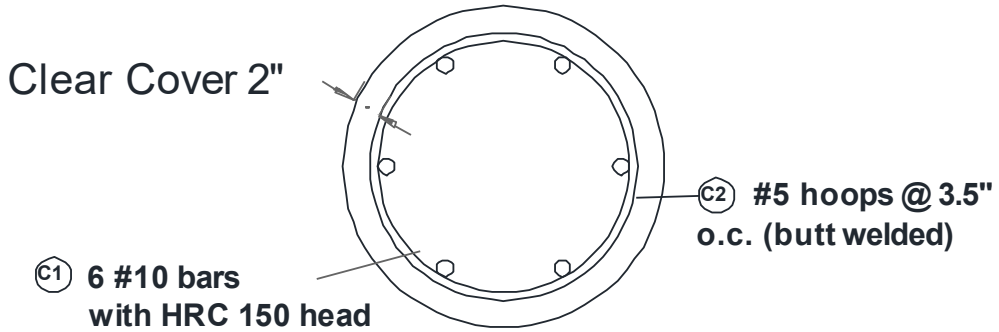

Figure A.16 – Column reinforcement for Specimen #3

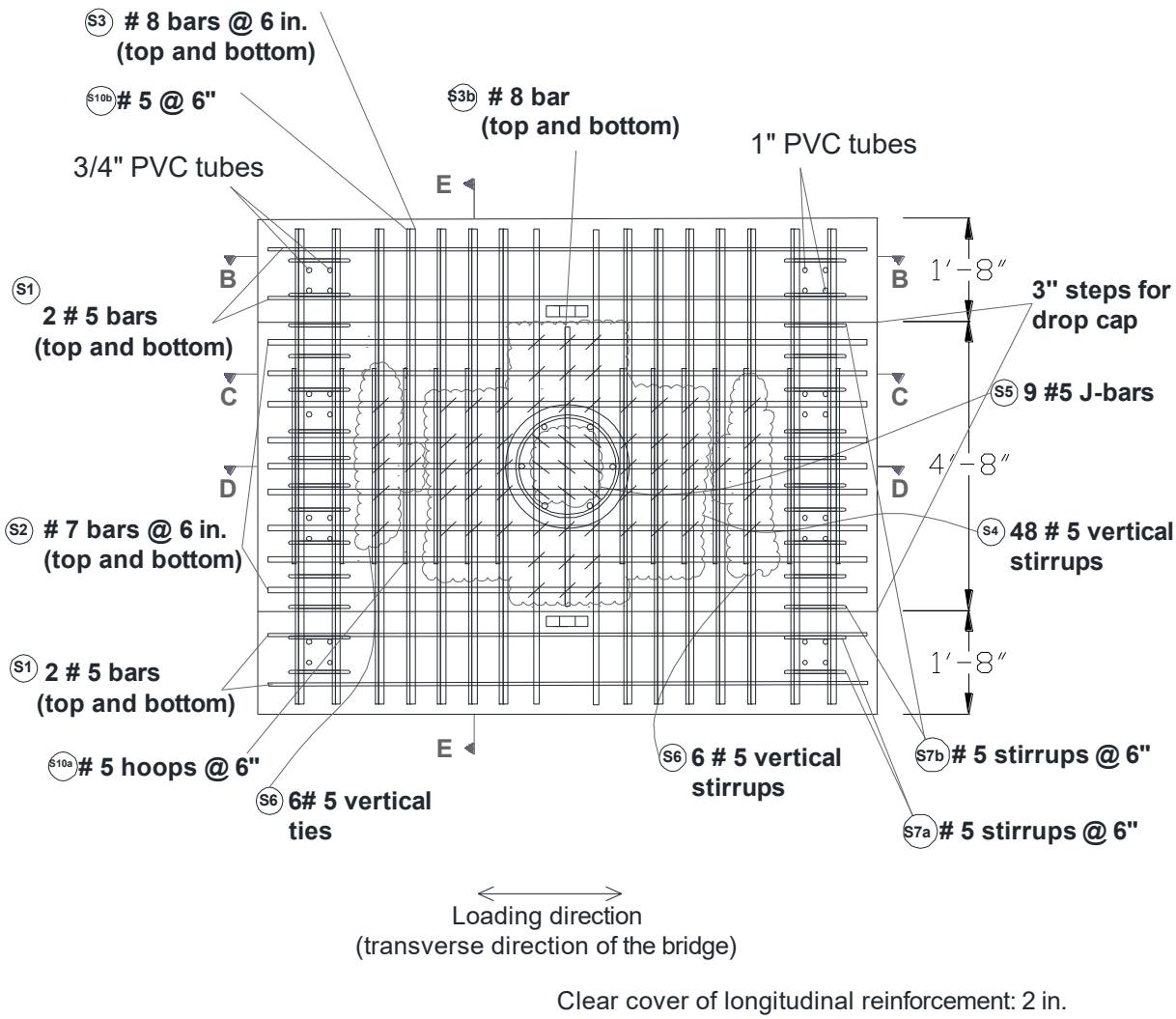

Clear cover of longitudinal reinforcement: 2 in.

Figure A.17 – Plan view of slab reinforcement for Specimen #3

Section BB

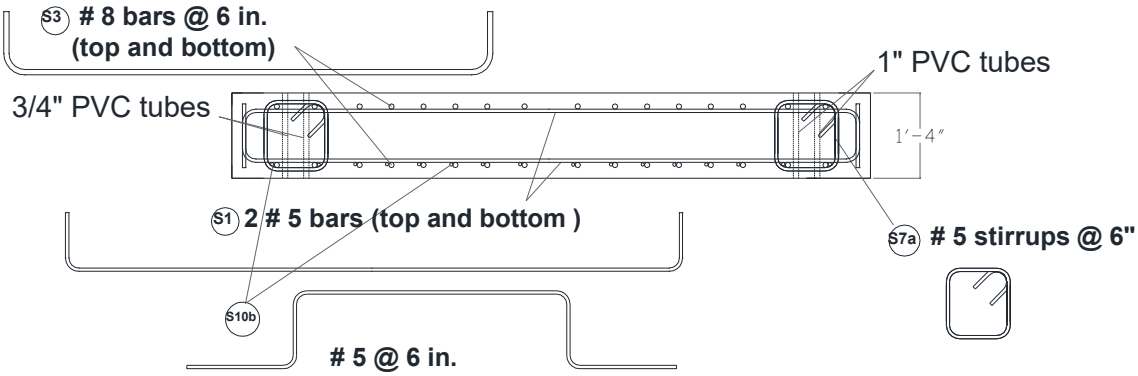

Figure A.18 – Elevation view of slab reinforcement at Section BB for Specimen #3

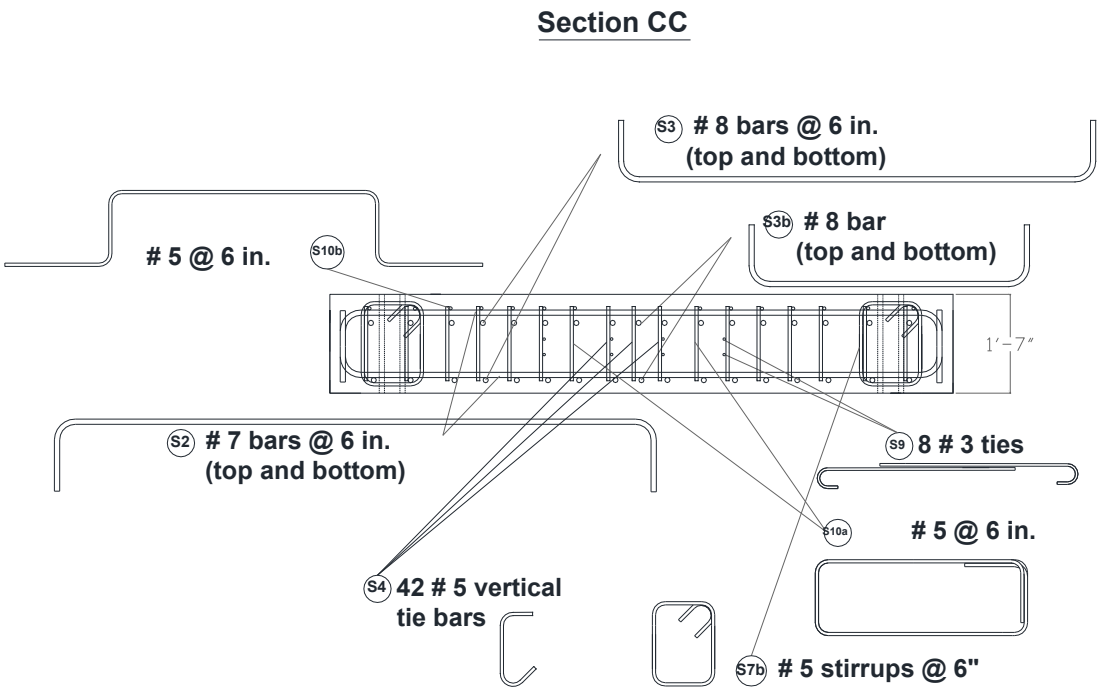

Figure A.19 – Elevation view of slab reinforcement at Section CC for Specimen #3

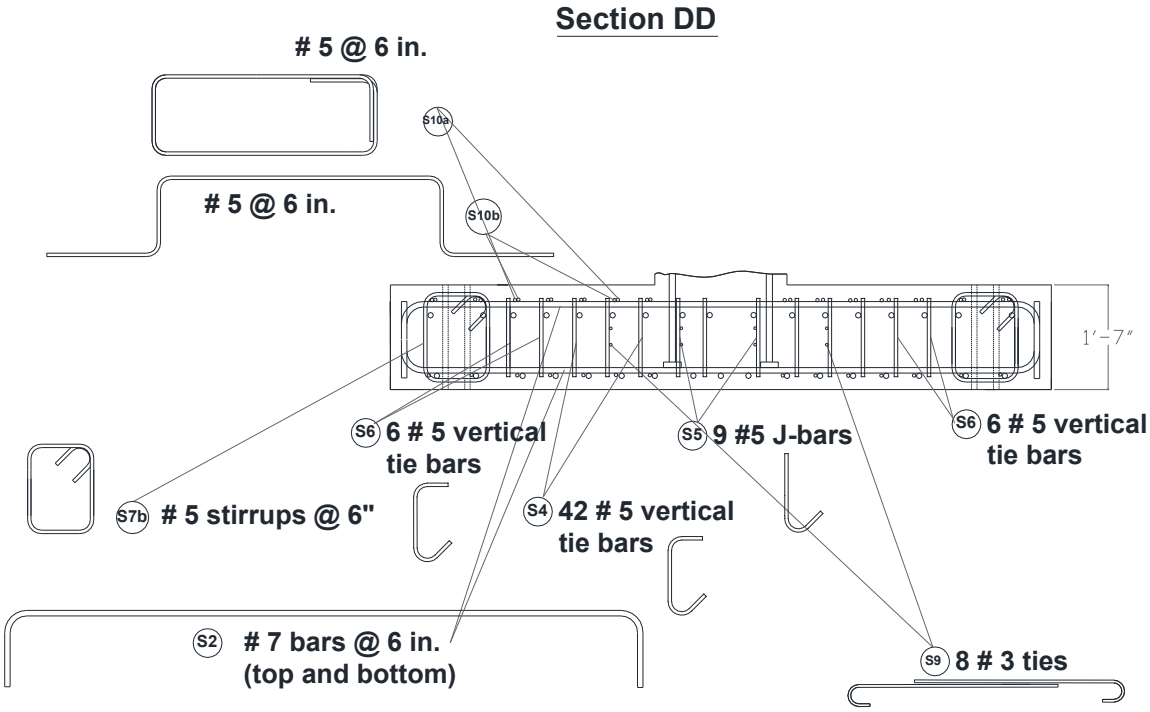

Figure A.20 – Elevation view of slab reinforcement at Section DD for Specimen #3

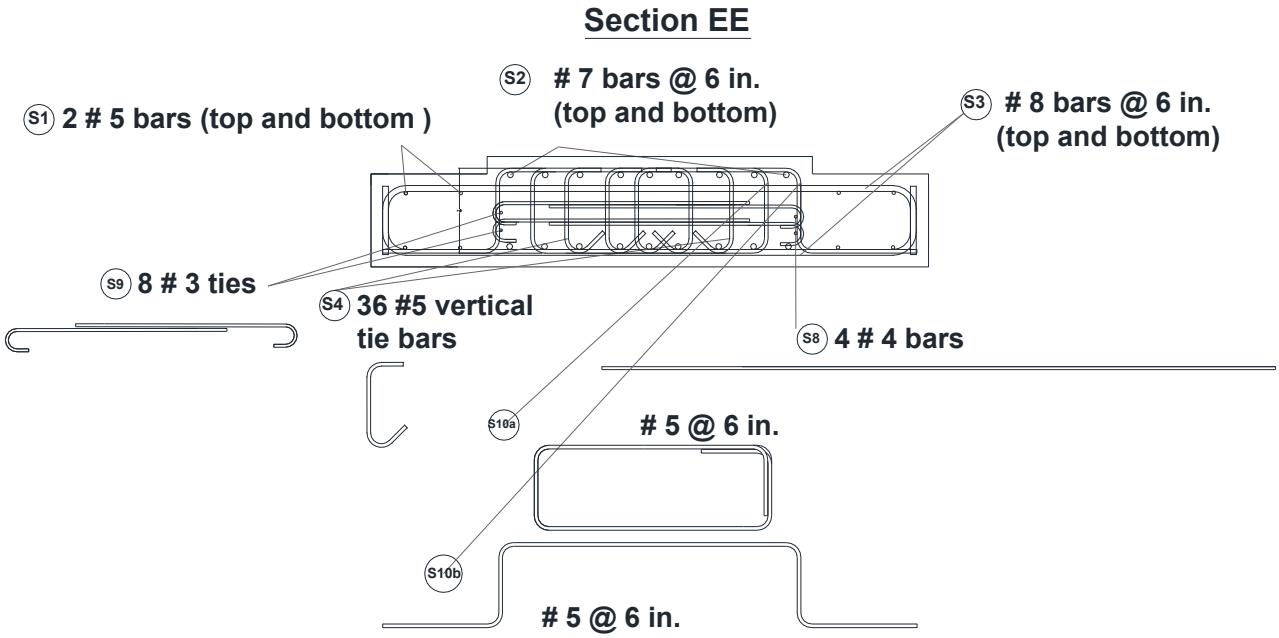

Figure A.21 – Elevation view of slab reinforcement at Section EE for Specimen #3

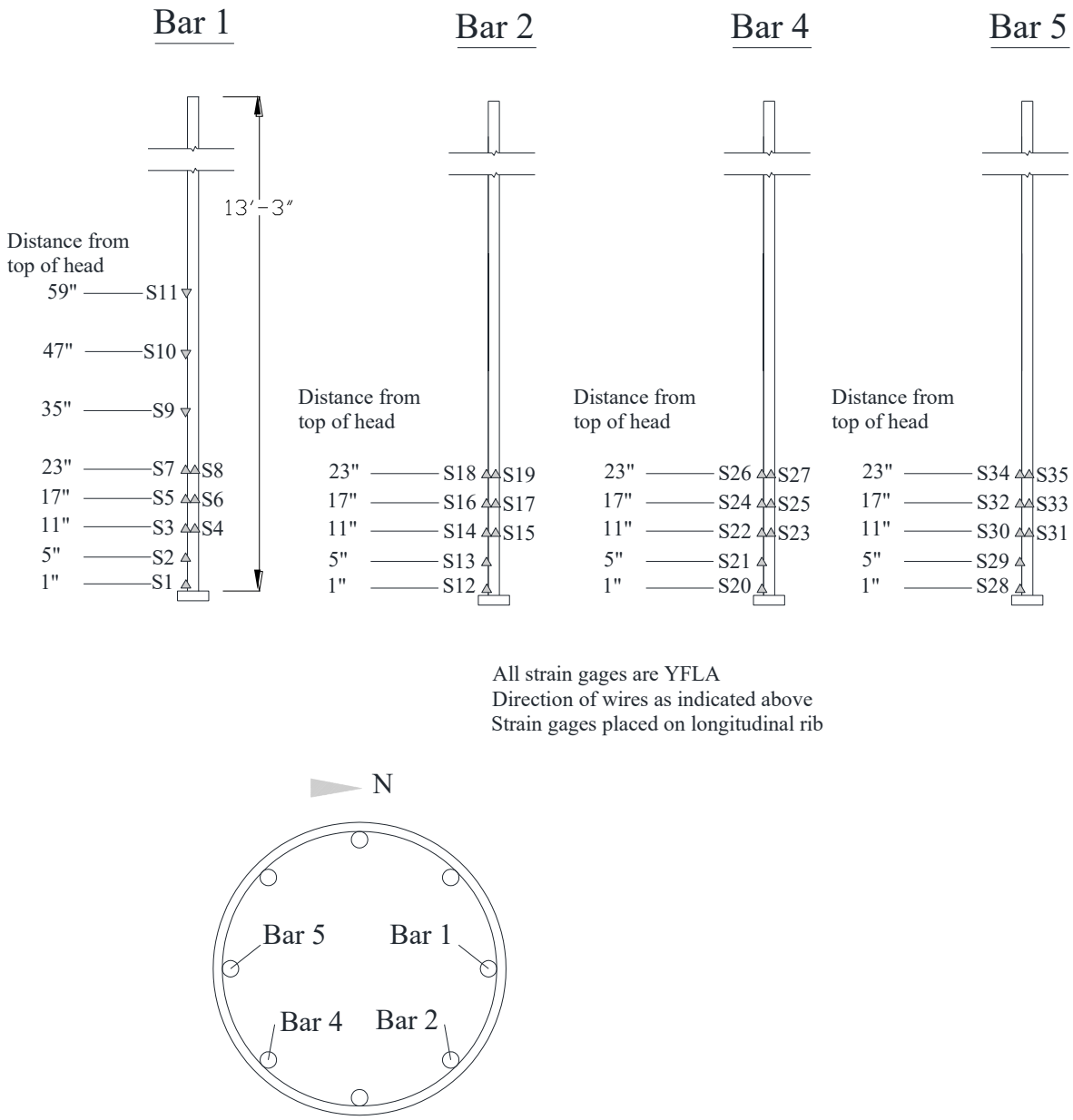

Figure A.22 – Strain gages on longitudinal bars in the column of Specimen #1

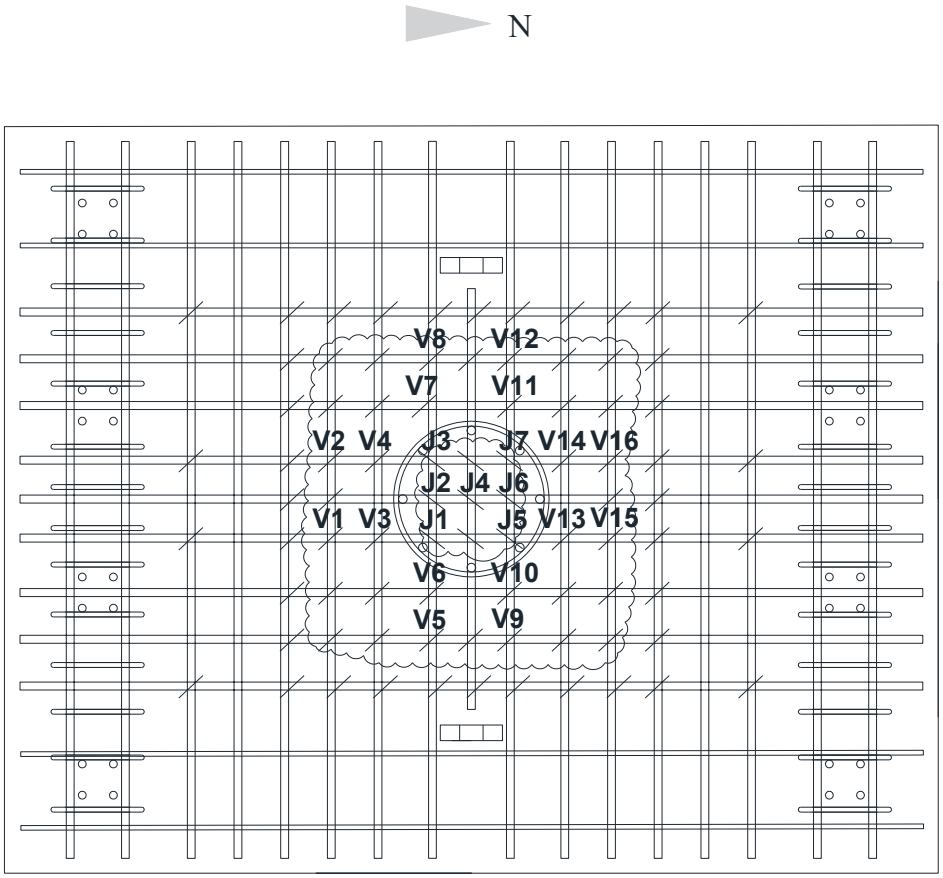

7 No. 5 J-bars instrumented

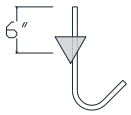

16 No. 5 vertical stirrups instrumented

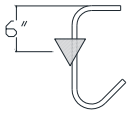

Figure A.23 – Strain gages on J-bars and vertical stirrups in the slab of Specimen #1

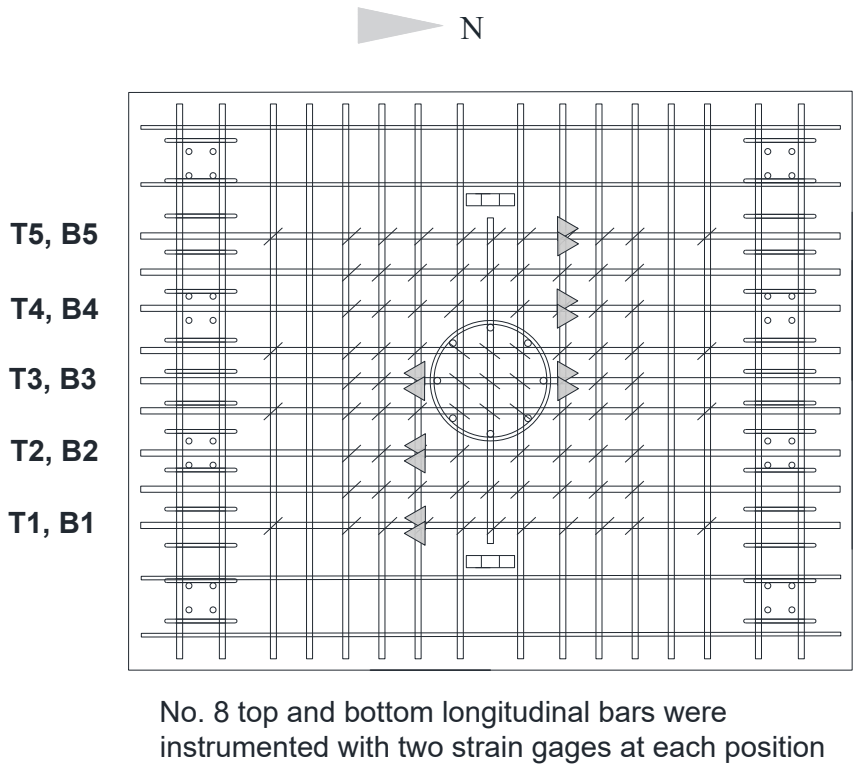

Figure A.24 – Strain gages on the longitudinal bars in the slab of Specimen #1

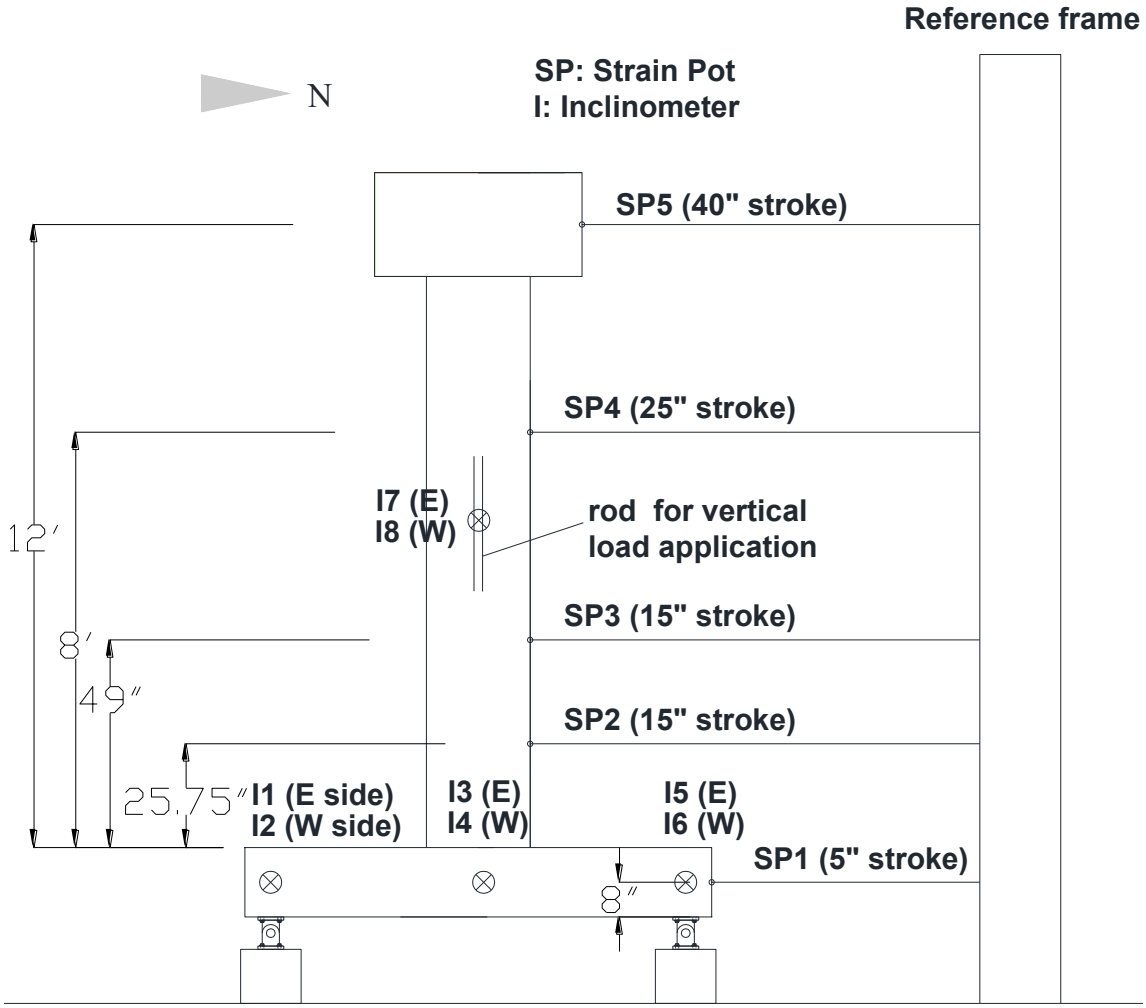

Figure A.25 – Strain pots and inclinometers mounted on Specimens #1

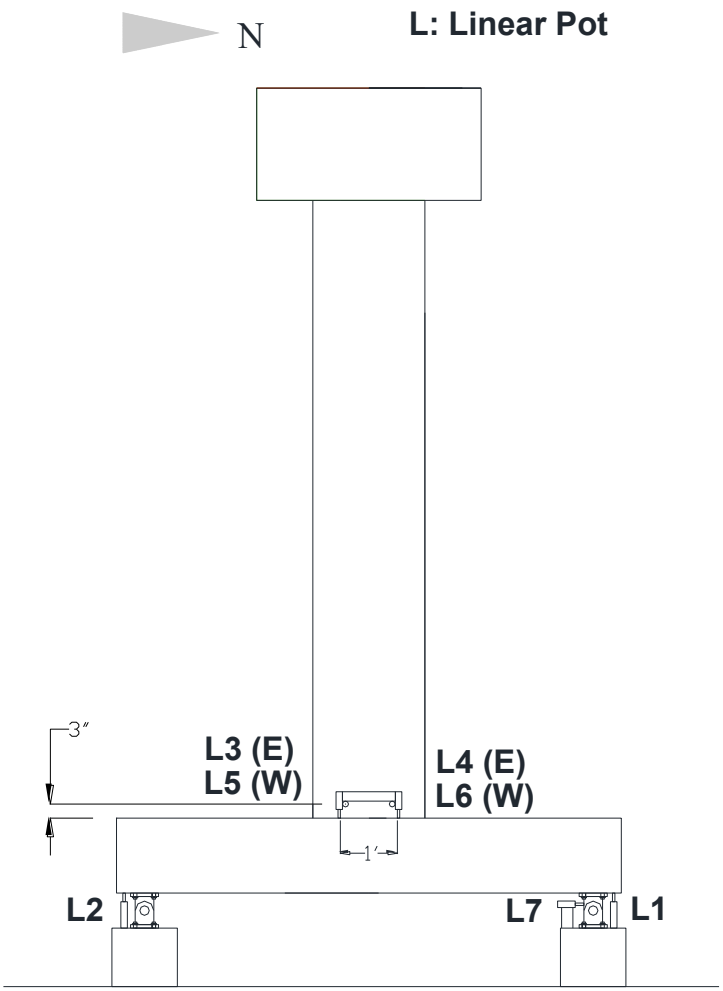

Figure A.26 – Linear pots mounted on Specimen #1

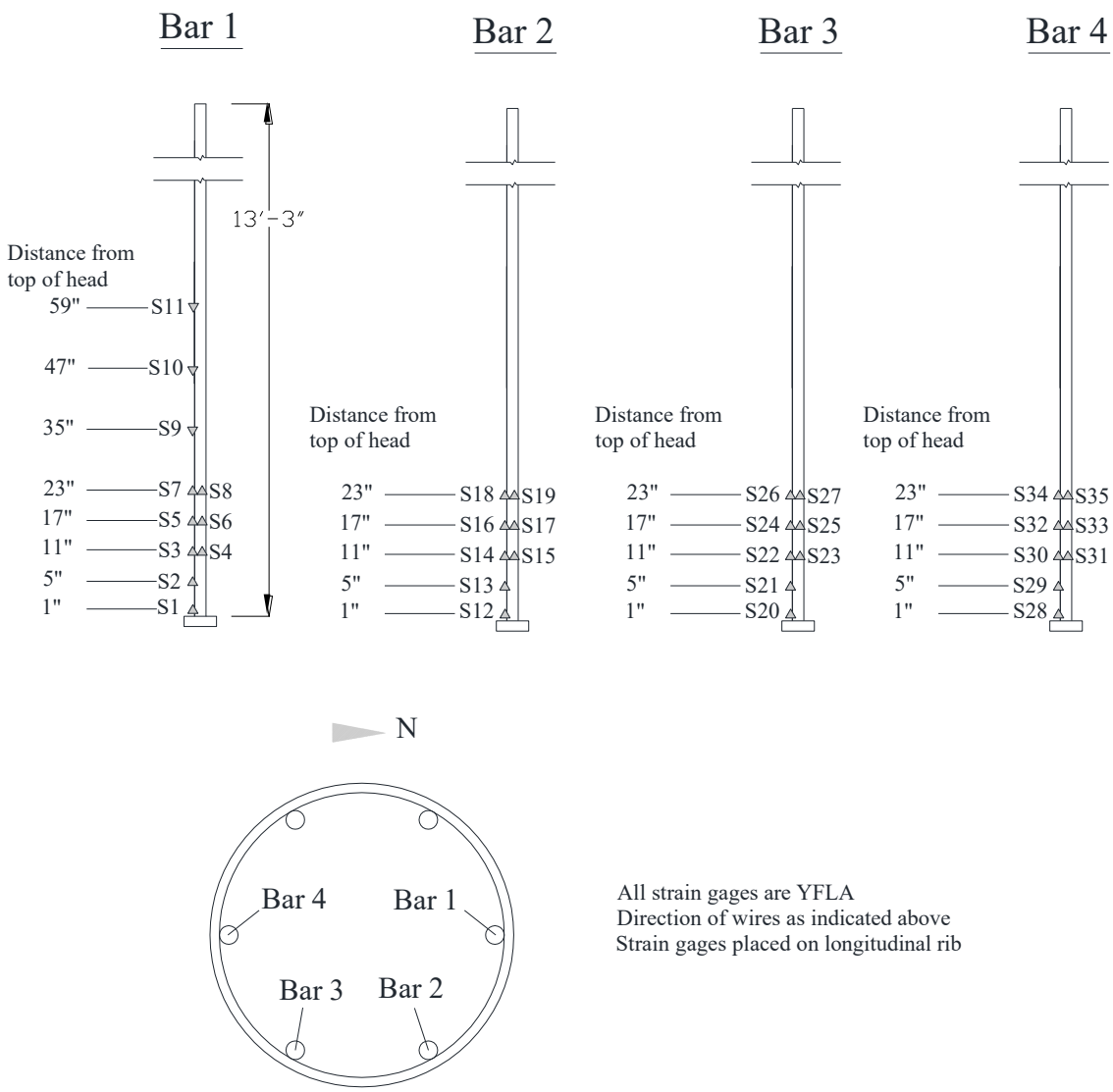

Figure A.27 – Strain gages on longitudinal bars in the column of Specimen #2

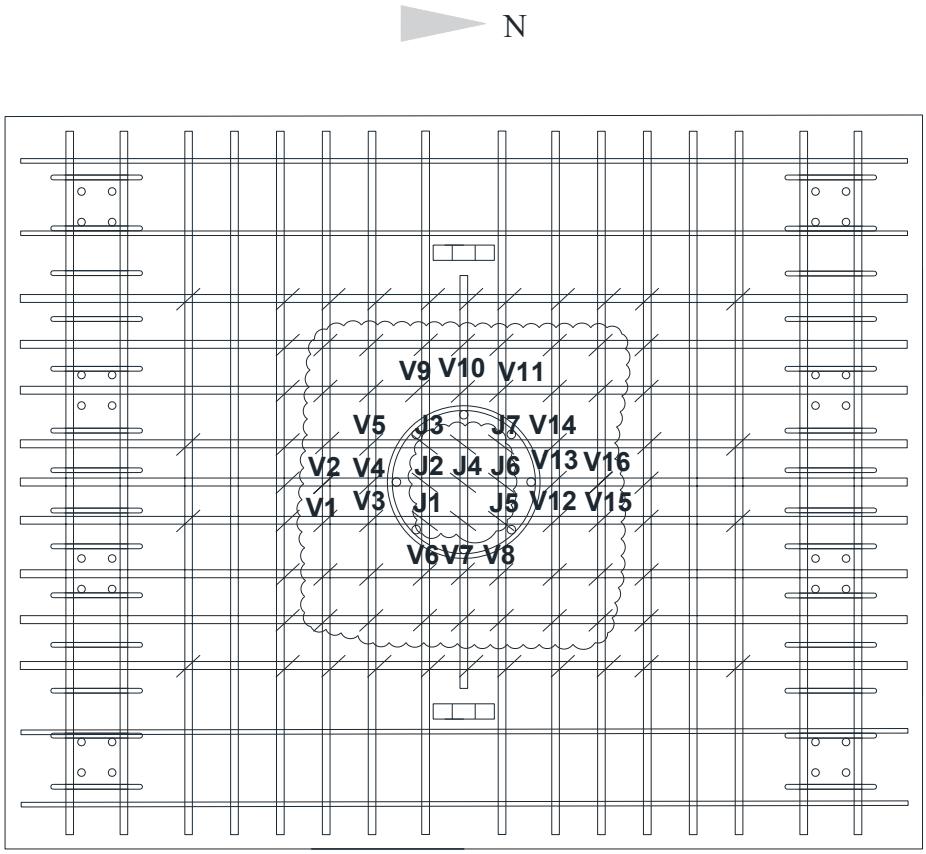

7 No. 5 J-bars instrumented

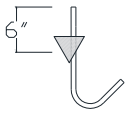

16 No. 5 vertical ties instrumented

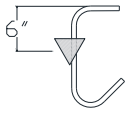

Figure A.28 – Strain gages on J-bars and vertical stirrups in the slab of Specimen #2

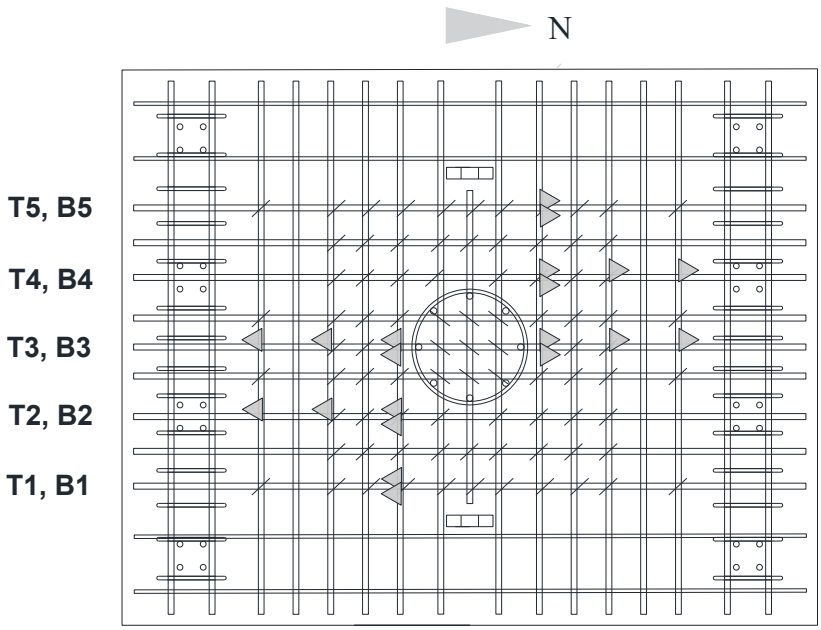

No. 8 top and bottom longitudinal bars were instrumented

Figure A.29 – Strain gages on the longitudinal bars in the slab of Specimen #2

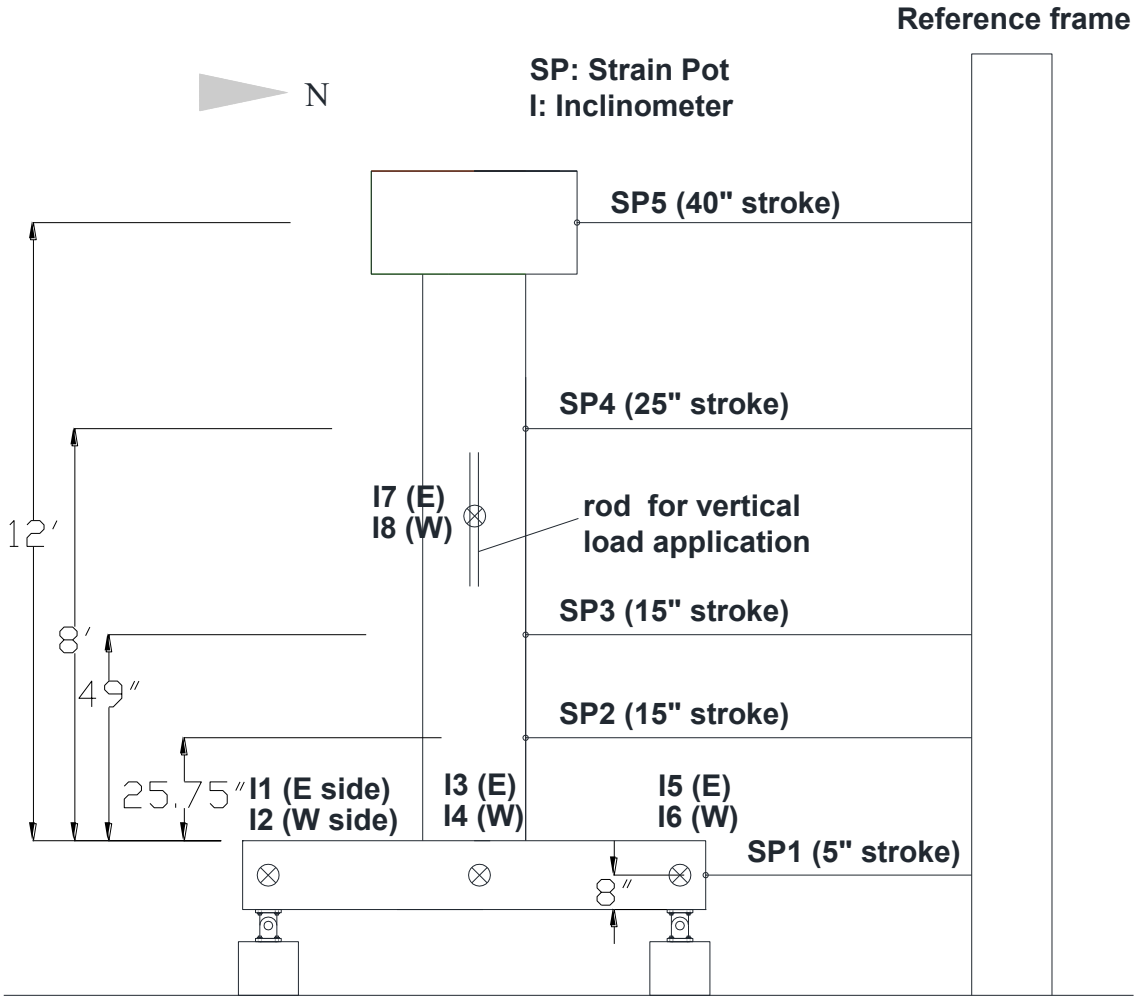

Figure A.30 – Strain pots and inclinometers mounted on Specimens #2

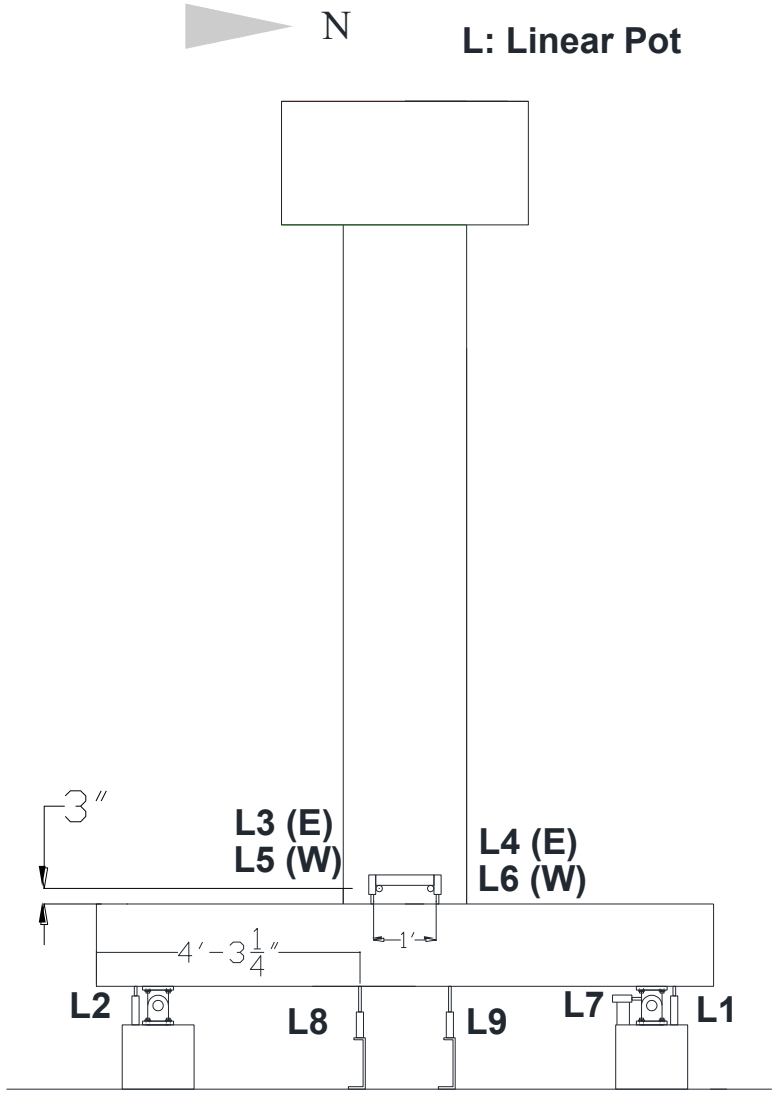

Figure A.31 – Linear pots mounted on Specimen #2

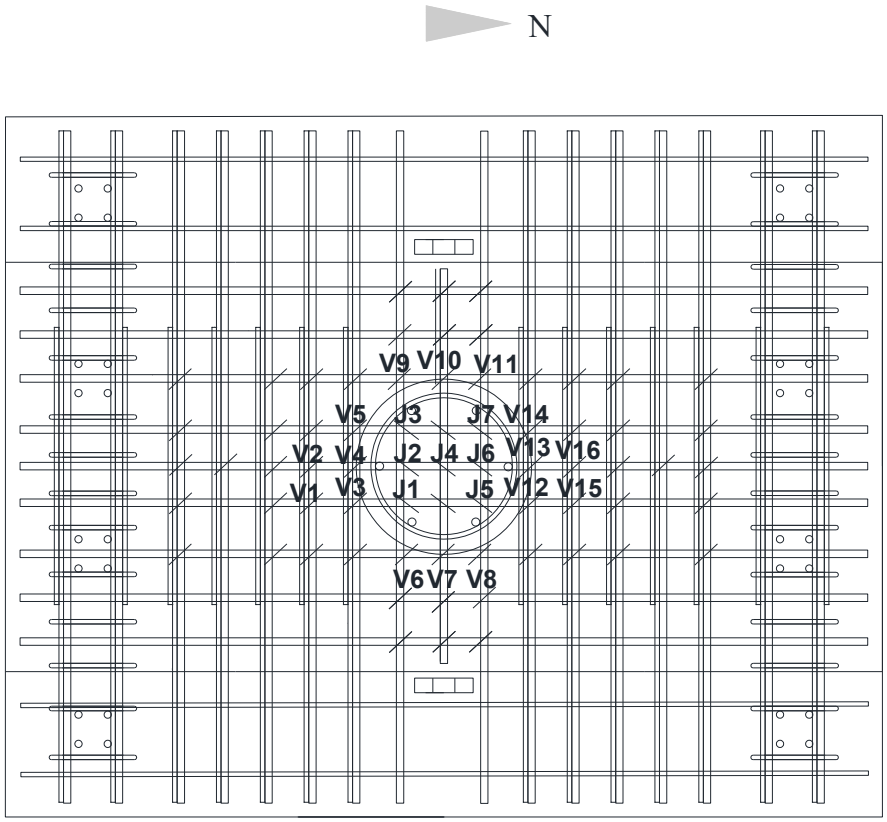

7 No. 5 J-bars instrumented

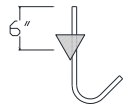

16 No. 5 vertical ties instrumented

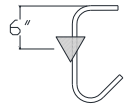

Figure A.32 – Strain gages on J-bars and vertical stirrups in the slab of Specimen #3

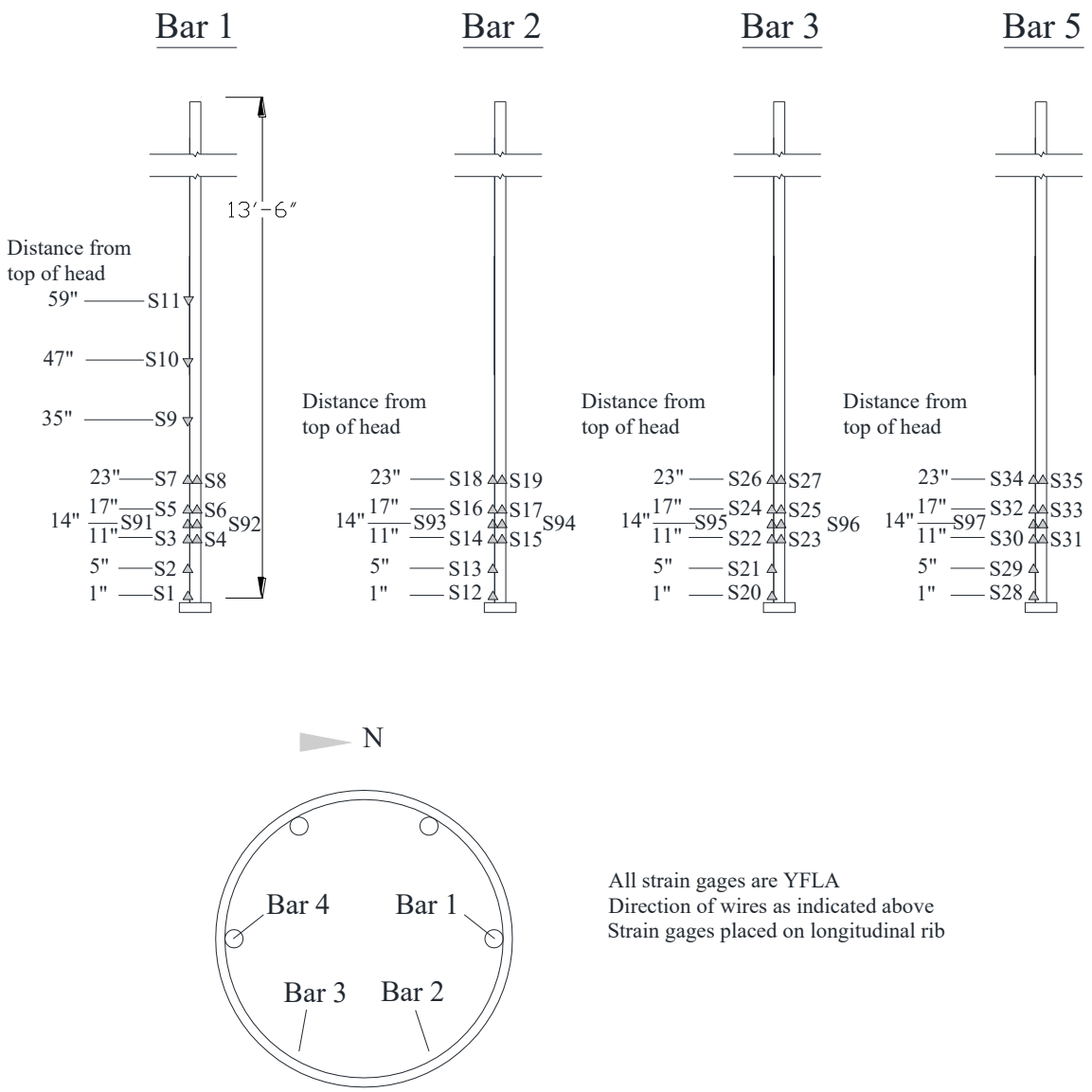

Figure A.33 – Strain gages on longitudinal bars in the column of Specimen #3

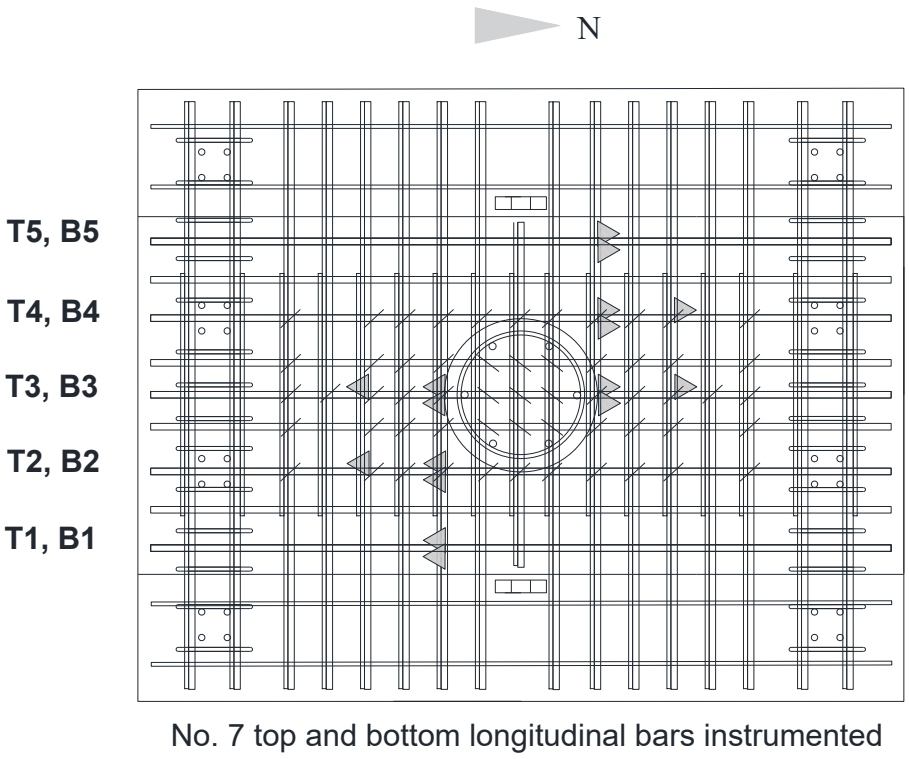

Figure A.34 – Strain gages on the longitudinal bars in the slab of Specimen #3

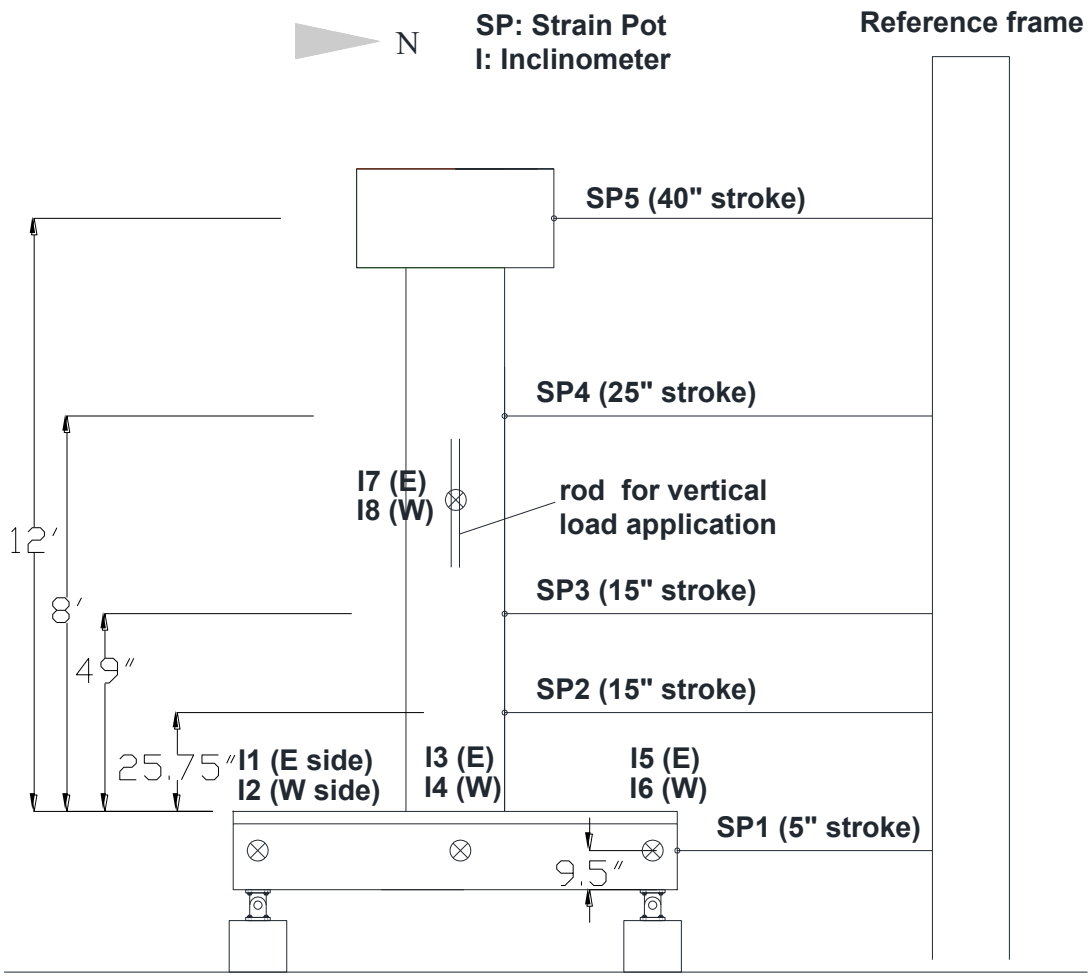

Figure A.35 – Strain pots and inclinometers mounted on Specimen #3

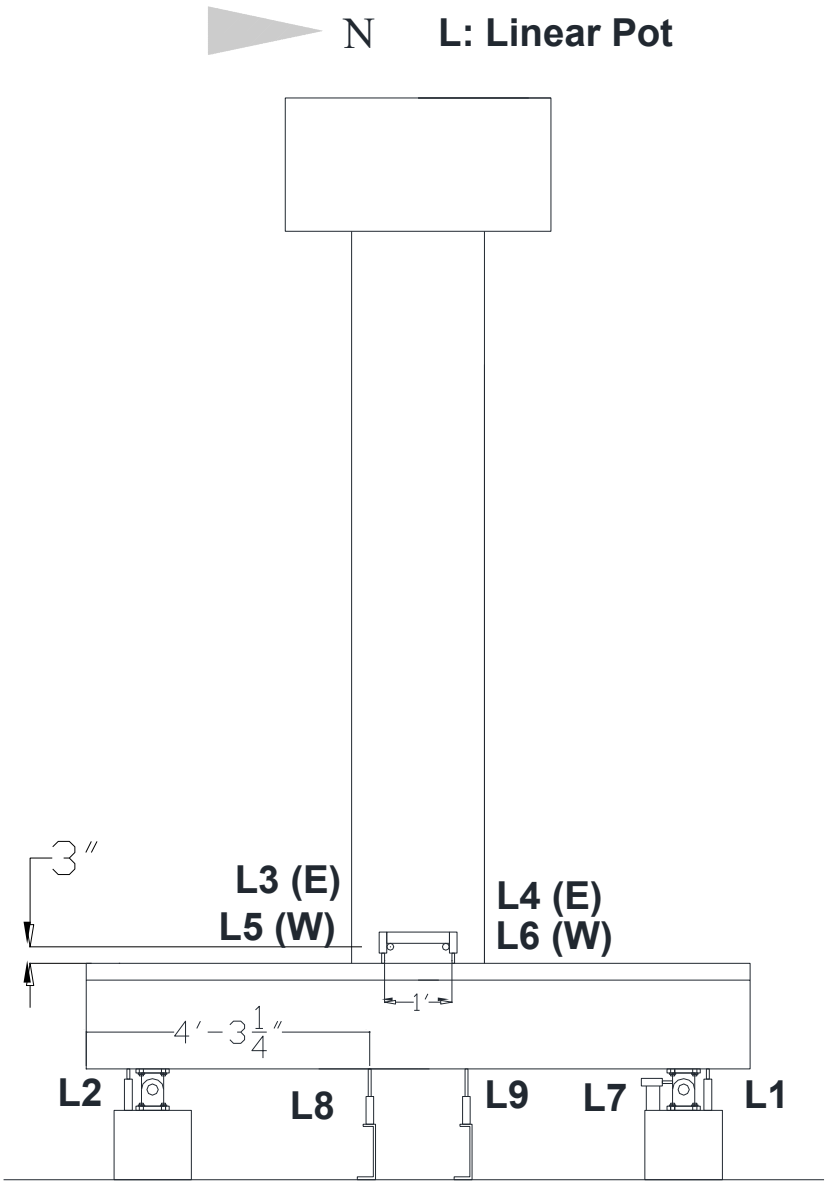

Figure A.36 – Linear pots mounted on Specimen #3.

REFERENCES

ACI (2011), *Building Code Requirements for Structural Concrete (ACI 318-11)*. American Concrete Institute, Farmington Hills, MI.

AASHTO (2014), *AASHTO LRFD Bridge Design Specifications*. American Association of State Highway and Transportation Officials, Washington, DC.

Ayoub, M. and Sanders, D. (2010), "Behavior of Pile Extension Connections to Slab Bridges under Cyclic Loafing." *UNR Report No. CCER 10-06*, Center for Earthquake Engineering Research, Department of Civil and Environmental Engineering, University of Nevada, Reno, NV.

Bashandy, T.R. (1996), "Application of Headed Bars in Concrete Members." *PhD Dissertation*, University of Texas, Austin, TX.

Caltrans (2009), "Design of Standard Slab Bridge." *Bridge Design Aids (BDA) 4-10*, California Department of Transportation, Sacramento, CA.

Caltrans (2013), *Caltrans Seismic Design Criteria*. Version 1.6, California Department of Transportation.

Caltrans (2013), "Seismic Requirements of Head Reinforcement." *Memo to Designers (MTD) 20-19 (Draft)*, California Department of Transportation, Sacramento, CA.

Caltrans (2014), "Seismic Design of Slab Bridges." *Memo to Designers (MTD) 20-7*, California Department of Transportation, Sacramento, CA.

Choi, D.-U., Hong, S.-G., Lee, and C.-Y. (2002), "Test of Headed Reinforcement in Pullout," *ACI Concrete Journal*, Vol. 14, No. 3, pp.102-110.

De Vries, R.A. (1996), "Anchorage of Headed Reinforcement in Concrete." *Ph.D. Dissertation*, University of Texas, Austin, TX.

De Vries, R.A., Jirsa, J.O., and Bashandy, T. (1999), "Anchorage Capacity in Concrete of Headed Reinforcement with Shallow Embedments." *ACI Structural Journal*, Vol. 96(5), pp. 728-736.

Drucker, D. C., and Prager W. (1952), "Soil Mechanics and Plastic Analysis or Limit Design." Quarterly of Applied Mathematics, vol. 10, pp. 157-165.

Eligehausen, R. and Balogh, T. (1995), "Behavior of Fasteners Loaded in Tension in Cracked Reinforced Concrete." *ACI Structural Journal*, Vol. 92(3), pp. 365-379.

Fuchs, W., Eligehausen, R., and Breen, J.E. (1995), "Concrete Capacity Design (CCD) Approach for Fastening to Concrete." *ACI Structural Journal*, Vol. 92(1), pp. 73-94.

Kang.T.H.-K., Ha, S.-S., and Choi,D.-U. (2010), "Bar Pullout Tests and Seismic Tests of Small-Headed Bars in Beam-Column Joints," ACI Structural Journal, V. 107, No. 1, pp. 32-42.

Murcia-Delso, J., and Shing, P. B. (2015), "Bond-Slip Model for Detailed Finite-Element Analysis of Reinforced Concrete Structures", *J. Struct. Eng.*, 141(4), 04014125.

Papadopoulos, V., Shing, P. B. (2015), "Influence of the Spacing of Longitudinal Reinforcement on the Performance of Laterally Loaded CIDH Piles – Analytical Investigation", *Report No. SSRP-15/07*, University of California, San Diego.

Simulia (2010), ABAQUS V. 6.10, Dassault Systems Simulia Corp., Providence, RI.

Stoker, J.R., Boulware, R.L., Crozier, W.F., and Swirsky, R.A. (1974), "Anchorage Devices for Large Diameter Bars." CA-DOT-TL-6626-1-73-30, Transportation Laboratory, California Division of Highways, Sacramento, CA.

Thompson, M.K., Jirsa, J.O., Breen, J.E., and Klingner, R.E. (2002), "Anchorage Behavior of Headed Reinforcement: Literature Review." *Research Report 1855-1*, Center for Transportation Research, University of Texas, Austin, TX.

Thompson, M.K., Ziehl, M.J., Jirsa, J.O., and Breen, J.E. (2005), "CCT Nodes Anchored by Headed Bars - Part 1: Behavior of Nodes." *ACI Structural Journal*, Vol. 102(6), pp. 808-815.

Thompson, M.K., Jirsa, J.O., and Breen, J.E. (2006a), "CCT Nodes Anchored by Headed Bars - Part 2: Capacity of Nodes." *ACI Structural Journal*, Vol. 103(1), pp. 65-73.

Thompson, M.K., Ledesma, A., Jirsa, J.O., and Breen, J.E. (2006b), "Lap Splices Anchored by Headed Bars." *ACI Structural Journal*, Vol. 103(2), pp. 271-279.

Thompson, M.K., Jirsa, J.O., and Breen, J.E. (2006c), "Behavior and Capacity of Headed Reinforcement." *ACI Structural Journal*, Vol. 103(4), pp. 522-530.

Wright, J.L. and McCabe, S.L. (1997), "The Development Length and Anchorage Behavior of Headed Reinforcing Bars." *SM Report No. 44*, University of Kansas Center for Research, Inc., Lawrence, Kansas.